

# Large-scale turbulence structures in shallow separating flows

Grootschalige turbulente structuren  
in ondiepe loslatende stromingen

Proefschrift

ter verkrijging van de graad van doctor  
aan de Technische Universiteit Delft,  
op gezag van de Rector Magnificus prof.ir. K.C.A.M. Luyben,  
voorzitter van het College voor Promoties,  
in het openbaar te verdedigen op maandag 30 mei 2011 om 15.00 uur

door

Harmen TALSTRA  
civiel ingenieur  
geboren te Amsterdam.

Dit manuscript is goedgekeurd door de promotoren:

Prof.dr.ir. W.S.J. Uijttewaal

Prof.dr.ir. G.S. Stelling

Samenstelling promotiecommissie:

Rector Magnificus,	voorzitter
Prof.dr.ir. W.S.J. Uijttewaal,	Technische Universiteit Delft, promotor
Prof.dr.ir. G.S. Stelling,	Technische Universiteit Delft, promotor
Prof.dr.ir. G.J.F. Van Heijst,	Technische Universiteit Eindhoven
Prof.dr. N.G. Wright,	University of Leeds
Prof.dr.ir. B.J. Boersma,	Technische Universiteit Delft
Dr.ir. R.J. Labour,	Technische Universiteit Delft
Dr.ir. R.E. Uittenbogaard,	Deltares Software Centre
Prof.dr.ir. A.E. Mynett,	Technische Universiteit Delft / UNESCO-IHE, reservelid

This research is supported by the Dutch Technology Foundation STW, applied science division of NWO and the Technology Programme of the Ministry of Economic Affairs in the Netherlands, under grant number DCB.6037.

Cover design by Optima Grafische Communicatie, Rotterdam, the Netherlands

Cover photo: groyne fields along the River Waal near Opijnen, Gelderland, taken from Hydraulic Engineering Section picture database (Delft University of Technology)

Copyright © 2011 by H. Talstra

Typeset by L<sup>A</sup>T<sub>E</sub>X

Printed by Optima Grafische Communicatie, Rotterdam, the Netherlands

ISBN 978-94-6169-058-6

*Voor Inge*

*Ter nagedachtenis aan mijn moeder Elizabeth Schulp  
(1948-2006)*

HEER, niet trots is mijn hart,  
niet hoogmoedig mijn blik,  
ik zoek niet wat te groot is  
voor mij en te hoog gegrepen.

Nee, ik ben stil geworden,  
ik heb mijn ziel tot rust gebracht.  
Als een kind op de arm van zijn moeder,  
als een kind is mijn ziel in mij.

Israël, hoop op de HEER,  
van nu tot in eeuwigheid.

*Psalm 131*

*“Het werk is opwindend. Het is nog het best te vergelijken met dat van een detective in een ingewikkelde misdaadroman. Het is het verzamelen van stukjes evidence die verscholen zitten tussen stapels irrelevante informatie. Het zoeken van goudkorrels in het zand. Je kijkt er overheen, je wordt voortdurend op het verkeerde been gezet. Het vergt, behalve logisch combineren en deduceren, ook geduld, intuïtie, creativiteit. Totdat dan, op sommige momenten, de stukjes op hun plaats vallen tot een logisch samenhangend geheel. Die momenten zijn niet talrijk, maar ‘bevrediging’ is een te zwak woord om zo’n beleving mee uit te drukken. Vreugde, geluk komt er dichterbij.*

*De weg die naar zulke momenten leidt is fascinerend, maar prettig is hij niet. Prettig is het woord dat de wereld beschrijft die ons in reclameboodschappen wordt voorgetoverd. Daar zien wij uitsluitend onbewolkte luchten, stralende gezichten, gelukkige gezinnetjes. Er is geen zweetdruppel te zien, er wordt geen traan vergoten. Geluk dat niet kost. In zo’n wereld leeft de wetenschappelijk onderzoeker niet. Van zijn werk heeft Edison gezegd dat het voor 99% uit transpiratie en voor 1% uit inspiratie bestaat. Zwoegen dus. Vertwijfeling als je alweer een doodlopende weg bent ingeslagen. Woede over banaliteiten als het uitvallen van de stroom of de watertoevoer, waardoor het werk van weken ongedaan gemaakt wordt. Dat is allemaal vergeten in de grootse momenten van de doorbraak. Of liever nog: juist tegen de achtergrond van het gezwog krijgen die momenten hun werkelijke glans. Het was de moeite waard vooral omdat het moeite heeft gekost.”*

A. van den Beukel, *De dingen hebben hun geheim*, p. 156  
Uitgeverij Ten Have, Baarn, 1990

*“Wat doe je nou moeilijk? Je moet gewoon beginnen.”*

Arendjan Talstra

# Preface

The present thesis is the result of a Ph.D. research project on large-scale shallow-flow turbulence, which has been performed in the Environmental Fluid Mechanics Laboratory at Delft University of Technology. This research project was initiated as a follow-up of a previous project, performed by Bram Van Prooijen, which has been reported in the Ph.D. thesis *Shallow Mixing Layers* [99]. While the former project has focused on large-scale turbulence dynamics in shallow mixing layer geometries, the present study has extended the analysis toward flow geometries that involve separation. The dynamics of quasi two-dimensional turbulence structures in shallow separating flows have been studied both experimentally and numerically.

This thesis can be divided into three parts: respectively on laboratory experiments, three-dimensional simulations and two-dimensional simulations. A number of schematized flow cases have been investigated in a large-scale shallow laboratory flume, using the free-surface measurement technique of Particle Image Velocimetry (PIV). Subsequently, detailed three-dimensional Large Eddy Simulations (LES) have been performed on a parallel cluster, providing useful 3D data on the flow cases studied experimentally as well as on additional flow geometries. The conclusions drawn may prove useful for e.g. design purposes in engineering practice. Finally, the flow cases studied before have been revisited by means of 2D depth-averaged computations, testing a new approach to accurately resolve large-scale shallow-flow turbulence in a 2D schematization. The thesis offers a rather complete picture of the turbulent flow cases that have been studied, both in terms of physical behavior and numerical modeling.

The author gratefully acknowledges the Dutch Technology Foundation STW (Stichting Technische Wetenschappen), who supported this research project.



# Abstract/Samenvatting

## Abstract

*‘Large-scale turbulence structures in shallow separating flows’*

Environmental shallow flows, like rivers, frequently contain large-scale turbulence structures (also called coherent structures, vortices or eddies) with length scales that are much larger than the water depth. As the shallow flow domain is confined in vertical direction by a bottom and a free surface while flow structures extend over larger horizontal distances, such large-scale eddies are often considered “quasi two-dimensional”; in this thesis they are abbreviated by the term 2DCS (Two-Dimensional Coherent Structures).

Sequences of 2DCS often emerge in regions of considerable transverse shear; this shear region can be induced by various causes, e.g. by the confluence of two streams with different flow velocities or by separation of the flow field from an obstacle or a sharp edge. Examples of the latter flow type are a shallow wake flow past an island, or the complex turbulent flow along harbor entrances or a series of river groynes. Shallow separating flows usually give rise to regions of flow recirculation (gyres); at the interface between steady gyres and the separated main flow region, sequences of dynamic vortices are often found which are continuously shed from the location of separation. These 2DCS gradually grow in size and energy while moving in downstream direction, and eventually dissipate due to the action of bottom friction. In real-life shallow flow situations complex large-scale turbulence may cause practical problems, with respect to e.g. river morphology (navigation depth), manoeuvrability of ships and stability of hydraulic structures.

In this thesis the genesis and behavior of quasi-2D 2DCS in a shallow separating flow are studied. The primary objective is to elucidate how these shed vortices are impacted by the presence of steady gyres. Subsequently, it is aimed to find methods to influence the large-scale turbulence pattern by means of geometry adaptations. Finally, it is investigated how the computational prediction of 2DCS by means of 2D numerical models can be improved. The key object of research is a schematized shallow-flow geometry, named Shallow Lateral Expansion (SLE); this refers to a straight channel with an abrupt side-ward widening, which gives rise to separation. This flow type is frequently compared to a so-called Shallow Mixing Layer (SML), which involves the confluence of two parallel streams.

The research work applies three methodologies: 1. laboratory experiments, 2. three-dimensional (3D) simulations and 3. two-dimensional depth-averaged (2DH) simulations.

The basis of the research work is given by laboratory data. Three basic variants of the SLE geometry have been investigated, systematically varying the width of the inflow section and the lateral expansion. Using the measurement technique of free-surface Particle Image Velocimetry (PIV), the spatial and temporal structure of the large-scale fluid motion at the water surface has been captured. The scale of the present experiments and their level of detail form an extension to previous work. The acquired data result in an analysis of

flow characteristics at the free surface: mean velocity field, kinetic energy and Reynolds stress levels, the width of the 2DCS region (mixing layer), length scales of 2DCS and steady gyres, as well as energy density spectra. It is observed that, while the separation event is forced by the solid wall topography, the process of vortex shedding is forced by the steady gyre configuration. The presence of a well-developed steady secondary gyre appears to be essential for the emergence of 2DCS. The length scale of these 2DCS, as well as the width of the mixing layer, can be described by means of a relatively simple model based on the assumption of self-similarity. The associated 2DCS turbulence intensities are significantly influenced by the water depth. For a relatively shallow steady gyre region, traveling 2DCS interact with the primary gyre, effectively enhancing the kinetic energy level of these large eddies. This eddy boosting effect appears to be weaker or absent for a relatively deep steady gyre region; hence, the underlying “gyre-vortex interaction” mechanism is considered a phenomenon that is typical for quasi-2D turbulence.

Supplementary data on the experimental flow cases mentioned above are provided by detailed 3D Large Eddy Simulations (LES). Although LES data systematically resolve much more energy of small-scale turbulent motion, the large-scale results compare well with previous PIV data, while the LES data yield additional information about the 3D structure of the flow. Despite the predominantly quasi-2D character of the 2DCS, secondary flow structures like upwelling and downdraft regions are present which play a significant role in lateral exchange of momentum along the mixing layer. Furthermore, the 3D data allow for checking the influence of inflow boundary conditions on the resulting turbulence. It is confirmed that the SLE geometry is quite insensitive to the upstream turbulence level due to the topographical forcing effect earlier mentioned. In contrast, similar LES data of a SML geometry show a large sensitivity of the 2DCS to upstream velocity fluctuations, as in this case 2DCS are initiated by large-scale components of upstream 3D bottom turbulence. Hence, SML and SLE flow cases exhibit two distinctively different mechanisms of 2DCS generation.

As a spin-off from the above LES computations, the basic SLE geometry is adapted systematically and its impact on the development of mixing layer 2DCS is assessed. It is found that the way in which steady gyres are exposed to the mainstream flow has consequences for large-eddy scales and energy. The placement of a downstream obstacle to compress the gyre pattern, such as a groyne, in combination with an upstream splitter plate to reduce the transverse shear turns out to be an effective measure to achieve a weaker 2DCS development. This measure also reduces lateral shear due to flow contraction upstream of the location of separation. The applicability of these insights was tested experimentally for a realistic groyne field flow case, both on laboratory scale and prototype scale; this has been a contribution to a pilot project initiated by the Dutch Ministry of Public Works. The placement of a splitter plate or pile sheet in front of a groyne head has proven effective to reduce flow contraction as well as lateral shear and secondary flow intensity along a groyne field, which is advantageous with respect to river morphology and navigation. Despite this successful outcome, a careful and critical approach remains necessary when one applies theoretical insights stemming from laboratory-scale data to real-world environmental hydraulic problems.

The methods used so far have aimed to generate data in order to identify physical processes that are relevant for shallow separating flow turbulence; the final part of this research focuses on improving the 2DH modeling of these flow types, as a simple and useful tool for engineering practice. Although 2DCS can be essentially captured by the 2D Shallow Water Equations, it is known that the essential dynamic interaction between these 2D eddies and smaller-scale 3D turbulence is lacking. This interaction hence must be modeled explicitly;



such a model is often called a backscatter model. In the present study a new backscatter model is proposed, which is coined Depth-Averaged Navier-Stokes with Large-Eddy Stimulation (DANSLES). This model integrates elements of several existing 2D turbulence models and combines their advantages. The resulting implementation is both generic and calibrated in a physically relevant way, while the computational cost is quite low thanks to the use of Fast Fourier (FFT) algorithms. DANSLES and various other 2D turbulence models are calibrated against a simple straight channel flow and subsequently tested against SML and SLE geometries. Shallow-flow turbulence patterns are satisfactorily reproduced by DANSLES. Nevertheless, the physical absence of secondary flow within 2D numerical models remains a natural shortcoming of depth-averaged turbulence modeling, which is not easily overcome except by the actual addition of some mesh resolution over the water depth. The DANSLES formulation is considered applicable to flow cases with arbitrary horizontal topography, provided that the water depth is constant. Extending the model toward cases with variable bathymetry would be a desirable improvement. Furthermore, the applicability of the model to prototype-scale problems should be checked by ample testing against field data, in addition to the present laboratory-scale calibrations for most existing backscatter models.

The present thesis offers new insights concerning the physical processes underlying large-scale turbulence development in a shallow separating flow. The impact of steady gyre patterns on 2DCS have been explained, as well as the distinctive difference between the SML and SLE geometries with respect to 2DCS generation. It has been demonstrated how large-scale turbulence structures can be manipulated by geometry adaptations. Finally, an elegant 2D turbulence model has been developed which may prove useful for simulating shallow-flow turbulence in practice.

## Samenvatting in het Nederlands

*‘Grootschalige turbulente structuren in ondiepe loslatende stromingen’*

In ondiepe waterlopen, zoals rivieren, komen regelmatig grootschalige turbulente structuren voor (ook wel coherente structuren of wervels genaamd) met afmetingen die aanzienlijk groter zijn dan de waterdiepte. Omdat de stroming in verticale richting wordt begrensd door een bodem en een vrij oppervlak, terwijl stromingsstructuren in horizontale richting veel groter kunnen zijn, worden zulke grootschalige wervels vaak beschouwd als “quasi-tweedimensionaal”; in dit proefschrift worden ze aangeduid met de afkorting 2DCS (Twee-Dimensionale Coherente Structuren).

Een serie van opeenvolgende 2DCS ontstaat vaak in gebieden met een aanzienlijke schuifspanning in de dwarsrichting van de stroming. Deze schuifspanning kan op verschillende manieren ontstaan, bijvoorbeeld door het samenvloeien van twee waterlopen met een verschillende stroomsnelheid, of doordat een stroming loslaat van de oever ter plaatse van een obstakel of scherpe rand. Enkele voorbeelden van loslatende stromingen zijn de zogstroming rondom een eiland en het complexe turbulente stroombeeld langs haveningangen of strekdammen (kribben) in rivieren. Loslating in ondiepe stromingen leidt vaak tot het ontstaan van recirculatiezones (neren); op het grensvlak tussen stationaire neren en de losgelaten hoofdstroom zijn vaak opeenvolgende dynamische wervels te vinden, die voortdurend worden “afgeschud” van het loslaatpunt. Deze 2DCS bewegen in stroomafwaartse richting en groeien geleidelijk in afmeting en energie; uiteindelijk zullen ze uitdempen als gevolg van bodemwrijving. In praktijksituaties kan complexe grootschalige turbulentie

praktische problemen veroorzaken: ze kan nadelige gevolgen hebben voor bijvoorbeeld de bodemligging van rivieren (een lokale ondiepte kan leiden tot verminderde bevaarbaarheid) en de stabiliteit van waterbouwkundige kunstwerken.

In dit proefschrift wordt het ontstaan en gedrag van grootschalige quasi-tweedimensionale wervels in ondiepe loslatende stromingen onderzocht. De kernvraag die daarbij is gesteld, is welke invloed het stationaire nerenpatroon heeft op dergelijke afgeschudde wervels. Vervolgens is gezocht naar manieren om het patroon van de grootschalige turbulentie te beïnvloeden door middel van het aanpassen van de stromingsgeometrie. Tenslotte is onderzocht hoe het gedrag van 2DCS beter kan worden voorspeld met behulp van numerieke berekeningen in twee dimensies. Het belangrijkste voorwerp van onderzoek is een geschematiseerde ondiepe stromingsgeometrie die met Shallow Lateral Expansion (SLE) wordt aangeduid. Dit is een recht ondiep kanaal met een abrupte zijwaartse verbreding, die loslating van de stroming veroorzaakt. Dit stromingstype wordt in dit onderzoek regelmatig vergeleken met een zogeheten Shallow Mixing Layer (SML); deze geometrie bestaat uit de samenvloeiing van twee parallel gelegen rechte ondiepe kanalen.

Het onderzoekswerk omvat drie benaderingen: 1. experimenten in een laboratorium-schaalmodel, 2. driedimensionale (3D) computersimulaties en 3. tweedimensionale dieptegemiddelde (2DH) simulaties.

De basis van het onderzoek bestaat uit de laboratoriumgegevens. Drie basale varianten van de SLE-geometrie zijn onderzocht, waarbij de breedte van het instroomgedeelte en van de zijwaartse expansie systematisch zijn gevarieerd. Voor het bepalen van de grootschalige vloeistofbeweging aan het wateroppervlak (in ruimte en tijd) is gebruik gemaakt van de meettechniek Particle Image Velocimetry (PIV) aan het vrije oppervlak. De uitgevoerde metingen vormen (gezien hun schaal en hun detailniveau) een aanvulling op reeds bestaand onderzoek. Met behulp van de verkregen data zijn de stromingskarakteristieken aan het wateroppervlak onderzocht: naast het gemiddelde snelheidsveld zijn de kinetische energie en de spanningen van Reynolds bepaald, alsmede de breedte van de 2DCS-zone (de menglaag), lengteschalen van 2DCS en stationaire neren en de bijbehorende energiedichtheidspectra. Waargenomen wordt dat, daar waar de loslating van de stroming geforceerd wordt door de topografie van vaste oevers, het verschijnsel wervelafschudding wordt geïnduceerd door de configuratie van stationaire neren. Met name de aanwezigheid van een voldoende ontwikkelde secundaire neer blijkt essentieel voor het ontstaan van 2DCS. De lengteschalen van deze 2DCS kunnen, evenals de menglaagbreedte, worden beschreven met behulp van een relatief eenvoudig model dat is gebaseerd op de aanname van gelijkvormigheid (“self-similarity”). De bijbehorende turbulentie-intensiteiten van 2DCS hangen sterk af van de waterdiepte. Als de zone met stationaire neren relatief ondiep is vindt een wisselwerking plaats tussen grootschalige wervels en de primaire neer, die de energieinhoud van deze wervels effectief doet toenemen. Dit wervelversterkende effect blijkt zwak of afwezig te zijn indien het gebied met stationaire neren relatief diep is. Om die reden kan worden verondersteld dat het onderliggende mechanisme van “wervel-neer-interactie” een typisch verschijnsel voor quasi-tweedimensionale turbulentie is.

Aanvullende data met betrekking tot de bovenstaande stromingsgevallen zijn verkregen door middel van gedetailleerde 3D Large-Eddy Simulaties (LES). Hoewel met dit soort simulaties systematisch veel meer energie van kleinschalige turbulente bewegingen wordt opgelost dan met behulp van PIV-metingen, komen de resultaten wat betreft grootschalige turbulentie goed met elkaar overeen. Daarnaast bieden de LES-data aanvullende informatie over de 3D-structuur van de stroming. Ondanks het overheersende quasi-tweedimensionale karakter van de 2DCS, blijken hierin toch secundaire stromingspatronen aanwezig te zijn die een niet-verwaarloosbare bijdrage leveren aan de uitwisseling van impuls in de menglaag-

zone. Daarnaast bieden 3D-data de mogelijkheid om na te gaan welke invloed de randvoorwaarden bij de instroomrand hebben op de grootschalige turbulentie. Zoals reeds tevoren verwacht blijkt de SLE-geometrie tamelijk ongevoelig te zijn voor het niveau van bovenstroomse turbulentie, aangezien de grootschalige wervels in deze geometrie worden geforceerd door de configuratie van oevers en neren. Vergelijkbare LES-data van een SML-geometrie laten daarentegen een sterke gevoeligheid van de 2DCS voor bovenstroomse turbulentie zien, aangezien in dit geval de grote wervels worden opgewekt door grootschalige componenten van de 3D-bodemturbulentie. Dit toont aan dat de SML- en SLE-stromingsgevallen corresponderen met twee onderscheidend verschillende mechanismen voor het ontstaan van 2DCS.

Naar aanleiding van het bovenstaande zijn aanvullende LES-berekeningen uitgevoerd, waarbij de basale SLE-geometrie telkens systematisch is aangepast. Op deze manier is het effect hiervan op de ontwikkeling van grootschalige menglaagwervels afgeschat. Het blijkt dat de mate waarin stationaire neren worden blootgesteld aan de losgelaten hoofdstroming gevolgen heeft voor de schaal en energie van menglaagwervels. Het aanbrengen van een benedenstrooms obstakel (zoals een strekdam) om het nerenpatroon te comprimeren blijkt een effectieve maatregel om de 2DCS-ontwikkeling te verzwakken, met name in combinatie met een bovenstroomse scheidingsdam om de grote schuifspanning nabij het loslaatpunt te verminderen. Door een dergelijke maatregel kan ook eventuele stromingscontractie in de omgeving van het loslaatpunt worden verminderd, hetgeen eveneens bijdraagt aan de reductie van de schuifspanning. De bruikbaarheid van bovenstaande inzichten is getest met behulp van een aanvullend experiment in een realistische kribvakstroming, zowel op laboratoriumschaal als op prototypeschaal. Dit experiment vormde een bijdrage aan een pilot-project in de rivier de Waal, dat werd geïnitieerd door de directie van Rijkswaterstaat Oost-Nederland. Het is gebleken dat plaatsing van een scheidingsdam of damwand recht voor een kribkop, parallel aan de rivierstroming gericht, een effectieve maatregel is: zowel de stromingscontractie ter plaatse als de lokale schuifspanning en de secundaire stromingsintensiteit in de menglaag langs een kribvak worden aanzienlijk gereduceerd, hetgeen voordelig is voor wat betreft de bodemligging en de scheepvaart. Ondanks dit succesvolle resultaat blijft een voorzichtige en kritische houding altijd noodzakelijk bij het vertalen van theoretische inzichten naar praktijkproblemen in de waterbouwkunde.

De hierboven gebruikte onderzoeksmethoden hebben als doel gehad om data te genereren, waarmee de voor ondiepwaterturbulentie relevante fysische processen zijn geïdentificeerd. Het sluitstuk van het onderzoek is gericht op de verbetering van de 2D-modellering van deze ondiepe stromingen, ten behoeve van een bruikbaar instrument voor de ingenieurspraktijk. Hoewel 2DCS in principe zonder problemen kunnen worden opgelost door middel van de tweedimensionale ondiepwatervergelijkingen, ontbreekt in een 2D-model uiteraard de essentiële wisselwerking tussen grootschalige 2D-wervels en kleinschaliger 3D-turbulentie. Deze interactie moet daarom expliciet worden toegevoegd met behulp van een aanvullend turbulentiemodel, een zogeheten “backscattermodel”. In dit proefschrift wordt een nieuw backscattermodel voorgesteld met de naam DANSLES (Depth-Averaged Navier-Stokes with Large-Eddy Stimulation). Dit model is een unificatie van enkele bestaande 2D-turbulentieformuleringen en combineert de voordelen van deze modellen. De implementatie van DANSLES is generiek en op fysisch relevante wijze gecalibreerd. Dankzij het gebruik van Fast Fourier-algoritmen (FFT) vereist toepassing van het model geen significante extra rekenkracht. DANSLES en verscheidene andere 2D-turbulentiemodellen zijn gecalibreerd met behulp van een eenvoudige rechte kanaalstroming, en zijn vervolgens getest op de eerder onderzochte SML- en SLE-geometrieën. De kenmerkende patronen van ondiepwaterturbulentie worden door DANSLES op bevredigende wijze gereproduceerd.

Niettemin blijft een dieptegemiddelde turbulentiemodellering een belangrijke natuurlijke tekortkoming houden, namelijk de afwezigheid van secundaire stroming. Deze moeilijkheid kan alleen worden opgelost door het feitelijk toevoegen van enige resolutie in de verticaal. Het DANSLES-model kan in principe worden gebruikt voor stromingsgevallen met arbitraire horizontale topografie; de belangrijkste beperking van het model is de vooralsnog constante waterdiepte. Uitbreiding van het model, teneinde het geschikt te maken voor gevallen met variabele bathymetrie, is voor de toekomst zeker wenselijk. Daarnaast zou in het algemeen de bruikbaarheid van backscattermodellen voor stromingsgevallen op prototype-schaal moeten worden onderzocht door middel van tests met velddata; dit zou een nuttige aanvulling zijn op de bestaande calibraties op laboratoriumschaal van veel backscattermodellen.

Het onderhavige proefschrift biedt nieuwe inzichten met betrekking tot de fysische processen die aan de ontwikkeling van grootschalige turbulente wervels in ondiepe loslatende stromingen ten grondslag liggen. De invloed van stationaire nerenpatronen op de ontwikkeling van 2DCS is uiteengezet, alsmede het onderscheidende verschil tussen de SML- en SLE-geometrieën voor wat betreft het ontstaan ervan. Getoond is hoe grootschalige turbulente wervels kunnen worden beïnvloed door geometrie-aanpassingen. Tenslotte is een elegant 2D-turbulentiemodel ontwikkeld dat nuttig kan blijken te zijn voor de simulatie van ondiepwaterturbulentie in de praktijk.

# Contents

<b>Preface</b>	<b>v</b>
<b>Abstract/Samenvatting</b>	<b>vii</b>
Abstract . . . . .	vii
Samenvatting in het Nederlands . . . . .	ix
<b>1 Introduction</b>	<b>1</b>
1.1 Research context . . . . .	1
1.2 General aspects of shallow-flow turbulence . . . . .	2
1.3 Examples . . . . .	3
1.4 Influence of solid walls; various geometries . . . . .	7
1.5 Objective and thesis outline . . . . .	9
<b>2 On shallow-flow turbulence and flow separation</b>	<b>11</b>
2.1 Introduction . . . . .	11
2.2 Shallowness and its effect on turbulence . . . . .	11
2.2.1 Basic equations; vorticity and vortex stretching . . . . .	11
2.2.2 Theoretical behavior of two-dimensional flows . . . . .	13
2.2.3 Real-life behavior of a quasi-2D shallow flow . . . . .	15
2.3 On flow separation . . . . .	20
2.3.1 Definition . . . . .	20
2.3.2 Terminology: recirculation zones and vortex shedding . . . . .	21
2.4 Investigation of shallow recirculating flows . . . . .	25
2.5 Research methodology . . . . .	26
<b>3 Laboratory experiments</b>	<b>29</b>
3.1 Introduction . . . . .	29
3.2 Experimental setup . . . . .	29
3.3 Measurement techniques . . . . .	31
3.3.1 Visualization of the flow . . . . .	31
3.3.2 Particle Image Velocimetry (PIV) . . . . .	32
3.3.3 Detection of coherent structures: vector potentials . . . . .	34
3.4 Test run observations: general flow features . . . . .	36
3.4.1 Effect of shallowness on the primary gyre . . . . .	37
3.4.2 Effect of shallowness on the secondary gyre . . . . .	39
3.4.3 Intermittency effects in the main flow . . . . .	39
3.4.4 The vortex shedding process . . . . .	40
3.5 PIV data analysis: time-averaged flow statistics . . . . .	43
3.6 PIV data analysis: spectral statistics . . . . .	52

3.7	PIV data analysis: conditional statistics . . . . .	57
3.7.1	Principles of conditional averaging . . . . .	57
3.7.2	Conditionally averaged output: length and velocity scales . . . . .	58
3.8	Summary and discussion . . . . .	62
<b>4</b>	<b>3D LES computations: basic geometries</b>	<b>65</b>
4.1	Introduction . . . . .	65
4.2	Description of the 3D LES model . . . . .	66
4.2.1	The concept of Large Eddy Simulation . . . . .	66
4.2.2	General modeling aspects . . . . .	67
4.2.3	Boundary conditions . . . . .	68
4.2.4	Solution algorithm . . . . .	70
4.3	Model input . . . . .	71
4.4	Comparison with PIV data . . . . .	75
4.4.1	Flow patterns and length scales . . . . .	76
4.4.2	Energy content . . . . .	81
4.4.3	Energy density spectra . . . . .	86
4.5	Influence of upstream perturbations . . . . .	88
4.6	Secondary flow . . . . .	93
4.7	Lateral momentum transfer . . . . .	97
4.8	Summary and discussion . . . . .	101
<b>5</b>	<b>Influence of geometry variations</b>	<b>103</b>
5.1	Introduction . . . . .	103
5.2	Strategies for geometry adaptations . . . . .	103
5.3	Geometry variations: 3D LES results . . . . .	106
5.3.1	Mean flow patterns . . . . .	106
5.3.2	Horizontal length scales . . . . .	110
5.3.3	Lateral momentum transfer . . . . .	110
5.3.4	Horizontal anisotropy . . . . .	111
5.3.5	Vertical turbulence intensities . . . . .	118
5.4	Review of geometry variations: effectiveness . . . . .	118
5.5	Application to groyne fields: experimental data . . . . .	120
5.6	Summary and discussion . . . . .	128
<b>6</b>	<b>2D depth-averaged computations</b>	<b>131</b>
6.1	Introduction . . . . .	131
6.2	Background; importance of a backscatter model . . . . .	131
6.3	Basic equations . . . . .	133
6.3.1	2D Shallow Water Equations . . . . .	133
6.3.2	Residual closure terms . . . . .	134
6.3.3	Eddy viscosity-type models: Elder's term and HLES . . . . .	135
6.4	The DANSLES backscatter model . . . . .	137
6.4.1	DA-LES . . . . .	138
6.4.2	2D-TRANS+KS . . . . .	141
6.4.3	The unified DANSLES formulation . . . . .	145
6.5	Description of the 2DH model implementation . . . . .	151
6.5.1	Numerical solver (FINLAB) . . . . .	151
6.5.2	Model input . . . . .	152

6.6	Numerical results . . . . .	155
6.6.1	Straight Channel Flow (SCF) . . . . .	155
6.6.2	Shallow Mixing Layer (SML) . . . . .	161
6.6.3	Shallow Lateral Expansion (SLE) . . . . .	164
6.7	Evaluation of various backscatter models . . . . .	168
6.8	Extension to computations with multiple layers . . . . .	169
6.9	Summary and discussion . . . . .	172
<b>7</b>	<b>Conclusions and recommendations</b>	<b>175</b>
7.1	General overview . . . . .	175
7.2	Synthesis . . . . .	177
7.2.1	Generation mechanisms of 2DCS and vortex shedding . . . . .	177
7.2.2	Effects of shallowness on 2DCS development . . . . .	177
7.2.3	Sensitivity to upstream perturbations . . . . .	178
7.2.4	Impact of geometry variations . . . . .	179
7.2.5	2DH modeling aspects . . . . .	180
7.3	Utilization . . . . .	181
7.4	Recommendations . . . . .	182
<b>A</b>	<b>On vector potential functions</b>	<b>185</b>
<b>B</b>	<b>Construction of IFFT velocity fields</b>	<b>187</b>
<b>C</b>	<b>Integration of backscatter spectra</b>	<b>191</b>
	<b>Bibliography</b>	<b>193</b>
	<b>Notation</b>	<b>201</b>
	<b>Nawoord</b>	<b>205</b>
	<b>Curriculum Vitae</b>	<b>209</b>
	<b>Poëtisch supplement</b>	<b>211</b>





# Chapter 1

## Introduction

### 1.1 Research context

This thesis is about turbulence in shallow-water flows, especially about large-scale horizontal turbulence structures that can be found in such flows. As only a few conversations with various people will indicate, the term “turbulence” in general is most often associated by the wider public with the well-known irregular and uncomfortable type of air motion experienced by airplanes. Turbulent flows, however, do abundantly occur in all kinds of fluid media in nature, both liquids and gases. When it comes to the context of environmental fluid mechanics, it can be stated that practically all fluid flows that are relevant for civil engineering practice have a turbulent character. Obvious examples of these are e.g. river flows, channel flows and tidal flows in oceans or coastal seas.

Generally a turbulent flow contains vortices, also called “eddies”, “coherent structures” or “turbulence structures”. These are structures of dynamic recirculation, emerging from internal flow instabilities. Although usually the size and boundaries of individual vortices cannot be uniquely determined, it is often possible to define length scales  $\mathcal{L}$  and velocity scales  $\mathcal{U}$  to characterize the behavior of various eddy types within a flow, particularly the dominant energy-containing large eddies. Environmental shallow flows often involve a wide range of eddy length scales, ranging from micro-scale vortices up to large-scale coherent structures with horizontal length scales that are much larger than the water depth ( $\mathcal{L} \gg H$ ). The existence of such large structures is a typical characteristic of shallow-flow turbulence. Such large eddies are frequently observed in regions of large horizontal velocity differences or in the neighborhood of obstacles, where the flow is separating from the wall (see Chapter 2 for a full description of flow separation). Examples are e.g. flow past river groynes, a confluence of two rivers, wakes of islands in coastal seas, or flow past harbor entrances. The shallow-flow turbulence situations investigated in this thesis are mainly representative for river flow situations, where the mean flow is usually unidirectional.

Like all turbulence, environmental shallow-flow turbulence cannot be straightforwardly predicted in detail because of its chaotic nature. Usually it will take elaborate experimental work (field data or laboratory data) or detailed numerical simulations to predict turbulence behavior in real-life situations with some accuracy. It is of practical relevance to improve the understanding and modeling of large-scale shallow-flow turbulence. Environmental flows, like rivers, usually accommodate many different functionalities: e.g. the discharging of (waste)water, navigation, transport, recreational use and ecological values. These purposes may often conflict. On behalf of an optimal river management, it is necessary to know with some accuracy what effects will occur if the flow system (including turbulence) is changed

by human intervention.

A relevant example is given by several problems induced by groynes along lowland rivers in the Netherlands (see Figure 1.5). Such obstacles induce complex flow patterns, including large-scale turbulence structures, at the interface between the main river channel and consecutive groyne fields. Shallow-flow turbulence in these regions enhances lateral exchange of momentum and conveyed material like sediment and pollutants. The induced flow pattern impacts river morphology: a sequence of alternating scour holes and deposition areas is often found along groyne field series. The former may threaten the stability of groyne constructions, whereas the latter lead to a decrease of navigation depth. Besides, large-scale turbulence itself can be problematic too for the manoeuvrability of ships, especially near harbor entrances. Finally, complex turbulent flow patterns imply a certain drowning hazard; in the Dutch situation, newspapers have reported numerous accidents with drowned swimmers along rivers with groynes over the years. The adaptation of large-scale turbulence patterns could be an effective way to mitigate some of these unwanted effects (see Chapter 5, especially Section 5.5).

In recent decades, various characteristic shallow-flow situations that contain large-scale eddies have been intensively investigated (both experimentally and numerically): e.g. shallow wakes (Chen and Jirka [22]), shallow jets (Giger et al. [39], Dracos et al. [32]), shallow mixing layers (Chu and Babarutsi [26], Uijttewaal and Tukker [94], Van Prooijen [99]) and shallow grid turbulence (Uijttewaal and Jirka [92]). These flow geometries have in common that its large-scale eddies arise from internal velocity gradients (free turbulence). The present study is mainly concerned with shallow-flow turbulence that arises from flow separation and involves the influence of sidewalls. A groyne field flow is one example of such a flow. Shallow separating flows often give rise to steady flow recirculations, also called gyres, which may impact the development of large-scale coherent structures (see Chapter 2). A key challenge encountered in this thesis is how to clarify this interaction between steady recirculations and dynamic large eddies.

The following sections contain a brief general description of shallow-flow turbulence, including some examples of flow situations where large-scale turbulence structures play a role. Based on this information a number of research questions can be formulated, together with a complete research objective and a brief thesis outline (Section 1.5).

## 1.2 General aspects of shallow-flow turbulence

Turbulent flows are present everywhere in nature and amongst them, shallow turbulent flows form an important subset. Essentially, turbulence is a chaotic phenomenon; shallow-flow turbulence, however, can be characterized as being “organized chaos”. The organization in such flows is visible by the presence of turbulence structures with length scales typically larger than the water depth ( $\mathcal{L} \gg H$ ), which can have relatively long lifetimes ( $\mathcal{T} \gg \mathcal{L}/U$ ) and are often strongly intercorrelated: sequences of large-scale turbulence structures often exhibit quite regular patterns.

A shallow flow is defined as a three-dimensional flow with one dimension significantly smaller than the other two dimensions. In the context of environmental fluid mechanics, this smaller dimension is usually the water depth. Jirka [47] describes several mechanisms inducing large-scale turbulence structures which are typical for shallow flows (see Section 2.2.3). Such large eddies have a predominantly two-dimensional character. Their dynamics are essentially different from smaller-scale eddies ( $\mathcal{L} < H$ ) that have a fully 3D character: i.e. a relatively short lifetime ( $\mathcal{T} \approx \mathcal{L}/U$ ), a weaker mutual correlation and a continuous

tendency to break up into smaller eddies. Although all turbulence in nature is essentially 3D, shallow-flow turbulence is often named “quasi-2D” (see e.g. Van Heijst [98]). Jirka [47] coined the abbreviation 2DCS in order to refer to *large-scale quasi-2D coherent structures*. This abbreviation will be used throughout this thesis. Obviously, 2DCS in a flow are always accompanied by smaller-scale 3D structures.

Generally turbulence is induced by shear in a direction normal to the local flow velocity, causing the flow to become unstable. The origins of such lateral shear can always be traced back to either wall friction (wall turbulence) or a transverse velocity gradient in the interior of the domain (free turbulence). An important mechanism responsible for the occurrence of internal velocity gradients is flow separation. Separation occurs when a flow boundary layer loses contact with the associated solid wall and breaks away from it. This can be due to geometrical reasons (e.g. the flow is not able to follow a complex boundary form or to smoothly bend around a corner) or dynamical reasons (a pressure gradient in the flow is disturbing the local boundary layer equilibrium). Separating flows include a region of strong transverse shear downstream of the location of separation, giving rise to large turbulence intensities and often an area of flow recirculation.

The shallow flows addressed in this thesis can be defined as quasi two-dimensional, mainly unidirectional, fully turbulent flows, in which a horizontal transverse velocity gradient is present that is caused by separation. Such shallow separating flows can give rise to a sequence of 2DCS (“mixing layer”) at the interface between main flow and recirculation area. Furthermore, the presence of bottom friction and sidewall friction induces smaller-scale turbulence that interacts with the larger-scale 2DCS. Hence, both 3D and quasi-2D turbulence play a role of significance.

### 1.3 Examples

Sometimes environmental shallow turbulent flow patterns can be easily captured by means of aerial photography. This section presents a few typical examples of quasi-2D turbulence in sea/river flow and atmospheric flow situations.

Figure 1.1(a) is an example of a shallow turbulent wake flow: it depicts the vortex street behind the stranded oil tanker *Argo Merchant* on the Nantucket Shoals (near Massachusetts, USA), visualized by spilled oil that flows into the Atlantic Ocean<sup>1</sup>. Figure 1.1(b) shows a sequence of large atmospheric eddies (visualized by cloud patterns) in a wake behind the island of Guadalupe, at about 400 km from the west coast of Baja California, Mexico<sup>2</sup>. The volcanic mountains on the island (reaching to 1300 m above sea level) are an obstacle in the actual wind field (blowing from northwest to southeast). In both figures above, the flow is forced to bend along the obstacle and to separate behind it, giving rise to a shallow wake flow. Both wake flows are beautiful examples of a so-called Von Kármán vortex street (see e.g. Lloyd et al. [58]). As the 2DCS move downstream, they grow in size and eventually dissipate in the far field. In Figure 1.1(a) the ratio between vortex size and water depth  $\mathcal{L}/H$  is approximately 600 m/15 m  $\approx 40$ . In Figure 1.1(b) the length scale  $\mathcal{L}$  of the eddies is about 50 km while the flow height  $H$  is in the order of 1–2 km. Hence, both turbulent flows have a quasi-2D character. On the other hand,  $\mathcal{L}$  is sufficiently small in both cases to neglect the influence of earth rotation (Coriolis force) on the 2DCS.

<sup>1</sup>Image source: M.D. Van Dyke, “An Album of Fluid Motion”, Stanford, Parabolic Press, 1982.

<sup>2</sup>Image source: NASA Science Focus Website ([http://disc.sci.gsfc.nasa.gov/oceancolor/additional/science-focus/ocean-color/science\\_focus.shtml/vonKarman\\_vortices.shtml](http://disc.sci.gsfc.nasa.gov/oceancolor/additional/science-focus/ocean-color/science_focus.shtml/vonKarman_vortices.shtml)).

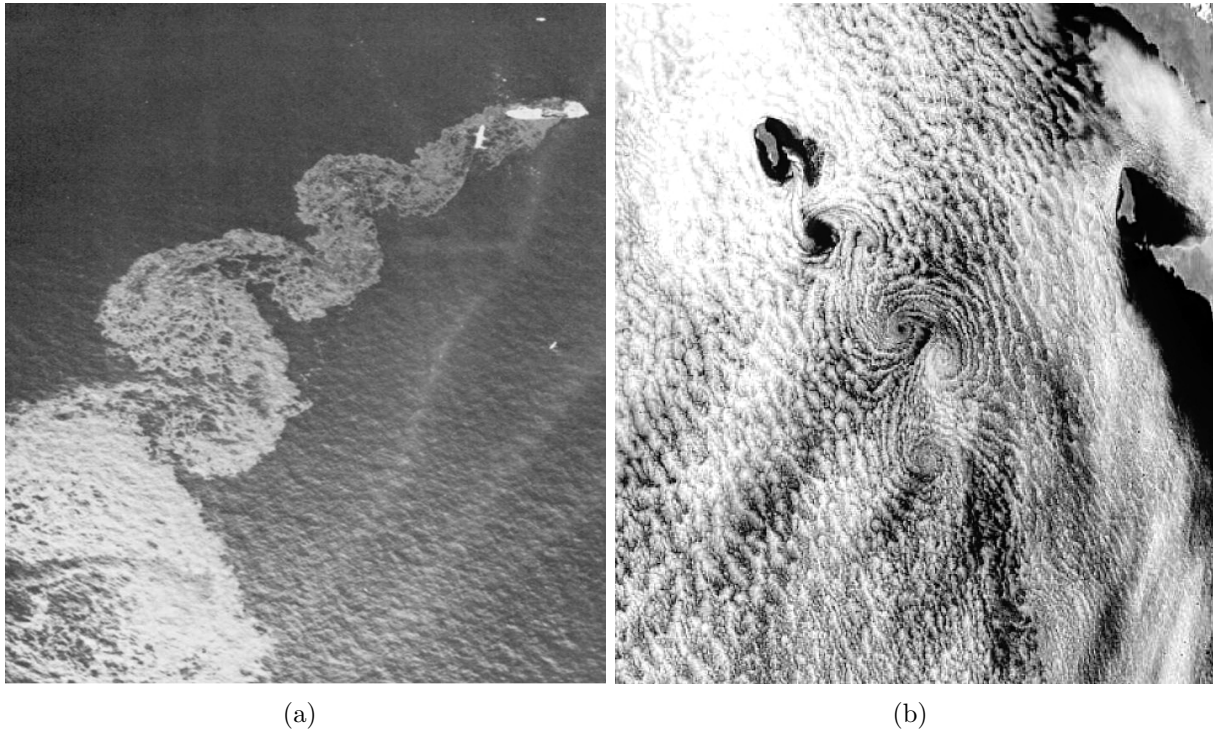


Figure 1.1: *Two examples of shallow turbulent wake flows: (a) Oil spill of stranded oil tanker Argo Merchant on the Nantucket Shoals, USA (source: Album of Fluid Motion, 1982); (b) Vortex street in the atmospheric wake behind the island of Guadalupe, Mexico (source: NASA).*

Another example is found at the outflow of the Dutch river IJssel into the Ketelmeer lake (Figure 1.2). In this case large-scale turbulence is visualized by a difference in sediment concentration between lake and river. The river flow forms a shallow jet that penetrates into the lake. Especially at the southern edge of the sediment-laden jet flow, large eddy structures are well visible. They show a typical length scale of about 30-50 m, which is presumably equal to about 6 to 10 times the water depth. As smaller-scale turbulence structures are visible too, it is confirmed that both 2DCS and 3D turbulence due to bottom friction are present.

A third typical example of a shallow shear flow can be found at the confluence of two rivers, provided that a velocity difference is present. Figure 1.3 gives a rather spectacular view on the confluence of the rivers Danube and Inn, in the city of Passau near the German-Austrian border. The presence of large-scale turbulence is visible thanks to the pronounced color difference between both rivers. From the south the river Inn conveys water from the Alpes that is strongly sediment-laden whereas the river Danube, coming from the northwest, contributes rather clear water. A shallow mixing layer (due to the lateral velocity difference) is developing. Again, both larger-scale 2DCS and smaller-scale 3D structures are visible. Furthermore it can be observed that the 2DCS induce lateral mixing, leading to a downstream decrease of the transverse sediment concentration gradient.

Shallow wakes, jets and mixing layers are three common types of free shallow shear flows. In other cases, the presence of sidewalls causes a separating flow to develop a region of recirculation. Two typical examples are recirculating flows in river harbors and groyne fields. Figure 1.4 shows a number of flow structures, induced by separation, at the entrance of a harbor along the Dutch river Waal. The shallow mixing layer in the harbor entrance



Figure 1.2: *Shallow turbulent jet at the outflow of the river IJssel, Netherlands (source: Google Earth 2010).*



Figure 1.3: *Shallow mixing layer at the confluence of the rivers Danube and Inn, Passau, Germany (source: Google Earth 2010).*



Figure 1.4: *Large eddies due to flow separation at a harbor entrance along the river Waal, Ochten, Netherlands (source: Google Earth 2010).*



Figure 1.5: *Separating and recirculating flow in groyne fields along the river Lek, Vianen, Netherlands (source: Google Earth 2010).*

gives rise to a weak recirculation flow inside the harbor region. Due to a slight difference in sediment content, turbulence structures at the river-harbor interface are visible that are responsible for the exchange of sediment. Finally, the groyne fields shown in Figure 1.5 are accommodating regions of strong flow recirculation and 2DCS, although groyne field eddies are often difficult to visualize by means of aerial photography (as the associated color differences are usually small here). Groyne fields are an example of a shallow separating flow where the presence of recirculations affects the large eddy development and consequent exchange processes (see Uijttewaal, Lehmann and Van Mazijk [93]).

## 1.4 Influence of solid walls; various geometries

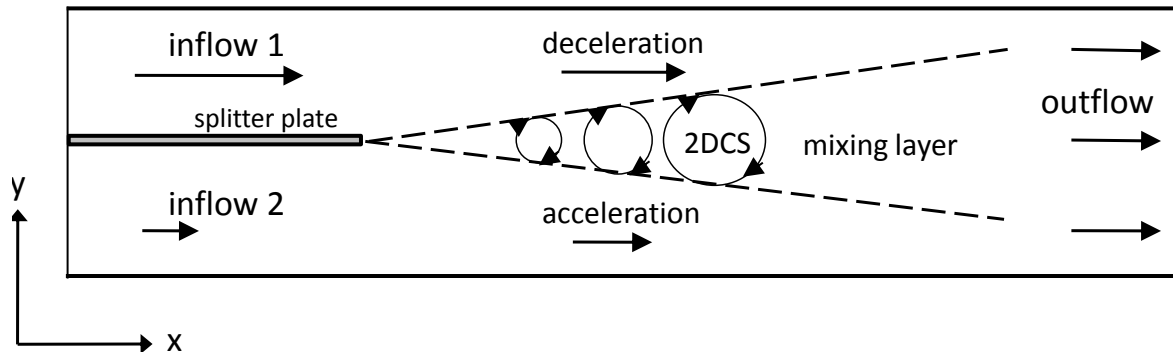
The shallow flow types depicted in Figures 1.1(b)-1.3 are the quasi-2D counterparts of three important types of plane free shear flows: wakes, jets and mixing layers. These are typical examples of free turbulence, arising from internal flow velocity gradients. Theoretically, plane free shear flows are characterized by an “infinite” depth and by a transverse gradient in the mean streamwise velocity, which decreases in downstream direction due to turbulent mixing. In these cases the downstream turbulence development is not impacted by solid walls (although the associated internal velocity gradient must obviously be induced by a solid structure upstream). It has been found that the transverse mean velocity profile can usually be described by some universal shape function, which is a function of streamwise flow quantities and geometrical parameters only; such a velocity profile is called a self-similar profile (see Pope [71]).

In contrast with plane free shear flows, shallow shear flows include a finite depth and hence the over-all presence of bottom friction. This implies that the influence of solid walls can never be neglected. An open-channel flow is a turbulent wall flow that extends over the full water depth, giving rise to complex small-scale 3D coherent structures (see Nezu and Nakagawa [66]). The presence of this so-called “3D bottom turbulence” (as it has often been coined) influences the over-all shear flow: it acts as an effective turbulence viscosity on the mean flow field and its larger-scale instabilities can trigger quasi-2D turbulence (see Section 2.2.3). In principle the presence of bottom friction spoils the self-similarity of these shallow flows. Nevertheless, it has been found that shallow shear flows do show a form of self-similarity, if the bottom friction effects are correctly incorporated into the self-similarity functions (see e.g. Van Prooijen [99]). This result can be explained by the fact that no sidewall effects are present.

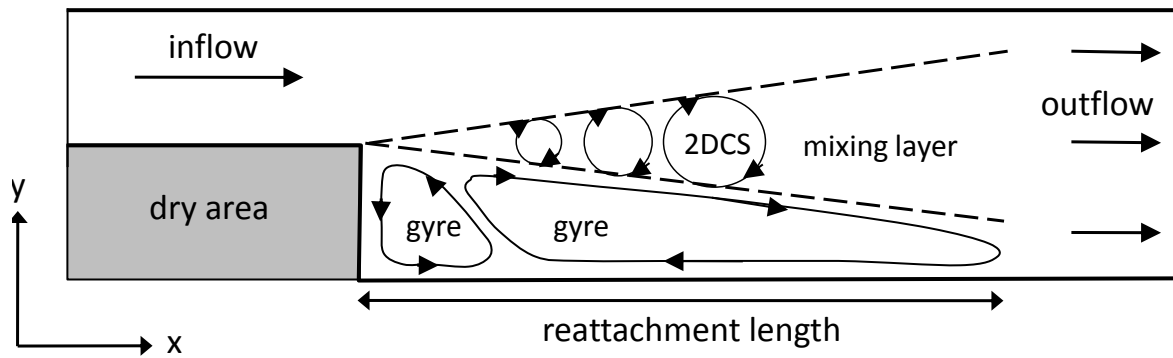
This thesis is concerned with shallow shear flows that have their origin in flow separation. More specifically, we are interested in separating flows containing a zone of steady recirculation. Such a recirculation (also called a gyre) can be considered as another large-scale shallow flow structure. Although statistically belonging to the mean flow and not to the dynamic turbulence fluctuations, a gyre is actually a large-scale coherent structure having quasi-2D properties. Therefore, dynamic 2DCS may be influenced not only by small-scale 3D bottom turbulence but also by the presence of steady gyres.

In fact, steady gyres represent the influence of sidewall friction on the mean flow. Therefore the concept of self-similarity is not automatically valid. Furthermore (as explained in Section 2.2.2), it is known that shallow flow structures having the same vorticity direction are able to interact with one another (“vortex merging”), whereas structures of opposite vorticity sign are not (see Van Heijst [98]). This typical quasi-2D turbulence behavior might play a role with respect to the genesis and evolution of 2DCS.

In order to illustrate the possible impact of steady gyres on 2DCS, two schematized shal-



(a)



(b)

Figure 1.6: *Top view on two schematized shallow flow geometries employed in this study: (a) the Shallow Mixing Layer (SML) and (b) the Shallow Lateral Expansion (SLE).*

low flow geometries are presented here that will play an important role throughout this thesis (see Figure 1.6). The first geometry contains the confluence of two parallel streams experiencing a lateral velocity difference (a); the second geometry involves an abrupt side-ward widening of a uniform channel flow, giving rise to flow separation (b). These cases will be referred to as Shallow Mixing Layer (SML) and Shallow Lateral Expansion (SLE) respectively; both flow geometries are suitable to be investigated on a laboratory scale, both experimentally and computationally.

In Figures 1.6(a)-(b) a number of geometrical features and characteristic flow phenomena have been indicated in order to illustrate the essential differences between both flow types. Apart from Figure 1.6(a), other basic outlines of the SML geometry can be found in Figures 4.2(b) and 6.2(b) throughout this thesis. Additional outlines of the SLE geometry can be found in Figures 3.1, 4.2(a) and 6.2(c).

It should be noted that the term “mixing layer” is often used in two ways. Firstly, it defines a specific shallow flow geometry which has been studied by many authors, e.g. by Tukker [89], Uijttewaai and Booij [91] and Van Prooijen [99]; this geometry has been coined SML throughout this thesis for the sake of brevity (see Figures 1.3 and 1.6(a)). Secondly, the term “mixing layer” can be defined in a more general sense: “a region of lateral mixing and lateral shear, widening in downstream direction, containing a sequence of large-scale 2DCS that move downstream”. The second (general) definition is usually adopted in this thesis, unless explicitly stated otherwise.



From the sketches in 1.6(a)-(b), it follows that both flow types (SML and SLE) include a shallow mixing layer. In both cases, sequences of large-scale eddy structures are induced by lateral shear over the mixing layer, which is caused by an upstream velocity difference. In both cases, lateral shear decreases with increasing downstream distance while streamwise momentum is transferred from the high toward the low velocity side due to momentum advection by 2DCS. In both cases, smaller-scale 3D turbulence due to bottom friction is obviously present as well. However, the difference in sidewall configuration impacts the over-all flow picture. The SML (a) is not impacted by sidewall friction as long as the widening mixing layer region does not touch any sidewall boundary layer. In case of the SLE (b), however, the event of *separation* (or *detachment*) gives rise to a shallow recirculation zone, usually containing two gyres; the zone length is often referred to as the *reattachment length*. The quasi-2D gyres actually penetrate into the mixing layer region and may therefore impact the development of associated 2DCS.

Although steady flow patterns of SLE-type geometries have been studied by e.g. Babarutsi et al. [7, 8] and Stelling [82], the interaction between 2DCS and steady gyres in such flow cases has not yet been elucidated in detail. An experimental onset to address this topic has been given by Uijtewaal, Lehmann and Van Mazijk [93]) for the case of groyne fields. Turbulent groyne field flows bear some similarity with SLE-type flows; however, they contain considerably more geometrical complexity. In this thesis, the emphasis will be on the explanation of the aforementioned interaction for a schematized turbulent flow case on a laboratory scale, which can be analyzed both experimentally and computationally.

## 1.5 Objective and thesis outline

Based on the introduction by the previous sections, the following relevant research questions can be formulated:

1. How does the presence of steady gyres influence the development of large-scale coherent structures (2DCS) in a shallow separating flow? Does this imply actual differences in shallow-flow turbulence behavior between e.g. SLE and SML flows?
2. In view of the former question: are there effective ways to manipulate 2DCS development by adapting the flow geometry (and hence the gyre pattern)? Does this provide any options to mitigate or remove unwanted effects of shallow-flow turbulence in practical engineering situations, e.g. in groyne field flows?
3. More generally: what are suitable options to improve the computational prediction of 2DCS, especially in two dimensions (as full 3D turbulence simulations will often be not feasible for practical problems)?

This thesis concerns the genesis and behavior of quasi-2D coherent structures in a shallow separating flow. The primary objective is to elucidate how such 2DCS are influenced by the presence of steady recirculation areas. Throughout this study, we obviously aim to address the research questions given above. Apart from this general objective, it is furthermore desired to fully investigate one specific shallow turbulent flow geometry on a laboratory scale, both experimentally and computationally, applying up-to-date measurement and simulation techniques which provide sufficiently detailed data in order to capture and analyze individual quasi-2D coherent structures.

The research work involves three approaches: laboratory experiments, three-dimensional (3D) turbulence simulations and depth-averaged (2DH) shallow-flow simulations.

In Chapter 2, we start with a general study on the topics of shallow-flow turbulence and flow separation. Based on this review, the research objective of this thesis can be translated into a methodology. It is furthermore argued that the Shallow Lateral Expansion (SLE) geometry is chosen to be the key object of research.

The basis of the research work is presented in Chapter 3. Laboratory experiments are performed on three variants of the SLE in order to visualize and analyze the development of 2DCS. The scale of the current experiments and their level of detail form an extension to previous work. The measurement technique of free-surface Particle Image Velocimetry (PIV) is used to capture the spatial structure of the fluid motion at the surface (see Weitbrecht et al. [112]).

The flow cases addressed in Chapter 3 are revisited in Chapter 4, being subject to full 3D numerical computations following the concept of Large Eddy Simulation (LES). Based on a LES implementation presented by Boersma [14], the large eddy dynamics of the flows are analyzed in a way analogous to the PIV experiments. A critical comparison between PIV data and LES results is given. These results are compared with LES computations of a basic SML geometry as well. Furthermore, the influence of the third dimension on quasi-2D turbulence patterns (e.g. secondary flow) are investigated by means of the acquired 3D data.

Chapter 5 contains a spin-off from the previous LES computations. The basic SLE geometry is adapted systematically in order to analyze how the genesis of 2DCS can be influenced by geometrical manipulations. It turns out that the way in which steady gyres are being exposed to the mainstream flow has consequences for large-eddy scales and turbulence intensities. These insights are subsequently applied to a test case from civil engineering practice, i.e. the design of groyne fields.

As the majority of numerical models used in civil engineering practice are still two-dimensional, Chapter 6 investigates the way in which 2D depth-averaged numerical models can represent quasi-2D turbulence in shallow shear flows. Although 2DCS can be essentially captured by 2D models, it is known (see Van Prooijen et al. [102], Hinterberger et al. [44]) that the essential dynamic interaction between these 2D eddies and smaller-scale 3D turbulence is lacking. Therefore, this interaction has to be modeled explicitly. In Chapter 6 a new 2D turbulence model is proposed (coined DANSLES), which integrates and improves several existing formulations for 2D turbulence. Together with the existing approaches, the new model is tested against various shallow flow test cases; based on the results its suitability for practical shallow flow applications can be assessed.

In the final Chapter 7 the main conclusions are summarized and briefly discussed, together with a number of recommendations for future research.

# Chapter 2

## On shallow-flow turbulence and flow separation

### 2.1 Introduction

As pointed out in Chapter 1, two key characteristics of the turbulent flows addressed in this study are shallowness and separation. In the present chapter, some theoretical aspects of both topics are briefly reviewed. In Section 2.2 it is explained that shallowness has a profound impact on the dynamics of large-scale turbulence structures; furthermore, a number of physical mechanisms responsible for the generation of such structures are outlined. Section 2.3 addresses the topic of flow separation and the associated terminology. Both topics are brought together in Section 2.4, which gives a review of previous experimental and computational research performed on shallow separating and recirculating flows. Based on this information, Section 2.5 describes the methodology that is adopted to answer the research questions given in Section 1.5.

### 2.2 Shallowness and its effect on turbulence

#### 2.2.1 Basic equations; vorticity and vortex stretching

The turbulent channel flows addressed in this thesis satisfy the incompressible Navier-Stokes Equations, which read in conservative form (see Pope [71]):

$$\frac{\partial u_i}{\partial x_i} = 0 \quad \text{and} \quad (2.1)$$

$$\frac{\partial u_i}{\partial t} + \frac{\partial u_i u_j}{\partial x_j} + \frac{\partial P/\rho}{\partial x_i} - \frac{\partial}{\partial x_j} \nu \left( \frac{\partial u_i}{\partial x_j} + \frac{\partial u_j}{\partial x_i} \right) = f_i, \quad (2.2)$$

where  $u$  is the fluid velocity vector (in m/s),  $P$  is the hydrodynamic pressure (kg/ms<sup>2</sup>),  $\rho$  is a constant density (fresh water, 1000 kg/m<sup>3</sup>),  $\nu$  is a constant kinematic molecular viscosity (10<sup>-6</sup> m<sup>2</sup>/s) and  $f$  is a body force vector per unit mass (m/s<sup>2</sup>), which usually accounts for the gravity. Dimensional indices are represented by:  $i, j \in \{1, 2, 3\}$ . The velocity field  $u$  is said to be divergence free or solenoidal. The gravity body force can be eliminated by incorporating it into the pressure gradient. If we set  $f_i = -\partial(gx_3)/\partial x_i$  (with  $g = 9.81$  m/s<sup>2</sup> the gravitational acceleration) and define the so-called *non-hydrostatic normalized pressure* by  $p = P/\rho + gx_3$  (in m<sup>2</sup>/s<sup>2</sup>), Equation (2.2) can be rewritten into:

$$\frac{\partial u_i}{\partial t} + \frac{\partial u_i u_j}{\partial x_j} + \frac{\partial p}{\partial x_i} - \frac{\partial}{\partial x_j} \nu \left( \frac{\partial u_i}{\partial x_j} + \frac{\partial u_j}{\partial x_i} \right) = 0 \quad (2.3)$$

In this thesis,  $p$  is used throughout for the pressure instead of  $P$ . Equations (2.1) and (2.3) are to be completed with appropriate initial conditions and boundary conditions. At impermeable solid walls physically a no-slip boundary condition holds, whereas at the surface (considered as either a movable free surface or a rigid lid) a free-slip condition is valid (wind and atmospheric influences are neglected in this study).

Fluid motion is induced by hydrodynamic pressure gradients, while the velocity field is continuously deformed by the action of nonlinear momentum advection and viscosity. When equation (2.3) is written in dimensionless form, using a velocity scale  $\mathcal{U}$  and a length scale  $\mathcal{L}$ , the ratio of advective and viscous forces can be expressed by a single dimensionless parameter, the well-known Reynolds number:

$$Re = \frac{\mathcal{U}\mathcal{L}}{\nu} \quad (2.4)$$

Two features within the Navier-Stokes Equations are the essential cause of turbulence. Firstly, for large values of  $Re$  (typical values  $> 2000$ ), a flow problem can become hydrodynamically unstable (see [67, 71]) and eventually exhibit chaotic behavior. Secondly, the action of viscous forces (combined with no-slip boundary conditions) introduces rotation (or *vorticity*) into the velocity field, even when the initial flow field did not contain rotation. Due to the presence of vorticity, a chaotic flow field will always contain vortices or “eddies”. A quite compact definition of turbulence has been given by Nieuwstadt [67]: “*turbulence is chaotic vorticity*”.

Because of the important role of vorticity, turbulence is essentially a 3D phenomenon. From a physical point of view, the increasing chaos in turbulent flows is illustrated by the fact that vortices are unstable and tend to break up into smaller vortices. This basically implies that turbulent kinetic energy is transferred toward smaller scales, until the smallest eddies reach length scales at which their energy is transformed into heat by the action of viscosity (the so-called Kolmogorov scales). This ongoing breakdown of turbulent kinetic energy is often referred to as the “3D energy cascade”. The energy flux toward smaller length scales often leaves its footprint in the *energy density spectrum* of the turbulent motion. With respect to the 3D energy cascade, Kolmogorov (see Pope [71]) states on dimensional arguments that the spatial energy density spectrum  $E$  ( $\text{m}^3/\text{s}^2$ ) at small isotropic turbulence scales (the co-called inertial range) must be of the following form:

$$E(k) \sim \epsilon^{\frac{2}{3}} k^{-\frac{5}{3}} \quad (2.5)$$

where  $\epsilon$  ( $\text{m}^2/\text{s}^3$ ) is the rate of energy dissipation per unit mass, and  $k$  ( $\text{m}^{-1}$ ) is the “wave number” associated with a certain turbulence length scale  $\mathcal{L}$ . Vorticity plays a vital role in the energy cascade mechanism, as can be seen by taking the curl of equation (2.3), which yields the so-called *vorticity equation*:

$$\frac{D\omega_i}{Dt} \equiv \frac{\partial \omega_i}{\partial t} + u_j \frac{\partial \omega_i}{\partial x_j} = \omega_j \frac{\partial u_i}{\partial x_j} + \nu \frac{\partial^2 \omega_i}{\partial x_j^2} \quad (2.6)$$

where  $\omega$  ( $\text{s}^{-1}$ ) is the vorticity vector. This equation shows that the material derivative of the vorticity of a moving fluid particle is determined by two contributions, given by the right-hand side of the equation. The first term describes the interaction between the vorticity field and the velocity deformation field; the second term describes vorticity diffusion by

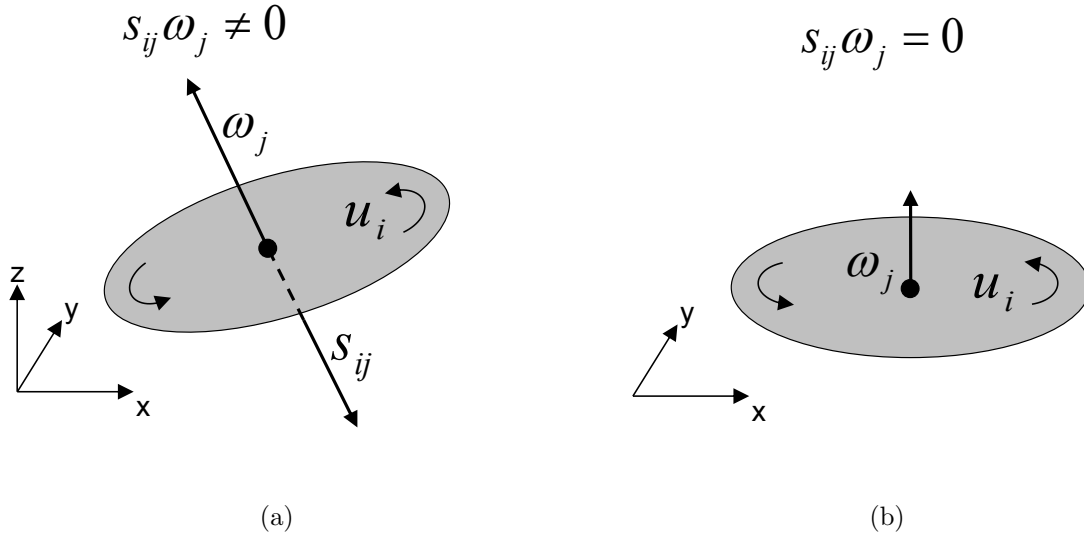


Figure 2.1: *Impact of the number of dimensions on vortex dynamics. In 3D space vortices can be stretched in the direction of the local vorticity vector, normal to the vortex plane (a); a vortex in a 2D plane cannot be stretched in the direction normal to that plane (b).*

molecular viscosity. The first term is called *vortex stretching term* and can be rewritten as:

$$\omega_j \frac{\partial u_i}{\partial x_j} = \frac{1}{2} \omega_j \left( \frac{\partial u_i}{\partial x_j} + \frac{\partial u_j}{\partial x_i} \right) = \frac{1}{2} \omega_j s_{ij} \quad (2.7)$$

If the velocity field is stretched in the direction of the local vorticity vector (i.e. normal to the associated vortex plane, see Figure 2.1(a)), the local vorticity in that direction will increase; rotational kinetic energy will be transferred to higher frequencies and hence to smaller scales, both in space and time. This vortex stretching mechanism is responsible for the spectral energy flux within the 3D energy cascade (see [71]).

### 2.2.2 Theoretical behavior of two-dimensional flows

Despite the intrinsic three-dimensionality of turbulence, many turbulent flow domains in nature are confined in the vertical direction. Such a flow is called a shallow flow; its large-scale turbulence is often considered as quasi two-dimensional. Although 2D turbulence is a *contradictio in terminis*, this classification yet makes sense because in practice the dynamics of quasi-2D turbulence structures can differ significantly from “normal” 3D turbulence. This can be shown by revisiting the vorticity equation (2.6). In two dimensions the vorticity vector consists of only one component, being perpendicular to the 2D velocity field everywhere (see Figure 2.1(b)). However, stretching of the 2D velocity field is impossible in this perpendicular direction. Hence the vortex stretching term vanishes, leading to:

$$\frac{D\omega_i}{Dt} = \nu \frac{\partial^2 \omega_i}{\partial x_j^2} \quad (2.8)$$

The remaining terms show that, theoretically, vorticity is a conserved quantity in 2D. Moreover, from (2.8) it follows that the total enstrophy (a measure for the amount of rotational kinetic energy) is approximately conserved too, apart from a small quadratic dissipation term due to viscosity:

$$\frac{D\Omega}{Dt} \equiv \frac{\partial\Omega}{\partial t} + u_j \frac{\partial\Omega}{\partial x_j} = \nu \frac{\partial^2\Omega}{\partial x_j^2} - \nu \left( \frac{\partial\omega_i}{\partial x_j} \right)^2, \quad (2.9)$$

where  $\Omega = \frac{1}{2}\omega_i^2$  ( $\text{s}^{-2}$ ) is the total enstrophy. The principle of enstrophy conservation is similar to that of energy conservation: kinetic energy is also conserved except for a quadratic dissipation term. This result follows from multiplication of equation (2.3) by  $u_i$ :

$$\frac{DE_k}{Dt} + \frac{\partial u_i p}{\partial x_i} = \frac{\partial}{\partial x_j} \nu u_i \left( \frac{\partial u_i}{\partial x_j} + \frac{\partial u_j}{\partial x_i} \right) - \frac{\nu}{2} \left( \frac{\partial u_i}{\partial x_j} + \frac{\partial u_j}{\partial x_i} \right)^2, \quad (2.10)$$

where  $E_k = \frac{1}{2}u_i^2$  ( $\text{m}^2/\text{s}^2$ ) is the total kinetic energy. Therefore, in the inviscid limit, the energy budget of a 2D flow in time and space is constrained by two conservation laws (2.9) and (2.10) (instead of only (2.10) for the 3D case). The conserved quantities  $E_k$  and  $\Omega$  can be written in spectral form:

$$E_k \equiv \frac{1}{2}u_i^2 = \int_0^\infty E(k) dk \quad (2.11)$$

$$\Omega \equiv \frac{1}{2}\omega_i^2 = \int_0^\infty k^2 E(k) dk \quad (2.12)$$

Hence  $\Omega$  can be expressed as the second moment of the spectral kinetic energy distribution, see Van Heijst [98]. This means that in a 2D flow not only the total amount of kinetic energy is conserved but also its variance over all length scales. According to Kraichnan [51] and Batchelor [10], this fact implies two simultaneous energy cascades. Suppose that a 2D flow situation is disturbed by some forcing mechanism with a characteristic length scale  $\mathcal{L}$ ; then it is possible to define a *forcing wave number*  $k_i \sim \mathcal{L}^{-1}$  where kinetic energy is added to the system. The combination of conservation laws (2.9) and (2.10) will cause energy redistribution: if kinetic energy is transferred from scale  $k_i$  to higher wave numbers (small scales)  $k > k_i$ , a compensating energy flux towards lower wave numbers (large scales)  $k < k_i$  must be present in order to keep the variance conserved. This transport of energy toward larger length and time scales is often called *backscatter* or *inverse energy cascade*; this principle is illustrated by Figure 2.2. Based on dimensional arguments, Kraichnan [51] proposes the following spectral forms to account for these two simultaneous processes:

$$E(k) \sim \begin{cases} \epsilon^{\frac{2}{3}} k^{-\frac{5}{3}} & \text{if } k < k_i \quad (\text{“inverse energy cascade”}) \\ \eta^{\frac{2}{3}} k^{-3} & \text{if } k > k_i \quad (\text{“enstrophy cascade”}) \end{cases} \quad (2.13)$$

where  $\epsilon$  ( $\text{m}^2/\text{s}^3$ ) is the rate of energy dissipation and  $\eta$  ( $\text{s}^{-3}$ ) is the rate of enstrophy dissipation per unit mass. The existence of the inverse energy cascade in the region  $k < k_i$  implies that, after some initial stage, kinetic energy tends to concentrate in large-scale vortices that are stable and do not break up. This principle is often referred to as “self-organization”, see Van Heijst [98]. Experiments and numerical simulations by e.g. Lilly [57], Van Heijst [98], Gotoh [40], Borue [17], Clercx et al. [28, 29] and Wells and Van Heijst [113] support the existence of two-dimensional flow structures according to the theory outlined above. From both experiments and simulations, specific vortex types come up that have been classified by Van Heijst [98]: e.g. monopolar, dipolar and tripolar vortex formations can be distinguished. These configurations are characterized by the fact that adjacent 2D vortices are able to coexist when they have opposite vorticity signs. Two monopolar 2D vortices of the same vorticity sign, on the other hand, are able to amalgamate

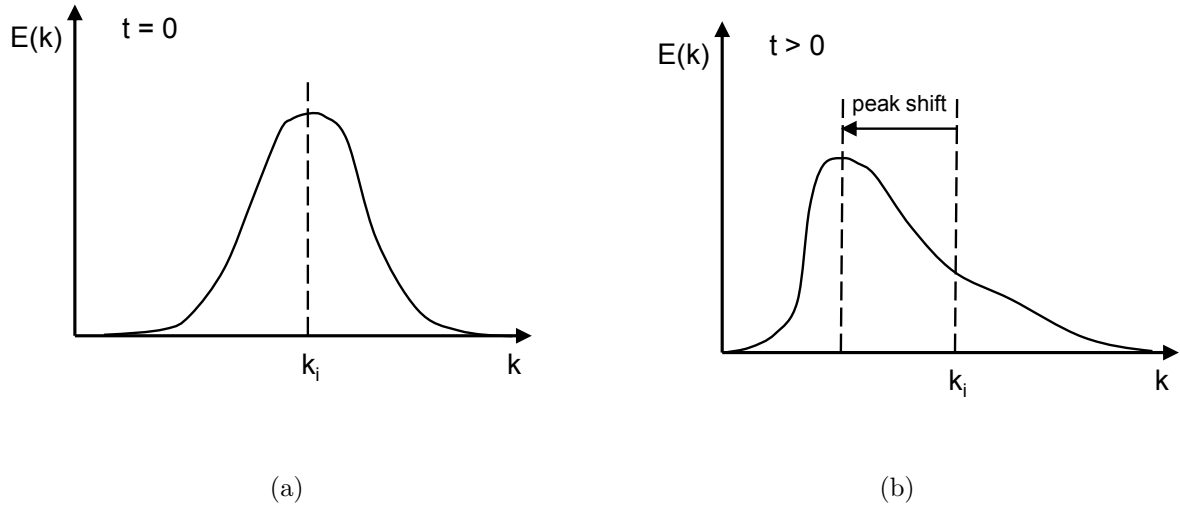


Figure 2.2: *Conceptual sketch of the spectral backscatter of kinetic energy toward larger scales (inverse energy cascade) in 2D flows. Initial situation (a); redistribution of energy while both  $E_k$  and  $\Omega$  remain conserved (b). This leads to a shift of the spectral peak (representing the energy-containing vortices) from the initial forcing scale to larger scales.*

and form a new larger eddy. This phenomenon, known as *vortex merging*, is a very visible and spectacular consequence of the existence of the inverse energy cascade. It is the natural counterpart of the vortex stretching mechanism that is responsible for eddies breaking up (Figure 2.1). An example of vortex merging in a numerical computation is given by Figure 2.3: panels (a)-(d) show four stages of the merging process. These results stem from a strictly 2D Large Eddy Simulation (LES), performed by the author of this thesis (see Chapter 4 for more information about the LES model applied).

### 2.2.3 Real-life behavior of a quasi-2D shallow flow

In principle the theoretical considerations of the last subsection are valid only for ideal 2D configurations in the inviscid limit. Reality usually tends to be both viscous and three-dimensional. In practical cases, nevertheless, shallow turbulent flows exhibit many 2D characteristics. This is referred to as quasi two-dimensional flow behavior. Although in a shallow flow the vortex stretching mechanism is not completely excluded, it is at least strongly hindered in the vertical dimension. If large-scale quasi-2D coherent structures are present in a shallow flow, these are often observed to be quite stable and only weakly dissipative. As pointed out in Section 1.2, Jirka [47] addresses these structures as “2D coherent structures” (2DCS).

The examples in Figure 2.4 give an extra illustration of the significant difference in behavior between 3D and quasi-2D coherent structures. Typical 3D turbulence configurations like smoke from a cigarette<sup>1</sup> in 2.4(a) exhibit a continuous breakup of vortices, leading to an eventually amorphous cloud of diffusive small eddies with a relatively short lifetime  $\mathcal{T} \approx \mathcal{L}/\mathcal{U}$  (see Section 1.2). A typical quasi-2D problem like the SML geometry, on the other hand, is characterized by both small 3D turbulence and 2DCS: the latter are well-discernible large-scale structures that remain intact for relatively long times  $\mathcal{T} \gg \mathcal{L}/\mathcal{U}$  while traveling through the flow domain. The SML geometry on laboratory scale depicted

<sup>1</sup>Image source: WellSphere health care website (<http://www.wellsphere.com>).

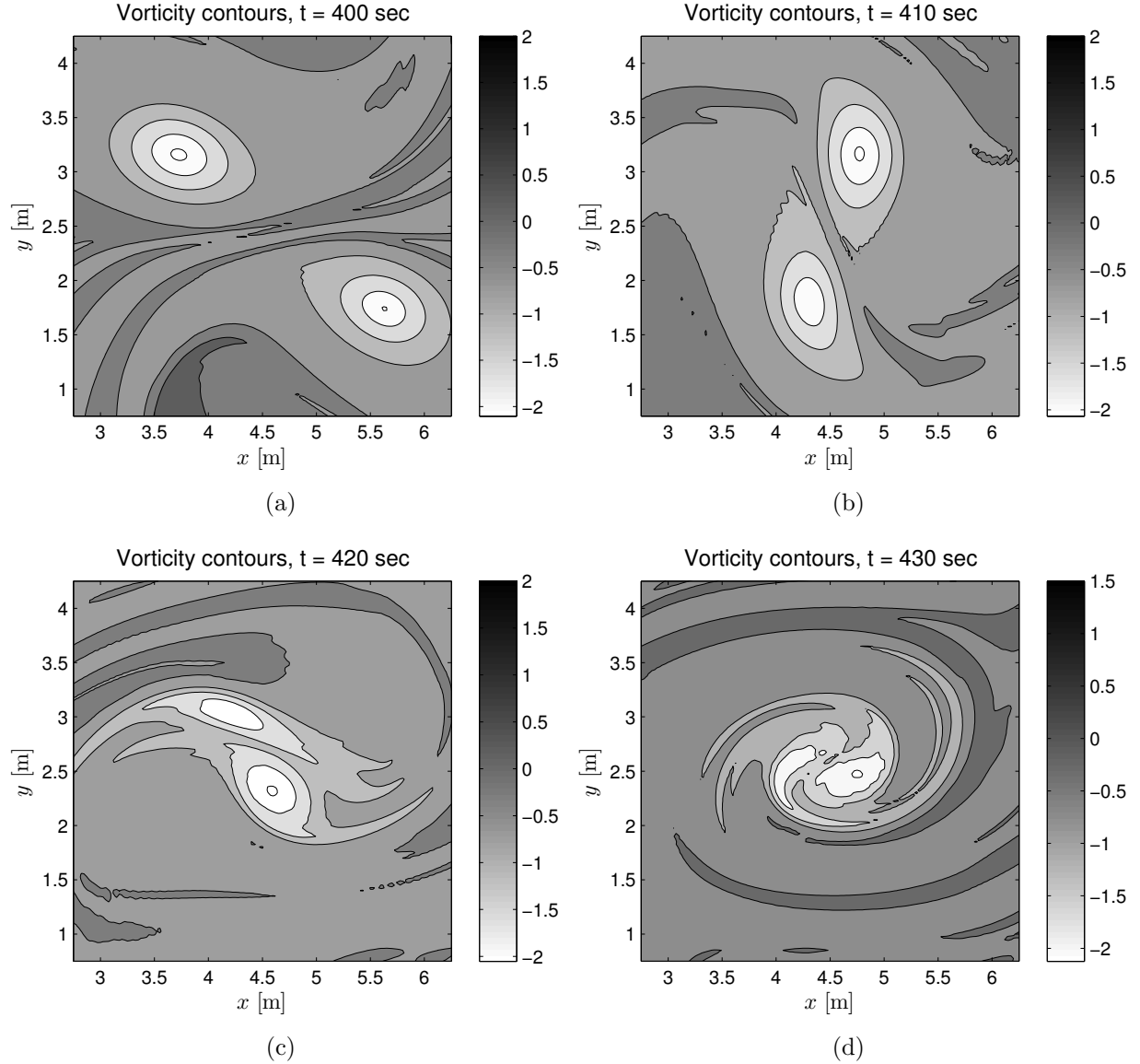


Figure 2.3: *Vortex pairing and merging due to the existence of the inverse energy cascade: vorticity contour plots. Results of two-dimensional Large Eddy Simulation (LES).*

in 2.4(b) has been investigated by Van Prooijen [99]. Other examples of shallow flows containing 2D coherent structures have already been given in Section 1.3.

Within the context of open-channel flows, the term “coherent structure” is usually applied to name the 3D vortical elements at sub-depth scale that are present near solid walls, especially near the bottom. These coherent structures are produced by ejection and sweep events near the wall; in terms of mean flow, they cause the well-known logarithmic velocity profile. See Nezu and Nakagawa [66] for a full review of these coherent structures.

In this study, the term “coherent structures” is always used to address 2DCS at supra-depth scale. They are defined by Jirka [47] as “connected large-scale turbulent fluid masses that extend uniformly over the full water depth and contain a phase-correlated vorticity, with the exception of a thin near-bottom boundary layer”. In [47], three types of generation mechanisms for 2DCS are distinguished, see Figure 2.5(a)-(c):

1. *Topographical forcing.* This is the strongest generation mechanism: due to the presence of obstacles in the flow field (e.g. groynes or islands), the flow is forced to



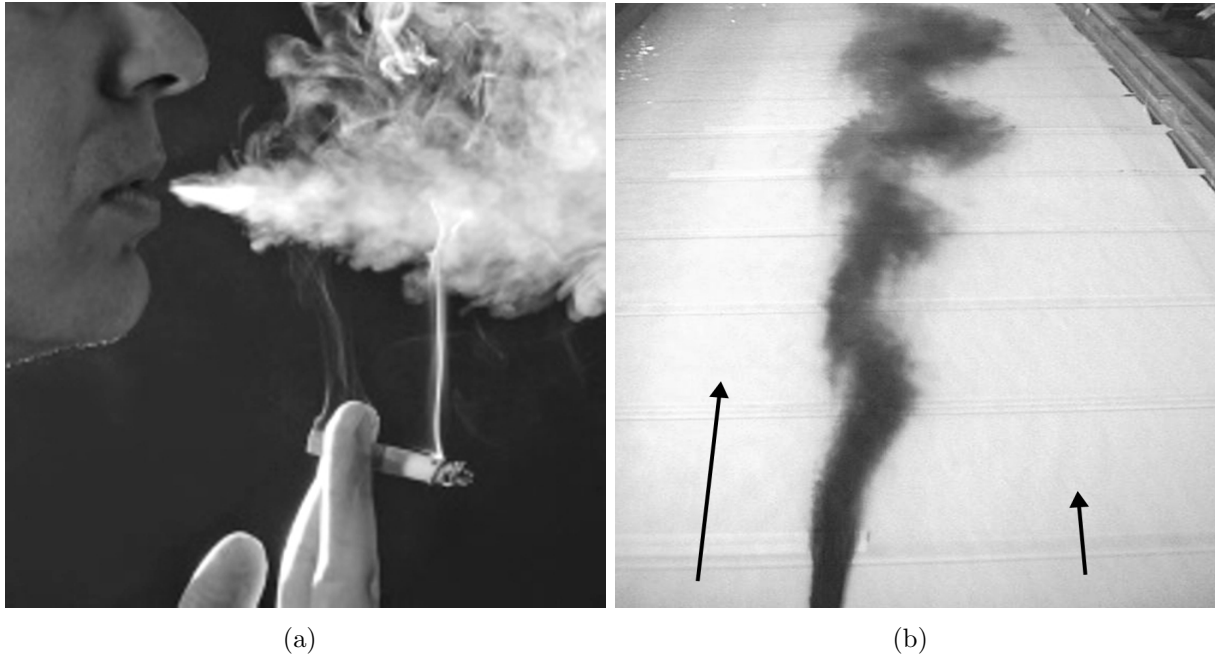


Figure 2.4: *Illustration of characteristic differences between 3D and 2D coherent structures: (a) 3D axisymmetric turbulent jet; (b) 2D shallow mixing layer (SML geometry, see [99]).*

separate from a solid wall, inducing return velocities and strong transverse shear giving rise to 2DCS. A well-known example of this mechanism is the Von Kármán vortex street in the wake of a bluff body within an otherwise uniform flow.

2. *Internal transverse shear instabilities.* In this case no separation occurs; due to a lateral velocity difference, hydrodynamic instabilities will emerge and gradually grow into 2DCS. Lateral velocity differences can be caused by e.g. river confluences (similar to SML geometries) or differences in depth and roughness (compound channels). This type of coherent structure generation is a fully internal turbulence feature; there is no external forcing besides the bottom friction.
3. *Secondary instability of base flow.* This is the weakest of the three mechanisms; there is only limited experimental evidence for it, although it has been actually observed in detailed numerical simulations (see e.g. Hinterberger [42] and Van Prooijen [99]). It describes the generation of 2DCS by the “upcascading” (backscatter) of 3D turbulence structures to larger scales. Theoretically, this is possible because of the existence of the inverse energy cascade. The backscatter effect might be triggered by e.g. underwater obstacles or by gradual decelerations in the base flow, but can also occur in a uniform turbulent wall flow, as is shown by Kim and Adrian [50]. It is stated by Van Prooijen [99] and Uijttewaai and Jirka [92] that the backscatter effect described here does not only account for the emergence of 2DCS in a uniform base flow, but is also essential for the development of 2DCS in flows with internal transverse shear (at least if no topographical forcing mechanism is present as well).

In all cases the generation and development of 2DCS sequences takes a certain travel time and a certain spatial distance from their origin. Various authors (Giger et al. [39], Uijttewaai and Tukker [94]) distinguish three different regions of 2DCS development, based on the ratio of eddy traveling distance  $x$  and water depth  $H$ . In the “near-field” region ( $x/H < 1$ ), 3D small-scale turbulence is dominant, but the mean transverse shear that is present is usually two-dimensional, mainly due to the shape of the geometry. At this

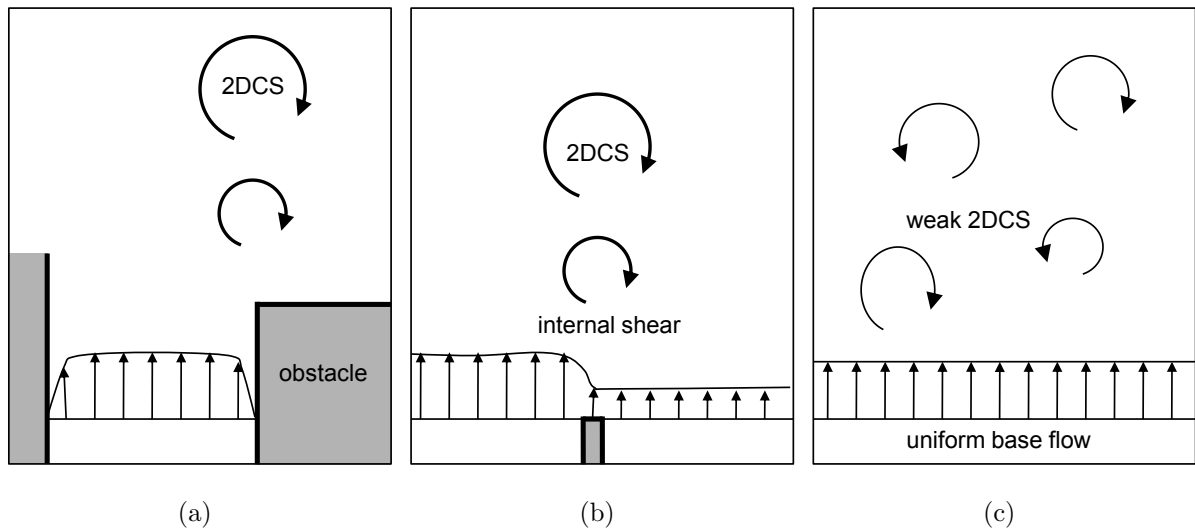


Figure 2.5: *Illustration of the principles of three generation mechanisms for 2DCS (see [47]): (a) Topographical forcing; (b) Internal transverse shear instabilities; (c) Secondary instability of base flow.*

point the emerging 2DCS do not yet “feel” the shallowness of the flow. In the “far field” ( $x/H > 10$ ), the 2DCS are well-developed in horizontal direction and eventually dissipate due to bottom friction; both mean flow and large-scale turbulence have a pronounced 2D character. The “middle field” ( $1 < x/H < 10$ ) is characterized by interaction between the growing 2DCS, mean flow and 3D bottom turbulence, resulting in mean secondary flow effects and 3D effects within the 2DCS, e.g. regions of upwelling and downdraft of fluid.

The development of 2DCS in shallow flows often forms a good illustration of the processes that govern quasi-2D turbulence, including the merging of individual vortices. Furthermore, the growth of 2DCS is characterized by *entrainment*: from outside the vortex street, non- or weakly turbulent fluid is continuously enclosed and absorbed into the growing coherent structures. Due to this entrainment, 2DCS are usually growing while moving in downstream direction. Eventually 2DCS will decay in the far-field region; the major mechanism governing this decay is energy loss due to bottom friction. The larger the size of an eddy relative to depth, the quicker the direct dissipation of its kinetic energy. This fact limits the maximum large eddy size  $\lambda$  that can be found in real-life shallow flows. Jirka [47] mentions a theoretical upper limit of  $\lambda_{max} = 2H/c_f$ ; a 2D coherent structure of this size will lose its rotational energy within one turnover. In very shallow flow cases, even the generation of 2DCS can already be suppressed by bottom friction.

Among the variety of shallow flow configurations that can contain 2DCS, a few basic types are often recalled: wakes, grid turbulence, jets and mixing layers. These basic configurations, originating from general 3D turbulence research, have their counterparts in shallow flow theory. Three of these four configurations have been illustrated in Section 1.3.

In 3D cases, the turbulence regime of these flow types is governed by the ratio between advective and viscous forces, which is expressed by the Reynolds number  $Re$ . In the corresponding quasi-2D cases, bottom friction is more important than (molecular) viscosity; hence, the behavior of these shallow flows is governed by the ratio between *horizontal lateral shear* and *bottom friction*. These two quantities respectively govern the production and dissipation of 2DCS kinetic energy. The ratio between both is expressed in a dimensionless stability parameter  $S$ , often called the *bed friction number* (see e.g. Alavian and Chu [2],

Babarutsi et al. [7] and Van Prooijen [99]).

The bed friction number  $S$  can be expressed in various ways, dependent on the flow geometry. For shallow mixing layers (SML, see Section 1.4),  $S$  is expressed by [2] as follows:

$$S = c_f \frac{\delta}{H} \frac{U_c}{\Delta U}, \quad (2.14)$$

where  $c_f$  is the bottom friction coefficient,  $\delta$  is the mixing layer width,  $H$  is the water depth,  $\Delta U$  is the velocity difference over the mixing layer and  $U_c$  is the mean velocity in the mixing layer center (see Figure 1.6(a)). The parameter  $S$  expresses the relative influence of bottom friction; its value may strongly vary but is typical of the order 0.01 – 1.0. For small values of  $S$  the production of 2DCS kinetic energy dominates over dissipation; such small values do typically occur in the near field. For large values of  $S$  (typically in the far field), bottom friction accounts for the decay of 2DCS while the production of new structures is prohibited. An expression for  $S$  that is used for shallow wakes is given by e.g. Chen and Jirka [23]:

$$S = c_f \frac{D}{H}, \quad (2.15)$$

where  $D$  is the size of the obstacle causing the wake. Babarutsi et al [7] give a similar expression of  $S$  for a Shallow Lateral Expansion (SLE geometry, see Section 1.4):

$$S = c_f \frac{D}{2H}, \quad (2.16)$$

where  $D$  is the expansion width (equal to the width of the inflow section, see Figure 1.6(b)). The basic flow types mentioned above have been investigated by various authors with respect to their sensitivity to the stability parameter  $S$  and to other circumstances like inflow turbulence conditions. A few results are briefly addressed below:

1. *Wakes.* Experimental work on shallow wakes past a cylindrical obstacle has been performed by e.g. Chen and Jirka [22, 23]. For  $S < 0.2$ , a Von Kármán vortex street is found with highly unsteady separation at the cylinder wall; for  $S > 0.5$ , the wake consists of a steady bubble without oscillations. For values  $0.2 < S < 0.5$  an unsteady bubble is observed that shows sinuous oscillations in downstream direction. Similar results have been obtained by Lloyd and Stansby [58], who investigated the shallow wake past conical islands.
2. *Grid turbulence.* A special case of wake flow is shallow grid turbulence, a large number of parallel shallow wakes; see Uijttewaals and Jirka [92]. Grid turbulence offers a spectacular illustration of quasi-2D vortex behavior, like vortex pairing and merging as well as final decay due to bottom friction. It has been shown by [92] that the characteristic size of the grid elements (relative to the water depth  $H$ ) governs the decay of the 2DCS that are continuously shed from the grid.
3. *Jets.* The formation of 2DCS in shallow jets has been addressed by Giger et al. [39], Dracos et al. [32] and Chen and Jirka [24]. It is shown that, for decreasing ratio of depth and nozzle width ( $H/D$ ), the shallow jet starts to clearly exhibit 2DCS rather than dominant 3D eddy structures. Also, these structures start to develop closer to the jet entrance for decreasing relative depth. Secondary currents play an important role within the middle field ( $1 < x/H < 10$ ).
4. *Mixing layers.* In the context of this thesis, shallow mixing layers (SML) are an important basic type of quasi-2D turbulent flows. Chu and Babarutsi [26] have performed laboratory experiments on a SML geometry; they investigated the way in which the

2DCS behavior is governed by the bed friction number  $S$ , defined by Alavian and Chu [2] according to Equation (2.14). It was concluded that a critical value of the bed friction number is given by  $S \approx 0.1$ ; for larger values the SML flow will be stable. Uijttewaal and Tukker [94] have developed an analytical model of the mean flow field of shallow mixing layers, based on Laser-Doppler Anemometry (LDA) experiments. Van Prooijen [99] improved this analytical model with new information from experiments using Particle Tracking Velocimetry (PTV) and added new information about the spatial development of the associated 2DCS. The sensitivity of 2DCS in SML geometries to upstream turbulence has been investigated by means of linear stability analysis; see also Van Prooijen and Uijttewaal [101]. It is stated by Van Prooijen, De Nijs and Uijttewaal (2003) that turbulent perturbations at the inflow boundary are somehow required in order to trigger any development of 2DCS within SML flows; usually, the presence of 3D bottom turbulence will provide such perturbations.

The four shallow shear flow types listed here have in common that they are examples of free turbulence (except for the presence of bottom friction). In case of shallow flows including separation, however, the influence of sidewalls on the flow should be taken into account as well. In the next section, general aspects of flow separation are addressed.

## 2.3 On flow separation

### 2.3.1 Definition

Flow separation occurs when a boundary layer loses contact with the associated solid wall. This phenomenon is caused by an adverse pressure gradient acting against the local flow direction. In such a case, both wall friction and pressure gradient act against the flow and thus prevent the equilibrium of forces that enable a boundary layer to exist. The flow rate near the solid wall will therefore turn to zero and change sign (return flow). Flow separation can occur in both laminar and turbulent flows; it may occur in any flow where viscosity plays a role, in other words, any finite Reynolds number flow in which boundary layers are present. The local physical micro-scale behavior of turbulent separating flows around streamlined and bluff bodies has been reviewed by Simpson [78].

Pressure gradient and wall shear stress are usually counteracting forcing terms within the local momentum balance along a solid wall (see Figure 2.6). The equilibrium between both forcing terms determines the boundary layer width. A favorable pressure gradient (pointing in the mean flow direction) will cause a large wall shear stress and a large velocity gradient, and hence quite a narrow boundary layer (Figure 2.6(a)). An adverse gradient (against the flow direction) will cause the opposite to happen, thus forcing a boundary layer to become “infinitely wide” and therefore ultimately unstable (Figure 2.6(b)).

A location in which a local boundary layer flow rate changes sign is called a *separation point*; this point is also a stagnation point. The exact location of separation points is highly dependent on the flow geometry, on local wall roughness and on the actual turbulence conditions. Therefore separating point locations are often oscillating along solid walls, or even the entire separation event may be *intermittent* (i.e. occurring periodically during only a part of the total time). Consequently, some different definitions of a separation point are in use; it may be defined as e.g. the location where instantaneous backflow occurs during 50% of the time, or as the location where the time-averaged wall shear stress equals zero (see Simpson [78]). Fortunately, the description of large-scale quasi-2D phenomena in (shallow) separating flows is not very sensitive to the exact definition of

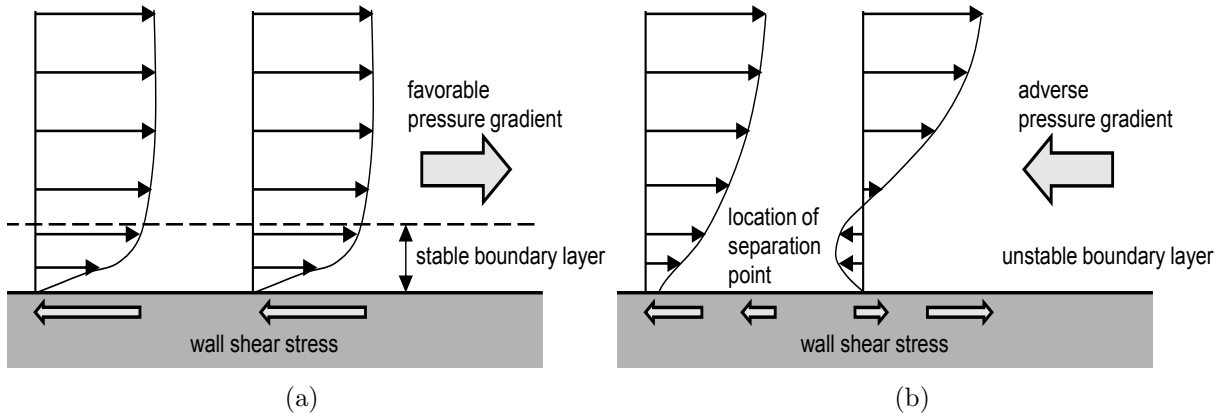


Figure 2.6: *Principal cause of flow separation: impact of pressure gradient on a boundary layer equilibrium (see [78]). (a) Favorable pressure gradient, stable boundary layer; (b) Adverse pressure gradient, separating boundary layer.*

the separation event. In this thesis, the emphasis is on large-scale 2DCS rather than on small-scale phenomena in the neighborhood of a separation point.

Essential about separation is the fact that it is a *boundary layer* that separates. Separation only occurs if a developed upstream boundary layer is present. A poorly developed boundary layer has less tendency to separate and will behave more or less like a potential flow. This fact can be used for reducing wake sizes in an artificial way. If a boundary layer is somehow removed or disturbed just upstream of a possible separation point, the flow may bend along sharp edges much better. The same phenomenon is observed when a separating flow starts to develop from a state of rest (e.g. in numerical simulations as performed in the present thesis). While the flow accelerates, initially no boundary layer is present and the flow smoothly bends along future separation points, remaining attached to the solid wall. Only after the development of a boundary layer, separation events will be induced.

Flow separation may occur either at a wall discontinuity (fixed location) or along a continuous solid boundary (variable location) with or without surface curvature, see Figure 2.7(a)-(c). In practice, these types of separation points can often be found combined in one and the same flow geometry. In all cases, however, an adverse pressure gradient is present; such a gradient is usually caused by deceleration of the velocity field in a region of flow expansion, but may also be induced by some artificial perturbation of the turbulent flow field.

### 2.3.2 Terminology: recirculation zones and vortex shedding

A separation event obviously influences both time-averaged flow and the over-all turbulence pattern. In this section, several characteristic flow features associated with flow separation are illustrated. We use a concrete example of a *shallow* separating flow situation: a channel flow past a single rectangular groyne (see Figure 2.8). This flow case stems from a quick laboratory experiment by Van Prooijen [99]. Details of the turbulent flow field have been visualized by the injection of colored dye in the neighborhood of the groyne tip. Although most flow features outlined in Figure 2.8 are relevant for separating flows in general, we are specifically focusing on shallow separating flows using the present example. Panels (a)-(b) outline several terms regarding the mean flow pattern, whereas the panels (c)-(d) concern

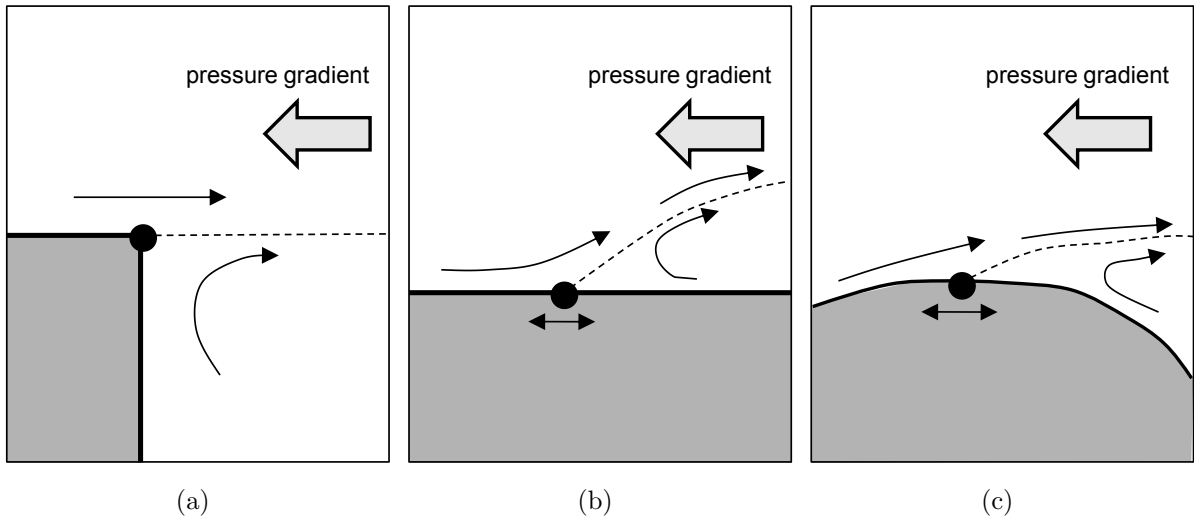


Figure 2.7: *Basic possibilities for separation point locations: (a) Fixed location; (b) Variable location with straight surface; (c) Variable location with surface curvature.*

terminology with respect to large-scale turbulence dynamics.

In general a separation event induces a lateral velocity gradient between the separated incoming flow (coined *external region*) and the separation area (named *internal region*); see panel (a). This lateral shear will induce lateral transfer of streamwise momentum, which is usually accounted for by means of large-scale eddies, see (d). This lateral momentum transfer, combined with conservation of mass (flow field solenoidality) eventually gives rise to a region of fluid recirculation. In a shallow flow situation with solid sidewalls, such a recirculation is usually steady; in this thesis it is referred to as the *primary recirculation* or *primary gyre* (b), see Uijttewaal et al. [93]. The separation point giving rise to this gyre can be referred to as *primary separation point*. The gyre size is measured in terms of the so-called *reattachment length* (a), which is given by the streamwise distance from the primary separation point toward the downstream location where the external region touches a solid sidewall again. This location is called the *reattachment point*, see (a)-(b); this is a stagnation point and it often has a slightly oscillating character, depending on local turbulence conditions. Further downstream, the reattached boundary layer will gradually recover due to the re-establishment of the equilibrium between streamwise pressure gradient and wall shear stress (a). Experiments performed by Castro and Epik [21] and numerical work by Le, Moin and Kim [55] illustrate that this recovery process can be quite slow: only at a downstream distance of more than two times the reattachment length of a separation region, the boundary layer has fully recovered.

A primary gyre does not necessarily occupy the entire internal region. Dependent on the local geometry, the primary gyre may in turn induce an adverse pressure gradient and separate from the wall. In such a case, a *secondary gyre* is being formed (b), see [93]. In the present study, the separation point giving rise to this secondary gyre is coined *secondary separation point* (b). Usually the development of secondary gyres takes much more time than that of primary gyres. Both in practice and in laboratory situations, shallow separating flows have often primary separation points that are more or less fixed in space, whereas secondary separation points are often located along a continuous wall and may move freely along it. This fact makes the modeling of secondary separation more sensitive to the type of wall modeling and hence more difficult to accomplish.

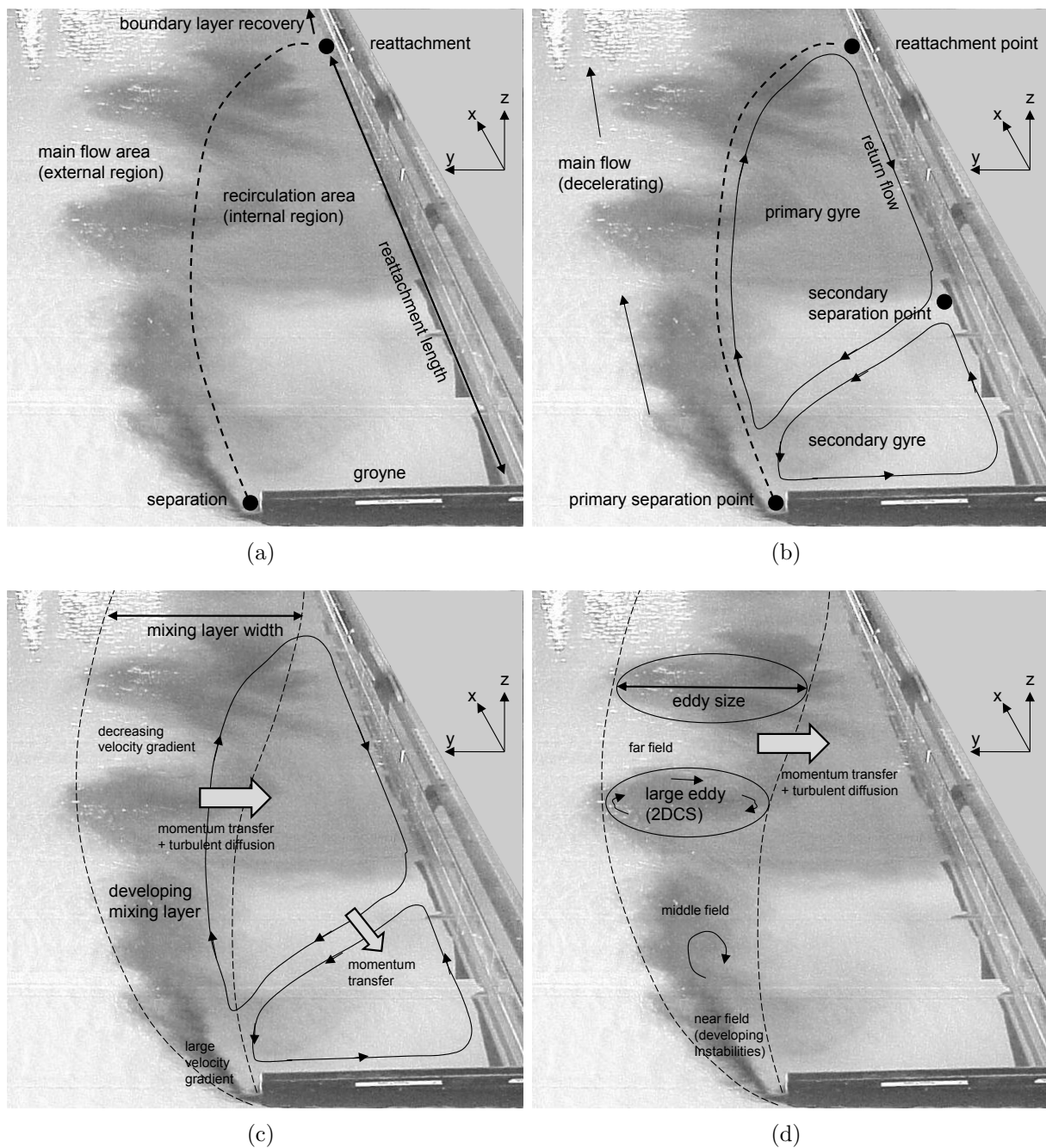


Figure 2.8: *Explanation of general terminology for shallow separation events (example: shallow flow past single groyne, laboratory experiment by Van Prooijen [99]). Turbulent flow details are visualized by dye which has been injected in the neighborhood of the groyne tip. Four terminology categories are presented: (a) definition of separation region; (b) general features of time-averaged flow pattern; (c) mixing layer development, velocity gradients, momentum transfer and turbulent diffusion; (d) large eddy development (vortex shedding).*

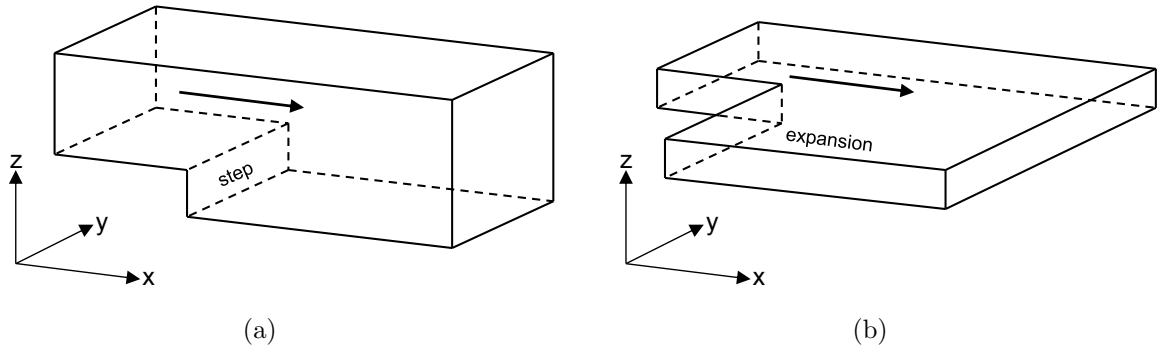


Figure 2.9: *Similarity and distinction between BFS and SLE geometries: (a) Backward Facing Step; (b) Shallow Lateral Expansion.*

At the interface between main flow and recirculation area a lateral velocity gradient is present, often inducing a *mixing layer* (c). The associated coherent structures, starting as Kelvin-Helmholtz instabilities (see Nieuwstadt [67]), represent the key mechanism that is responsible for the lateral transfer of momentum toward the recirculation area. The mixing layer enhances the effective horizontal diffusivity at the interface. It widens in downstream direction and is shifting toward the low-velocity side, while the velocity difference gradually decreases. Coherent structures grow in downstream direction, roughly proportional to the mixing layer width (d). This emergence of coherent structures from a primary separation point along a mixing layer is often referred to as *vortex shedding*. In a shallow-flow situation, these large-scale shed vortices are obviously 2DCS. (It should be noted that the term “vortex shedding” has a wider meaning than just the situation of a mixing layer containing 2DCS; the term applies as well to e.g. vortex streets in wakes and grid turbulence flows. In general, the term “vortex shedding” can be applied to any situation – not necessarily quasi-2D – where dynamic large eddies are induced by flow separation.)

A certain dominant vortex shedding frequency  $f$  can often be observed; this frequency is made dimensionless by the Strouhal number  $St = f\mathcal{L}/U$ , where  $\mathcal{L}$  is a flow length scale and  $U$  is a velocity scale. For many separation geometries the associated value of  $St$  is in the range from 0.1 to 1.0, dependent on the precise value of scaling parameters. A vortex shedding frequency may be an important quantity that should be known for determining flow forces on solid structures, e.g. bridge piers or armor layers. Furthermore, it has been found by various researchers that disturbing a separating flow at its vortex shedding eigen frequency may strongly enhance turbulence intensities and vortex length scales. This mechanism can be used to manipulate separation zones, e.g. in order to shorten reattachment lengths, to reduce drag forces or to improve mixing behavior. Such kind of advanced techniques are mostly applied in the field of industrial flows and aerospace engineering; see e.g. Greenblatt and Wygnanski [41], Chun and Sung [27] and Yoshioka et al. [117, 118].

One of the separation geometries most widely studied is the Backward Facing Step (BFS), a 3D channel flow geometry with an expansion (step) in vertical direction. Experimental work on the BFS has been performed by e.g. Nakagawa and Nezu (1987), Scarano et al. [73] and Spazzini et al. [81]. Direct Numerical Simulations (DNS) of BFS flows have been performed by Neto et al. [65] and by Le, Moin and Kim [55]; examples of Large Eddy Simulations (LES) on BFS flows have been given by Cabot [20] and Avancha and Pletcher [4], and  $k-\epsilon$  (RANS) simulations by e.g. Thangam and Speziale [87]. A smoothly contoured “streamlined” BFS



has been analyzed computationally by Wasistho and Squires [110,111]. In fact, the Shallow Lateral Expansion (SLE) introduced in Section 1.4 is the quasi-2D horizontal counterpart of the BFS geometry; the distinction between both geometries has been depicted in Figure 2.9. In terms of turbulence dynamics, the most important distinction is that BFS flows do not necessarily involve quasi two-dimensionality, whereas quasi-2D properties always play a prominent role in SLE flow cases.

## 2.4 Investigation of shallow recirculating flows

The presence of separation in shallow turbulent flows implies that the influence of steady recirculations must be taken into account when investigating turbulence behavior. When steady gyres are present, the size of full-developed 2DCS in the mixing layer is often of the same order of magnitude as the width of the gyre area; both structures have dimensions much larger than the water depth ( $\mathcal{L} \gg H$ ). This means that both unsteady 2DCS and steady gyres behave like quasi-2D structures. Therefore, some typical quasi-2D interaction between them may possibly be expected. A brief review of experimental and computational research on various types of shallow separating and recirculating flows is given in this section.

Uijtewaal, Lehmann and Van Mazijk [93] have performed laboratory-scale experiments on a series of 8 river groyne fields, in order to analyze the large-eddy behavior and their impact on mixing and dispersion of pollutants. Their observation is that two different types of dynamic 2DCS play a role in a groyne field situation. Firstly, 2DCS are developing in the “ordinary” mixing layer that is present at the interface between river and groyne field. These 2DCS are starting as smaller-scale 2D instabilities and gradually grow in size while moving through the mixing layer. Secondly, it is observed that frequently large vortices are formed directly downstream of each groyne tip (separation point), staying in place while growing in size and energy. When such a 2DCS has grown sufficiently in size to sense the primary gyre, it separates from the groyne tip and is advected downstream, eventually merging with the primary gyre. This second mechanism is coined *direct vortex shedding* in this thesis. It is observed by [93] that this direct mechanism accounts for a much larger exchange of mass and momentum than a stand-alone mixing layer that contains gradually growing 2DCS (“indirect” vortex shedding). Furthermore, the occurrence of direct vortex shedding is observed to be dependent on the presence of a sufficiently large, stationary secondary gyre, comparable with the secondary gyre in Figure 2.8(b)-(c). This can be understood for the area between secondary gyre and main stream is often a stagnant zone experiencing strong lateral shear, in which vorticity can accumulate. Apparently, the presence of a secondary gyre gives rise to considerable interaction between 2DCS and steady gyres. A relevant question to be asked is whether this interaction, causing direct vortex shedding, is typical for groyne field flows only or that it also applies to other shallow recirculating flow types. This question will be addressed in Chapter 3. Another relevant observation regarding quasi-2D turbulence behavior is reported by Chen and Ikeda [25] in their study on groyne field flow: mixing layer 2DCS past groynes can grow significantly in downstream direction as they can merge together into a new larger eddy.

Harbor entrances along rivers are another important example of shallow recirculating flows. In this case, the length of the interface between main flow and harbor in streamwise direction is usually short (see e.g. Figure 1.4). Usually no secondary gyres are present in such geometries, so that all 2DCS and mixing processes are accounted for by the mixing layer on the harbor-river interface. Square harbor geometries along rivers have been investigated

both experimentally and numerically by Langendoen et al. [53, 54] and Bijvelds et al. [12, 13]. Concerning harbors, the emphasis of the research is often on the way in which large eddies influence the exchange of sediment; it is usually desired to find ways to reduce the amount of sediment entering harbor basins, in order to effectively reduce dredging costs (e.g. Winterwerp [115]).

The simplest and most generic shallow flow geometry containing separation and flow recirculation is the Shallow Lateral Expansion (SLE), already introduced before. The SLE is the quasi-2D counterpart of the Backward Facing Step (BFS); it has been studied in literature under various other names. Important experimental work on the SLE has been performed by Babarutsi et al. [7], using the measurement technique of hot-film anemometry. In a relatively small laboratory flume of length 7 m, width 0.61 m and maximum depth 0.13 m, the effect of shallowness on the mean flow pattern was investigated for  $3000 < Re < 12000$ . It was concluded that the time-averaged flow pattern depends on a single dimensionless parameter, the bed friction number  $S$ ; see Equation (2.16). An attractive property of the SLE geometry is that it contains only two length scales (expansion width  $D$  and water depth  $H$ ). It has been observed by [7] that the reattachment length is proportional to  $H/c_f$  for very shallow cases ( $S > 0.1$ ) and to  $D$  when the flow is relatively deep ( $S < 0.05$ ). In between these regimes a region of transition exists. If bottom friction dominates (large values of  $S$ ), it can suppress both vortex shedding and the effective mixing of pollutants. Although (in theory) bottom friction has no direct influence on eddy diffusivity, the indirect impact of bottom friction on the turbulent flow field and its effective diffusion is significant, as observed by e.g. Nassiri and Babarutsi [62] or Altai and Chu [3] in their studies on retention times of pollutants in SLE-type geometries.

The experimental results from [7] have been reproduced by a 2D numerical model, solving the shallow water equations and using various RANS turbulence models (Babarutsi et al. [8]). This model was able to reproduce the primary gyre. A similar result was obtained by Stelling [82], who simulated unsteady harmonic (tidal) flow situations in a SLE geometry (validated by corresponding laboratory experiments by Wang [109]). In this study the 2D shallow water equations were solved numerically with an emphasis on stabilizing the momentum advection terms without introducing excessive artificial viscosity. It was found by [82] that the latter is important for a correct reproduction of the gyre pattern. In Nassiri et al. [64] the secondary gyre has been reproduced as well, applying a 3D  $k$ - $\epsilon$  model. A distinction is made here between the horizontal and vertical length scale in the turbulence model; also, the two-layer wall function includes both the logarithmic layer and the viscous sublayer. This accurate wall model turned out to be essential for the secondary gyre to be captured by the computation.

The experimental and computational results mentioned above have provided predominantly ensemble-averaged output (e.g. mean velocities, gyre length scales, Reynolds stresses), rather than quantitative information about individual 2DCS and their dynamics. More detailed measurement and simulation tools are needed in order to capture these phenomena, e.g. Particle Image Velocimetry (PIV) and Large Eddy Simulation (LES). In this thesis attention will be paid to the direct measurement (Chapter 3) and simulation (Chapter 4) of 2DCS and their properties.

## 2.5 Research methodology

In order to formulate the scientific approach adopted in this thesis, we recall the three basic research questions given before in Section 1.5.

The primary challenge encountered in this study is to clarify how the genesis and behavior of 2DCS in shallow separating flows is influenced by the steady gyre pattern (research question no. 1). In the previous sections, some typical quasi-2D mechanisms present in shallow separating flows have been encountered; more detailed data about these mechanisms are desirable. It is aimed to investigate one specific shallow flow geometry both experimentally and computationally, while for the data a sufficient level of detail is required in order to actually resolve 2DCS and the possible quasi-2D interactions that we are looking for.

The first step is to select the actual shallow flow geometry to be studied. It is aimed to have a geometry that guarantees the occurrence of flow separation and recirculation as well as the emergence of 2DCS (by the mechanism of *topographical forcing*), but contains only a minimum of geometrical complexity. Therefore it is chosen to investigate a schematized Shallow Lateral Expansion (SLE) geometry with constant water depth  $H$ . In this way, the number of relevant flow length scales is minimized. A worthwhile extra option is the systematic variation of the ratio of inflow width and outflow width of the SLE. This variation provides interesting new information in addition to previous experiments reported by e.g. Babarutsi et al. [7]. Furthermore, it is aimed to obtain data with higher Reynolds numbers than achieved by [7], while maintaining moderate Froude numbers and sufficiently shallow flow conditions ( $D \gg H$ ).

In recent years, laboratory experiments at Delft University of Technology and the Institut für Hydromechanik (IfH) Karlsruhe have provided valuable experience with the technique of large-scale free-surface velocity measurements, applying Particle Image Velocimetry (PIV) or Particle Tracking Velocimetry (PTV). If flow features to be measured have a quasi-2D character, these are effective tools to acquire velocity data (see Weitbrecht, Kühn and Jirka [112]). The PTV approach has been successfully applied by Van Prooijen [99]. PIV and PTV share the same data acquisition technique; the PIV approach however includes a more straightforward and user-friendly method of data post-processing. In the present research the PIV approach is adopted. Both PIV and PTV allow for the visualization of instantaneous surface velocity fields, which provides useful information about 2DCS behavior. It should however be kept in mind that, although instantaneous large eddy patterns can be well captured, smaller-scale turbulent fluctuations are often missed out due to insufficient resolution; also, only the free surface velocity field can be measured. It must hence be anticipated that only a part of the total turbulent kinetic energy content can be resolved using free-surface PIV.

With respect to 3D numerical computations, the technique of Large Eddy Simulation (LES) is adopted in this study. In recent years, progress has been made in improving the Reynolds-averaged (RANS) modeling of shallow separating flows. Bijvelds et al. [13], Thangam and Speziale [87] and Nassiri et al. [64] have emphasized the advantages of anisotropic  $k-\epsilon$  models, which make a distinction between horizontal and vertical length scales and associated eddy viscosities. Such formulations allow for a better simulation of e.g. stationary gyre patterns than classical isotropic  $k-\epsilon$  models can do. Investigation of 2DCS, however, is not fully possible when using RANS models. Also the transfer of energy between larger and smaller turbulence scales is not reproduced, as the modeled parts of RANS models involve all length scales simultaneously. As the focus of this thesis is on 2DCS dynamics, it is important to be able to resolve individual structures. Large Eddy Simulation allows for this. In terms of computational effort, LES computations of laboratory-size geometries have become within the grasp of parallel clusters and, recently, even of fast desktop computers. Hence, it is chosen to perform full 3D LES computations of the SLE and to make a comparison with the acquired PIV laboratory data. Furthermore, the acquired LES data allow for an investigation of 3D effects within the quasi-2D flow field and the sensitivity of

large-scale turbulence to upstream conditions.

After validation of LES results by PIV data, it is possible to systematically adapt the basic LES geometry in order to analyze the effects of flow geometry variations on 2DCS behavior (thus addressing research question no. 2). This, of course, is a less expensive and time-consuming operation than performing many different laboratory experiments. Also, accepting a certain level of uncertainty, the results of LES geometry adaptations can be translated toward real-life environmental separating flow situations. In this way, the conceptual results of the experimental and numerical work can be beneficial for e.g. the understanding of large-scale turbulence in the neighborhood of groyne fields and harbor entrances. This can also be of use for design purposes.

Usually full 3D LES computations are not feasible for application to field-scale environmental flows. Often 2D models are applied to reduce the computational effort. It is desired to know (in order to address research question no. 3) whether shallow separating flows can be represented by 2D depth-averaged numerical models, including the relevant 2DCS behavior. Various authors have proposed methods to incorporate 2DCS behavior in depth-averaged 2D flow simulations. Ghidaoui and Kolyshkin [38] have illustrated the fundamental ability of the 2D shallow water equations to capture 2DCS patterns. On the other hand, whenever the emergence of 2DCS is triggered by small-scale 3D instabilities (as is often the case in shallow shear flows due to *backscatter*, see [101] and Section 2.2), a simple 2D model will never be able to capture these 3D instabilities and hence no 2DCS will occur. Somehow, the basic LES principle of resolving large eddy scales and modeling the small scales should be maintained in a 2D model. Such models have been developed by e.g. Uittenbogaard and Van Vossen [95], Hinterberger [42] and Van Prooijen and Uijttewaal [102].

The model by [95] is called Horizontal Large Eddy Simulation (HLES); it basically fine-tunes the dissipation rate of 2D large eddies by introducing a 2D sub-grid scale viscosity. Hence, the model has mainly a dissipative character. The other two models include an explicit 2D forcing vector field which actively triggers the emergence of 2D eddy motion. As such models explicitly prescribe the effect of the inverse energy cascade, they are called *backscatter models*. The model in [42] is named Depth-Averaged Large Eddy Simulation (DA-LES); the influence of backscatter on large-scale 2D motion is modeled here by means of a stochastic model. The model in [102] is a 2D transient RANS model with kinematic simulation (2D-TRANS+KS). In this model a complete spatial spectrum of 2D motions is imposed on the velocity field to trigger 2DCS.

In order to complete the picture of this thesis (PIV experiments, 3D LES computations and 2D depth-averaged simulations), the topic of 2D turbulence modeling is addressed. It will be shown that the two backscatter models mentioned above can be integrated into a unified 2D backscatter approach, which is coined Depth-Averaged Navier-Stokes with Large Eddy Stimulation (DANSLES). Together with the existing models, the new approach will be analyzed and tested against various turbulent shallow flow geometries.

# Chapter 3

## Laboratory experiments

### 3.1 Introduction

As a first step in addressing the research objective outlined in Section 1.5, this chapter presents laboratory experiments performed on the Shallow Lateral Expansion (SLE) geometry. As pointed out in Section 2.5, these experiments have multiple functions. New information is added to existing SLE data whereas the larger flume dimensions and higher Reynolds numbers of the current experiments provide an extension to previous work. Attention is paid not only to time-averaged flow quantities, but also to the analysis of individual 2DCS and their behavior. Finally, the experimental results are used to validate the numerical results addressed in Chapter 4.

This chapter presents the laboratory setup that has been used; it describes the way in which the acquired data have been analyzed and discusses the way in which the results can be interpreted.<sup>1</sup> Three versions of the SLE geometry have been adopted, systematically varying the width of the inflow section. These flow cases have been coined Case 1, 2 and 3 (see Section 3.2). Firstly, for each case a number of experimental test runs has been performed (27 in total) in order to investigate the sensitivity of large-scale flow phenomena to basic parameters like discharge and water depth (Section 3.4). After exploring the parameter space of the experimental setup in this way, for each flow case a final experiment is defined. These three experiments are performed using Particle Image Velocimetry (PIV), in order to acquire the final data set which is analyzed in Sections 3.5 to 3.7.

### 3.2 Experimental setup

The laboratory setup has been chosen in order to allow for sufficient shallowness and sufficient detail. Experiments have been conducted in a shallow free-surface flume with a total length of 20 m, a width of 2 m and a maximum depth of 0.16 m. This flume, located at the Environmental Fluid Mechanics Laboratory at Delft University of Technology, has previously been in use for shallow flow experiments carried out by e.g. Tukker [89], Uijtewaal and Booij [91], Van Prooijen [99] and Kadota et al. [48]. In order to have a sufficiently large flume length relative to the width, the original width of 3 m was reduced to 2 m for the present research. With an average water depth-width ratio of about 1:20 and a depth-length ratio of 1:200, the flume can be called sufficiently shallow.

Figure 3.1 gives a top view and side view on the experimental setup and some of the

---

<sup>1</sup>Parts of the results of this chapter have been published in Talstra et al. [83].

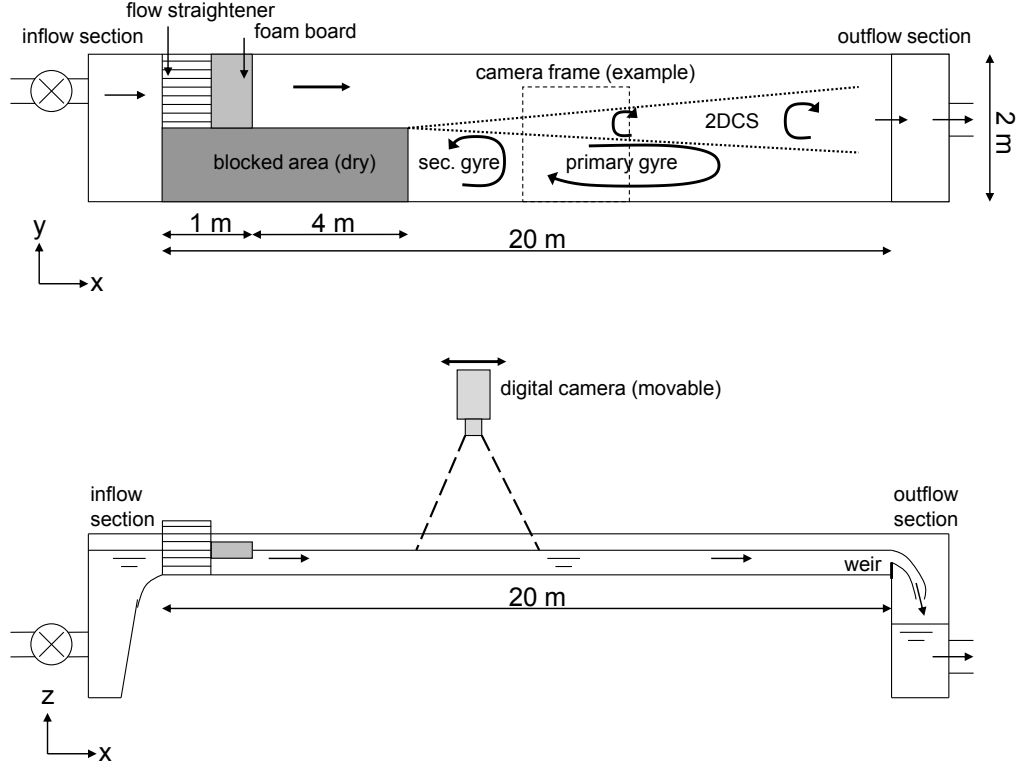


Figure 3.1: *Top view and side view of the experimental setup (slightly distorted scale). Arrows show the flow direction from upstream pump to outflow weir, as well as the expected primary and secondary gyre. Dotted lines indicate the shallow mixing layer which contains 2DCS. The dashed square indicates a PIV measurement camera frame.*

expected flow features therein. An inflow section of length 5 m and variable width is located at the upstream side. Downstream of the expansion, the outflow section fills the remaining 15 m and the full flume width of 2 m. Bottom and sidewalls consist of glass and smoothly varnished wood respectively, leading to hydraulically smooth wall conditions and hence a small over-all water level gradient. During all experiments the water level drop over the total flume length remained beneath 2 mm; hence, the water depth has been considered as constant. Water depth and total discharge can be varied by means of an upstream pump and a downstream sharp-crested weir. A few representative values of flow quantities are given by: water depth  $H = 0.1$  m, discharge  $Q = 0.03$  m<sup>3</sup>/s, inflow velocity  $U_0 = 0.3$  m/s and bottom friction coefficient  $c_f \approx 0.0027$  (Chézy coefficient  $C \approx 60$  m<sup>1/2</sup>/s). Upstream from the inflow section, the flow contracts as it enters the flume from the pump section. A honeycomb is placed here in order to ensure uniform inflow with straight streamlines. Behind the flow straightener, a thin foam board is floating on the water surface to suppress small waves. From that point on the flow has an inflow length of 4 m available to develop a fully turbulent boundary layer.

The SLE geometry adopted here involves three basic length scales: the inflow width  $B_1$ , the outflow width  $B_2$  and the depth  $H$ . From the first two length scales the expansion width  $D$  can be derived:  $D = B_2 - B_1$ . In literature on SLE experiments it is common practice to take  $B_1 = D$ , so that the ratio  $B_1/B_2$  equals 1:2. In this way, the number of length scales is effectively reduced to two. In the present study, three different ratios  $B_1/B_2$  are chosen: 1:4, 2:4 and 3:4. These cases are referred to as Case 1, 2 and 3 respectively. This variation adds new information to existing data (on Case 2 only), as it gives information

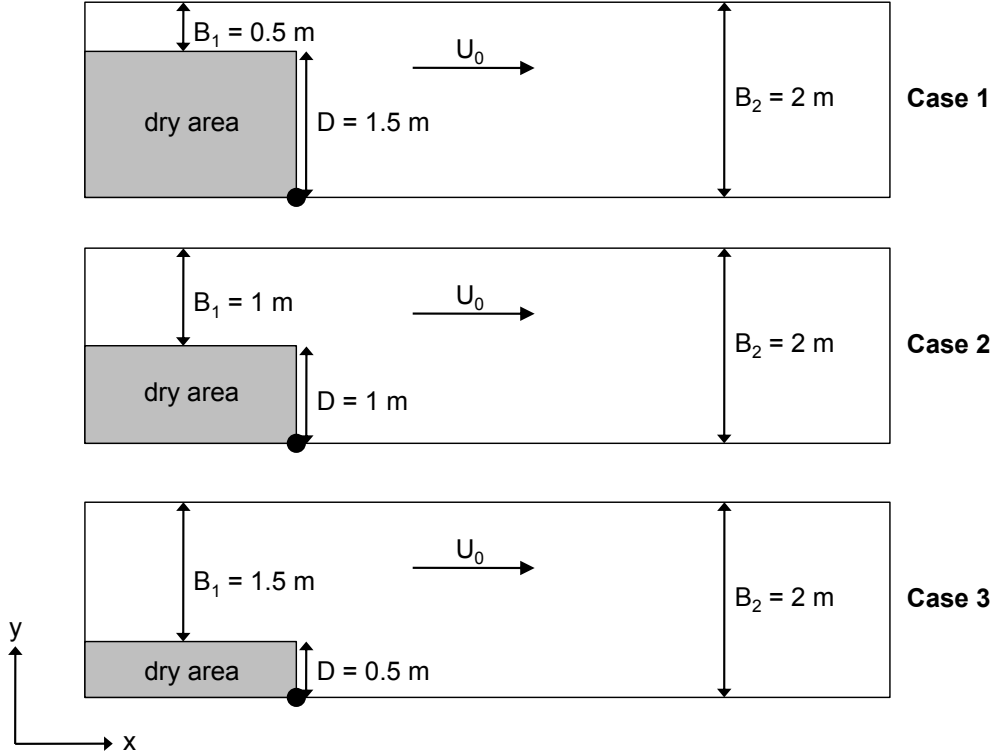


Figure 3.2: Overview of the three SLE versions considered (Cases 1-3 with relevant flow length scales. The solid dots indicate the origin of the reference frame ( $x = y = 0$ ).

about the impact of the ratios  $D/H$  and  $B_1/H$  on the turbulent flow. Figure 3.2 depicts the relevant length scales for the Cases 1, 2 and 3.

The key advantage of the present flume is the ability to achieve relatively large Reynolds numbers at moderate (subcritical) Froude numbers and sufficiently shallow conditions. In comparison, experiments by Babarutsi et al. [7] were carried out in a flume allowing for depth-based Reynolds numbers  $3000 < Re < 12000$  and Froude numbers  $0.25 < Fr < 0.55$ . The current flume experiments have  $13500 < Re < 50000$  for virtually the same Froude number range and a comparable depth-width ratio  $H/B_2$  (about 1:20).

### 3.3 Measurement techniques

#### 3.3.1 Visualization of the flow

All measurements are based upon visualization and camera registration of the flow. A global impression of the mean velocity field and turbulence behavior can be obtained by injecting dye at a location upstream from the separation point, at some point within the mixing layer or within the steady gyres. The dye is advected by the large-scale flow and spreads out due to the action of small-scale 3D turbulent diffusion. As dye is being entrained by the mixing layer at the interface between main flow and gyres, it reveals the existence of large-scale coherent structures, their growth in size and their pathway. The visualization of 2DCS and steady gyre return flow by means of dye injection has already been demonstrated in Figure 2.8.

For the eventual purpose of camera registration, floating black polypropylene tracer particles with a diameter of 2.0 mm are used instead of dye. These particles have a good contrast

with the white flume bottom. The particles are used to visualize the free surface velocity field only; as they are submerged for more than 90%, they are expected to follow the fluid flow sufficiently well. Obtaining a homogeneous spreading of particles on the water surface can be problematic sometimes because the surface velocity field is quite inhomogeneous itself. In practice, only the uniform inflow section is suitable for a continuous seeding of the surface with particles. Direct continuous seeding of steady gyres or mixing layers is not possible, as these are the regions of interest which are not to be disturbed. A practical solution however is to use the property of (especially) the secondary gyre that it “traps” sediment and pollutants for relatively long times and eventually exchanges them with the mixing layer. If the secondary gyre area surface is saturated with particles at a sufficiently long time before camera registration starts, these trapped particles will contribute significantly to the seeding of the mixing layer (due to entrainment) for the entire measurement duration. In turn, the mixing layer seeds the primary gyre and the primary gyre will seed the secondary gyre again. In combination with a permanent seeding of the inflow section, this method yields a sufficiently homogeneous particle distribution in the entire flow domain, except for possible regions of vertical upwelling of fluid (secondary flow). Dye injection and particle seeding are both useful to acquire a global impression of the turbulent flow field. Both methods were applied when performing the 27 test runs that are described in Section 3.4. On behalf of the three final experiments described in Sections 3.5 to 3.7, only tracer particle seeding has been applied.

### 3.3.2 Particle Image Velocimetry (PIV)

In order to analyze sampled camera images of the water surface, the method of Large-scale Surface PIV (LSPIV) has been used, a technique belonging to the family of PIV methods (Particle Image Velocimetry). An elaborate explanation of LSPIV has been given by Weitbrecht et al. [112]. The method will be named PIV throughout this thesis. A key advantage of the method is the easy way in which camera images can be obtained. As the measurements are carried out at the water surface, no laser light sheet is needed. It would be even possible to perform measurements with only daylight. In the present experiments, a constant halogen light source has been used in order to enlarge the contrast between flume bottom and tracer particles.

Using a sampling frequency of either 10 Hz or 15 Hz, camera frames with size 1.50 x 1.50 m<sup>2</sup> have been recorded by a RedLake 1 MegaPixel digital camera (resolution 1008 x 1018 pixels, 8-bit gray-scale). The camera was placed on top of a movable bridge construction built over the flume (see Figures 3.1 and 3.3) and was directed exactly vertically downward. After a correction for image distortion (achieved by careful calibration) and subtraction of background information, all pairs of consecutive camera frames containing tracer particle patterns were spatially correlated (using a commercial PIV algorithm) in order to obtain instantaneous surface velocity fields. This has been done by computing the average particle displacement in each point of the fluid, using square correlation areas that are called *interrogation windows*. To this end, the PIV/PTV software package Davis 6.2 (LaVision) has been used.

Because of the large amount of tracer particles and their sufficiently homogeneous distribution over the water surface, it has been chosen to use the PIV algorithm instead of PTV (Particle Tracking Velocimetry). The PIV approach enables the user to capture all particle information into one structured grid of vectors, whereas the PTV technique requires the exact tracking of thousands of separate particle pathways; the latter eventually yields a large unstructured set of vectors, which must be restructured toward a regular grid after





Figure 3.3: *Picture of the experimental SLE setup; flume width and main flow direction have been indicated. The background shows part of the movable bridge construction on which the digital camera has been placed.*

all in order to be useful. In other words, PIV requires less experimental and computational effort than PTV in the present application.

Every set of 2 consecutive camera frames has been cross-correlated by the PIV algorithm, using interrogation windows of size  $96 \times 96 \text{ mm}^2$  (i.e.  $64 \times 64$  pixels) with a mutual spatial overlap of 75% in both  $x$ - and  $y$ -direction. The output consists of samples of 2D surface velocity vector fields on a rectangular co-located grid with a resolution of  $0.024 \text{ m}$  in both  $x$ - and  $y$ -direction (grid size  $64 \times 63$  data points). The measurement duration of all samples is 700 seconds; this corresponds with sample sizes of 7000 frames for 10 Hz recordings and 10500 frames for 15 Hz recordings. Because the spatial domain of the camera image is limited to  $1.50 \times 1.50 \text{ m}^2$  by resolution requirements, the camera was displaced for each sampling session in order to cover the entire region of interest. In this way camera sequences of neighboring areas have been obtained, with a mutual overlap of approximately 20%. As could be expected, the statistical flow data of these samples fit together quite well (see Section 3.5); in the overlapping areas, the fitting has been performed by means of linear interpolation. It is however fundamentally impossible to make a correlation between individual instantaneous turbulence structures in different samples, because these samples are two completely distinct turbulent flow realizations, even if their ensemble-averaged flow statistics correspond very well. The data series of Case 1, 2 and 3 consist of respectively 14, 6 and 4 camera samples. For each flow case these samples visualize the domain of interest, at least including the mixing layer region containing 2DCS and the greater part of the steady gyre pattern.

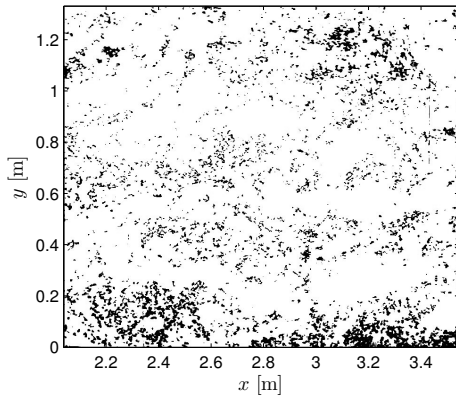
### 3.3.3 Detection of coherent structures: vector potentials

A topic requiring special attention is the way in which large-scale eddies within PIV samples can be detected and visualized. Although a simple look at the velocity vector field often reveals these eddies immediately, defining an efficient detection algorithm for such patterns is not always straightforward. Adrian et al. [1], Bonnet et al. [15] and Scarano et al. [73] give extensive overviews of commonly used identification methods for coherent structures. These approaches are usually a combination of two operations: decomposition of the flow field into a large-scale and a small-scale contribution, as well as the computing of some flow-related quantity which reveals the local presence of vortical structures.

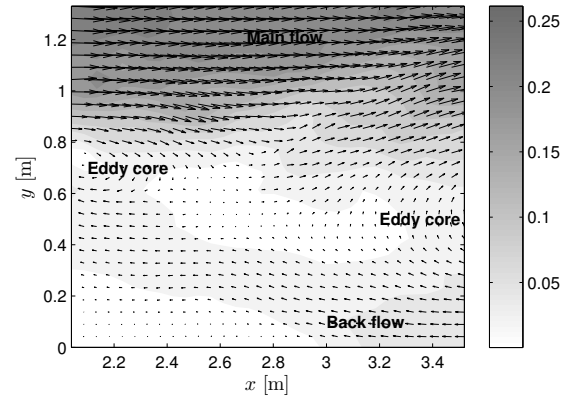
The operation most widely used to decompose turbulent velocity fields  $\mathbf{u}$  is Reynolds decomposition ( $\mathbf{u} = \bar{\mathbf{u}} + \mathbf{u}'$ ), effectively separating the mean flow field from all turbulence scales. Other decomposition approaches addressed by [1] are Galilean decomposition and spatial filtering operations like LES filtering (see Section 4.2.1) which apply low-pass spatial filters that are either homogeneous (e.g. the Gaussian filter) or inhomogeneous in space (Proper Orthogonal Decomposition). Among these methods Reynolds decomposition has remained quite popular for its simplicity and unambiguity, as no filtering criterion needs to be predefined and the ensemble averaging operation can often be performed by means of time averaging. Reynolds decomposition is suitable and convenient as well for the computing of statistical flow quantities. For the purpose of eddy detection, however, it should be kept in mind that Reynolds decomposition removes relevant time-averaged contributions (like gyres) from the turbulent flow field. Therefore subtraction of a time-averaged shear flow (e.g. near-wall flow) may impact the location and properties of detected eddies. In such cases, the analysis of a Reynolds-decomposed field  $\mathbf{u}'$  should always be combined with the analysis of the associated full instantaneous velocity map  $\mathbf{u}$ .

The method most commonly applied to actually detect turbulence structures is based on velocity gradients, computing e.g. the vorticity or the swirling strength of a flow field. An alternative approach is the computing of spatial correlations of the velocity field with a predefined filtering kernel, which is often called “mask eddy”. The latter method is used by Scarano et al. [73] and Van Prooijen [99]. Each eddy detection method has advantages and drawbacks. Gradient-based methods give higher weight to small length scales within the velocity signal (see also Appendix A). Therefore they are particularly suited to detect small-scale eddies; unfortunately, larger-scale structures remain invisible due to noise. The filtering of the velocity field by means of mask eddies necessarily involves (like LES decomposition and Proper Orthogonal Decomposition) the computation of spatial correlations; this is a cumbersome and time-consuming operation, and spatial correlations computed near boundaries of confined measurement areas are not very reliable because not all desired data are present. Moreover, choosing the initial shape and size of a mask eddy partially determines the outcome of the correlation procedure.

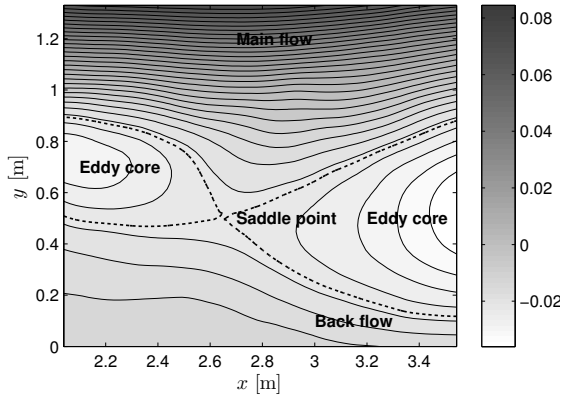
In this study a different detection algorithm is chosen: the computation of the vector potential function  $\psi$  of instantaneous velocity maps  $\mathbf{u} = (u, v)$ . The use of vector potentials is common within the context of electromagnetism but not quite within fluid dynamics, in spite of the mathematical analogies between both scientific fields. Yet, vector potentials are elegant in use: they are well-suited to detect large-scale eddies directly from instantaneous velocity fields, regardless of the vicinity of boundaries. Vector potentials are essentially three-dimensional quantities, but in this study their quasi-2D counterpart is being used. As such, they are partially equivalent to the concept of 2D stream functions. 2D vector potentials are however computed in a different way in order to make a correction for the non-solenoidality of a 2D plane within a 3D flow field. In fact, the non-solenoidal PIV



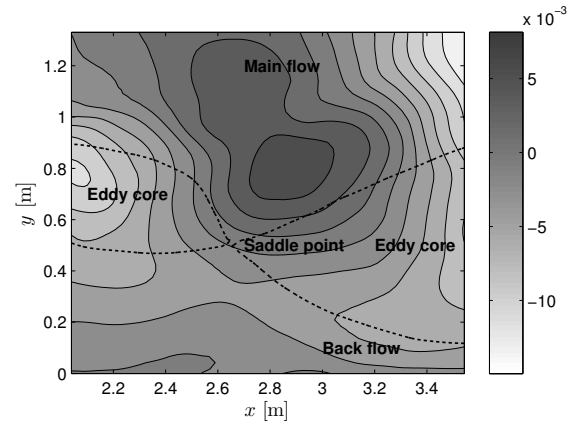
(a) A representative camera image with patterns of black tracer particles (Case 2 for  $2.05 < x < 3.5$  m, after subtraction of background).



(b) Instantaneous velocity vector field  $\mathbf{u} = (u, v)$ , showing two consecutive large eddies moving downstream, in between the main flow and primary gyre back flow. Background colors indicate the absolute velocity.



(c) Instantaneous vector potential function  $\psi$  of the velocity field in (b). The vector potential function shows approximate streamlines, identifying two large eddy contours. Theoretical eddy boundaries are marked by dotted lines, intersecting in a saddle point (a point with zero vorticity).



(d) Vector potential function from (c), after subtraction of the time-averaged flow pattern (Reynolds decomposition):  $\psi' = \psi - \bar{\psi}$ . Both eddies correspond with (shifted) local minima in the function, and the saddle point with a local maximum.

Figure 3.4: PIV *postprocessing algorithm*: from camera image to velocity field.

velocity sample is projected upon a solenoidal 2D velocity field with equal vorticity. Vector potentials can be constructed by solving a Poisson equation for each component of the vorticity, using homogeneous Neumann boundary conditions. See Appendix A for a full explanation on the construction of vector potentials and their relevance for large eddy detection.

Each local maximum or minimum of a vector potential function  $\psi$  uniquely identifies a large eddy core of positive, respectively negative vorticity sign. The shape of the eddy is given by the surrounding vector potential isolines, which are aligned with the local direction of the velocity vector  $\mathbf{u}$  (see Figure 3.4(b)-(c)).

Vector potentials can be applied in combination with a Reynolds decomposition of the flow field:  $\psi = \bar{\psi} + \psi'$ . If instantaneous vector potential fields of a SLE geometry are plotted, the result will show a series of consecutive large eddies whose kernels are situated

along the center line of the primary gyre (Figure 3.4(c)). When the time-averaged pattern is subtracted from the instantaneous pattern, the resulting plot shows the same vortices slightly shifted side-ward (Figure 3.4(d)). This lateral shift can be explained by the non-uniformity of the time-averaged flow. As the mean flow contains non-zero mean shear and vorticity, local minima in the instantaneous vorticity pattern (i.e. vortex kernels) will shift towards the high velocity side when the mean flow pattern is subtracted.

Figure 3.4 gives an overview of the total process of PIV analysis: from camera image via vector field toward the computing of a vector potential function.

### 3.4 Test run observations: general flow features

In order to explore the parameter space of the SLE experimental setup, 27 test runs have been performed and interpreted by visual inspection (without camera registration), using dye and tracer particles. Every test was running for approximately 1 hour. In all cases an initial transition time of about 15 minutes was sufficient to obtain a fully stationary turbulent situation. The test cases were used to gain insight in the characteristic flow features: the influence of the variation of water depth, discharge and geometry on the over-all flow pattern, on gyre sizes and on large eddy length scales.

Two essential dimensionless numbers determine the parameter space of the SLE setup: the bulk Reynolds number ( $Re$ ) and the Froude number ( $Fr$ ). Water depth  $H$ , discharge  $Q$  and inflow-outflow width ratio  $B_1/B_2$  have been varied in such a way that the flow remained sufficiently turbulent and fully subcritical. The experimental setup can handle water depths up to 0.16 m and discharges up to 0.08 m<sup>3</sup>/s. An additional constraint on the parameter space is the requirement that the recirculation zone has to fit within the length of the flume. This requirement is very restrictive for Case 1, whereas it has no impact at all on Case 3. Hence, among the three geometries Case 3 is the most flexible one, which allows for higher discharges and lower water depths than the two other geometries.

Figure 3.5 shows the effective parameter spaces of all 3 cases. All  $(Q, H)$ -points for the test runs have been chosen in the region  $Fr < 1$  and at the right side of the  $Re = 10000$  limit. The lower limit for  $Re$  has been chosen 10000 instead of  $\approx 2000$  in order to guarantee sufficiently turbulent flow in the entire recirculation zone, even in the relatively stagnant secondary gyre.

It should be noted that the  $Fr = 1$  upper limit in Figure 3.5 is related to the Froude number in the *inflow* section of the flow, which is obviously larger than the outflow section Froude number. If flow in the inflow section is already subcritical, certainly the outflow section will have  $Fr < 1$  as well. On the other hand, the  $Re = 10000$  constraint refers to the *outflow* Reynolds number, which will always be smaller than  $Re$  inside the inflow section. Hence both limits have been chosen in a conservative manner.

Some test run results can be found in Figure 3.6. For all 27 runs, the primary gyre length  $L_1$  and secondary gyre length  $L_2$  are shown as a function of  $Q$ ,  $H$  and  $B_1/B_2$ . The data points in the figure legends are corresponding to those in Figure 3.5. The primary gyre size is defined by the reattachment length ( $L_1$ ); the secondary gyre size is defined by the time-averaged  $x$ -coordinate of the secondary separation point along the wall ( $L_2$ ). Both definitions take the inner corner of the recirculation area as the origin (see Figures 3.2 and 3.7). In this thesis, this corner is usually the lower left corner of a diagram. Both water depth and gyre sizes are made dimensionless by the lateral expansion width  $D$ . Since the locations of the primary reattachment point and the secondary separation point are usually slightly oscillating (due to the passing by of 2DCS), Figure 3.6 shows time-averaged values

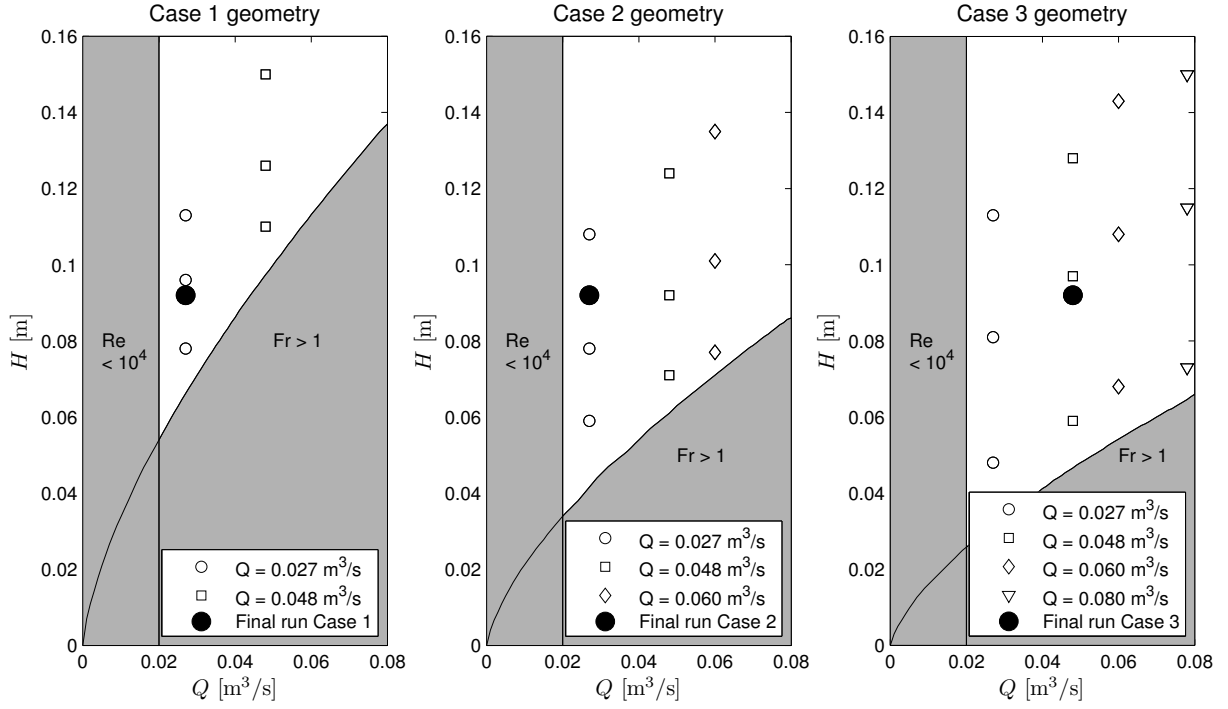


Figure 3.5: Location of the 27 test runs in the parameter space of the experimental setup. The solid dots indicate the locations of the three final PIV runs for Case 1, 2 and 3.

of  $L_1$  and  $L_2$ . The maximum uncertainty in both values is estimated to be  $\approx 0.3$  m. The following subsections outline four characteristic flow features that have been observed within the test runs. In Figure 3.7, a few important flow features that will be mentioned in these subsections are listed and indicated.

### 3.4.1 Effect of shallowness on the primary gyre

First a general trend is observed: the reattachment length  $L_1$  decreases for decreasing depth. This holds for each value of  $Q$  and for each geometry separately. The experiments by Babarutsi et al. [7], carried out on a SLE equivalent with Case 2, showed that the gyre length  $L_1$  scales with the expansion width  $D$  in the deep-water limit and with  $H/cf$  in the shallow-water limit. Which limit does prevail is determined by the bed friction number  $S$ , representing the ratio between dissipation and production of 2DCS energy (see Sections 2.2.3 and 2.4):

$$S = c_f \frac{D}{2H} \quad (3.1)$$

This stability parameter has been derived from the general formula by Alavian and Chu [2] for shallow mixing layers in general (see also Van Prooijen and Uijttewaai [101], Booij and Tukker [16] and Uijttewaai and Booij [91]):

$$S = c_f \frac{\delta}{H} \frac{U_c}{\Delta U} = c_f \frac{\delta}{H} \frac{\frac{1}{2}(U_1 + U_2)}{U_1 - U_2}, \quad (3.2)$$

where  $\delta$  is the local mixing layer width,  $U_c = \frac{1}{2}(U_1 + U_2)$  is the mean velocity in the mixing layer center and  $\Delta U = U_1 - U_2$  is the lateral velocity difference. For a SLE geometry with

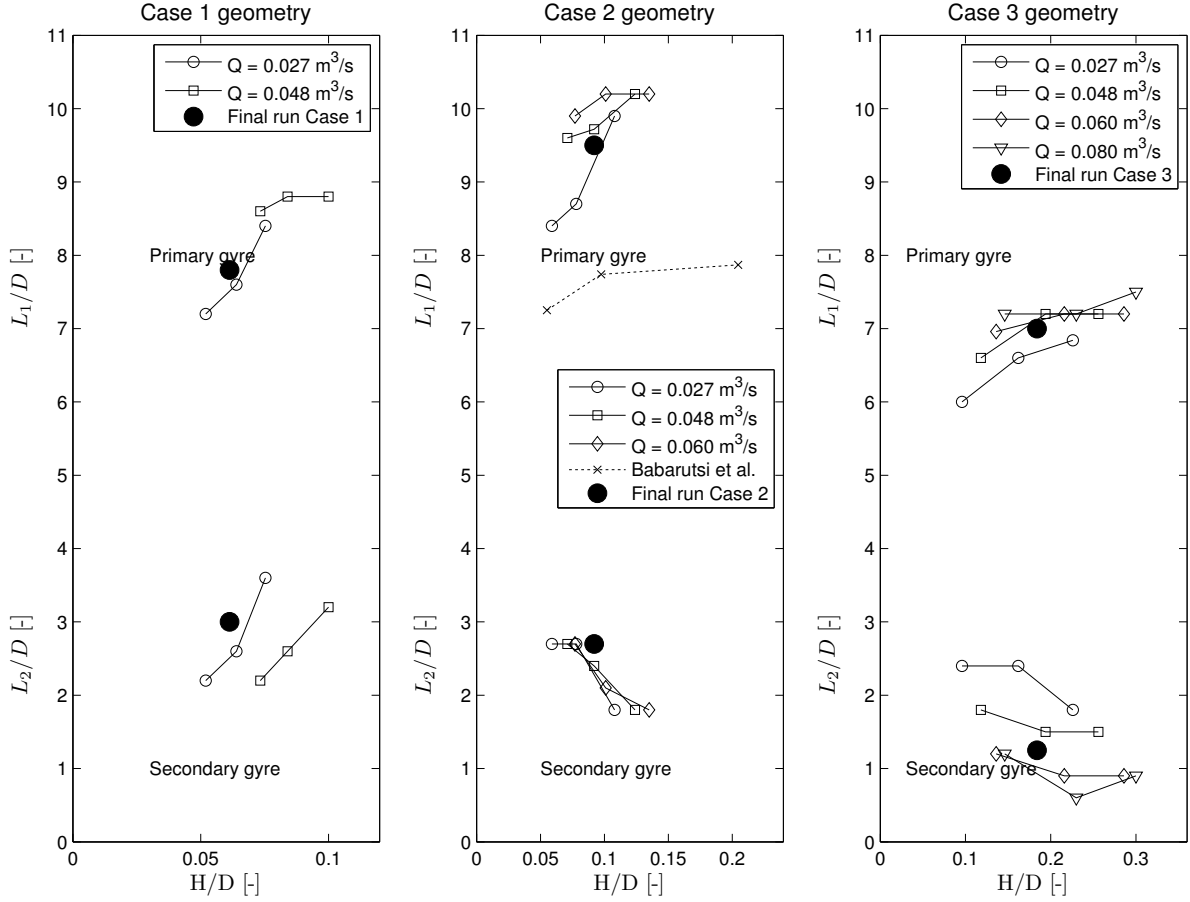


Figure 3.6: Scaled primary and secondary gyre lengths  $L_1/D$  and  $L_2/D$  as a function of  $H/D$  for the 27 test runs, sorted by geometry and discharge. The three solid dots indicate the results for the final PIV runs for Case 1, 2 and 3 (see Section 3.5-3.7). Results of SLE experiments by Babarutsi et al. [7] are shown as well.

bulk inflow velocity  $U_0$  we obviously have  $U_1 = U_0$  and  $U_2 = 0$ , hence  $U_c = \frac{1}{2}U_0$  and  $\Delta U = U_0$ . If it is furthermore assumed that  $\delta \approx D$  (which is usually true in the far field), equation (3.2) reduces to (3.1). The deep-water limit given by Babarutsi et al. is  $L_1 = 8.0D$  for  $S < 0.05$ ; the shallow-water limit is given by  $L_1 = 1.2H/c_f$  for  $S > 0.10$  (see [7, 8]).

The values for  $L_1$  found in the current experiments are located in a wider range than the values found by Babarutsi et al. Because we have  $S = 0.022$  for Case 1,  $S = 0.015$  for Case 2 and  $S = 0.007$  for Case 3, the deep-water limit  $L_1/D = 8.0$  was initially expected in all geometries. This upper limit is however exceeded in all tests for Case 2 and in most tests for Case 1; for large values of  $Q$  even  $L_1/D = 10$  has been reported (see Figure 3.6). The opposite holds for Case 3: all  $L_1/D$  values measured lie between 6.0 and 7.2. Apparently the deep water upper limit for  $L_1/D$  is not equal for all three geometries. Furthermore it is found that (in general) an increase of  $Q$  (with  $H$  unchanged) leads to a slight increase of  $L_1/D$ . The exceeding of  $L_1$  values in Cases 1 and 2 may be explained by two causes. Firstly, the hydraulically smooth wall conditions of the present experimental setup: in comparison, the experiments by Babarutsi et al. were performed in a flume with considerable roughness (even up to  $c_f = 0.024$ ). Secondly, the relatively high Reynolds number of the present flume (compared to the previous experiments) is expected to be important for the steady gyre pattern.

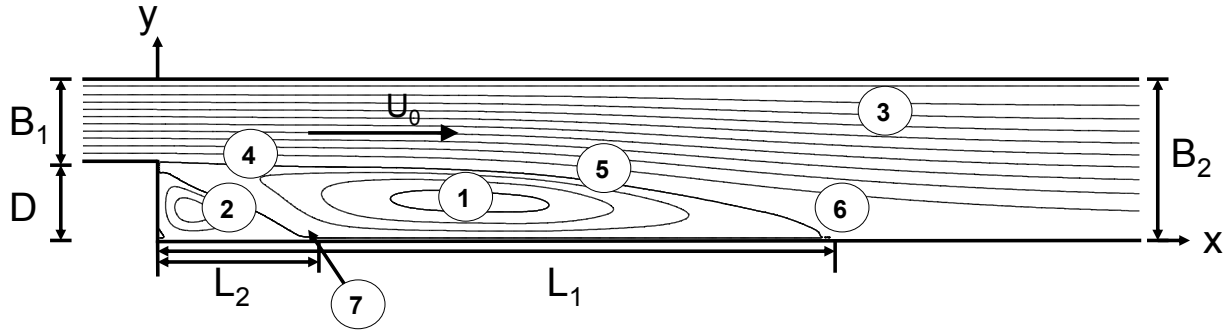


Figure 3.7: *Sketched example of a representative flow pattern in the experimental setup, showing the locations of some key flow features: 1) primary gyre; 2) secondary gyre; 3) intermittent gyre along the continuous sidewall; 4) near-field mixing layer, downstream of separation point; 5) far-field mixing layer; 6) primary reattachment point; 7) secondary separation point.*

The influence of geometry variation (as well as  $Re$  and  $c_f$ ) seem to be of such importance that it is questionable whether all 27 test observations can be fit into one generic formulation, governed by one stability parameter  $S$ . No attempt is made here to formulate such a generic formulation for a modified form of  $S$ ; however, it is anticipated that the length scales  $B_1$  and  $B_2$  play an important role.

### 3.4.2 Effect of shallowness on the secondary gyre

The second observation is that the secondary gyre length  $L_2$  (for Cases 2 and 3) shows a pattern opposite to the behavior of the reattachment length  $L_1$ . As relative depth decreases, the secondary gyre grows in size. The secondary separation point (feature no. 7 in Figure 3.7) moves further downstream. This can be understood by the weakening of the primary gyre. As the primary recirculation backflow decreases in discharge and energy for decreasing depth, it will separate more easily from the solid wall (due to the local adverse pressure gradient connected to the secondary gyre). As shown by the current experiments,  $L_2$  can reach a value up to 30-40% of the primary reattachment length  $L_1$ . With decreasing depth (i.e. increasing gyre shallowness ratio  $D/H$ ),  $L_1$  decreases and  $L_2$  increases. This implies that the primary gyre is losing terrain from two sides. On the contrary, the secondary gyre in the tests for Case 1 is growing and decreasing at a rate comparable with that of the primary gyre. Case 1 is the “shallowest” flow case; it is the flow geometry with the smallest value of  $H/D$ , which implies quite a shallow gyre region. It is observed that, in these cases, the secondary gyre has grown too big to maintain itself within such shallow conditions (due to the influence of bottom friction). Consequently, it breaks up into two structures: a smaller stable secondary gyre in the lower left corner and an intermittent structure directly downstream of it. This effect is illustrated by the time-averaged stream function of Case 1 in Figure 3.10. In some cases, even a very small “tertiary gyre” in the lower left corner (in the vicinity of the point  $x = y = 0$ ) has been observed.

### 3.4.3 Intermittency effects in the main flow

The third feature observed is associated with the continuous wall opposite to the recirculation zone (feature no. 3 in Figure 3.7), especially for the Case 1 tests. Because of its

relative shallowness (smallest value of  $H/D$ ) and its smallest inflow/outflow width ratio  $B_1/B_2$ , Case 1 includes a main flow pattern that tends to separate from the continuous wall. This effect is caused by considerable broadening and deceleration of the main flow in the far field; this deceleration occurs in combination with an adverse pressure gradient which may lead to separation. Indeed a separation area, with fluid rotating counterclockwise (opposite to the primary gyre), is actually observed in the most shallow tests. This opposite gyre is an intermittent feature; its presence strongly depends on the instantaneous passing by of 2DCS inside the mixing layer. In Case 1, these 2DCS are able to entrain so much main flow fluid into the mixing layer that the main flow temporarily separates from the continuous wall. The frequency of this intermittent feature is equal to the temporal frequency of the passing by of 2DCS. The phenomenon, unfortunately, is located too close to the outflow boundary to be studied in an accurate way. In the tests for Case 2 and Case 3 it is absent, probably due to higher values of  $H/D$  and  $B_1/B_2$  and hence a weaker mean flow deceleration (resulting in a smaller adverse pressure gradient).

### 3.4.4 The vortex shedding process

The fourth and final process studied is the emergence of large-scale 2DCS. These quasi-2D structures can be described in detail because of the abundance of tracer particles in the mixing layer, whereas the local injection of dye yields additional information about 3D flow effects. In all test runs a sequence of large-scale vortices is observed. As in other shallow shear flow experiments, eddies grow in energy and size as they move downstream. Both the 2DCS and mixing layer width  $\delta$  widen in downstream direction, until a final equilibrium width is reached due to the increasing influence of energy dissipation by bottom friction. The final mixing layer width  $\delta$  is observed to be of the same order of magnitude as the expansion width  $D$ .

The pathway of 2DCS cores (when they are analyzed after subtraction of the time-averaged flow, see the following sections) is roughly a straight line along the interface between main flow and recirculation zone (dotted line in Figure 3.8). In the near field this pathway can be approximated by the line  $y \approx D$ , which is the “shadow line” directly downstream of the primary separation point. In the far field the pathway slightly bends toward the low velocity side, as the primary gyre gradually becomes narrower toward the primary reattachment point. It is observed however that 2DCS still survive for a long distance after passing the reattachment point. Eventually the 2DCS kinetic energy dissipates under the action of bottom friction, whereas kinetic energy production by lateral shear becomes negligible in the far field. However, although turbulence intensities are gradually decaying, the 2DCS length scales often remain intact all the way down to the outflow weir.

A key question to be answered is how 2DCS development is influenced by the presence of steady gyres in the recirculation zone. In the work by Van Prooijen [99] on SML flows, the mixing layer develops at the interface of two uniform flows without much influence of side walls. This situation allows for an elegant theoretical model, i.e. the assumption of self-similar velocity profiles and a description of the growth of eddy energy modes in terms of linear stability analysis. In case of a recirculating flow, no straightforward linear behavior or self-similarity can be expected beforehand. The presence of a primary and secondary gyre gives reason to investigate how large eddies behave in the presence of these gyres.

In the region  $0 < x/D < 1$ , directly downstream of the separation point, the lateral difference of streamwise velocity has its maximum. (It is even larger than the bulk velocity of the main flow, due to the neighboring return velocity of the secondary gyre.) Mixing



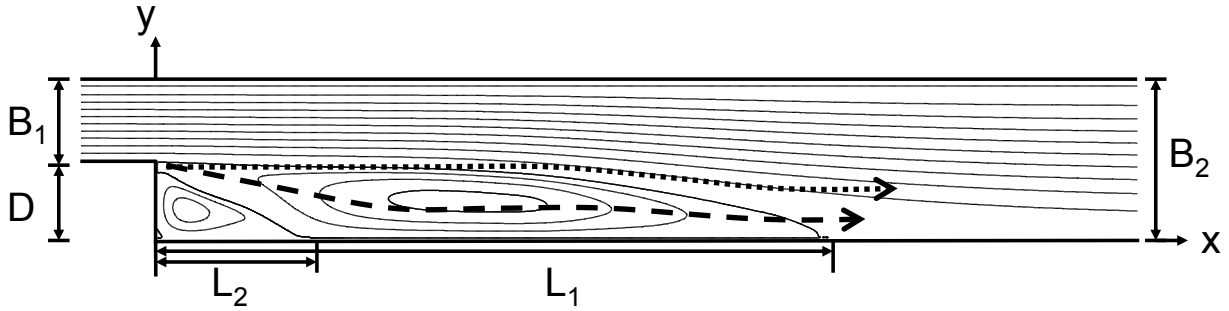


Figure 3.8: Average pathways of 2DCS shed from the separation point. Dashed line: pathway of instantaneous eddy pattern; dotted line: eddy pathway after subtraction of the mean flow field.

layer vortices are continuously shed from the separation point and advected downstream (feature no. 4 in Figure 3.7). Basically they start as Kelvin-Helmholtz instabilities. The near-field tracer particle behavior clearly exhibits that three-dimensionality (in the form of upwelling and downdraft regions) plays a role in the near field, as may be expected according to Jirka [47]. In all 27 test runs, no significant dynamic interaction between near-field shed vortices and the secondary gyre is observed. This can be explained by the fact that the gyre and the eddies have opposite vorticity sign in the horizontal plane. The growing 2DCS are observed to act like “gear-wheels” in between the secondary gyre and main flow, effectively separating them. The near-field mixing layer does not penetrate into the secondary gyre and appears not to be influenced by the secondary gyre as well. This observation is in accordance with the theory presented in Section 2.2.2, in spite of the importance of 3D effects within the near field.

When moving downstream, however, the dynamic interaction between mixing layer eddies and the primary gyre is significant. Looking at *instantaneous* flow patterns (i.e. without subtraction of the mean flow field), the large-scale eddies are observed to follow the center line of the primary gyre, approximately along the line  $y \approx \frac{1}{2}D$  (dashed line in Figure 3.8). As mixing layer eddies and the primary gyre are quasi-2D structures with equal vorticity sign, these structures are able to interact with one another (“vortex merging”, see Section 2.2.2), effectively transferring turbulent kinetic energy to larger length scales.

This merging process can be actually observed in the experimental setup; it may be coined *gyre-vortex interaction*. Emerging 2DCS are engulfed into the primary gyre and their vorticity cores travel downstream over the full gyre length, causing the entire gyre pattern to oscillate. This explains the frequently observed “breathing” of the primary gyre, e.g. the upstream-downstream oscillation of the primary reattachment point and secondary gyre separation point. If the flow field is Reynolds-decomposed (see Figures 3.4(c) and 3.4(d)), the 2DCS pattern shifts from the line  $y \approx \frac{1}{2}D$  toward  $y \approx D$  due to the subtraction of time-averaged lateral shear. This residual pattern represents the large-scale turbulence fluctuation around the mean flow field. The length scales of these 2DCS gradually grow in downstream direction due to entrainment, whereas dynamic gyre-vortex interaction contributes to the kinetic energy level of these larger scales. Quantitative results presented in the following sections confirm that the growth rate of 2DCS sizes and mixing layer width can be described by the combination of entrainment and far-field bottom friction, whereas the kinetic energy level (velocity scale) of these eddies depends on relative shallowness. It is conjectured that the relative shallowness ratios  $H/D$  and  $H/B_1$  are important for the presence of gyre-vortex interaction.

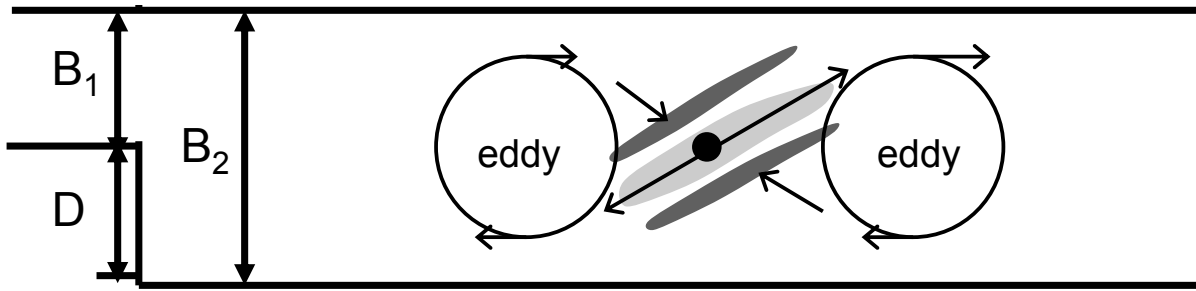


Figure 3.9: *Conceptual sketch (distorted scale) of vertical upwelling (light gray region) and downdraft (dark gray regions) in between two 2DCS (as observed at the free surface). The solid dot indicates a saddle point: zero vorticity and strong deformation of the inter-2DCS flow field.*

In various test runs it is observed that the shallow mixing layer development incidentally gives rise to very large eddies with significant transverse velocity components, considerably penetrating into the main flow. Such 2DCS can be held responsible for the sometimes observed intermittent separation events along the continuous wall in Case 1 (see Section 3.4.3). Apparently large 2DCS play an important role in the entrainment of main flow fluid into the mixing layer.

It should be noted that it takes time to establish the vortex shedding pattern described above. The secondary gyre is initially absent in every test run. After starting the flow, the primary gyre fills the entire upstream corner of the separation zone, resulting in only small lateral shear downstream of the separation point. No significant 2DCS development is observed whatsoever during this initial stage. Gradually the primary gyre starts to separate from the wall  $y = 0$  in its upstream corner, giving rise to the secondary gyre. After approximately 10 minutes (at most, in the present test cases), the secondary gyre has grown sufficiently in size to fill the entire near-field expansion region and induce a return flow close to the separation point. Consequently, the near-field lateral shear increases considerably and mixing layer eddies start to be shed from the separation point, boosted by the primary gyre-vortex interaction.

In the middle field and far field, large eddies have a predominantly 2D character and their growth is limited by the influence of bottom friction. However, even quasi-2D structures do exhibit a certain 3D behavior, visible by the presence of secondary flow. Due to strong vorticity in each 2DCS kernel, centrifugal forces induce a vertical circulation flow pointing outward near the water level and pointing inward near the bottom. This gives rise to a zone of net divergence at the free surface of each eddy. To some extent this effect can be compared to the well-known spiral flow in river bends. It also has been observed in laboratory experiments on shallow wake flows (see Von Carmer et al. [107]). The effect is strongest in the middle field of a shallow shear flow, where energy production due to lateral shear dominates over dissipation due to bottom friction. In the far field secondary flow (like 2DCS kinetic energy) is gradually fading out.

In the present experiments, not only some secondary flow inside eddies is observed; also the region in between two consecutive 2DCS is influenced by 3D effects. The flow in these regions involves saddle points within the instantaneous vector potential function (see Figure 3.4(c)). Such saddle points are characterized by zero vertical vorticity and maximum shear

		Case 1	Case 2	Case 3
$B_1$	[m]	0.5	1.0	1.5
$B_2$	[m]	2.0	2.0	2.0
$D$	[m]	1.5	1.0	0.5
$H$	[m]	0.092	0.092	0.092
$Q$	[m <sup>3</sup> /s]	0.027	0.027	0.048
$U_0$	[m/s]	0.58	0.29	0.34
$Re_{inflow}$	[-]	54000	27000	32000
$Re_{outflow}$	[-]	13500	13500	24000
$Fr_{inflow}$	[-]	0.61	0.30	0.37
$Fr_{outflow}$	[-]	0.15	0.15	0.27

Table 3.1: *Input parameters of final PIV experiments for Case 1, 2 and 3.*

in the horizontal plane. This implies that 3D secondary flow effects emerging from 2DCS kernels can be intensified here by means of the vortex stretching mechanism (see Chapter 2). This intensification often results in regions of considerable upwelling and downdraft of fluid, which have been actually observed in most test runs. In between traveling 2DCS a couple of long streaks of black tracer particles are often found, as well as an empty region in between, which indicates the presence of consecutive zones of vertical upwelling (divergence) and downdraft (convergence). Figure 3.9 gives a conceptual sketch of this situation. The 3D secondary flow effects described above cannot be studied in detail by means of 2D surface PIV data. In Chapter 4 more attention will be paid to this phenomenon when analyzing 3D simulation data.

It must be emphasized that the observed gyre-vortex interaction is most pronounced in the shallowest test cases ( $H/D \ll 1$ ), as this interaction is a typical quasi-2D turbulence phenomenon. The largest interaction is found in the Case 1 and Case 2 tests (where  $H/D = 0.067$  and  $H/D = 0.1$  respectively), especially in the “symmetrical” Case 2, where  $B_1 = D$ . Presumably a geometrical effect also plays a role here: the largest 2DCS energy levels are observed in Case 2, where main flow and recirculation zone have the same width and hence offer relatively much room for the development of 2DCS with minimal sidewall influence. Both in Case 1 and Case 3, the developing mixing layer is located in the vicinity of a solid sidewall: either  $D$  or  $B_1$  is small. Moreover, Case 3 is the “deepest” SLE geometry considered in this study (with  $H/D = 0.2$ ). The gyre-vortex interaction effect is observed to be weak in this geometry, as the quasi-2D character of the mixing layer is limited. This implies a lower 2DCS energy level than in Case 1 and Case 2. The secondary gyre size in Case 3 remains relatively small as well, as can be seen in Figures 3.6 and 3.10.

Based on the 27 test runs described in this section, three representative flow cases have been selected for detailed PIV analysis. The dimensions and input parameters of these three final SLE runs are outlined in Table 3.1. Results of the PIV analysis are presented in the following sections.

### 3.5 PIV data analysis: time-averaged flow statistics

All recorded PIV time series have a sampling period of 700 s, which is equivalent to about 50-70 consecutive large eddies. In this section, time-averaged flow statistics such as mean flow pattern, turbulent kinetic energy and Reynolds stresses are presented for all three

cases. For each case, quantities belonging to neighboring recording areas have been fitted by linear interpolation in the overlapping region.

Figure 3.10 shows contour plots of the time-averaged stream functions  $\bar{\psi}$  of Case 1, 2 and 3. The stream functions have been acquired by time-averaging of instantaneous vector potential functions  $\psi$ . The resulting mean flow patterns shown in Figure 3.10 are rather representative for the range of 27 test runs. All cases show a primary and a secondary gyre. The primary gyre of Case 1 is captured for approximately 60%. (Due to practical problems, it was not possible to acquire PIV data further downstream.) The gyre lengths  $L_1$  and  $L_2$  measured in the present cases have already been indicated in Figure 3.6, see Section 3.4. It should be noted that  $L_2$  in Case 3 is much smaller than in the other two cases (both absolute and relative to  $D$ ). As pointed out in Section 3.4.4, this can be explained by the relatively high  $H/D$  ratio in Case 3. In Case 1, the tendency of the secondary gyre to break up in two parts (see Section 3.4.2) is visible in the region near  $x \approx 4$  m.

Figures 3.11 to 3.14 show sequences of transverse profiles (bold lines) of the following time-averaged flow quantities: streamwise mean velocity  $\bar{u}$ , streamwise turbulent kinetic energy  $\overline{u'^2}$ , transverse turbulent kinetic energy  $\overline{v'^2}$  and horizontal Reynolds stress  $\overline{u'v'}$ , all made dimensionless with  $U_0$ . In each picture the left horizontal axis shows the  $x$ -position of the cross-sections chosen (dashed lines), whereas the right horizontal axis refers to the scale of the flow quantity considered. All spatial distances have been scaled by  $D$ . The dash-dot lines give an impression of the mixing layer widening throughout the domain.

The mean velocity profiles  $\bar{u}$ , given in Figure 3.11, indicate a gradual decrease of the lateral velocity difference and a gradual widening of the mixing layer region for all cases. Negative values of  $\bar{u}$  indicate the primary gyre return flow along the wall  $y = 0$ . In the cross-section at  $x/D = 1$  separation of the return flow is visible, and hence the emergence of the secondary gyre.

The components of turbulent kinetic energy (TKE) and Reynolds stress exhibit a comparable pattern: the profiles are widening and flattening in downstream direction. After an initial stage of broadening, TKE and Reynolds stress profiles tend towards a constant final width. As pointed out by Van Prooijen [99], this can be ascribed to a far-field decrease of lateral shear and increasing influence of bottom friction (i.e. increasing far-field values of the bed friction number  $S$ ).

With respect to the transverse TKE and Reynolds stress distributions, Case 2 shows the largest peak and Cases 1 and 3 have slightly smaller peak values (Figures 3.13–3.14). Apparently both the relative shallowness ratios  $H/D$  and  $H/B_1$  influence the relative turbulence intensity. The peaks are growing over the entire near field and middle field length and reach a far-field equilibrium value (see also Figure 3.17(b)–(c)). The final decay of these quantities occurs even further downstream and is not captured by the present measurement data. Unlike the transverse TKE and Reynolds stress peaks, the streamwise TKE peaks (Figure 3.12) appear to grow quickly in the near field, reaching a final value that remains more or less constant over the length of the measurement domain (see also Figure 3.17(a)). The streamwise TKE values found in Case 3 are surprisingly large, even larger than the corresponding values found in Cases 1 and 2. This can possibly be explained by the large relative depth of Case 3 and hence the relative dominance of transverse shear over bottom friction (small values of  $S$ ).

It is clear that the profiles shown in Figures 3.11–3.14 are too irregular to be fully described by means of a self-similarity assumption. Self-similar profiles have often been found for both deep and shallow geometries; see Chu and Babarutsi [26], Uijttewaai and Booij [91] and Van Prooijen [99]. In a self-similar flow time-averaged flow quantities are described by one single shape function involving length scales that are valid everywhere in the turbulent

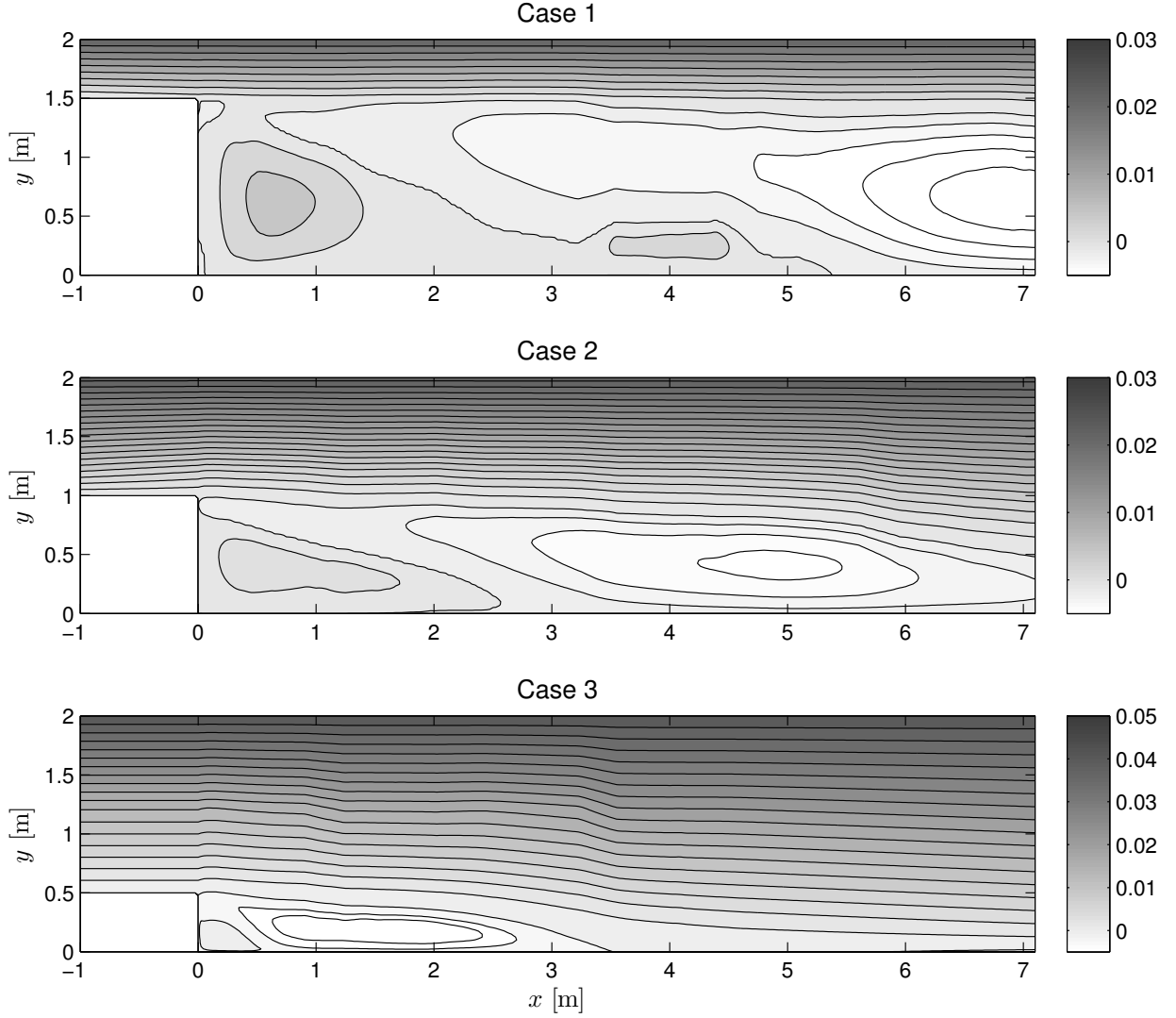


Figure 3.10: *Time-averaged and depth-integrated stream functions  $\bar{\psi}$  in  $m^3/s$ , for PIV Cases 1, 2 and 3.*

part of the flow (see Nieuwstadt [67]). Due to the influence of sidewalls in the present experiments, especially due to the presence of two steady gyres, such uniform length scales are not properly defined. Therefore a straightforward theoretical model of the SLE geometry based on shape functions is not possible here.

Nonetheless, some of the modeling tools from the integral mixing layer model presented by Van Prooijen [99, 101] are applicable in the present context as well. If we erroneously neglect the influence of sidewalls on the mixing layer and try to model various mixing layer characteristics (e.g. mixing layer width and maximum lateral shear) in a way analogous to [99], we can recognize the actual differences between the SLE and SML mixing layer behavior and assess the applicability of the integral model to the present cases.

To this end, we borrow some definitions from the SML research context. The initial lateral velocity difference over the mixing layer is denoted by  $\Delta U_0 = U_1 - U_2$ , where  $U_1$  and  $U_2$  respectively denote the high and low inflow section velocities (see Figure 1.6(a)); the mean velocity in the mixing layer center is defined by  $U_c = \frac{1}{2}(U_1 + U_2)$ . For a SLE geometry we have  $U_1 = U_0$  and  $U_2 = 0$ , hence  $U_c = \frac{1}{2}U_0$  and  $\Delta U_0 = U_0$  (see Figure 1.6(b)). Following [26] and [99], the mixing layer width  $\delta$  is defined as:

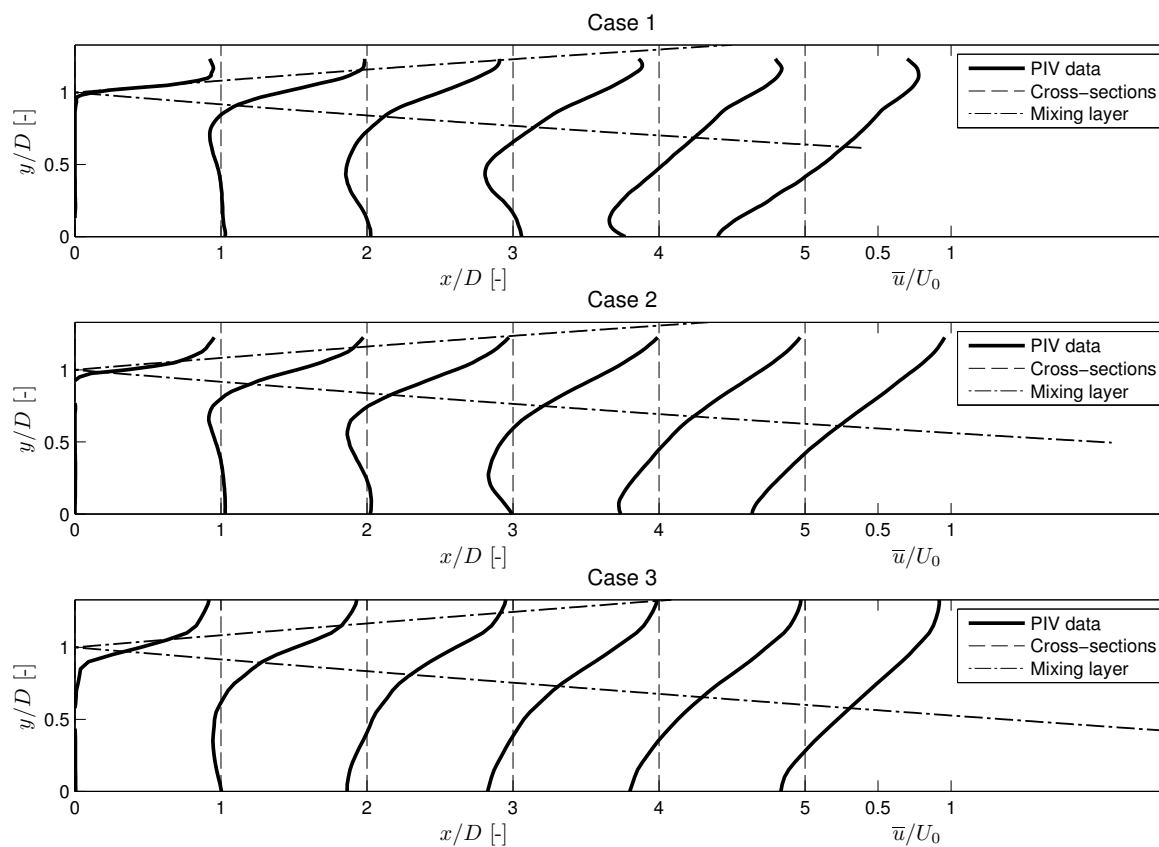


Figure 3.11: *Transverse profiles of the streamwise mean velocity  $\bar{u}$ .*

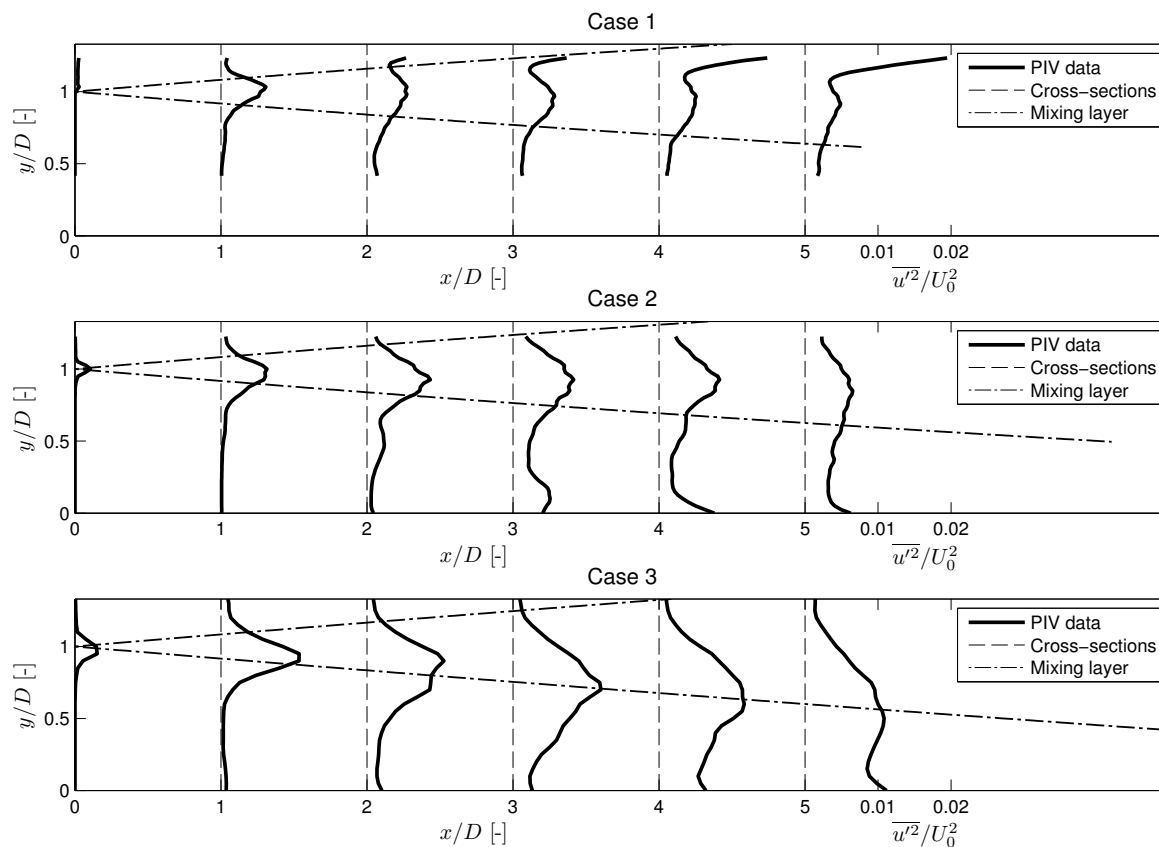


Figure 3.12: *Transverse profiles of the streamwise turbulent kinetic energy  $\overline{u'^2}$ .*

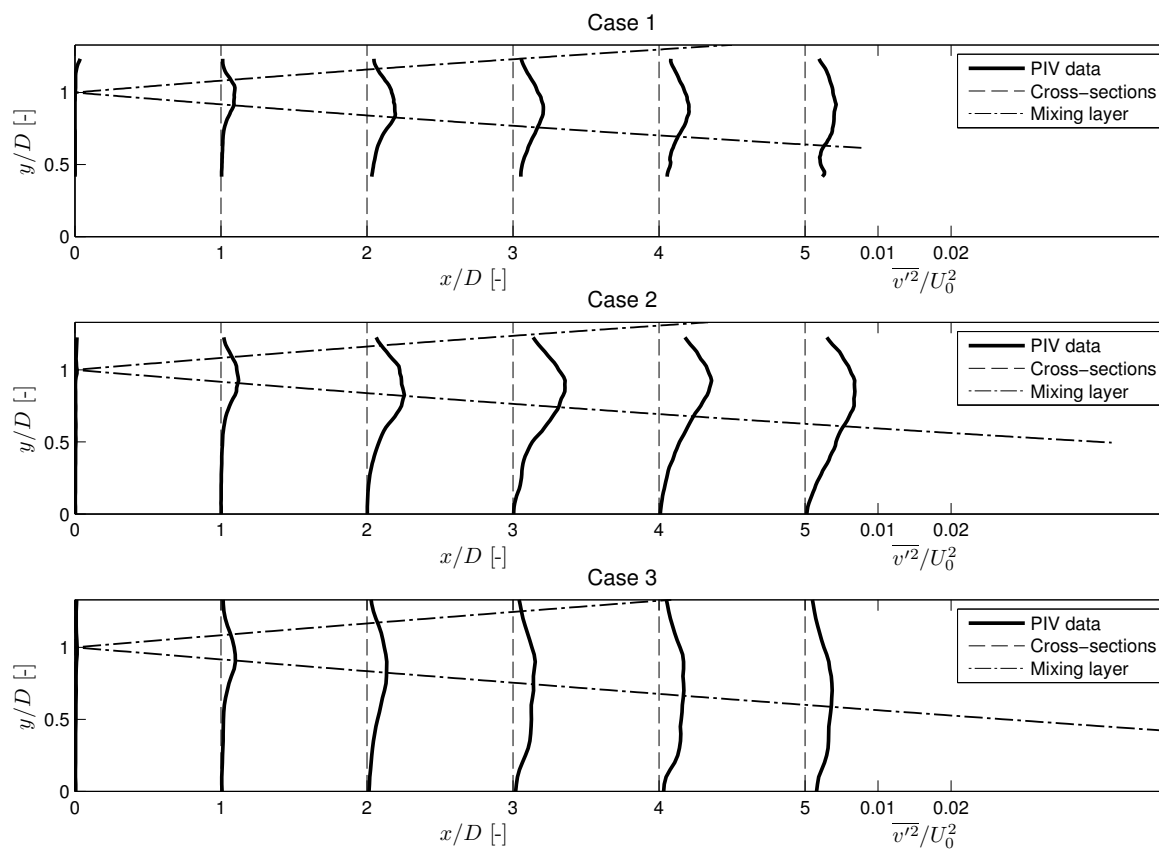


Figure 3.13: *Transverse profiles of the transverse turbulent kinetic energy  $\overline{v'^2}$ .*

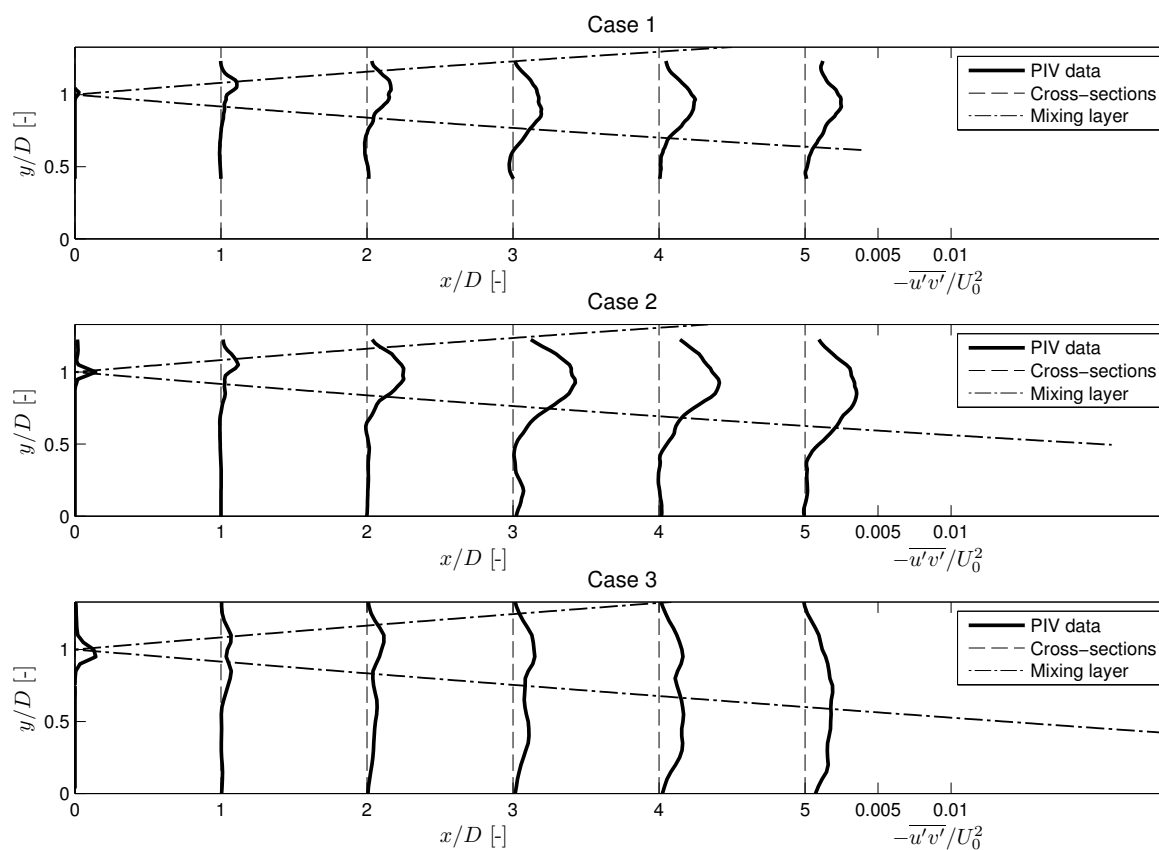


Figure 3.14: *Transverse profiles of the horizontal Reynolds stress  $\overline{u'v'}$ .*

$$\delta(x) = \frac{\Delta U(x)}{\left(\frac{\partial U}{\partial y}\right)_c}, \quad (3.3)$$

where  $\left(\frac{\partial U}{\partial y}\right)_c$  is the lateral velocity gradient in the center of the mixing layer. The mixing layer center is defined here as the location of the local peak in the transverse Reynolds stress profile; alternative definitions are e.g. the location of mean maximum lateral shear, or the position of the dividing stream line between both inflow sections. In practice, these definitions do virtually coincide.

The quantities  $\delta(x)$  and  $\left(\frac{\partial U}{\partial y}\right)_c$  can be obtained in two ways. First, their values can be computed directly from the PIV velocity fields. Secondly, their theoretical values can be derived from the self-similarity theory by Van Prooijen [99]. When comparing the results, we can conclude to what extent the self-similarity theory can be applied.

Based on the self-similarity assumption, the streamwise growth rate of  $\delta$  can be expressed as:

$$\frac{\partial \delta}{\partial x} = \alpha \frac{\Delta U(x)}{U_c}, \quad (3.4)$$

where the (decreasing) maximum lateral velocity difference in streamwise direction is given by:

$$\Delta U(x) = \Delta U_0 \exp\left(-\frac{2c_f}{H}x\right) \quad (3.5)$$

Equation (3.5) implies that the lateral shear development in the mixing layer is governed by the initial shear and by the friction length scale  $H/c_f$ . The constant  $\alpha$  in (3.4) is called *entrainment coefficient*. Its empirical value of  $\alpha = 0.085$ , originally determined by Lesieur [56] for unbounded mixing layers, was found by Van Prooijen [99] to be valid for SML flows as well. From the PIV experiments in the present study, it is concluded that the same value can be used for SLE flows too, especially in the near field. This is not surprising as the initial development of shallow mixing layers in the near field is very similar to that of unbounded mixing layers, because both water depth  $H$  and sidewalls do not have much influence in that stage of the mixing layer development.

Substitution of (3.5) into (3.4) and setting  $\Delta U_0 = U_0$  and  $U_c = \frac{1}{2}U_0$  leads to:

$$\frac{\partial \delta}{\partial x} = 2\alpha \exp\left(-\frac{2c_f}{H}x\right) \quad (3.6)$$

Hence the near-field growth rate of the mixing layer width is expected to equal  $2\alpha \approx 0.17$ . Integration of (3.6) with respect to  $x$  yields a theoretical expression for  $\delta$ :

$$\delta(x) = 2\alpha \frac{H}{2c_f} \left(1 - \exp\left[-\frac{2c_f}{H}x\right]\right) + \delta_0, \quad (3.7)$$

where  $\delta_0$  ( $\approx H$ ) is defined as a small initial mixing layer width, emerging from the boundary layer that has developed upstream of the separation point.

If  $\delta(x)$  is computed using equation (3.7), theoretical mixing layer boundaries can be plotted into the time-averaged flow pattern of the SLE. In Figure 3.15, this has been done for Case 2. It can be seen that the mixing layer boundaries (dashed lines) are following the contour lines of the horizontal Reynolds stress quite well. This suggests a direct relation between the mixing layer width and the size of large-scale 2DCS.



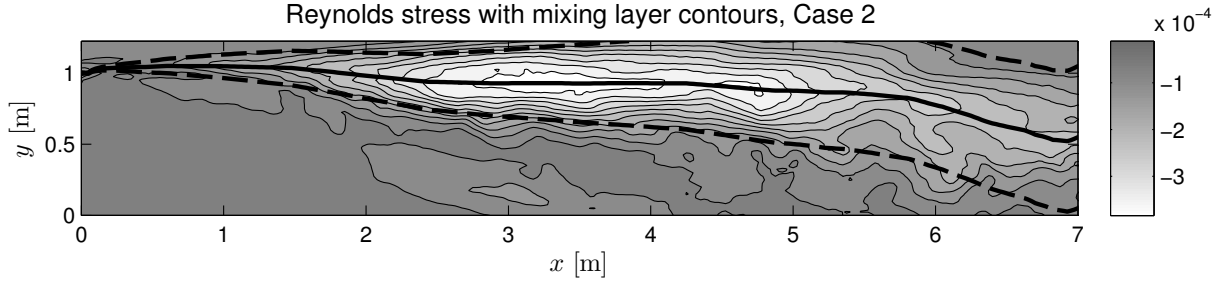


Figure 3.15: *Horizontal Reynolds stress contour lines (Case 2), compared with theoretical mixing layer width contours (dashed lines). The bold solid line indicates the mixing layer center, taken equal here to the Reynolds stress minimum.*

Figure 3.16 compares the measured (a,c) and theoretical (b,d) development of the mixing layer width  $\delta$  and lateral shear  $\left(\frac{\partial U}{\partial y}\right)_c$  (actually the reciprocal of the lateral shear is being shown). It is concluded that the acquired PIV data compare well with the theory outlined above, especially in the near field and middle field ( $x/D < 3$  to 4). From Figure 3.16(a) it follows that the far field SLE values for  $\delta$  start to deviate from unbounded mixing layer theory; the growth rates and final values of  $\delta$  are restricted by the flume width  $B_2$ . Especially Case 1 shows this behavior, as in this case the flume sidewalls are situated near the mixing layer everywhere.

While Figure 3.16 depicts two mean flow quantities along the mixing layer, Figures 3.17(a)–(c) show the corresponding peak values of the streamwise and transverse TKE and horizontal Reynolds stress in streamwise direction. Figures 3.17(a)–(c) correspond to the Figures 3.12, 3.13 and 3.14 respectively. The longitudinal profiles are chosen at the center line of the mixing layer in each flow case.

From Figure 3.17(a) it can be seen that longitudinal profiles of streamwise TKE (as pointed out before) are approximately constant over the greater part of the measurement domain, whereas transverse TKE and Reynolds stress values in the Figures 3.17(b) and 3.17(c) are gradually increasing throughout near field and middle field. This difference can be explained by the idea that streamwise turbulent kinetic energy is built up due to the presence of lateral shear, which is present everywhere and is strongest near  $x = 0$ , whereas the growth rate of transverse TKE and Reynolds stress can be associated with the presence of 2DCS that need time (and streamwise distance) to grow.

From Figures 3.17(b) and 3.17(c) it appears that, for Case 2, the far-field transverse TKE and Reynolds stress values (made dimensionless by  $U_0$ ) are about twice the values for Case 1 and Case 3. They are growing linearly for a longer time and finally stabilize at a higher level. This observation coincides with the fact that Case 2 has the most favorable geometrical properties ( $B_1 = D$ ) for shallow mixing layer growth. The dimensionless transverse TKE and Reynolds stress for Case 1 and Case 3 are almost coinciding, at approximately 50% beneath the Case 2 level, which renders a rather symmetric picture for the three experiments.

Reynolds stress values can be seen as time-averaged indicators for the presence of 2DCS (large-scale velocity correlations). In this way, mixing layer vortices leave their footprints within time-averaged flow statistics. Based on the measured Reynolds stress, it is possible to compute a time-averaged mixing length along the mixing layer center line, which can be interpreted as some 2DCS length scale. This can be done using the horizontal Reynolds

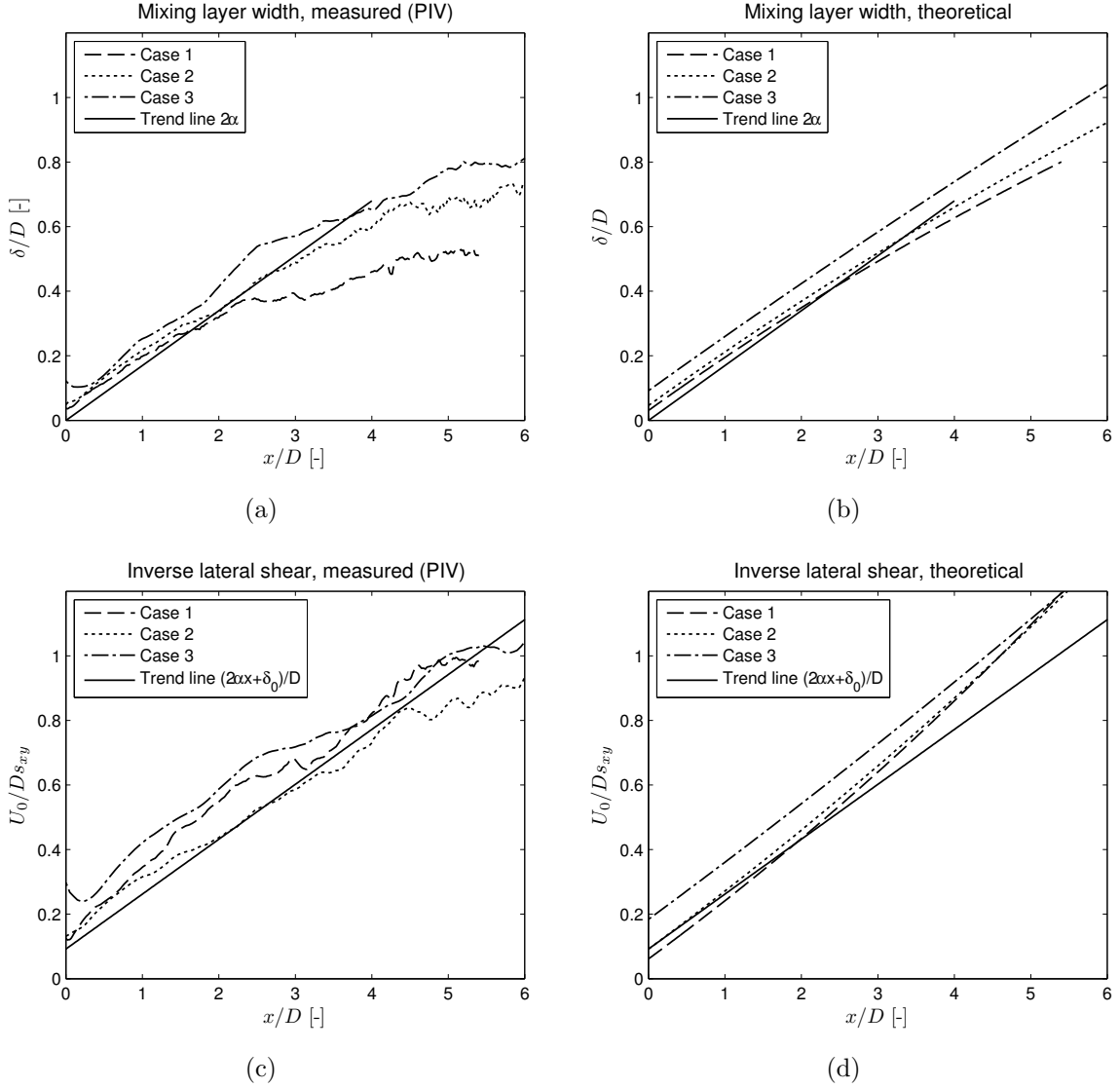


Figure 3.16: *Mixing layer width and maximum lateral shear along mixing layer center line (PIV data and theory compared).*

stress and the mean lateral shear in the following expression:

$$\overline{u'v'} = L_m^2 \bar{s}_{xy}^2 = L_m^2 \left( \frac{\partial \bar{v}}{\partial x} + \frac{\partial \bar{u}}{\partial y} \right)^2, \quad (3.8)$$

where  $L_m$  is the Prandtl mixing length and  $\bar{s}_{xy}$  is the mean horizontal shear. In the same way, an expression for a theoretical horizontal eddy viscosity can be derived:

$$\nu_{2D} = L_m^2 \bar{s}_{xy} = L_m^2 \left( \frac{\partial \bar{v}}{\partial x} + \frac{\partial \bar{u}}{\partial y} \right) = \frac{\overline{u'v'}}{\left( \frac{\partial \bar{v}}{\partial x} + \frac{\partial \bar{u}}{\partial y} \right)} \quad (3.9)$$

In Figures 3.17(d) and 3.17(e), the horizontal eddy viscosity  $\nu_{2D}$  and mixing length  $L_m$  are shown in dimensionless form as a function of  $x/D$ . Remarkable is the nearly linear behavior of the Cases 1 and Cases 3, whereas the behavior in Case 2 exceeds this linearity. Apparently large-scale 2DCS are containing relatively more energy in this case.

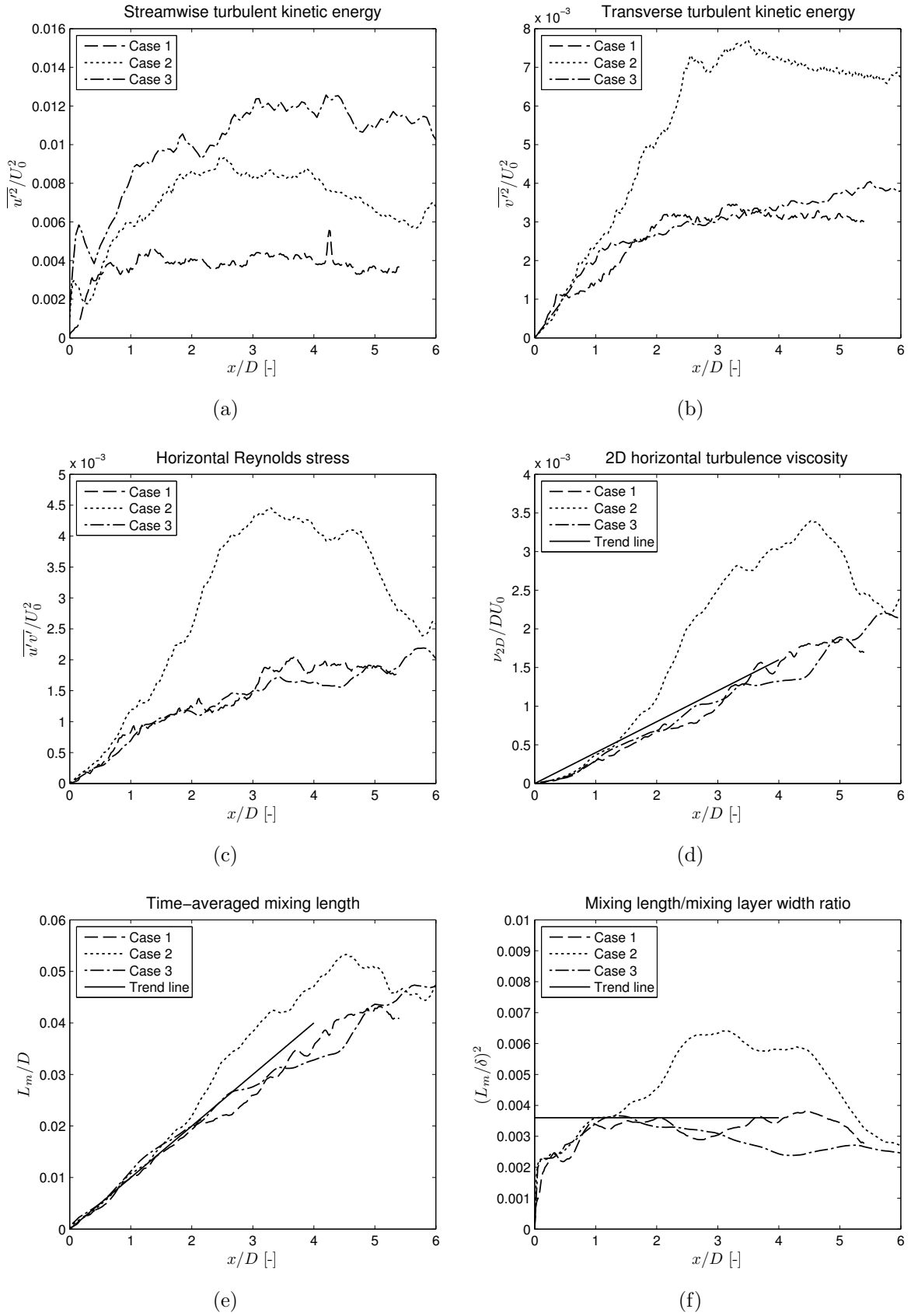


Figure 3.17: Statistical quantities at the center line of the mixing layer: turbulent kinetic energy (a-b), horizontal Reynolds stress (c), horizontal eddy viscosity (d), Prandtl mixing length (e) and Prandtl mixing length relative to mixing layer width (f).

The theoretical mixing length can be divided by the mixing layer width  $\delta$ , resulting in Figure 3.17(f). After a developing distance in the near field, the ratio  $(L_m/\delta)^2$  tends toward a constant value of  $\approx 0.003 - 0.004$  for Case 1 and Case 3. Again the Case 2 values exceed the other two cases: a constant value of  $(L_m/\delta)^2 \approx 0.006$  is reached in the region  $2 < x/D < 4$ , while in the far field a gradual decay is observed. Uijttewaal and Booij [91] have found that, for shallow mixing layers without significant sidewall influence, the ratio  $(L_m/\delta)^2$  usually reaches a constant value between 0.004 and 0.01. This is explained by the fact that the 2DCS length scales are growing proportionally with the mixing layer width. Apparently the proportionality coefficient is larger for the present Case 2, due to the geometrical reasons pointed out before.

It is not surprising that the mixing lengths  $L_m$  computed here are almost an order of magnitude smaller than the 2DCS length scales actually observed (as well as the values of  $\delta$  measured), as we are applying time-averaged statistical quantities to describe an intermittent phenomenon. Better alternatives to derive actual 2DCS time scales and length scales from the PIV data are given (respectively) by examining energy density spectra of measured layer velocity fluctuations and by conditional averaging of instantaneous velocity maps. These two operations are described in Sections 3.6 and 3.7.

### 3.6 PIV data analysis: spectral statistics

In order to reveal the distribution of turbulent kinetic energy over various time or length scales, energy density spectra of turbulence velocity signals can be derived. An energy density spectrum is defined as a (Fast) Fourier Transform (FFT) of the auto-covariance of the original signal. In order to construct spectra of turbulent velocity signals, the method given by Emery and Thomson [33] is adopted. Unfortunately, the horizontal dimensions of the present PIV camera samples ( $1.50 \times 1.50 \text{ m}^2$ ) are too limited to allow for reliable spatial spectra. Moreover, spatial energy density spectra are not easily interpreted due to the inhomogeneity and anisotropy of large-scale turbulence in the present experiments. Only spectra of temporal signals are feasible with sufficient resolution (measurement duration 700 s, sampling frequency 10 or 15 Hz). Nevertheless, if Taylor's frozen turbulence hypothesis is applied, time scales derived from energy density spectra can be fairly well converted into length scales multiplying them by a streamwise mean flow component.

Figures 3.18(a)-(f) represent series of energy density spectra along the center line of the mixing layer, for  $x = 2D$ ,  $x = 4D$  and  $x = 6D$ . The left column contains spectra  $E_{uu}$  of the streamwise velocity fluctuation  $u'$ , the right column shows spectra  $E_{vv}$  of the transverse velocity fluctuation  $v'$ . The dotted lines in each diagram indicate spectra of the "background" turbulence outside the mixing layer, measured inside the main flow section near the separation point. The vertical solid lines indicate the frequency that can be associated with a length scale equal to the water depth (using Taylor's hypothesis). Hence, the spectra shown in Figure 3.18 are almost entirely linked to supra-depth length scales. The sub-depth scale parts of the spectra, containing the isotropic inertial range, cannot be captured in the present free-surface PIV experiments and are not visible here. Furthermore, each spectrum exhibits an amount of noise at the high-frequency side due to aliasing.

In the transverse spectra  $E_{vv}$  of Case 1 and 2 (the most "shallow" geometries,  $H/D = 0.05$  and  $0.1$  respectively), the development of profound peaks can be observed. These peaks can be related to the presence of 2DCS in the horizontal plane. When moving downstream, the peak levels are rising (indicating an increase of eddy energy density) and the peak

locations shift toward the low frequency side of the spectrum (indicating a growing eddy length scale). For the relatively “deep” Case 3 ( $H/D = 0.2$ ), the spectral peak in  $E_{vv}$  is less pronounced (Figure 3.18(f)). This is an indication for weaker 2DCS development and also a weaker interaction of eddies with the primary gyre. As in all three cases the  $E_{vv}$  peak levels are rising for increasing  $x$ , it can be stated that the 2DCS kinetic energy production dominates over dissipation for the full length of the measurement domain. In case of a slightly shallower flow experiment probably a stronger influence of dissipation due to bottom friction will be found.

In the streamwise spectra  $E_{uu}$ , all peaks are somewhat wider and less pronounced than in the transverse spectra. Apparently the dominant energy-containing frequencies have a wider range in the streamwise spectra. This can be explained by the fact that large-scale fluctuations in streamwise direction do not only contain contributions from 2DCS turbulence itself, but also contributions from a possible random displacement of 2DCS in transverse direction. This phenomenon, explained before by Van Prooijen et al. [100], broadens the spectrum for the streamwise TKE whereas the spectrum of the transverse TKE is not influenced by this random displacement and hence remains narrower. From this observation it follows that transverse spectra are more useful for determining 2DCS characteristics than streamwise spectra (see also De Nijs [31]).

The total energy content of streamwise turbulent fluctuations is usually higher than the transverse fluctuation energy content. It has been conjectured by [99] that this difference is caused by streamwise elongation of the mixing layer eddies; this eddy anisotropy is induced by lateral shear inside the mixing layer. This explanation by [99] is followed here; however, in the present SLE experiments this vortex elongation in streamwise direction is observed predominantly inside the near field. As shown in Figure 3.19, the far field streamwise and transverse energy components may become equal, which indicates a growing isotropy of the associated 2DCS.

In most graphs of Figure 3.18, certain spectral slopes (on double-logarithmic scale) can be recognized. At the high-frequency side (approximately the region around  $f \approx 1$  Hz), it would be possible to identify the well-known  $-5/3$  power law in all cases, associated to the “inertial range”. However, the inertial range is only to be expected for very small turbulent scales having a fully 3D character. Such an inertial range completely falls outside the frequency domain of the present spectra, as free-surface PIV experiments have far insufficient resolution to capture this phenomenon. It must be concluded that the  $-5/3$  slopes actually observed are present within the spectra only coincidentally. A different and more convincing observation can be made at the low-frequency sides of the present spectra. At the right side of the low-frequency peaks, one can distinguish several slopes close to  $-3$ . These power laws are most distinctively present in the transverse spectra of Case 1 and Case 2. In the Case 3 the  $-3$  slope is more questionable, if not absent. A  $-3$  slope has been found in many shallow flow experiments, e.g. Chen and Jirka [24] and Uijttewaai and Booi [91]. Such a slope can be associated with the dissipation (and presence) of quasi-2D coherent structures, as derived by Kraichnan [51] and Batchelor [10] (see Section 2.2.2). It is remarkable that the most pronounced  $-3$  slope is found in the “shallow” Case 1 and Case 2 whereas it is not found in the “deep” Case 3.

In Figure 3.19, streamwise and transverse components of the energy density spectra from Figure 3.18 are compared more directly. This has been done for all three flow cases and for two different downstream positions:  $x = 2D$  (a,c,e) and  $x = 6D$  (b,d,f). Differences between near-field and far-field behavior can be analyzed. In all near-field spectra (left column) the streamwise component  $E_{uu}$  dominates, indicating anisotropical large-scale turbulence (i.e. the 2DCS are elongated in streamwise direction). In the far field (right

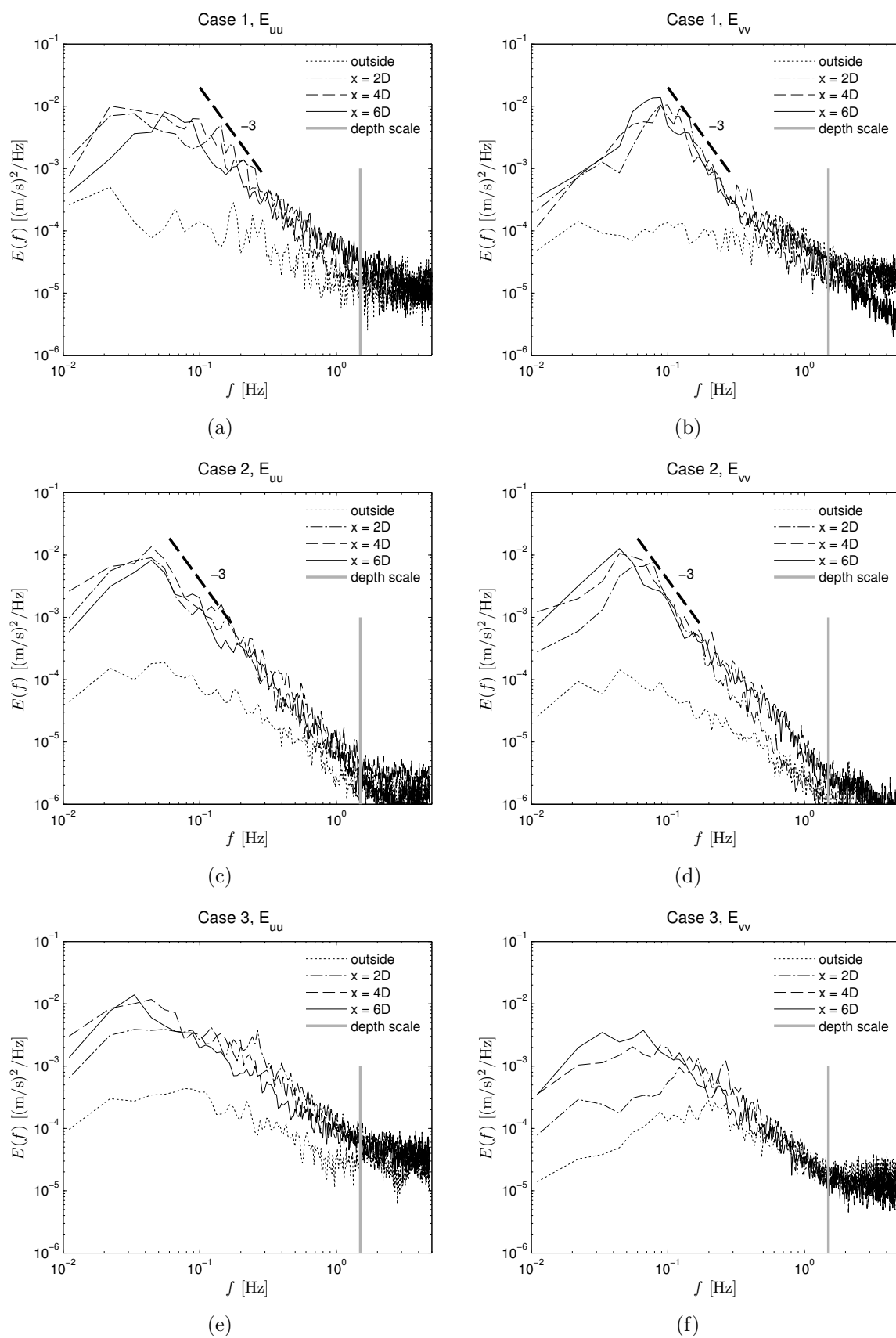


Figure 3.18: Energy density spectra of the streamwise (a,c,e) and transverse (b,d,f) velocities at the mixing layer center line, for various downstream locations.

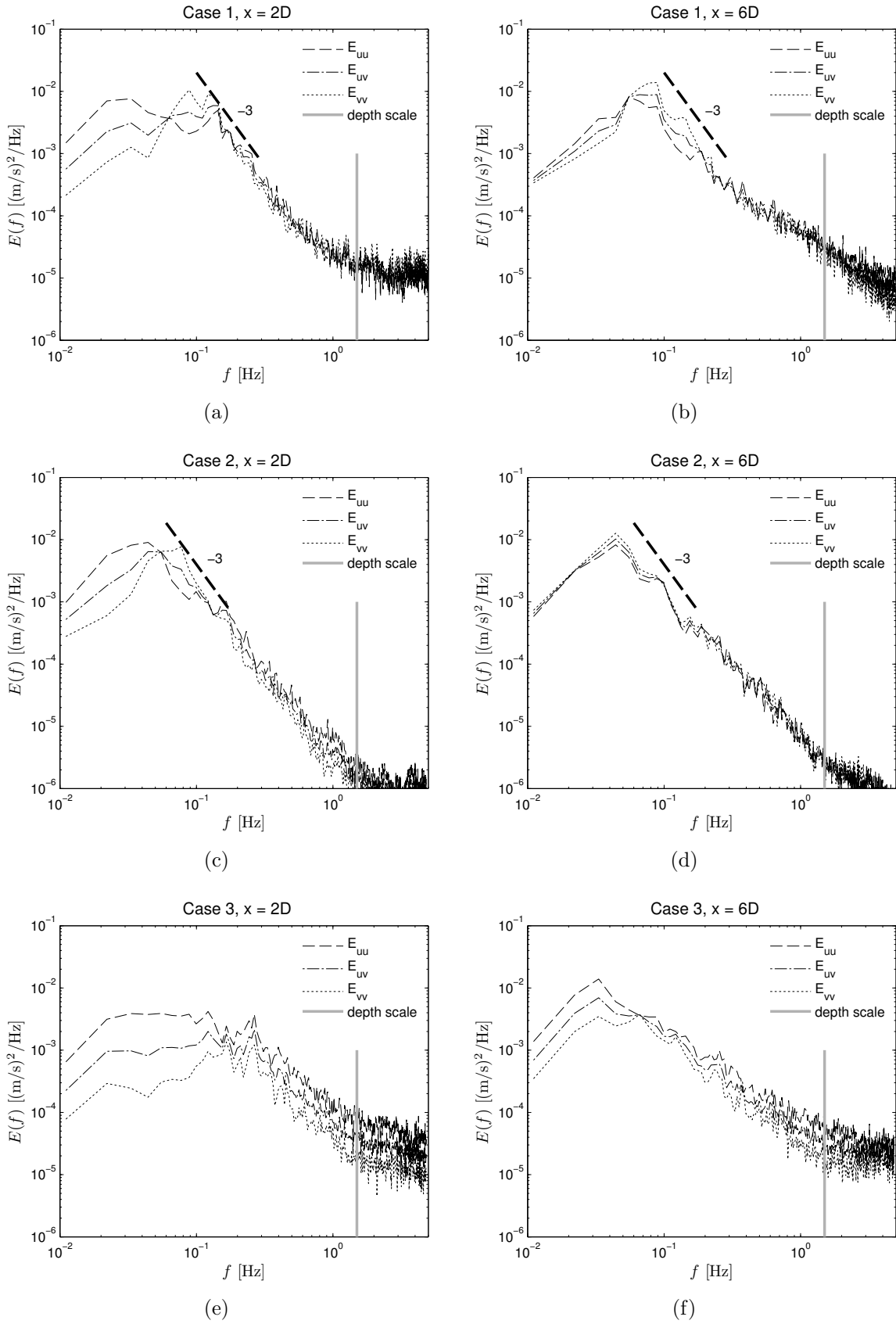


Figure 3.19: Comparison of energy density spectra ( $E_{uu}$  and  $E_{vv}$ ) and cross-covariance spectra ( $E_{uv}$ ) for Case 1 (a,b), 2 (c,d) and 3 (e,f) at  $x = 2D$  and  $x = 6D$ .

column), all flow cases show a decreasing difference between streamwise and transverse components. The Case 2 spectra are entirely isotropical in the far field and Case 1 is fairly isotropic, which indicates that the far-field large-scale 2DCS are virtually circular in those cases (dependent on the phase difference between streamwise and transverse velocity fluctuations). The anisotropy has remained strongest in Case 3 (the deepest geometry again). It is conjectured here that vortices are initially elongated due to the lateral shear which causes the mixing layer to exist, and that a development toward more isotropy is caused by a gradually downstream decrease of lateral shear as well as increasing dissipation by bottom friction (i.e. a gradual increase of the bed friction number  $S$ ).

For completion also the cross-covariance spectra  $E_{uv}$ , associated with the local Reynolds stress, are included in each graph. This cross-covariance spectrum is essentially a complex quantity, however in these graphs only the absolute norm (modulus) of the complex spectrum is shown. This norm has a value which is approximately equal to the square root of the product of  $E_{uu}$  and  $E_{vv}$ . In all cases shown in Figure 3.19, the values of  $E_{uv}$  are in between the values of the other two components.

Theoretically, it is also possible to determine a phase correlation spectrum by taking the complex argument of the associated cross-covariance spectrum. This calculation has been performed by Uijttewaai and Booij [91], using a Laser-Doppler Anemometry (LDA) measurement technique with a sampling frequency of 166 Hz. This experiment yielded a distinctive result: for low frequencies in a mixing layer the phase correlation of  $u'$  and  $v'$  converges to one single value (equal to  $-\pi$ ), whereas for high frequencies the phase correlation is randomly distributed on the interval  $[0, 2\pi]$ . A similar result may be expected for the present experiments. However it appears that, unfortunately, Surface PTV and PIV data contain too much noise to allow for such a phase correlation analysis (see also Van Prooijen et al. [100]). This can be ascribed to too low a sampling frequency (only 10 Hz) and especially to the use of interrogation windows, which destroys a proper phase correlation. Presumably LDA data of the present SLE flows (at 166 Hz, and without interrogation windowing) would give much more accurate results with respect to the complex argument of the cross-covariance spectrum. Also high-resolution PIV measurements of a 3D flow geometry (using high-speed cameras, a laser sheet and very fine tracer particles) allow for such an analysis. Such high-resolution PIV experiments are however outside the scope of the present work.

From the  $E_{vv}$  spectra shown in Figure 3.18 and 3.19, integral time scales  $\tau_{int}$  of the 2DCS vortex shedding process can be determined (see Nieuwstadt [67]) using the spectral peak value  $E_{max}$  and the spectral energy content  $m_0$ :

$$\tau_{int} = \frac{E_{max}}{m_0}, \quad \text{with} \quad m_0 = \int_0^\infty E_{vv}(f)df = \overline{v'^2} \quad (3.10)$$

In Figure 3.22(a), integral time scales (based on the transverse spectra  $E_{vv}$  and made dimensionless by  $U_0/D$ ) are shown as a function of  $x/D$ . For e.g. Case 2, the value of  $\tau_{int}$  converges to  $\approx 10$  s, which is indeed the right order of magnitude compared to the vortex shedding frequency actually observed by visual inspection. Furthermore, these integral time scales of 2DCS can be translated into integral length scales  $\lambda_{int}$  by means of Taylor's hypothesis:  $\lambda_{int} = \tau_{int}\bar{u}$  (see Figure 3.22(c)).

The dimensionless integral time scales of Figure 3.22(a) can be interpreted as inverse Strouhal numbers  $St^{-1}$ , i.e. as dimensionless vortex shedding frequency numbers (see Section 2.3.2). If the values in the graph are inverted, the near-field Strouhal numbers  $St = D/\tau_{int}U_0$  are centered around a value  $\approx 2.0$  and the far-field values are centered around a value  $\approx 0.4$ . These values are somewhat ambiguous, however, as it is questionable



whether the length scale within  $St$  should be defined by the expansion width  $D$  or by the water depth  $H$  in the present experiments.

## 3.7 PIV data analysis: conditional statistics

### 3.7.1 Principles of conditional averaging

The spatial characteristics of large-scale coherent structures, such as their length scales, are best determined by deriving them directly from instantaneous flow maps, rather than by time-averaging or by computing spectral statistics only. In order to acquire some statistical significance for particular events in the flow field, e.g. the passing by of a large eddy through a cross-section, a conditional averaging procedure can be used. This procedure implies that statistical operations are performed on a subset of instantaneous flow maps, under the condition that a certain event occurs within each map of the subset. As it is aimed to determine spatial characteristics of 2DCS throughout the mixing layer, the actual event is defined as the passing by of a large eddy core through a cross-section of the experimental flume; this procedure is repeated for each cross-section provided by the PIV data set (see e.g. Scarano [73] and Van Prooijen [99]).

The idea behind the algorithm of conditional averaging can be compared with a police camera along a highway monitoring the speed of cars. Obviously, the police is not interested in a continuous movie of the highway, for if this sequence of images would be averaged, the result is meaningless. One is only interested in those camera frames that contain a car passing by, or even more specific, a car driving too fast. Only this subset of relevant data needs to be handled.

As pointed out in Section 3.3.3, 2DCS cores are found in the present study by searching for local extrema in vector potential functions  $\psi$  of velocity maps  $\mathbf{u} = (u, v)$ . As all mixing layer 2DCS considered are rotating clockwise, all local extrema are actually minima. Each PIV sample series consists of 7000 or 10500 consecutive flow maps with a grid size of 64 x 63 velocity vectors (see Section 3.3.2); for each sample a 3D data structure containing discrete values of  $\psi(x, y, t)$  is thus available (covering a domain of 1.50 m x 1.50 m x 700 s). Two approaches are available to detect 2DCS: one can find local minima of  $\psi$  in  $(x, y)$ -space for each time level  $t$ , or one can find local minima of  $\psi$  within the space-time domain  $(y, t)$  for each cross-section  $x = \text{constant}$ . Because all 2DCS considered are actually traveling through the domain of interest and consequently pass all possible cross-sections  $x$  at some time level  $t$ , both methods are practically equivalent. In the first method, eddies are fully defined in terms of instantaneous flow kinematics; to detect a single eddy core at time  $t$ , only one instantaneous velocity map  $\mathbf{u}(x, y)$  is needed. This seems logical as the computation of  $\psi$  is merely spatial; it involves spatial derivatives only (see Appendix A). The second method is however more convenient for the present application, because time series of  $\psi$  contain much more data points than spatial data maps. All local minima in a certain cross-section  $x$  can be captured in one single calculation. For each time that a large eddy core passes cross-section  $x$ , a local minimum in  $\psi(y, t)$  is found. The second approach is adopted here for use in the conditional averaging operation.

Another fundamental choice to be made is whether to use the actual quantity  $\psi$  or the Reynolds-decomposed quantity  $\psi' = \psi - \bar{\psi}$  to be checked for the presence of 2DCS. The locations and properties of detected large eddy cores do strongly depend on its definition. When applying full  $\psi$  data, the dominant coherent structures are found near the line  $y \approx \frac{1}{2}D$  inside the primary gyre; when using  $\psi'$ , dominant large eddies are found approximately

along the line  $y \approx D$  (see Section 3.4.4). Moreover, the spatial spreading of detected eddies is much larger when using  $\psi'$  and hence the conditionally averaged eddy for each cross-section is less distinctive (and always weaker) than for the case where  $\psi$  is used.

Should either  $\psi$  or  $\psi'$  be applied? Because the definition of turbulence quantities in Section 3.5 (such as TKE and Reynolds stress) as well as the definition of the energy density spectra in Section 3.6 are based on Reynolds decomposition, it would be natural to adopt the same decomposition in order to obtain conditional flow statistics as well. In that case, large eddies are defined in terms of relative velocity fluctuations only. There is however an important objection to this approach, related to the nature of Reynolds averaging. Reynolds decomposition is a mathematical tool on behalf of the *a posteriori* statistical analysis of turbulent flows. Physical reality, however, does not bother with statistics; for the actual dynamics of large eddies, the term “mean flow” and the associated “flow fluctuation” have no physical meaning. Reynolds decomposition is an artifact emerging from mathematical modeling; however, when detecting turbulence structures within experiments, it is only the real instantaneous situation that matters.

This discussion is related to the question how a turbulent eddy should be actually defined. Can any instantaneous coherent structure around a vorticity kernel be named an eddy? Or can we only speak of eddies as dynamic fluctuations after subtraction of the mean flow? Can a steady gyre be considered to be a large eddy? Or should a large eddy be interpreted as a time-varying (transient) mean flow feature? Should a primary gyre be treated as the time-averaged result of many large eddies or, on the contrary, should one distinguish gyres and eddies from one another, being two completely different physical features?

In the present study, it is concluded that Reynolds-decomposed velocity data are not useful as input for conditional averaging operations. Of course, flow fluctuations and their statistics are interesting in terms of *a posteriori* data output, but when it comes to the individual detection of dynamic large eddies, they are preferably not used. Therefore 2DCS are always detected here using the entire velocity signal  $\mathbf{u}$  and the associated vector potential function  $\psi$ . It is only after the construction of conditionally averaged flow quantities that Reynolds composition can be used again to analyze these quantities.

### 3.7.2 Conditionally averaged output: length and velocity scales

The eduction of coherent structures from velocity maps is a time-consuming task. Each cross-section of the measured turbulent flow is checked at every time level for the presence of a large eddy core. Usually the local minima within the  $\psi(y, t)$  planes (for constant  $x$ ) are located at pretty regular distances from one another, suggesting the existence of a meaningful integral time scale  $\tau_{int}$ . As already expected, most large eddy cores are found along the neighborhood of the primary gyre center line  $y \approx \frac{1}{2}D$ . After acquiring the desired subsets of large eddies in each cross-section, statistical operations can be performed on them.

Figure 3.20 gives an example of the computed vector potential function  $\psi$  of a conditionally averaged eddy (Case 2). Panel (a) depicts the complete function  $\psi$  whereas panel (b) shows the Reynolds-decomposed fluctuation  $\psi' = \psi - \bar{\psi}$ . (One may note that this Reynolds decomposition has been done *a posteriori* after having performed the actual conditional averaging operation.) The conditionally averaged eddy is based upon detected 2DCS in the cross-section  $x = 3.15$  m, which is indicated by a dashed vertical line. As in Figure 3.4(c)-(d), some general flow features as well as the theoretical eddy boundary (dotted lines) have been indicated in Figure 3.20(a)-(b). A large eddy core corresponds to a local  $\psi$  minimum in both pictures, whereas a saddle point is represented by a local  $\psi$  maximum

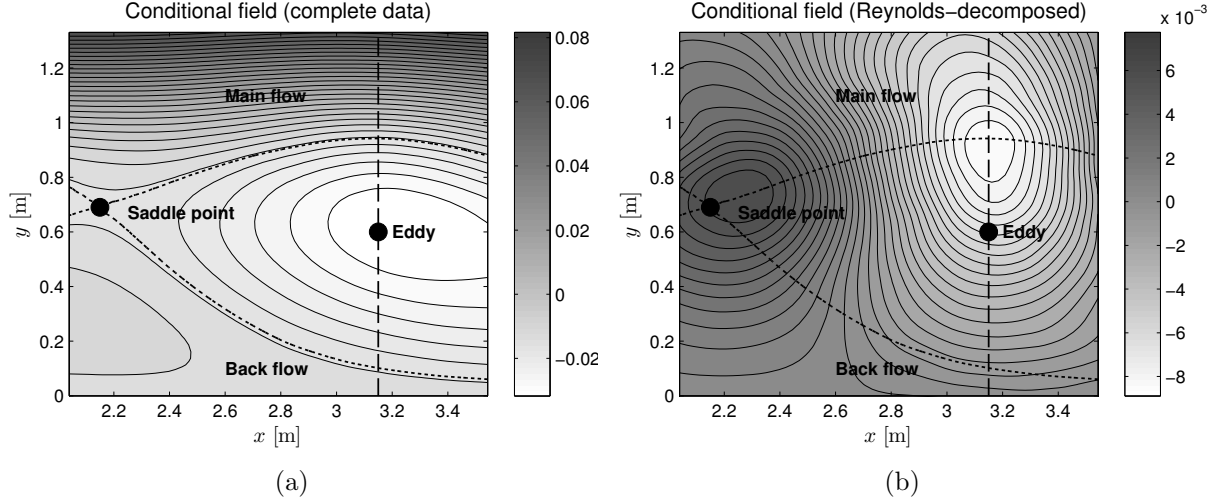


Figure 3.20: *Conditionally averaged vector potential function  $\psi$  of a large 2DCS around  $x/D = 3.15$  m (Case 2), without (a) and with Reynolds decomposition (b). The computed streamlines agree very well with the associated conditionally averaged vector field. The local minimum identifies a clockwise large eddy with a diameter of  $\approx 0.8$  m.*

in panel (b).

In principle, conditional averaging operations can be performed for any point in the sampled flow domain. Near the edges of the  $1.50 \times 1.50$  m<sup>2</sup> PIV recording domains, however, adjacent conditionally averaged flow fields from different data samples may show differences, even if the neighboring mean flow and TKE profiles do fit together quite well. The reason for this difficulty is the intrinsic impossibility to achieve exactly identical turbulent flow conditions in two distinct measurement sessions. Fortunately, the 20% overlap between all PIV sampling areas is useful to circumvent the problem by means of linear interpolation. If turbulent flow data are obtained from one uninterrupted sampling domain, e.g. a computational flow model (see Chapter 4), the problem described above does not exist.

Various length scales and velocity scales can be derived from the acquired conditionally averaged data (see Figure 3.21). The following scales are defined:

1. *Integral length scale ( $\lambda_{int}$ )*: this scale is defined as the streamwise distance between large eddy kernels, or accordingly, the streamwise distance between saddle points. As conditionally averaged data are centered around eddy kernels (local minima), it is straightforward to measure  $\lambda_{int}$  as the distance between two saddle points (local maxima);
2. *Large eddy length scale ( $\lambda_{eddy}$ )*: it is defined as the distance between two local extrema (one maximum and one minimum) in the transverse velocity signal surrounding an eddy kernel, i.e. the region inside which most of the large eddy vorticity is concentrated;
3. *Streamwise eddy velocity scale ( $U_{eddy}$ )*: i.e. the maximum Reynolds-decomposed velocity fluctuation  $u'$  in  $x$ -direction inside the region belonging to a conditionally averaged 2DCS;
4. *Streamwise eddy velocity scale ( $V_{eddy}$ )*, defined as the maximum velocity fluctuation  $v'$  in  $y$ -direction inside the region belonging to a conditionally averaged 2DCS.

From their definition, it is anticipated that  $\lambda_{int} \approx 2\lambda_{eddy}$ . This can be explained as follows.

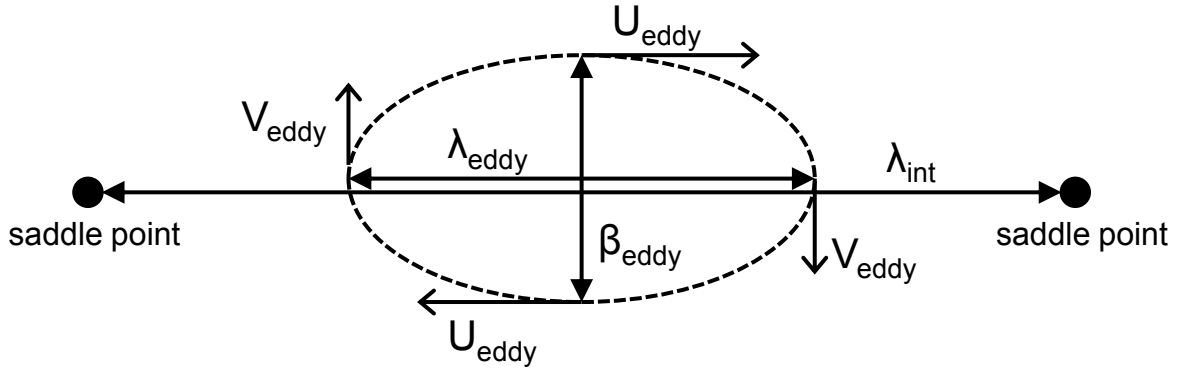


Figure 3.21: *Conceptual sketch of elongated 2DCS with the location of various length scales and velocity scales; satisfaction the continuity constraint requires that  $\lambda_{eddy}/\beta_{eddy} \approx U_{eddy}/V_{eddy}$ .*

Suppose that the longitudinal profile of the Reynolds-decomposed vector potential fluctuation  $\psi'$  resembles a cosine function, with saddle points at the local maxima ( $x = 0$  and  $x = 2\pi$ ) and a vortex kernel at the local minimum ( $x = \pi$ ). Then we have:

$$\psi' \cong \hat{\psi} \cos\left(\frac{2\pi x}{\lambda_{int}}\right), \quad (3.11)$$

in which case the transverse velocity fluctuation will resemble a sine function:

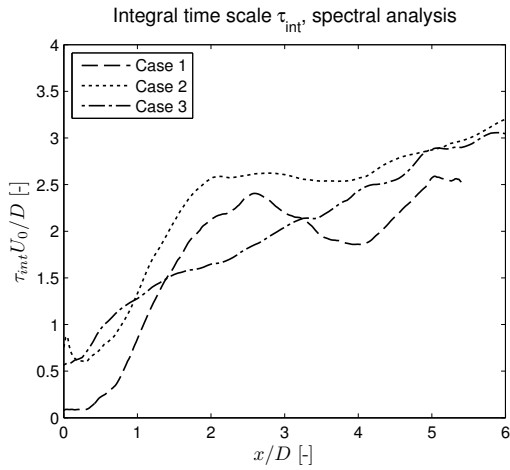
$$v' \cong -\frac{\partial\psi'}{\partial x} = \frac{2\pi\hat{\psi}}{\lambda_{int}} \sin\left(\frac{2\pi x}{\lambda_{int}}\right) = \hat{v} \sin\left(\frac{2\pi x}{\lambda_{int}}\right) \quad (3.12)$$

Two local maxima of the vector potential fluctuation are found at  $x = 0$  and  $x = 2\pi$ , hence the associated length scale is  $\lambda_{int}$ . The transverse velocity fluctuation shows a minimum and a maximum in respectively  $x = \frac{1}{2}\pi$  and  $x = 1\frac{1}{2}\pi$ , which results in an associated length scale  $\lambda_{eddy} = \frac{1}{2}\lambda_{int}$ .

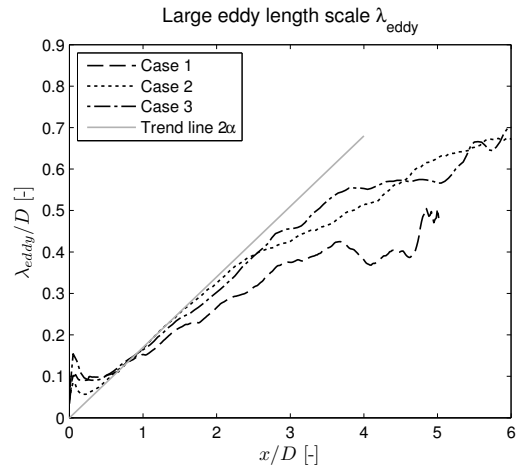
The eddy length scale defined above is a *streamwise* length scale. Defining a transverse eddy scale (named  $\beta_{eddy}$ ) is not straightforward as no sequence of eddies is available in transverse direction. A relevant criterion for determining  $\beta_{eddy}$  is however provided by the 2D continuity constraint of the depth-averaged flow field. If we require zero divergence for each 2DCS kernel, we consequently find  $\lambda_{eddy}/\beta_{eddy} \approx U_{eddy}/V_{eddy}$  (see Figure 3.21 for an illustration of this principle).

Figure 3.22 depicts the various length and velocity scales defined above as a function of  $x$  along the mixing layer center, for Case 1, 2 and 3. The integral time scale  $\tau_{int}$  defined in Section 3.6 is included as well: see panel 3.22(a).

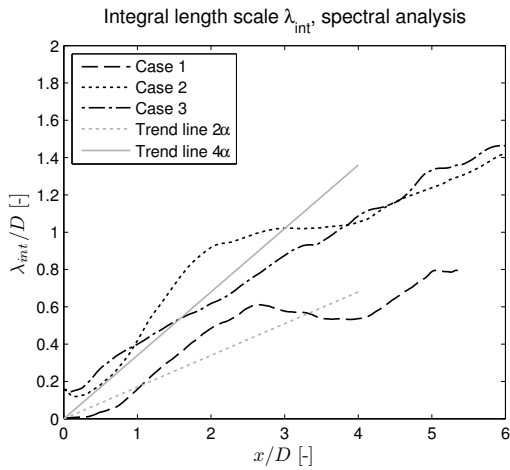
In panels (c)-(d) two versions of the integral length scale  $\lambda_{int}$  are shown. Panel (c) computes the integral length scale based on  $\tau_{int}$  and Taylor's hypothesis, according to:  $\lambda_{int} = \tau_{int}\bar{u}$ . Panel (d) depicts the integral length scales based on conditional averaging. Both panels have the same scaling by  $D$ . It can be seen that both types of integral length scales compare quite well. Obviously, both series of lines do not coincide perfectly; the latter is however not to be expected, since the determination of finite length scales in a continuous flow field always keeps an element of ambiguity. As a guideline to the eyes, two extra lines have been plotted: a trend line for the streamwise development of the mixing layer width



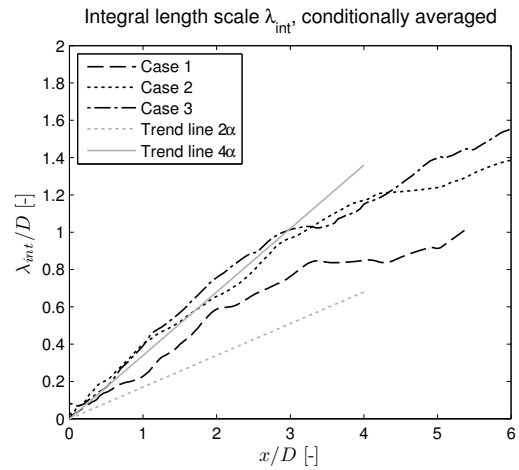
(a) Dimensionless integral time scales, based on spectral analysis ( $E_{vv}$ ).



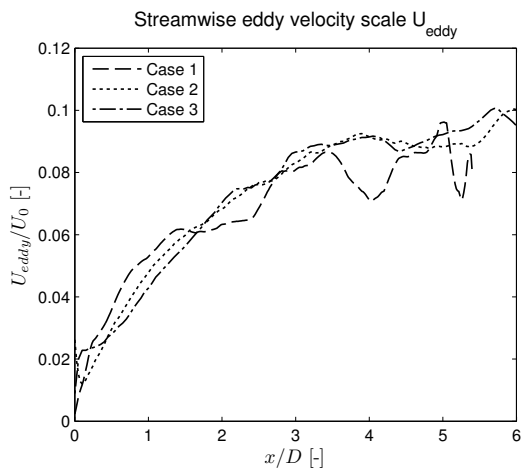
(b) Large eddy length scale, based on conditional averaging.



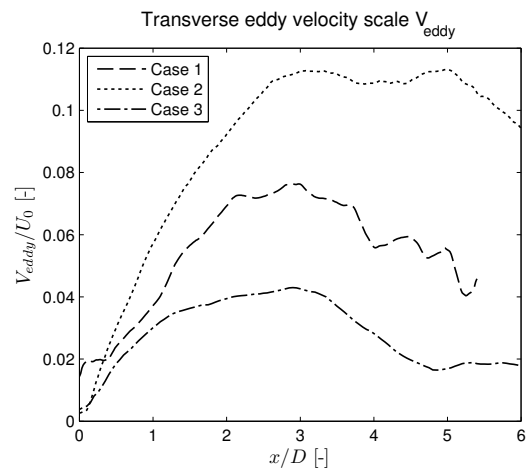
(c) Integral length scale, based on spectral analysis and Taylor's hypothesis.



(d) Integral length scale, based on conditional averaging.



(e) Streamwise eddy velocity scale, based on conditional averaging.



(f) Transverse eddy velocity scale, based on conditional averaging.

Figure 3.22: Quantities at the center line of the mixing layer, based on spectral analysis and conditional averaging: time scales (a), length scales (b,c,d) and velocity scales (e,f).

$\delta(x)$  (growing at a rate  $2\alpha$ ), as well as twice this growth rate ( $4\alpha$ ). Apparently  $\lambda_{int}$  in all three flow cases is bounded by an upper limit of  $\approx 2\delta(x)$ .

Panel (b) shows eddy length scales  $\lambda_{eddy}$ . Like  $\lambda_{int}$  their near-field behavior is linear and apparently bounded to a maximum value of  $\approx \delta(x)$ . From the data in (b) and (d), it is confirmed that indeed  $\lambda_{int} \approx 2\lambda_{eddy}$ .

Finally, panels 3.22(e)-(f) show the longitudinal development of the velocity scales  $U_{eddy}$  and  $V_{eddy}$ . A remarkable difference is observed between both figures. The three resulting lines for  $U_{eddy}$  (after scaling by  $U_0$ ) are almost coinciding, whereas the three results for  $V_{eddy}$  are very different. It can be concluded that streamwise velocity fluctuations are mainly dependent on the lateral shear (represented by  $U_0/D$ ), whereas the transverse velocity fluctuations depend on other causes as well, e.g. the depth ratios  $H/D$  and  $H/B_1$ . In accordance with Figure 3.17(b), the dimensionless transverse velocity scale has a maximum for Case 2, followed by Case 1 and Case 3. When the absolute values of  $V_{eddy}$  are examined (not scaled by  $U_0$ ), the results for Case 1 and Case 2 are comparable whereas Case 3 falls far behind the other two. This difference can be explained once more by the relative shallowness of Case 1 and 2 compared to the “deep” Case 3. Due to the weaker quasi-2D 2DCS dynamics in Case 3, the associated gyre-vortex interaction is weaker as well. This implies a smaller transverse eddy velocity scale and hence a smaller transverse TKE content (see also Figures 3.17(b) and 3.19(f)). It is also observed that, in accordance again with Figure 3.17(b), the “symmetric” Case 2 (with  $B_1 = D$ ) contains the largest transverse velocity scales. Furthermore, from panels 3.22(e)-(f) it can be concluded that the far-field ratio  $U_{eddy}/V_{eddy}$  is smallest ( $\approx 1$ ) for Case 2 whereas this ratio is largest for Case 3; consequently, the same holds for the ratio  $\lambda_{eddy}/\beta_{eddy}$  (see Figure 3.21). These ratios can be considered a measure for the far-field anisotropy of 2DCS, in accordance with the anisotropy observed in the energy density spectra in Figure 3.19.

From the data analysis performed in Section 3.5 to 3.7 it follows that relative shallowness does not have much influence on mixing layer width and streamwise large eddy length scales; in the near field, these scales can be scaled quite well with the help of the entrainment coefficient  $\alpha$ , whereas in the far field the flume width is a limiting factor. On the contrary, the relative shallowness and the associated quasi-2D gyre-vortex interaction have significant impact on large eddy anisotropy (with respect to their length and velocity scales), as well as on TKE levels and horizontal Reynolds stress.

### 3.8 Summary and discussion

Detailed PIV experiments have been performed on a set of SLE flows with variable inflow width. New data have been added to existing experimental data with respect to this geometry. Visual observation (on 27 test cases), as well as time-averaged statistics, spectral analysis and conditional averaging operations (on 3 final cases) have been used to study the development of the steady gyre pattern, shallow mixing layer properties and characteristics of quasi-2D large eddies shed from the separation point. To the knowledge of the author, the present study is the first one to apply large-scale free-surface PIV measurements on the SLE in combination with conditional averaging operations.

From all experiments it is concluded that the relative depth influences the primary and secondary gyre lengths. For decreasing  $H/D$  the primary gyre shortens whereas (in general) the secondary gyre grows in size. Along the entire length of the flume a shallow mixing layer containing traveling 2DCS is established. Despite the presence of 3D secondary flow within especially the middle field, the general picture of the mixing layer is quasi-2D. A

comparison is made between the current SLE experiments and the theoretical analysis by Van Prooijen [99] on SML flows. Although no assumption of self-similarity is intrinsically valid in the present context, the integral mixing layer model by [99] adequately describes various mixing layer properties in the SLE near and middle field.

It is concluded that the longitudinal development of mixing layer width and streamwise 2DCS length scales are well described by the entrainment coefficient  $\alpha$  (see Lesieur [56]). These length scales are not quite influenced by relative shallowness conditions. The associated transverse 2DCS length and velocity scales and turbulence intensities, however, are significantly influenced by the relative depths  $H/D$  and  $H/B_1$ . The relatively “shallow” Case 2 shows the largest transverse eddy velocity scales, as well as transverse TKE and Reynolds stress profiles. This effect is ascribed to the quasi-2D interaction between the steady primary gyre and dynamic 2DCS, as well as to the size of the secondary gyre which accounts for the upstream lateral shear. In Case 1 and Case 2, typically quasi-2D turbulence footprints can be found within the energy density spectra along the mixing layer. In the relatively “deep” Case 3 these quasi-2D effects are weaker, if not absent.

In the near field a slight elongation of 2DCS in streamwise direction is observed. This elongation disappears further downstream in the Cases 1 and 2, whereas it is maintained in Case 3. Vortex elongation comes up from an analysis of both energy density spectra and conditionally averaged 2DCS. It is concluded that this anisotropy arises due to near-field lateral shear; in the far field, decreasing lateral shear as well as increasing influence of bottom friction and gyre-vortex interaction give rise to increasing large-eddy isotropy.

A key element of new information in the present discussion is the idea that 2DCS energy can be enhanced by interaction between a dynamic vortex and a steady gyre. This internal gyre-vortex interaction can be called a typical shallow flow phenomenon, as it requires the quasi-2D character of both structures as well as an equal vorticity sign. Also, the observation that a fully developed secondary gyre gives rise to a stronger large-eddy development is a relevant aspect of this study. This leads to the idea that turbulence intensities of a shallow separating flow could be manipulated by adapting the geometry in such a way that it induces a smaller or weaker secondary gyre.

With respect to the 2DCS generation mechanisms listed in Section 2.2.3, mixing layer eddies in the present SLE are obviously generated by *topographical forcing* (see Jirka [47]). The concept of gyre-vortex interaction leads to a new interpretation of this mechanism. Certainly, the primary flow separation event and the associated primary gyre are induced by topographical forcing in the present geometry. However, these are no sufficient prerequisites to induce 2DCS; for the emergence of the latter, a fully developed secondary gyre is required. This implies that the quasi-2D vortex shedding phenomenon is not forced by *topography* itself but, instead, by the *steady gyre configuration*. Hence, the topographical forcing mechanism has an indirect or “secondary” character here; it is caused by quasi-2D gyre-vortex interaction rather than by solid wall topography.

At this point, it is relevant to recall the “direct vortex shedding” effect as observed by Uijttewaaij, Lehmann and Van Mazijk [93] in their experiments on shallow groyne fields. This mechanism (see Section 2.4) has not been observed in the present SLE experiments, neither by visual inspection nor by PIV data analysis. No 2DCS are observed that remain attached to the separation point, growing until they are launched into the mixing layer at once. Instead, a steady secondary gyre is observed in this region, leaving no room whatsoever for the development of directly shed vortices. All 2DCS observed start as small-scale instabilities between main flow and secondary gyre (“gear-wheels”); they continuously travel along the mixing layer, possibly experiencing gyre-vortex interaction further downstream. However, the mechanism observed here has one aspect in common with direct vortex shedding: a

sufficiently large *secondary gyre* is an essential prerequisite for it.

It is conjectured here that the direct vortex shedding mechanism is typical for groyne fields. Differences in water depth between main channel and groyne field, as well as mild slopes of groyne heads, may play a distinctive role for the development of this specific configuration. Adopting this idea, direct vortex shedding should not be expected in the context of a SLE flow geometry with constant depth and vertical walls. Instead, an “ordinary” shallow mixing layer (containing gyre-vortex interaction effects) is actually observed.

While interpreting SLE results, it should be kept in mind that real-life shallow flow configurations will always be much more complicated than the present idealized laboratory circumstances. Often they do not contain fully developed primary or secondary gyres (e.g. due to bathymetry variations or downstream obstacles like groynes), so that conclusions from the present experiments may not hold in those cases. Also, local bottom roughness variation and the presence of sloping sidewalls may have a profound impact on 2DCS development. A worthwhile next step in the research on shallow recirculating flows could therefore be to repeat the current SLE experiments while replacing the vertical sidewalls by sloping walls, possibly with increased hydraulic roughness.

In Chapter 4, full 3D numerical computations of the SLE flow cases are described; their output data are analyzed in full analogy with the PIV data presented in this chapter. After verification of the numerical results by the experimental data, the numerical 3D model can be used in Chapter 5 to investigate the impact of geometry variations on steady gyre patterns and large-scale 2DCS behavior.



# Chapter 4

## 3D LES computations: basic geometries

### 4.1 Introduction

From the experiments described in Chapter 3, it is concluded that the SLE mixing layer development (including 2DCS dynamics and their interaction with steady gyres) has a quasi-2D character. Nonetheless, the influence of the third dimension is obviously present within the experimental data. This three-dimensionality not only appears from locally observed secondary flow effects inside the mixing layer, but also from the over-all presence of 3D turbulence due to bottom friction. It has been shown by Van Prooijen [99] that the emergence of quasi-2D turbulence in shallow mixing layers is triggered by large-scale components of this 3D bottom turbulence. Hence, 3D turbulence dynamics should be taken into account when quasi-2D turbulence is studied numerically.

In this chapter three-dimensional Large Eddy Simulations (LES) of the three flow cases studied in Chapter 3 are performed.<sup>1</sup> Using conventional numerical techniques, we investigate how the quasi-2D turbulence pattern of the SLE mixing layer is influenced by the three-dimensionality of the flow. The performance of the LES model is checked by comparison to experimental PIV data on Case 1, 2 and 3. Furthermore, the SLE simulation results are compared with an additional simulation of a SML geometry (see Figure 1.6), which is coined Case 4; in this way, the sensitivity of both types of shallow shear flows to topography and upstream 3D turbulence conditions can be investigated.

The LES model used is rather conventional with respect to sub-grid scale (SGS) closure modeling and other numerical aspects. Initially formulated by Boersma [14], the model was applied before to shallow channel flows by e.g. Van Balen [96]. It has been implemented here with only minor numerical modifications, mainly regarding the treatment of solid wall boundary conditions. Despite its simplicity, the model offers reliable 3D flow data provided that the resolution adopted is sufficiently high for LES purposes. Developing innovative advanced LES modeling techniques has been outside the scope of this study.

The major advantage of applying LES above Reynolds decomposition-type models lies in the ability to simulate individual large eddies. This allows for a direct comparison with acquired PIV data. Also, the transfer of kinetic energy between larger and smaller length scales (larger than sub-grid scale) is actually resolved, which implies that dynamic interaction between 2DCS and 3D bottom turbulence is captured by the model.

Section 4.2 describes the setup of the 3D LES model and highlights some details of the

---

<sup>1</sup>Parts of the results in this chapter have been published in Talstra et al. [84].

numerical formulation. Special attention is paid to the way internal solid wall boundaries are being treated. Section 4.3 defines the model input for the simulation of Case 1, 2, 3 and 4. In Section 4.4, LES and PIV results are compared: i.e. time-averaged flow patterns and length scales, flow energy content, energy density spectra and some conditionally averaged quantities. The effect of upstream 3D turbulence on quasi-2D turbulence development is explained in Section 4.5. Finally in Sections 4.6 and 4.7 the secondary flow structures found inside the mixing layer are addressed, as well as their influence on momentum transport throughout the flow. A summary and discussion of the results can be found in Section 4.8.

## 4.2 Description of the 3D LES model

### 4.2.1 The concept of Large Eddy Simulation

The technique of Large Eddy Simulation makes a distinction in the way turbulent scales are treated by the numerical model. From a conceptual point of view (see Spalart [80] and Fröhlich and Rodi [35]), this is the major difference between LES-type models and two other groups of computational turbulence models: RANS (Reynolds-Averaged Navier-Stokes) and DNS (Direct Numerical Simulation). In RANS-type models, turbulent motions at all scales are equally represented by a closure model; on the other hand, DNS-type models do not require any turbulence closure formulation as they basically resolve all turbulence scales. In between those extremes, LES-type models offer an attractive optimum: larger turbulent scales are directly resolved on the computational grid, whereas smaller (sub-grid) scales are accounted for by a closure formulation. This simplification is justified by the assumption that small-scale turbulence behavior (within the inertial range) has an isotropic and geometry-independent character. An overview of available LES methods can be found in textbooks by e.g. Pope [71] and Sagaut [72].

The basic LES approach is derived directly from the Navier Stokes Equations (2.1) and (2.3). The decomposition between “large eddy” and “small eddy” motion in a turbulent velocity field  $u$  is denoted by:  $u = \bar{u} + u'$ . Formally, this LES decomposition is obtained by applying a spatial low-pass filter to  $u$ . Three types of filter kernels are often distinguished: Fourier filters (leading to a sharp spectral cut-off between larger and smaller scales), Gaussian filters (leading to a smooth cut-off) and top-hat or box filters (leading to a sharp spatial cut-off). Using these filter types (see [71, 72]), measured or computed velocity data can be decomposed *a posteriori*. In order to perform an *a priori* LES decomposition of turbulent flow fields that still need to be computed, the low-pass filtering operation is applied to Equations (2.1) and (2.3). This yields the filtered Navier-Stokes Equations:

$$\frac{\partial \bar{u}_i}{\partial x_i} = 0 \quad \text{and} \quad (4.1)$$

$$\frac{\partial \bar{u}_i}{\partial t} + \frac{\partial \bar{u}_i \bar{u}_j}{\partial x_j} + \frac{\partial \bar{p}}{\partial x_i} - \frac{\partial}{\partial x_j} \nu \left( \frac{\partial \bar{u}_i}{\partial x_j} + \frac{\partial \bar{u}_j}{\partial x_i} \right) + \frac{\partial \bar{\tau}_{ij}^{SGS}}{\partial x_j} = 0, \quad (4.2)$$

where the filtered normalized pressure  $\bar{p}$  includes the gravity body force. The residual stress tensor  $\bar{\tau}_{ij}^{SGS} = \overline{u'_i u'_j}$  represents the transfer of kinetic energy from the large-scale motion to smaller scales (3D energy cascade). In practice, the formal spatial low-pass filtering described above is often absent in actual LES models; in these implementations, the filtering operation is performed implicitly by means of the numerical discretization. Therefore, the small eddy scales that are filtered out of (4.1) and (4.2) are usually referred to as “sub-grid scales”.

The LES-decomposed Navier-Stokes equations look quite similar to the Reynolds-Averaged Navier-Stokes (RANS) equations (see [71]). However, the former are spatially filtered whereas the latter involve ensemble averaging, which is usually implemented as a time averaging operation. Moreover, the Reynolds stress tensor  $\overline{u'_i u'_j}$  in the RANS equations represents all scales of turbulent motion, whereas the subgrid-scale (SGS) stress tensor  $\overline{\tau}_{ij}^{SGS}$  in Equation (4.2) represents the turbulent stresses on sub-grid scale only. Hence, the velocity field  $\overline{u}_i$  is not an averaged quantity, but merely one specific realization of the resolved turbulent flow field.

The LES approach is given by solving Equations (4.1) and (4.2) applying a closure model for the subgrid stress tensor  $\overline{\tau}_{ij}^{SGS}$ . A classic and simple SGS closure model is the widely used algebraic model by Smagorinsky [79]. This model can be described as a combination of the eddy viscosity concept (Boussinesq hypothesis) with a generalized (more-dimensional) Prandtl mixing-length formulation:

$$\overline{\tau}_{ij}^{SGS} = -\nu^{SGS} \left( \frac{\partial \overline{u}_i}{\partial x_j} + \frac{\partial \overline{u}_j}{\partial x_i} \right) = -\nu^{SGS} \overline{s}_{ij} \quad (4.3)$$

$$\nu^{SGS} = (c_s \Delta)^2 \sqrt{\frac{1}{2} \overline{s}_{ij} \overline{s}_{ij}}, \quad (4.4)$$

with  $\overline{s}_{ij}$  the rate-of-strain tensor,  $\Delta$  a measure for the grid size and  $c_s$  the Smagorinsky parameter, which is typically  $\approx 0.1$ . The Smagorinsky SGS model causes a transfer of kinetic energy from the filtered motions to the residual motions; this transfer acts as a dissipation of energy from the resolved motions. From equation (4.4) it follows that the Smagorinsky closure term vanishes in the continuous limit ( $\Delta \rightarrow 0$ ); as dissipation due to this closure term scales quadratically with the grid resolution, its numerical effect can be compared with the effect of a second-order local discretization error. In order to fine-tune the Smagorinsky parameter  $c_s$  a great variety of SGS models have been proposed, e.g. the dynamic subgrid model by Germano [37]. An overview of commonly used SGS models is given by Pope [71]. For reasons of simplicity of implementation, the basic Smagorinsky model (taking  $c_s = 0.1$ ) is adopted in this thesis. From this point on the LES filtering operator  $(\dots)$  (though applied throughout this chapter) will not be denoted.

### 4.2.2 General modeling aspects

The LES model applied in this study is based on a numerical formulation by Boersma [14] suitable for shallow channel flows. This model has been validated by Van Prooijen [99] and Van Balen [96] against available Direct Numerical Simulation data by Moser et al. [61] for a uniform channel flow situation with periodic boundary conditions.

The model uses an equidistant rectangular grid in three dimensions. The velocity field is resolved by a predictor-corrector algorithm, in which the (pressure) correction step is used to satisfy the incompressibility constraint (see Wesseling [114]). The construction of predictor velocities involves the computation of advective terms, eddy viscosity terms and boundary conditions. In order to discretize these terms in space, a simple second-order accurate central differencing scheme has been used on a staggered (C-type) rectangular grid. For integration in time a second-order explicit Adams-Bashfort scheme has been used. The maximum allowable Courant (CFL) number has been set to 0.33 to guarantee stability of the solution.

In order to correct the predicted velocities each time step a 3D Poisson equation for the pressure is solved, leading to a large and sparse system of linear equations. The equidistant

grid allows for the use of an efficient spectral approach to solve the system. In both horizontal directions, the flow field is transformed to spectral space by a cosine transformation (or by a Fast Fourier Transformation in case of periodic boundary conditions). In vertical direction, the remaining tridiagonal system of transformed equations is readily solved using Gaussian elimination, after which the solution is transformed back to physical space. No water level update is required as the present numerical formulation uses the rigid-lid assumption instead of a free surface. This is justifiable as long as “stationary” turbulence situations with moderate Froude numbers are being considered.

### 4.2.3 Boundary conditions

In order to solve Equations (4.1)-(4.4) at the given staggered grid (fixed domain in space), boundary conditions must be specified along the entire boundary of the domain. In the following, we denote  $x_i = (x, y, z)$  and  $u_i = (u, v, w)$ . The direction of the outward normal vector to the boundary is denoted by  $n$  and  $u_n$  is the component of  $u_i$  in this direction.

At open inflow boundaries, the full velocity vector  $(u, v, w)$  is specified at each time level:  $u_i = u_{i,in}$ . If  $x$  is the direction normal to the boundary (example), then values of  $u_{in}(y, z)$  determine the inflow discharge, whereas the tangential velocities  $v_{in}(y, z)$  and  $w_{in}(y, z)$  specify the flow parallel to the boundary. It should be noted that  $u$ ,  $v$  and  $w$  are not located at the same points because the grid is staggered. This staggering has the effect that  $v_{in}$  and  $w_{in}$  actually induce a tangential stress instead of prescribing a tangential velocity. So in fact, we have a Dirichlet-type condition normal to the boundary and a Neumann-type condition parallel to it.

The prescription of  $v$  and  $w$  as well as  $u$  enables the user to prescribe a fully developed turbulent velocity profile at inflow boundaries. Such a developed turbulence profile can be obtained as output from another LES computation and subsequently be applied as boundary condition. A turbulent inflow boundary condition type is coined here *inflow condition A*. An alternative way to mimic turbulent fluctuations at inflow boundaries is to adopt a uniform inflow velocity  $U_{in}$  in  $n$ -direction with random (white) noise  $r_i$  in all directions: e.g.  $u = U_{in} + r_x$ ,  $v = r_y$  and  $w = r_z$ . This boundary type is coined *condition B*. Finally, if  $r_i = 0$ , we have a simple uniform inflow profile without prescribed fluctuations:  $u = U_{in}$  and  $v = w = 0$  (*condition C*). These inflow condition types will be used throughout this chapter (see also Section 4.3).

At outflow boundaries, a so-called kinematic boundary condition specified by Boersma [14] is adopted, which reads (for all velocity components):

$$\frac{\partial u_i}{\partial t} + u_n \frac{\partial u_i}{\partial n} = 0 \quad (4.5)$$

This condition is implemented in such a way that the net inflow/outflow of fluid across the entire domain boundary is always exactly zero, thus satisfying the incompressibility constraint as well as the compatibility condition emerging from the global Poisson problem. At solid walls (bottom as well as sidewalls), the wall-normal velocity is obviously zero ( $u_n = 0$ ); wall friction is accounted for by imposing a tangential shear stress  $\tau_{ij}$ , which is added to the momentum balance of each grid cell adjacent to a solid wall. In order to accurately predict this wall shear stress without the need for excessive local grid refinement, a wall function has been applied to model the viscous sublayer, buffer layer and turbulent inner layer. For the bottom shear stress (example), the associated components of  $\tau_{ij}$  read:

$$\tau_{xz} = \frac{u(x, y, z_1)}{|u|(x, y, z_1)} |\tau| \quad (4.6)$$

$$\tau_{yz} = \frac{v(x, y, z_1)}{|u|(x, y, z_1)} |\tau| \quad (4.7)$$

$$|\tau| = \rho u_*^2 \quad (4.8)$$

where  $|u| = \sqrt{u^2 + v^2}$  is the absolute velocity and  $z_1$  is the wall-normal distance to the first velocity grid point. The absolute value of the wall shear stress  $|\tau|$  is related to the friction velocity  $u_*$ . For hydraulically smooth wall conditions,  $u_*$  is determined implicitly by:

$$u_+ = \begin{cases} 2.44 \log(z_+) + 5.29 & \text{if } z_+ \geq 27.5 & \text{(turbulent inner layer)} \\ 4.91 \log(z_+) - 2.90 & \text{if } 5.0 \leq z_+ \leq 27.5 & \text{(buffer layer)} \\ z_+ & \text{if } z_+ \leq 5.0 & \text{(viscous sublayer)} \end{cases} \quad (4.9)$$

where  $u_+ = |u|/u_*$  is the dimensionless near-wall velocity,  $z_+ = u_* z_1/\nu$  is the number of wall units (dimensionless distance to the wall) and  $\nu$  is the molecular viscosity. The number of wall units  $z_+$  determines the wall flow regime. In order to have a SGS closure model that is compatible with general boundary layer theory, the near-wall eddy viscosity is reduced by applying a so-called Van Driest damping function to the Smagorinsky constant  $c_s$ :

$$c_s = c_{s0} [1 - \exp(-z_+/A_+)] , \quad (4.10)$$

where  $A_+ = 26$  is the Van Driest damping parameter (see Pope [71]). When a sidewall is considered instead of a bottom,  $z_1$  is replaced by  $x_1$  or  $y_1$  and the relevant velocity and shear stress components are replaced accordingly. At the rigid-lid fluid surface, located in the plane  $z = H$ , we obviously have  $\tau_{xz} = \tau_{yz} = 0$  (free-slip condition).

The expressions (4.9) actually assume a fully developed turbulent boundary layer along solid walls. This is usually not correct for separation regions. However, the primary separation event in the SLE geometry is topographically forced at a  $90^\circ$  corner, downstream from a long straight wall; hence, the assumption of sudden separation of a well-developed boundary layer is justifiable near this primary separation point. Some problems are to be expected for the modeling of reattachment points and secondary separation points, leading in general to gyre lengths that are computed slightly too short. However, no impact of this error on the mixing layer development has been observed, as demonstrated in Section 4.4. Because the computational domain is fully rectangular whereas a shallow shear flow geometry like a SLE is obviously not, solid wall boundaries as described above are often located at some place inside the computational grid. In order to handle such internal boundaries correctly, the numerical formulation by [14] has been supplemented with a basic variant of a so-called Immersed Boundary Method (IBM). In the IBM approach, body forces  $f_i$  are imposed on the momentum equations in order to satisfy the impermeability boundary condition  $u_n = 0$  at solid walls inside the domain. An overview of existing IBM techniques can be found in Mittal and Iaccarino [60].

After first having been developed by Peskin [69] to simulate the blood flow through heart valves, IBM techniques have been successfully applied to irregular-shaped boundaries on a regular grid. The advantage of the approach lies in the possibility to fully maintain the structured rectangular (or curvilinear) structure of the grid, which allows for a fast and efficient way to solve the large system of equations (like the Fast Fourier-based approach mentioned in Section 4.2.2). A wide class of interpolation techniques is available to simulate

the presence of complex (or even moving) surfaces. Two popular IBM classes are the ghost-cell finite difference approach (see e.g. Tseng and Ferziger [88], Van Balen [97]) and the cut-cell finite volume approach (Ye et al. [116]). The IBM approach to guarantee wall impermeability can be combined with advanced wall-layer models like those of Tessicini et al. [86] or Piomelli and Balaras [70].

In the present LES computations, internal boundaries are always fully aligned with the rectangular computational grid, such that boundary surfaces always coincide with staggered wall-normal velocity points  $u_n$ . This allows for the application of a rather simple IBM technique, similar to the Direct Forcing approach developed by Fadlun et al. [34] and Breugem [18]. A variant of this Direct Forcing method has been implemented as a part of the total LES solution procedure, which is treated in the next subsection.

#### 4.2.4 Solution algorithm

According to the Direct Forcing approach by [18,34], body forces normal to solid walls are explicitly imposed on the momentum equations, however in the predictor step of the algorithm only (see Figure 4.1). Including these IBM body forces, the total pressure correction numerical scheme reads as follows. The predictor step is given by:

$$\hat{u}_i = u_i^n - \Delta t \left( \frac{3}{2} RHS_i^n - \frac{1}{2} RHS_i^{n-1} \right) + \Delta t f_i^n, \quad (4.11)$$

where  $\hat{u}_i$  is the predictor velocity,  $f_i$  is the body force,  $\Delta t$  is the time step,  $i$  is the dimensional direction and  $n$  is the time level. The term  $RHS_i$  (at two consecutive time levels, due to the second-order Adams-Bashfort scheme) contains all explicit momentum fluxes:

$$RHS_i = \frac{\partial u_i u_j}{\partial x_j} + \frac{\partial p}{\partial x_i} - \frac{\partial}{\partial x_j} (\nu + \nu^{SGS}) \left( \frac{\partial u_i}{\partial x_j} + \frac{\partial u_j}{\partial x_i} \right) \quad (\text{flux terms}) \quad (4.12)$$

The divergence of  $\hat{u}_i$  is applied to build the Poisson problem for the pressure increment  $\hat{p}$ :

$$\frac{\partial^2 \hat{p}}{\partial x_i^2} = \frac{1}{\Delta t} \frac{\partial \hat{u}_i}{\partial x_i} \quad (4.13)$$

After solving the global system of equations the pressure is actually corrected by  $\hat{p}$ , yielding the final velocity field at the new time level:

$$u_i^{n+1} = \hat{u}_i - \Delta t \frac{\partial \hat{p}}{\partial x_i} \quad (4.14)$$

Finally, the pressure is updated to the new time level:

$$p^{n+1} = p^n + \hat{p} \quad (4.15)$$

As stated by Fadlun [34], the body force  $f_i$  at internal boundaries is simply equal to:

$$f_i^n = -\frac{u_i^n}{\Delta t} + \left( \frac{3}{2} RHS_i^n - \frac{1}{2} RHS_i^{n-1} \right) \quad (4.16)$$

This implies that the wall-normal predictor velocity  $\hat{u}_i$  is set to zero at solid walls (see Figure 4.1(a)). Sometimes IBM body forces are also applied to wall-parallel predictor velocities, in order to enforce a no-slip boundary condition. However, no-slip and partial-slip conditions are already accounted for by the wall shear stress  $\tau_{ij}$  (Equation (4.6)-(4.9)), which is a surface force. Therefore a different approach for the wall-parallel velocities is

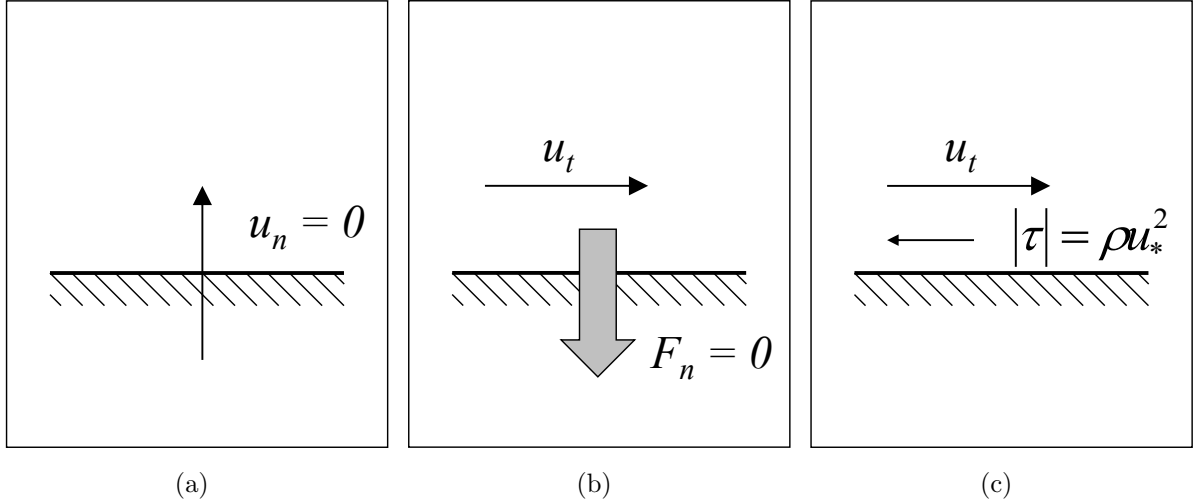


Figure 4.1: *Treatment of solid wall boundaries applying an IBM Direct Forcing method. (a) wall-normal velocities  $u_n$  are set zero (impermeability); (b) wall-normal fluxes  $F_n$  of wall-parallel momentum  $u_t$  are set zero; (c) momentum transfer from fluid to solid wall is accounted for by the wall shear stress  $\tau_{ij}$ .*

followed here, not based on wall-parallel body forces but on momentum fluxes. At internal boundaries, wall-normal fluxes of wall-parallel momentum (due to advection or viscosity) are set to zero (Figure 4.1(b)). This guarantees a proper momentum conservation near solid walls, except for the loss of momentum due to wall friction  $\tau_{ij}$  (Figure 4.1(c)). Otherwise, an erroneous “leakage” of momentum through solid walls would be possible.

It should be noted that the final corrected velocities  $u_i^{n+1}$  through solid walls will be not exactly zero. According to (4.14), small residual wall-normal velocities remain which are equal to:

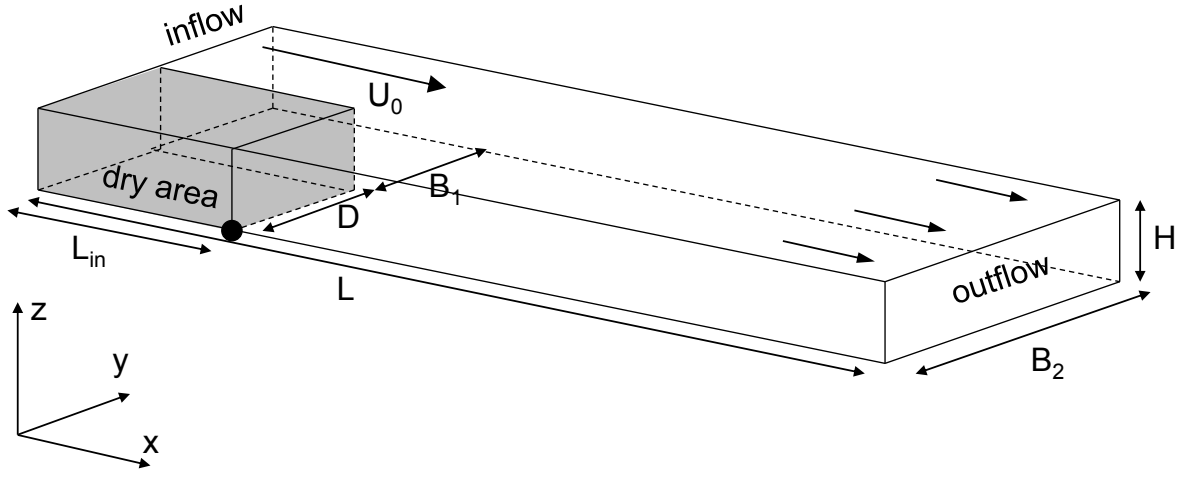
$$u_i^{n+1} = -\Delta t \frac{\partial \hat{p}}{\partial x_i} \quad (4.17)$$

As the pressure is updated every time step by Equation (4.15), both  $\hat{p}$  and residual velocities remain very small (usually many orders of magnitude smaller than velocities inside the flow domain). If the flow tends to become stationary, they will even tend to zero.

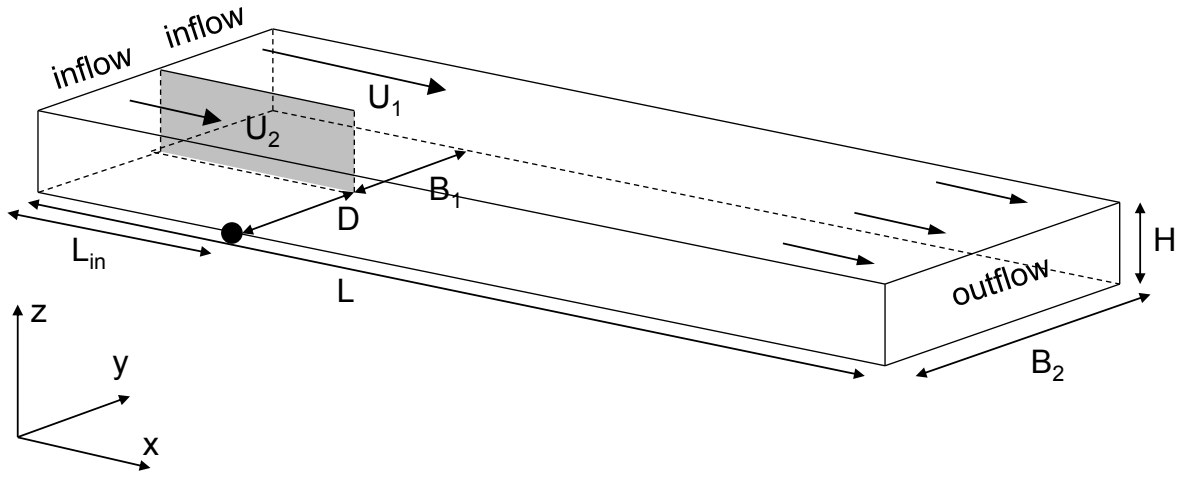
### 4.3 Model input

The LES model presented in Section 4.2 is applied to simulate the SLE Cases 1, 2 and 3 presented in Chapter 3. In order to compare these cases with a shallow shear flow without steady recirculations, a SML flow is simulated as well, which is coined Case 4. In this way, the sensitivity of 2DCS development to topography and upstream 3D turbulence conditions can be investigated for both types of shallow shear flows.

The inclusion of Case 4 is inspired by the PhD research of Van Prooijen [99], who performed surface PTV measurements and 2D computations on this geometry. From linear stability analysis of a base flow, it was concluded that the energy level of perturbations at the inflow boundary to a large extent determines the downstream development of 2DCS. This conclusion was tested using a 2D numerical model (RANS) with addition of a kinematic simulation procedure to mimick the inflow perturbations. It was confirmed that the



(a)



(b)

Figure 4.2: Overview on the LES computational domain for Case 1, 2 and 3 (a) and Case 4 (b). Relevant length scales and velocity scales have been indicated with arrows. The large solid dot indicates the location of the origin of the Cartesian reference frame:  $(x, y, z) = 0$ .

	Case 1	Case 2	Case 3	Case 4
$L$ [m]	30	20	15	20
$B_1$ [m]	0.5	1.0	1.5	1.0
$D$ [m]	1.5	1.0	0.5	1.0
$U_0$ [m/s]	0.30	0.30	0.30	
$U_1$ [m/s]				0.30
$U_2$ [m/s]				0.10
$Q_0$ [m <sup>3</sup> /s]	0.015	0.030	0.045	
$Q_1$ [m <sup>3</sup> /s]				0.030
$Q_2$ [m <sup>3</sup> /s]				0.010
$Re_0$ [-]	30000	30000	30000	
$Re_1$ [-]				30000
$Re_2$ [-]				10000

Table 4.1: Geometrical input parameters for LES cases 1 to 4.



	$L$	$B_2$	$H$	$N_x$	$N_y$	$N_z$	$\Delta x$ [m]	$\Delta y$ [m]	$\Delta z$ [m]	$N_{tot}$
Case 1A	30	2	0.1	2400	160	32	0.0125	0.0125	0.003125	12,288,000
Case 1B	30	2	0.1	2400	160	32	0.0125	0.0125	0.003125	12,288,000
Case 1C	30	2	0.1	2400	160	32	0.0125	0.0125	0.003125	12,288,000
Case 2A	20	2	0.1	1600	160	32	0.0125	0.0125	0.003125	8,192,000
Case 2B	20	2	0.1	1600	160	32	0.0125	0.0125	0.003125	8,192,000
Case 2C	20	2	0.1	1600	160	32	0.0125	0.0125	0.003125	8,192,000
Case 3A	15	2	0.1	1200	160	32	0.0125	0.0125	0.003125	6,144,000
Case 3B	15	2	0.1	1200	160	32	0.0125	0.0125	0.003125	6,144,000
Case 3C	15	2	0.1	1200	160	32	0.0125	0.0125	0.003125	6,144,000
Case 4A	20	2	0.1	1600	160	32	0.0125	0.0125	0.003125	8,192,000
Case 4B	20	2	0.1	1600	160	32	0.0125	0.0125	0.003125	8,192,000
Case 4C	20	2	0.1	1600	160	32	0.0125	0.0125	0.003125	8,192,000

Table 4.2: *Computational mesh sizes for LES cases 1A to 4C.*

presence of upstream perturbations is essential to trigger the growth of mixing layer 2DCS; in “real life” these perturbations are provided by 3D bottom turbulence, whereas in the 2D model by [99] they are accounted for by perturbations imposed on the inflow boundary. It is worthwhile to reaffirm this conclusion about SML geometries by means of a full 3D LES computation.

For SLE geometries, it is conjectured that perturbations are continuously provided by the separation event and by the presence of the primary and secondary gyre. It is therefore expected that Cases 1, 2 and 3 are less sensitive to upstream perturbations than Case 4. In this chapter we will test Case 1-3 against Case 4 for three types of inflow boundary conditions, which have been coined Condition A, B and C in Section 4.2.3. This implies  $3 \times 4 = 12$  LES computations altogether, from Case 1A to Case 4C (see Table 4.2).

Figure 4.2 outlines the computational domain for LES Cases 1, 2 and 3 (a) and Case 4 (b). The rectangular domain has length  $L$ , width  $B_2$  and height  $H$ . All cases have an inflow section length  $L_{in} = 5$  m, a width  $B_2 = 2$  m and a constant water depth  $H = 0.10$  m, while the total length varies between  $L = 15$  m and  $L = 30$  m. Compared to the PIV experimental setup, some LES cases have a larger domain length in order to exclude any significant influence of the outflow boundary on the mixing layer. Case 1, 2 and 3 have inflow sections with variable width  $B_1$  and expansion width  $D$ , bulk inflow velocity  $U_0$  and inflow discharge  $Q_0$ . Case 4 has two inflow sections, having equal width  $B_1 = D = 1$  m but two different bulk inflow velocities  $U_1$  and  $U_2$  and inflow discharges  $Q_1$  and  $Q_2$ . For Case 1-4 respectively, these input parameters (as well as the associated inflow Reynolds numbers  $Re_0$ ,  $Re_1$  and  $Re_2$ ) are summarized in Table 4.1.

Table 4.2 gives an overview of all 12 simulated flow cases and their mesh resolution. The LES formulation by Boersma [14] was applied before by Van Prooijen [99] and Van Balen [96], adopting vertical mesh resolutions of  $\Delta z = H/20$  and  $\Delta z = H/16$  respectively, in order to reproduce DNS data by Moser et al. [61] of a uniform shallow channel flow. In both cases the agreement with DNS data was satisfactory. In the present LES computations, the vertical grid resolution is set to  $\Delta z = H/32 = 0.003125$  m. In this way the bottom boundary layer is sufficiently resolved: for all LES cases, the local number of wall units varies between  $z_+ \approx 25$  (in uniform inflow sections) and  $z_+ < 10$  (in primary gyre regions) or even  $z_+ < 5$  (in secondary gyre regions). The present resolution also allows for resolving large-scale 3D bottom turbulence and secondary flow structures with sufficient accuracy.

In horizontal direction, a mesh spacing  $\Delta x = \Delta y = H/8 = 0.0125$  m has been used in order to resolve horizontal turbulent motions with length scales larger than order  $\approx H$ . Adopting this resolution, the width of the steady gyre area in Case 1, 2 and 3 is represented by 120, 80 and 40 grid cells respectively. Dependent on the value of  $L$ , the total mesh size  $N_{tot} = N_x \times N_y \times N_z$  varies between 6144000 and 12288000 grid cells.

With respect to time resolution, the maximum allowable CFL number was conservatively set to 0.33 (see Section 4.2.2). As the largest possible absolute velocities occurring in all cases are of the order of  $\approx 0.4$  m/s, the time step has been set to a constant value of  $\Delta t = 0.005$  s to guarantee stability. Each flow case was simulated for a period of 2000 s (400000 time steps). An initial adaptation time of 1000 s turned out to be sufficient in all cases, after which flow output was generated during another period of 1000 s. (In comparison: PIV output was generated during 700 s after an initial adaptation time of 900 s.)

Three types of output data have been generated for each case:

- Time-averaged flow statistics for the entire 3D domain (e.g. mean velocities and velocity gradients, turbulent kinetic energy, Reynolds stress components);
- Instantaneous velocity fields  $(u, v)$  and vector potential function  $\psi$  at the water surface, sampled each 0.1 s (hence 10000 2D frames per sample);
- Instantaneous velocity field  $(u, v, w)$  for the entire 3D domain at time level  $t = 2000$  s.

For all simulation cases listed in Table 4.2, corresponding simulations at a lower resolution have been performed as well. All grid cell sizes and time steps have been doubled:  $\Delta x = \Delta y = H/4 = 0.025$  m,  $\Delta z = H/16 = 0.00625$  m and  $\Delta t = 0.01$  s. In order not to give the reader an overload of information, low-resolution results will be shown only when they are relevant and distinctively different from the corresponding high-resolution results.

The LES computations took 14 days of running time on average for most cases, running on a parallel computer cluster (using 8 to 12 processors for each computation). For practical reasons, it was decided that the running time of each simulation should not exceed a limit of about two weeks. This restriction, as well as data storage capacity, have effectively limited the maximum numerical resolution that could be accomplished. For all LES computations presented in Chapters 4 and 5 of this thesis (see Tables 4.2 and 5.2), the total computational effort has been about 350 run-time days, providing roughly 400 Gigabyte of output data. For each of the 4 geometries three types of inflow conditions (Condition A, B and C) have been specified:

- A fully developed 3D turbulent velocity profile  $(u, v, w) = (u_{in}, v_{in}, w_{in})$ , with mean streamwise component  $\bar{u}_{in} = U_{in}$  (i.e.  $U_0$  for Case 1A-3A, or  $U_1$  and  $U_2$  for Case 4A);
- A uniform inflow velocity  $(u, v, w) = (U_{in}, 0, 0)$  plus random white noise fluctuations  $(r_x, r_y, r_z)$ , where the noise amplitude  $\hat{r}$  is 5% of  $U_{in}$  (Case 1B-4B);
- A uniform inflow velocity  $(u, v, w) = (U_{in}, 0, 0)$ , without explicitly imposed perturbations (Case 1C-4C).

In order to construct inflow velocity profiles with a turbulence energy density spectrum, Van Prooijen [102] applied a kinematic simulation procedure (imposing Fourier modes with prescribed amplitudes and random phases). Here a different approach has been followed: each turbulent velocity profile (for inflow condition A) has been retrieved from a 3D LES computation of a straight channel flow with periodic boundary conditions in  $x$ -direction. Each channel has a length  $L = 10$  m while its width, depth and grid resolution are identical to that of the associated SLE simulation. The channel flow is being driven by a constant

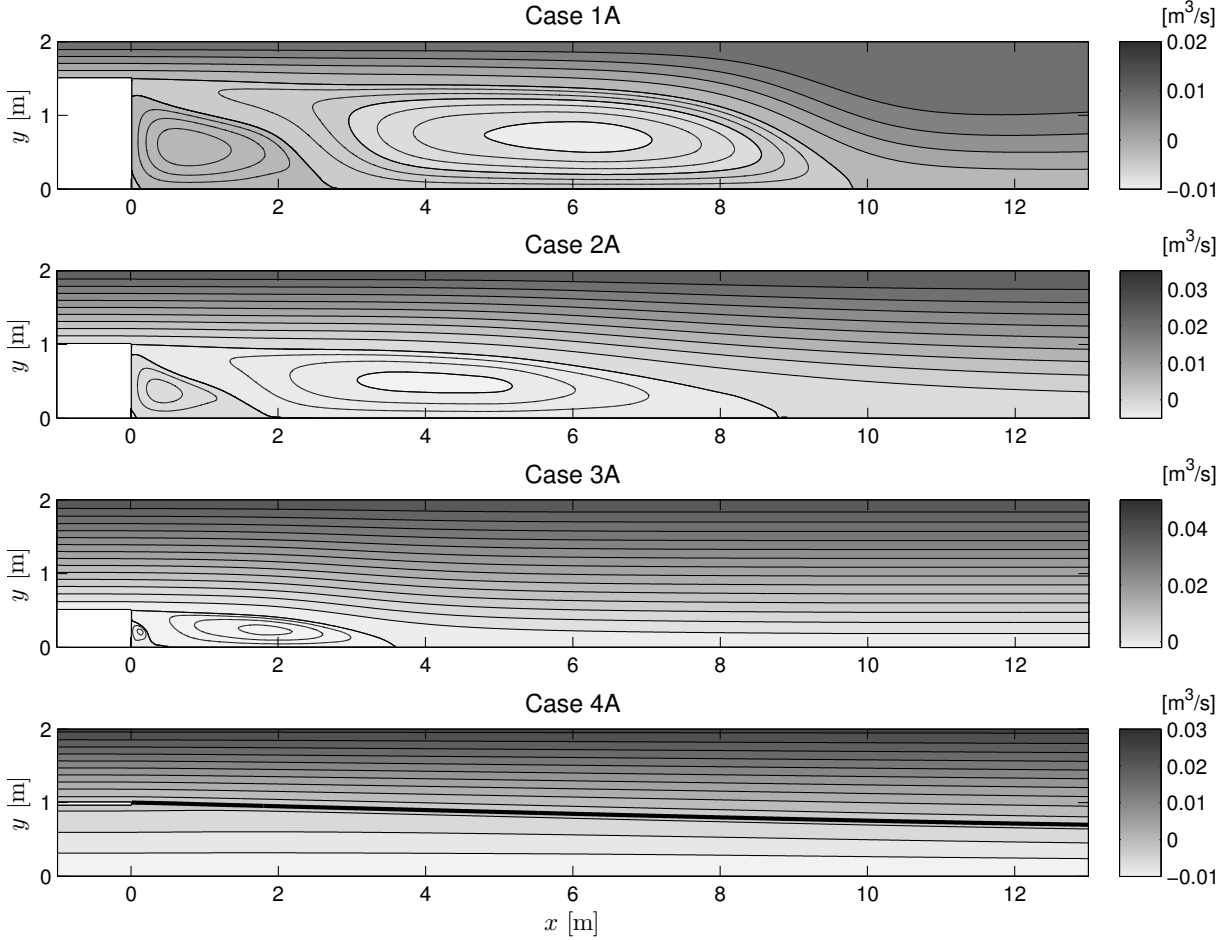


Figure 4.3: *Time-averaged and depth-integrated stream functions of LES Cases 1 to 4 (inflow condition type A). The bold line in Case 4 represents the mixing layer center line.*

pressure gradient that balances wall friction; the pressure gradient has been calibrated in such a way that the resulting streamwise mean velocity equals the bulk velocity  $U_0$  (or  $U_1$  or  $U_2$  respectively). A random white noise field (with amplitude  $\hat{r} = 0.05U_0$  in all directions) is used as initial condition throughout the domain in order to trigger the growth of 3D turbulence. An adaptation time of 1000 s was sufficient to reach a stationary turbulence situation, after which the flow in a cross-section has been sampled during 1000 s. The resulting time series have been used as inflow boundary conditions for Cases 1A-4A.

## 4.4 Comparison with PIV data

Among the three types of output data listed in Section 4.3, the sampled instantaneous surface velocity fields  $(u, v)$  are particularly useful. These samples have been taken every 0.1 s (sampling frequency 10 Hz), covering the entire flume width ( $0 < y < B_2$ ) within the region  $0 < x < 10$  m downstream from the separation point. From these instantaneous fields Reynolds-decomposed quantities as well as energy density spectra and conditionally averaged quantities at the water surface can be derived, which allow for a detailed comparison with corresponding PIV velocity data. Meanwhile, the acquired 3D output data allow for an analysis of the vertical flow structure (see Sections 4.6 and 4.7). The results presented in this section involve flow statistics at the free surface that are compared to

the results from Chapter 3. A selection of relevant results is shown: mean flow patterns, mixing layer characteristics, turbulent kinetic energy levels and energy density spectra.

#### 4.4.1 Flow patterns and length scales

Large-scale steady LES flow patterns, compared to PIV data, differ on details only. Figure 4.3 shows contour plots of the time-averaged and depth-integrated stream function of cases 1A to 4A. All simulations for Cases 1-3 reproduce the primary and secondary gyre; their length scales  $L_1$  and  $L_2$  are easily discerned. It should be noted that the streamline density inside the primary and secondary gyre is not a measure for the local velocity here; some extra streamlines have been drawn for a better representation of the flow pattern.

The bold line in the lower panel (Case 4A) represents the streamline that divides the high and low velocity sides of the SML. This line can be interpreted as the mixing layer center line (see e.g. Booij and Tukker [16] and Uijttewaald and Booij [91]). From theory and experiments by Van Prooijen [99] it follows that, going in downstream direction, the center line shifts toward the low velocity side due to continuity requirements. This behavior is recognized in Figure 4.3. The lateral shifting rate of the mixing layer center  $dy_c/dx$  for Case 4A initially equals -0.031 in the near field and gradually decreases toward the outflow boundary. The near-field value  $dy_c/dx = -0.031$  compares well with the experimental result  $dy_c/dx = -0.035$  by [99].

The computed time-averaged streamline patterns slightly vary for varying inflow conditions (Condition A/B/C, see Sections 4.2.3 and 4.3) and for high versus low resolution. Differences are found for  $L_1$  and  $L_2$  in Cases 1-3 and for  $dy_c/dx$  in Case 4. Table 4.3 gives an overview of these quantities, compared to experimental results.

It is observed that Condition B and C for high-resolution cases (as well as Condition A for low-resolution cases) yield the best results with respect to the primary gyre length  $L_1$ . Especially Condition B(high) compares well with the PIV results for Case 1-3 (see also Figure 3.6). For Case 1 and 2, Condition A(high) slightly underpredicts the value of  $L_1$  whereas Conditions B(low) and C(low) result in an overprediction. A possible error source may be the computation of the exact location of the reattachment point, which is not fully captured by the wall function that is applied. The “deep” Case 3 shows the smallest variation with respect to  $L_1$  (all values are close to 7.0). For the relatively “shallow” Cases 1 and 2, the general picture is that high resolution cases yield a smaller value of  $L_1$  than low resolution cases, whereas Condition A results in smaller values of  $L_1$  than Conditions

Resolution		High	High	High	Low	Low	Low	PIV data
Inflow condition		A	B	C	A	B	C	
$L_1/D$	Case 1	6.54	7.93	6.96	7.32	9.19	8.52	7.8
	Case 2	8.90	9.54	9.77	9.35	11.10	11.37	9.5
	Case 3	7.18	7.26	7.54	7.51	6.82	7.39	7.0
$L_2/D$	Case 1	1.88	2.14	2.21	2.20	2.91	3.11	3.0
	Case 2	2.04	1.84	1.74	1.78	2.64	2.91	2.7
	Case 3	1.02	0.70	0.78	1.14	1.08	1.10	1.2
$dy_c/dx$	Case 4	-0.031	-0.029	-0.029	-0.032	-0.020	-0.015	-0.035 (v.Prooijen)

Table 4.3: *Steady gyre lengths (Case 1-3) and lateral shift of the mixing layer (Case 4): differences between inflow conditions A/B/C, for high and low LES resolution.*

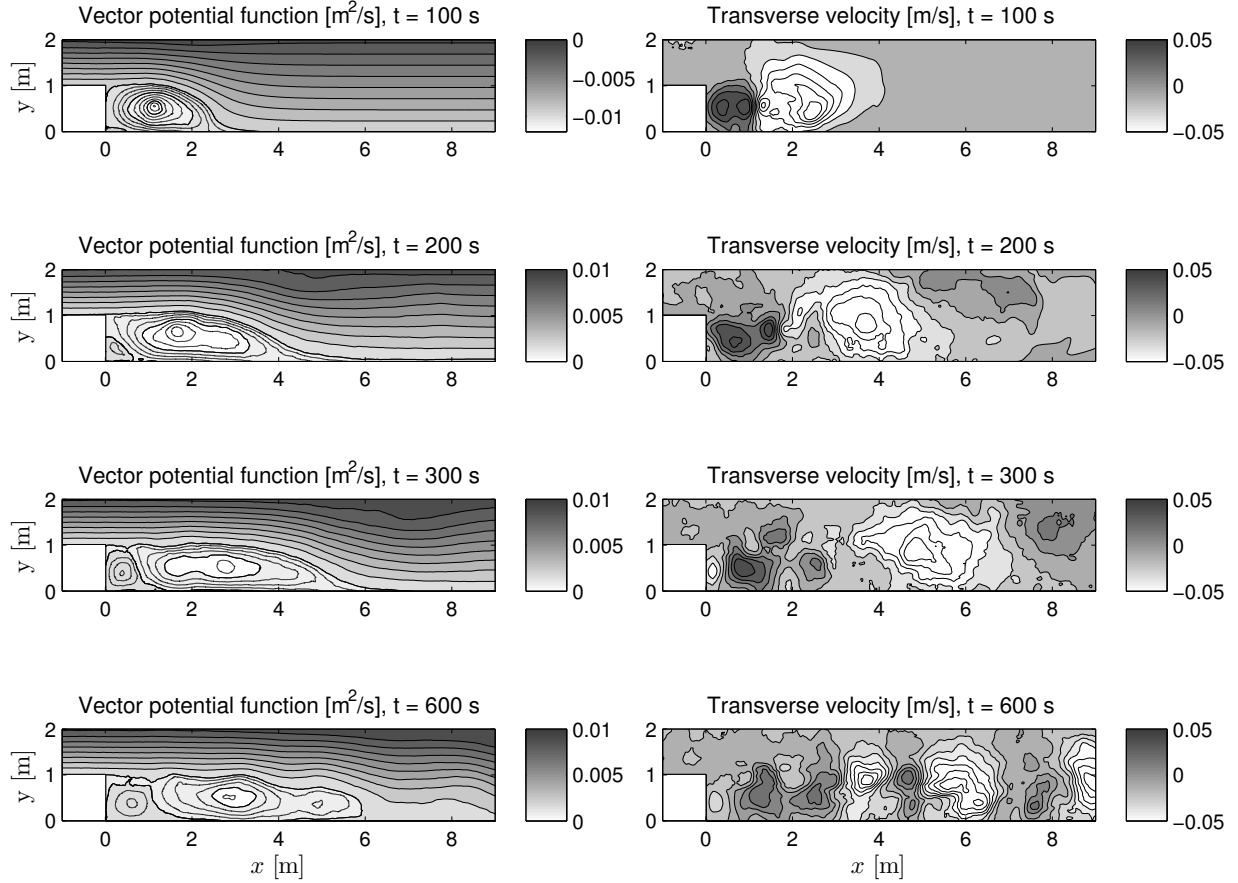


Figure 4.4: *Transition to vortex shedding pattern in Case 2A (starting from an initial rest state at  $t = 0$ ). Left panels: contours of instantaneous vector potential functions [ $\text{m}^2/\text{s}$ ], right panels: contours of instantaneous transverse velocities [ $\text{m}/\text{s}$ ].*

B and C. Apparently a fully developed turbulent inflow condition gives rise to a slightly larger lateral momentum transfer in the mixing layer and hence a shorter primary gyre length.

In most cases the secondary gyre length  $L_2$  is being underestimated by the LES results, even for high-resolution computations. The largest values of  $L_2$  are found for Cases 1B-1C(low) and 2B-2C(low). Presumably, the good agreement with PIV data for these cases is probably due to the overprediction of  $L_1$  in these cases; on the other hand, a good agreement for  $L_1$  is often linked to a  $L_2$  underprediction.

From numerous test computations it is concluded that the inclusion of the viscous sublayer and buffer layer into the wall function (4.9) is essential to capture a secondary separation event and hence a secondary gyre. A merely logarithmic law-of-the-wall formulation does not reproduce secondary gyres. This observation is in accordance with the work of Nassiri et al. [63,64] and Babarutsi et al. [5,6,8]. However, it is also concluded that the fairly simple wall model used in this study cannot correctly resolve the exact location of the secondary separation point, as this location is quite sensitive to the local equilibrium between pressure gradient and wall shear stress whereas the local boundary layer is not fully developed. These boundary layer properties can only be captured using more advanced boundary layer modeling (see e.g. Tessicini et al. [86] or Piomelli and Balaras [70]) or working with even finer LES grids. Both remedies are outside the scope of this study.

The last row of Table 4.3 shows that the lateral shift of the mixing layer center  $dy_c/dx$

in Case 4 has a virtually constant value for high-resolution simulations, irrespective of the inflow condition. For low resolution cases, a strong reduction of  $dy_c/dx$  is observed for Condition B and C. As will be pointed out in Section 4.5, the lack of appropriate upstream turbulence conditions in combination with a low resolution causes the mixing layer development to break down and hinders the growth of 2DCS. This breakdown causes a severe reduction of the lateral momentum transfer in these cases.

Although shallow mixing layers are not visible as such within the stream functions, the shedding of 2DCS contributes to the final shape of the mean flow pattern. Figure 4.4 illustrates the process of transition to vortex shedding in Case 2A (high resolution), starting from a state of initial rest at  $t = 0$ . Four time levels are shown.

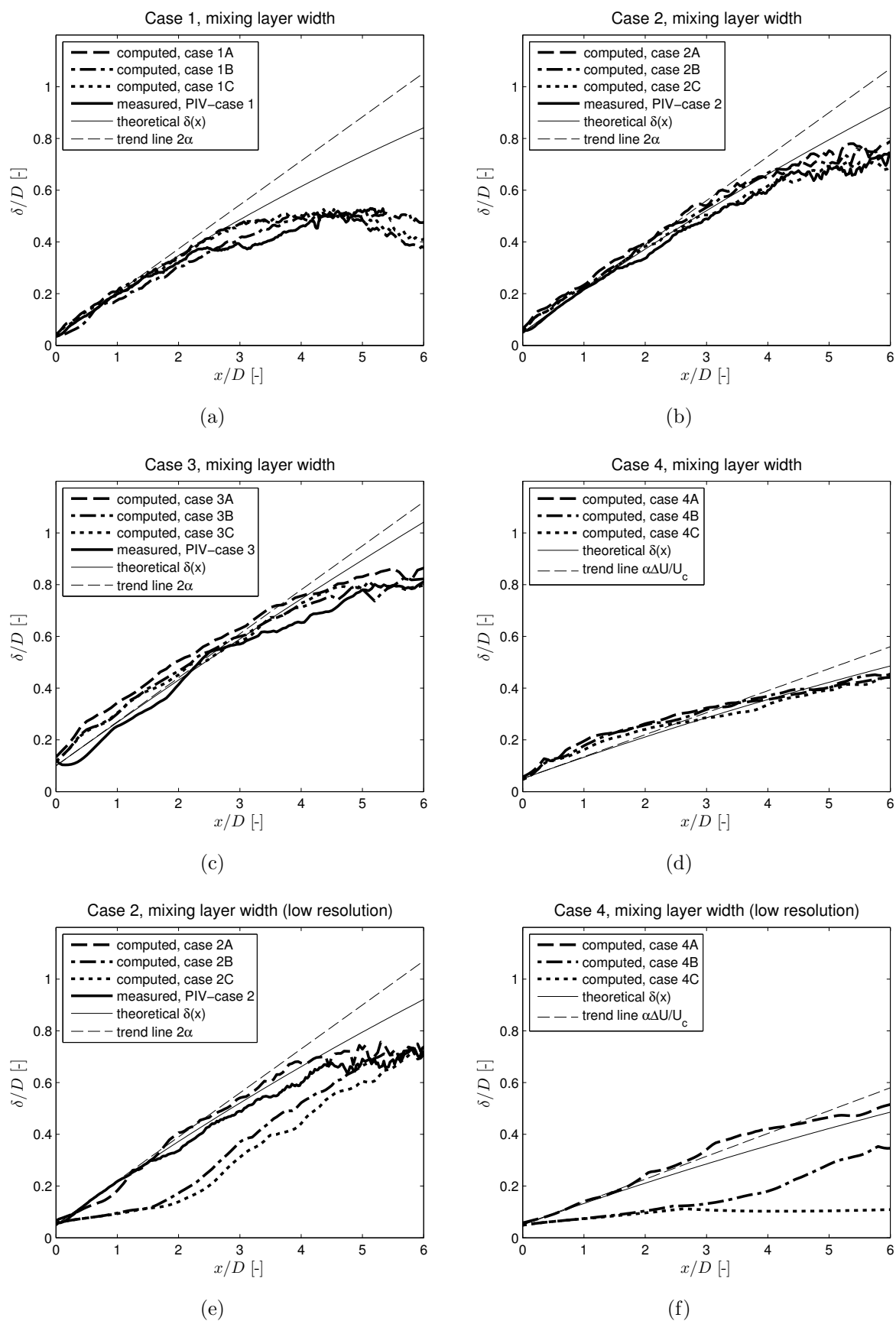
At  $t = 100$  s, an initially small primary gyre is developing quickly, leading to high transverse velocities. Yet the flow pattern is quite stable, as the primary gyre remains in place and does not travel in downstream direction, whereas the lateral shear downstream of the separation point is very small. At  $t = 200$  s, the primary gyre has grown in length and the first secondary separation event is visible in the lower left corner. At  $t = 300$  s the secondary gyre in the lower left corner has grown significantly, giving rise to an increased amount of lateral shear near the separation point. Downstream from this point a sequence of shed eddies (mixing layer) can be discerned in the transverse velocity field. Finally, at  $t = 600$  s, the primary and secondary gyre have nearly reached their final lengths  $L_1$  and  $L_2$  whereas the mixing layer 2DCS have grown considerably (both in size and energy).

Figure 4.4 confirms that vortex shedding events in a SLE geometry are being induced by the secondary gyre, or actually by the strong lateral shear induced by this gyre. Furthermore, it can be seen that the primary gyre does not actually consist of one single vortical structure. In the lower left panel multiple vorticity kernels can be discerned, including the near-field structures directly downstream from the separation point. It follows that 2DCS are traveling through the primary gyre and contribute to the gyre scale and energy by means of vortex merging processes.

In terms of large-scale turbulence length scales, the obtained LES results compare quite well with PIV experimental data. Figures 4.5 and 4.6 show a selection of relevant length scales for Cases 1-4, i.e. the mixing layer width  $\delta$  and conditionally averaged large eddy length scale  $\lambda_{eddy}$ . LES results are compared both with PIV results (for Cases 1-3) and the theoretical mixing layer model of Section 3.5. For Case 2 and Case 4, the low-resolution results are shown as well.

Figures 4.5(a)-(d) show that all high-resolution simulations of Cases 1-4 reproduce the correct growth rate for  $\delta$ , irrespective of the inflow turbulence condition. The agreement with PIV data for  $\delta$  is very satisfactory. From both PIV and LES data it follows that the mixing layer width complies to self-similarity theory in the near field ( $x/D < 4$ ), whereas the far-field values of  $\delta$  are restricted by the flume width  $B_2$ . It is confirmed that the near-field mixing layer growth is governed by the entrainment coefficient  $\alpha = 0.085$ . These conclusions are supported by the results for  $\lambda_{eddy}$ , which are depicted in Figures 4.6(a)-(d). It is found again that  $\lambda_{eddy}$  and  $\delta$  (scaled by  $D$ ) have equal order of magnitude. Conditionally averaged integral length scales  $\lambda_{int}$  (not shown here) are approximately equal to  $\approx 2\lambda_{eddy}$ , in accordance with PIV results (Section 3.7). We conclude that the inaccurate reproduction of gyre length scale  $L_2$  has no impact on the accurate reproduction of mixing layer properties and turbulence length scales.

A comparison with low-resolution results reveals the paramount importance of upstream turbulence conditions if 2DCS scales are insufficiently resolved. For Condition A a satisfactory behavior of  $\delta$  and  $\lambda_{eddy}$  is found, in good agreement with PIV results; see Figures 4.5(e)-(f) and 4.6(e)-(f). For Conditions B and C, however, deviations are observed. For

Figure 4.5: *Mixing layer width  $\delta$  (PIV-LES data compared).*

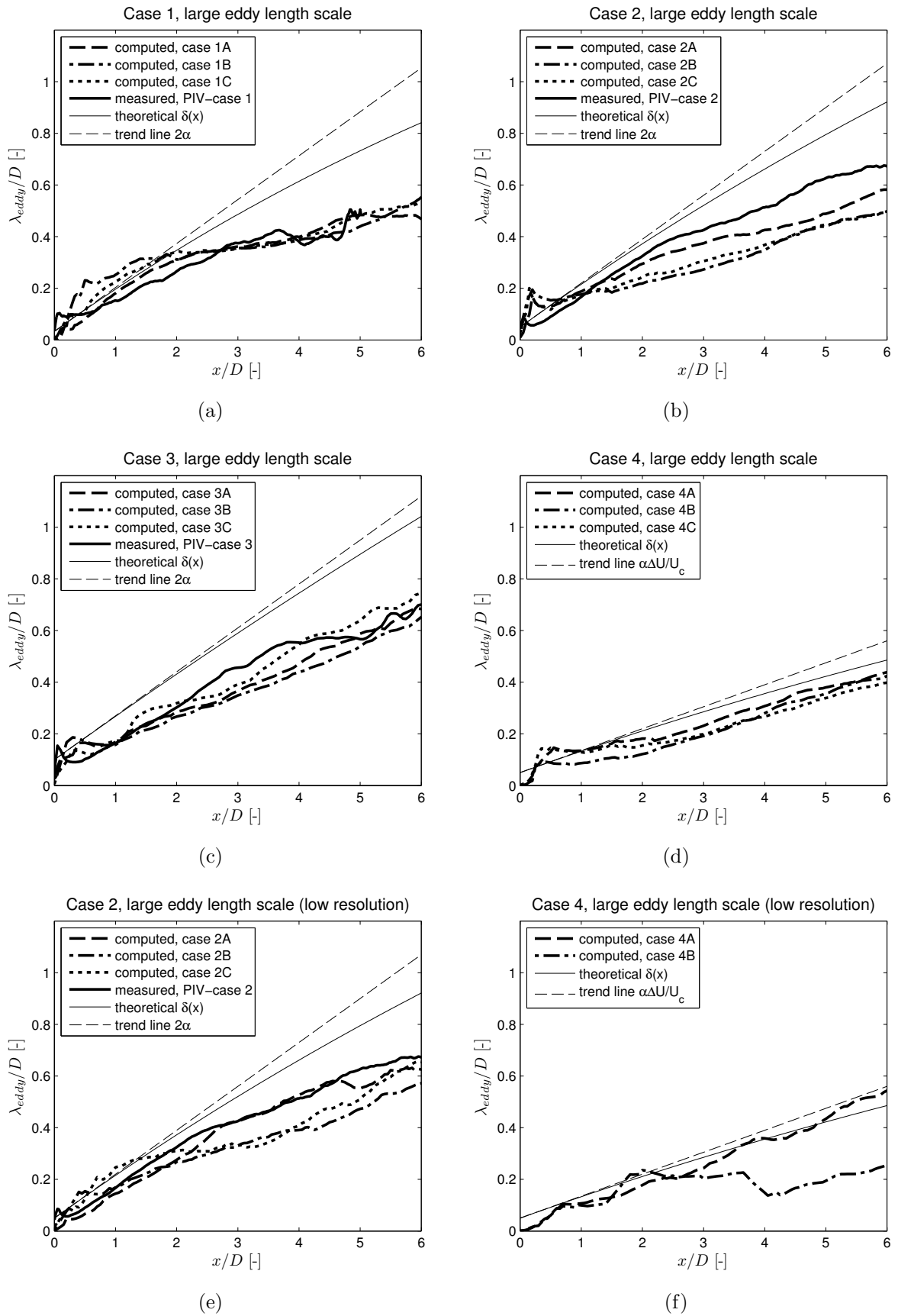


Figure 4.6: Conditionally averaged large eddy length scale  $\lambda_{eddy}$  (PIV-LES data compared).



Cases 2B and 2C, the near-field mixing layer width remains very small and develops only for  $x/D > 2$ . The relative importance of sub-grid eddy viscosity is relatively large for these coarse grids: emerging instabilities are often damped, whereas no developed upstream turbulence is available that could trigger near-field instabilities. However, the steady gyre pattern of the SLE geometry eventually forces the emergence of 2DCS, although the mixing layer is slightly shifting downstream. The presence of 2DCS is thus guaranteed for Case 2 (as well as Cases 1 and 3), irrespective of the inflow condition. This is not the case for Cases 4B and 4C: in the SML geometry, the combination of insufficient resolution and absence of upstream turbulence gives rise to a breakdown of the mixing layer development. This effect is strongest for Case 4C, which exhibits a completely stable velocity field; no 2DCS are developing. For this case no value of  $\lambda_{eddy}$  can be computed; hence Case 4C is absent in Figure 4.6(f) whereas the line computed for Case 4B is somewhat questionable. The Case 4C value of  $\delta$  in Figure 4.5(f) is close to zero. The absence of 2DCS can be linked to the reduction of the lateral shifting rate  $dy_c/dx$  of the mixing layer center, as shown in Table 4.3.

It is observed that all high-resolution LES computations include fully developed turbulent inflow sections, irrespective whether Condition A, B or C is imposed on the inflow boundary. Due to the relatively small influence of the Smagorinsky SGS model for fine grids, all simulations equally experience a transition to fully developed 3D bottom turbulence, which guarantees the growth of 2DCS (see the linear stability analysis by Van Prooijen [99]). For low-resolution computations, only cases with Condition A give rise to well-developed 3D bottom turbulence whereas Condition B and C cases do not. In the latter cases, 2DCS will only emerge if they are forced topographically (see Jirka [47] and Section 2.2.3). From the present results, we conclude that this topographical forcing is obviously present in the SLE Cases 1-3 whereas it is absent in the SML Case 4.

#### 4.4.2 Energy content

As shown in the previous section, mean flow patterns and turbulence length scales are well suited for comparison between PIV and LES results. For turbulent kinetic energy (TKE) and Reynolds stresses, such a comparison is more difficult as the LES procedure resolves much more small-scale TKE than the PIV procedure can capture. Hence, all LES kinetic energy levels are found to be higher than the associated PIV energy content, especially in the near field. Nevertheless it remains possible to compare the large-scale energy contents; to this end, the computed LES energies should be averaged or low-pass filtered in some way to remove the small-scale turbulent fluctuations.

The largest scales of turbulent motion that can be resolved by PIV measurements are limited by the size of the PIV interrogation window, which is of the order of the water depth  $H$  in the present case (see Section 3.3.2). Smaller-scale motion is not properly captured by the PIV algorithm; moreover, only the surface velocity is measured so that 3D turbulent motion at sub-depth scale is not included in the results as well. For comparison purposes, LES fluctuations with a length scale smaller than two times the water depth (see [99]) should be removed from the velocity field. To this end, instantaneous velocity maps are filtered using a low-pass box filter with a length scale  $\lambda_{filter}$ :

$$\lambda_{filter} = 2H \quad (4.18)$$

An alternative option is to decompose LES turbulent velocity fields into a depth-averaged (2D) and a residual (3D) contribution. This is done as follows. Adopting the notation by

Hinterberger et al. [45], the depth-averaging of a quantity  $\phi$  is denoted by a tilde:

$$\phi = \tilde{\phi} + \phi'', \quad \tilde{\phi} = \frac{1}{H} \int_0^H \phi(x, y, z, t) dz \quad (4.19)$$

The time-averaging operator (Reynolds decomposition over a time interval  $T$ ) reads:

$$\phi = \bar{\phi} + \phi', \quad \bar{\phi} = \frac{1}{T} \int_0^T \phi(x, y, z, t) dt \quad (4.20)$$

If we assume a constant depth  $H$ , the time-averaging operator commutes with the depth-averaging operator:  $\widetilde{\bar{\phi}} = \bar{\tilde{\phi}}$ , hence the mean depth-averaged flow equals the depth-averaged mean flow. Given an instantaneous velocity field  $\mathbf{u} = (u, v, w)$ , we define:

$$\mathbf{u}^{2D} = (\tilde{u}, \tilde{v}, 0) \quad \text{and} \quad \mathbf{u}^{3D} = (u - \tilde{u}, v - \tilde{v}, w) = (u'', v'', w) \quad (4.21)$$

Now it is possible to decompose the turbulent kinetic energy  $k$  in a 2D and 3D part:  $\tilde{k} = k^{2D} + \widetilde{k^{3D}}$ , with

$$\tilde{k} = \frac{1}{2} \left( \widetilde{u'u'} + \widetilde{v'v'} + \widetilde{w'w'} \right) \quad (4.22)$$

$$k^{2D} = \widetilde{k^{2D}} = \frac{1}{2} \left( \widetilde{u'u'} + \widetilde{v'v'} \right) \quad (4.23)$$

$$\widetilde{k^{3D}} = \frac{1}{2} \left( \widetilde{(u'')'(u'')} + \widetilde{(v'')'(v'')} + \widetilde{w'w'} \right) \quad (4.24)$$

A similar decomposition can be made for the depth-averaged horizontal Reynolds stress:

$$\widetilde{u'v'} = \widetilde{u''v''} + \widetilde{(u'')'(v'')} \quad (4.25)$$

The above decompositions are used by Hinterberger et al. to inspire a model for Depth-Averaged Large Eddy Simulation (DA-LES); see [42, 45] and Chapter 6 for more details. In this section, the 2D components of TKE and horizontal Reynolds stress are used to compare 3D LES results against PIV data.

Figure 4.7 illustrates the actual differences between various definitions of streamwise TKE (upper panels), transverse TKE (middle panels) and horizontal Reynolds stress (lower panels) for Case 2A-C, along the center line of the mixing layer. Four types of quantities are compared with PIV results:

1. Time-averaged values at the water surface, i.e.  $\overline{u'^2}$ ,  $\overline{v'^2}$  and  $\overline{u'v'}$ ;
2. Depth-averaged and time-averaged values, i.e.  $\overline{u'^2}$ ,  $\overline{v'^2}$  and  $\overline{u'v'}$ ;
3. Decomposed 2D part of the motion, i.e.  $\widetilde{u'u'}$ ,  $\widetilde{v'v'}$  and  $\widetilde{u'v'}$ ;
4. Time-averaged low-pass filtered values at the water surface, adopting  $\lambda_{filter} = 2H$ .

It is observed that differences between TKE at the surface and the depth-averaged TKE (in the six upper panels) are negligible, whereas differences for the Reynolds stress are slightly more pronounced. This is explained by the fact that the streamwise and transverse turbulence intensities are relatively uniform over the water depth whereas Reynolds stress profiles often have a maximum near the surface. In all cases, the values of  $\widetilde{u'u'}$ ,  $\widetilde{v'v'}$  and  $\widetilde{u'v'}$  are considerably smaller than the corresponding quantities  $\overline{u'^2}$ ,  $\overline{v'^2}$  and  $\overline{u'v'}$ . In the far field, this 2D decomposition according to Hinterberger compares well with PIV results; in the near

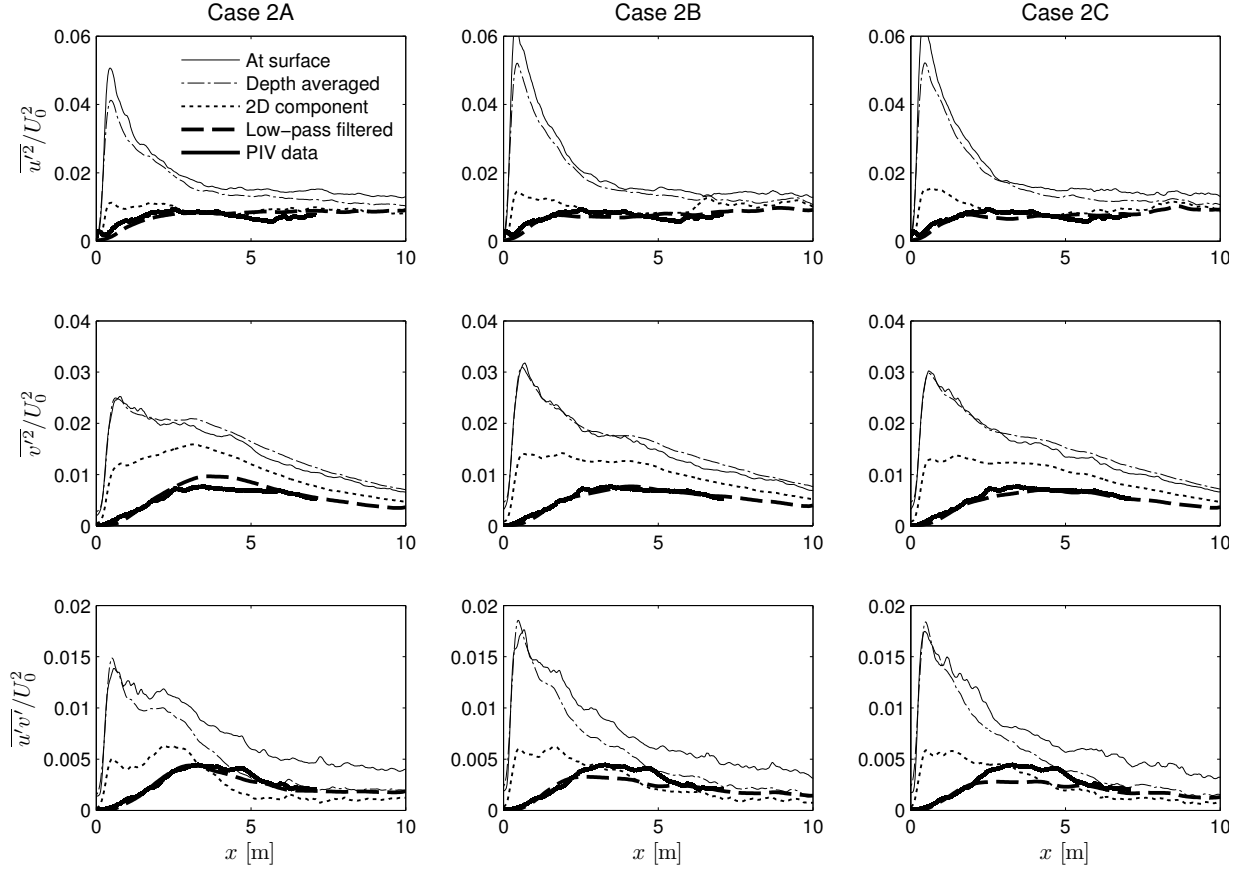


Figure 4.7: *Various ways to compare PIV and LES TKE and Reynolds stress longitudinal profiles: depth-averaging, 2D decomposition and low-pass filtering (Cases 2A/2B/2C).*

field, however, considerable differences remain because the 2D-decomposed flow field still contains small (sub-depth scale) fluctuations that are not captured by the PIV procedure. Looking at low-pass filtered LES data, we observe a good agreement with PIV data both in the near-field and far-field region (at least for the present Case 2). No significant differences in LES data for varying inflow conditions are observed; for Condition A, the near-field TKE and Reynolds maximum has a slightly lower peak value than for Condition B and C. The far-field values of 2D-decomposed and low-pass filtered quantities are almost equal in all 9 panels of Figure 4.7, which suggests that the large-scale turbulent motion in the far field has a 2D character indeed.

Figures 4.8 to 4.11 show transverse profiles of the streamwise mean velocity  $\bar{u}$ , streamwise TKE  $\overline{u'^2}$ , transverse TKE  $\overline{v'^2}$  and horizontal Reynolds stresses  $\overline{u'v'}$ , in analogy with Figures 3.11 to 3.14 in Section 3.5. In these figures, PIV surface measurements are compared with LES data at the surface which are low-pass filtered with  $\lambda_{filter} = 2H$ . The spatial filter has virtually no influence on the mean flow velocity  $\bar{u}$ , whereas it significantly reduces the TKE and Reynolds stress levels (which can be seen from Figure 4.7). Because no significant differences are found between results for varying inflow conditions, only the results for Condition A (at high resolution) are depicted here for the sake of clarity.

The most obvious difference between measurements and simulation data in Figure 4.8 is located around the line  $x/D \approx 3$  in Case 1 and Case 2 (upper panels). These differences are explained by the erroneous secondary gyre length  $L_2$  in these cases, see Table 4.3. Apart from these errors, the mean surface flow fields agree reasonably well. Furthermore

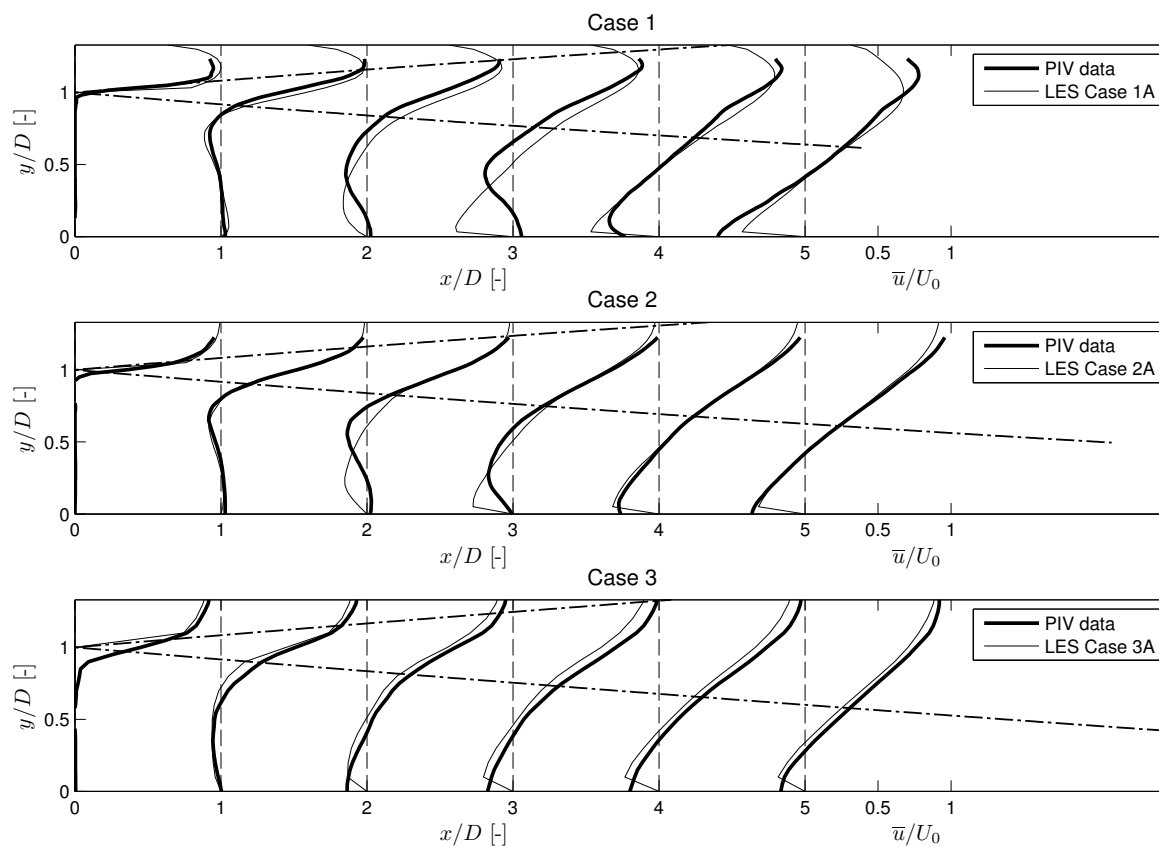


Figure 4.8: Comparison of PIV data and low-pass filtered LES results for  $\bar{u}$ .

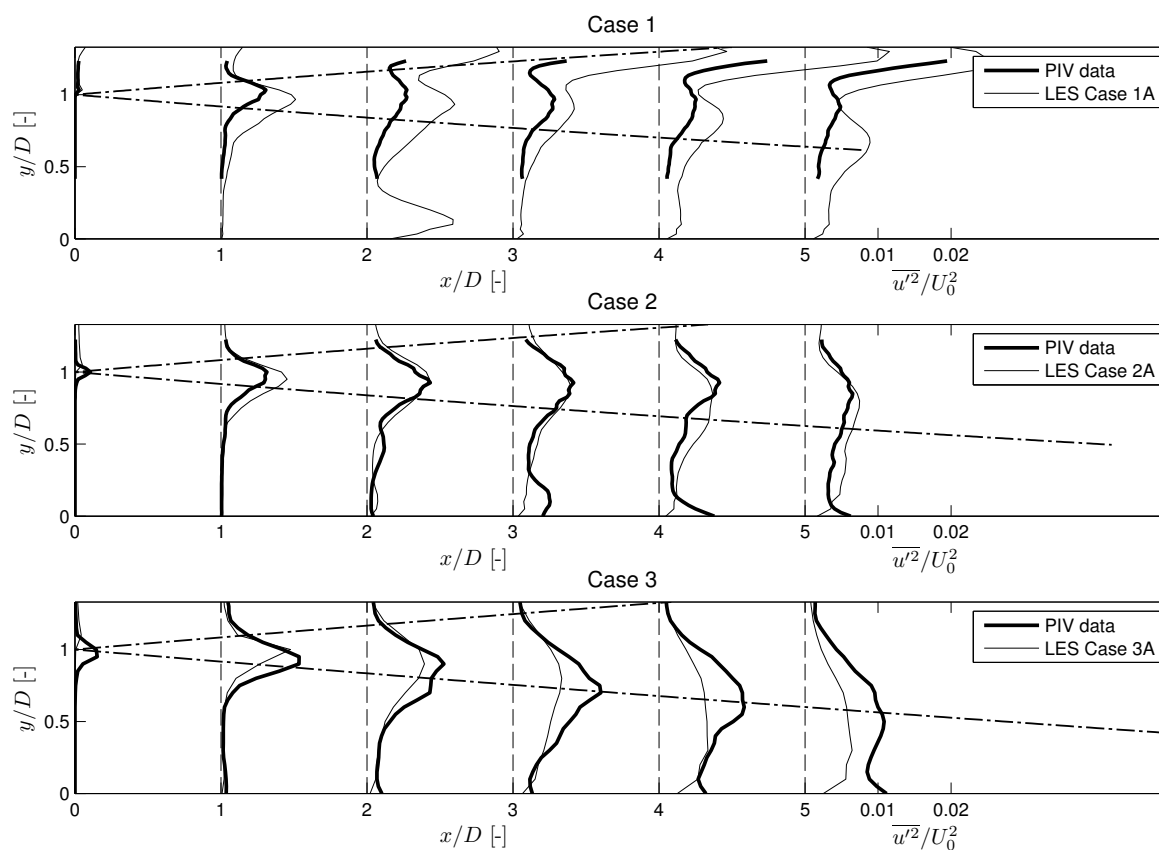


Figure 4.9: Comparison of PIV data and low-pass filtered LES results for  $\overline{u^2}$ .

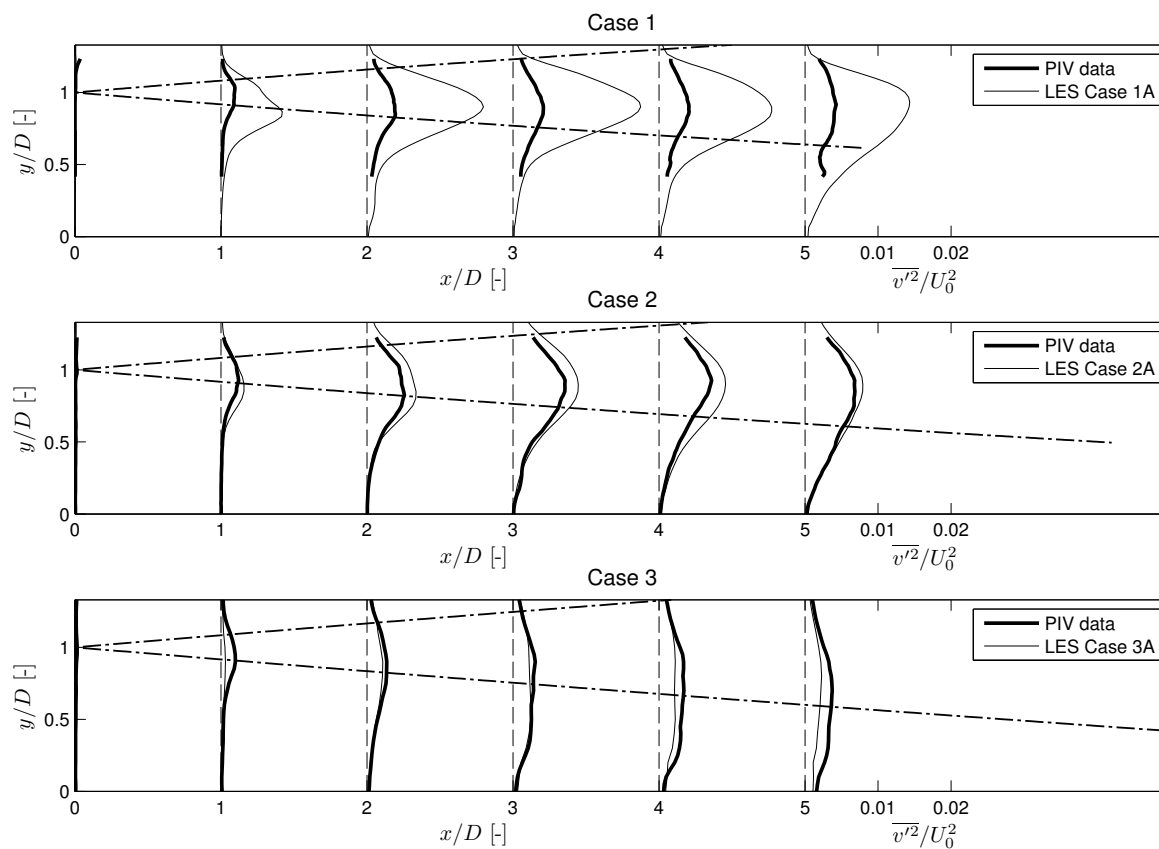


Figure 4.10: Comparison of PIV data and low-pass filtered LES results for  $\overline{v'^2}$ .

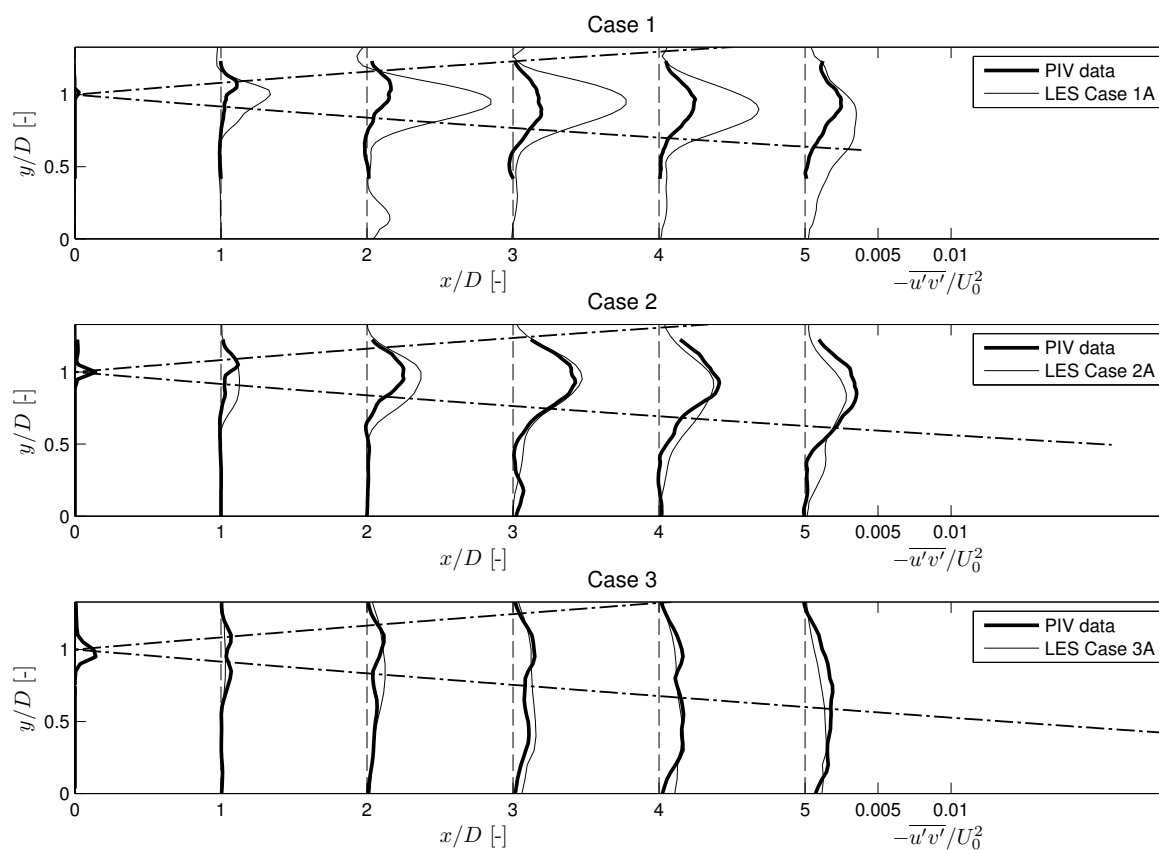


Figure 4.11: Comparison of PIV data and low-pass filtered LES results for  $\overline{u'v'}$ .

differences are found for the streamwise and transverse TKE and Reynolds stress in Case 1 (Figures 4.9–4.11), as well as the streamwise TKE in Case 3 (Figure 4.9). No sound explanation has been found for these errors, although it should be kept in mind that these deviations are sensitive to the exact choice of  $\lambda_{filter}$  (which has been set rather arbitrarily to exactly  $2H$ ). In most cases the location of peaks in the transverse profiles is reproduced correctly, especially within the transverse TKE profiles (Figure 4.10).

Figures 4.8 to 4.11 show that the spatial low-pass filtering operation yields the right order of magnitude for most TKE and Reynolds stress profiles (compared to PIV data). Nevertheless a perfect fit between measurements and simulations is not found in the present cases (which is actually not to be expected). Figures 4.7–4.11 are an attempt to “reconcile” the obtained PIV and LES time-averaged turbulence quantities, despite the very different way in which these quantities were obtained. From the author’s perspective, the differences shown in these figures mainly illustrate a shortcoming of large-scale surface PIV measurements, i.e. the inability to measure small-scale turbulence. This however does not at all disqualify the PIV method for the study of large-scale turbulence patterns, as Figures 4.5 and 4.6 show that these large scales are being captured quite well. Meanwhile the use of LES to investigate smaller-scale structures does still make sense, although no perfect agreement with corresponding PIV results can be achieved.

### 4.4.3 Energy density spectra

The fundamental difference between PIV and LES in their ability to capture small scales (as pointed out in Section 4.4.2) leaves its footprints in the comparison of PIV and LES energy density spectra. Figure 4.12 shows a small selection of computed LES spectra: a few results for Cases 2A and 4A (high resolution) are depicted, while the Case 2A results are compared with corresponding PIV data. No 2D decomposition or low-pass filtering has been applied.

Figure 4.12(a) depicts far-field spectra  $E_{uu}$  and  $E_{vv}$  for the streamwise and transverse TKE at the surface, for  $x = 6D$  and  $y = D$  (at the mixing layer center). LES results for Case 2A are compared with far-field PIV data at  $x = 6D$ , see also Figure 3.19(d). At the low-frequency side PIV and LES data are in fair agreement; the peak frequencies and the order of magnitude of the energy peak levels (associated with 2DCS) are reproduced reasonably well. At the high-frequency side, a considerable difference between PIV and LES spectra is observed: the latter contain much more energy for  $f > 0.2$  Hz. The maximum energy deficit is located around the frequency  $f \approx 1.5$  Hz, which corresponds with a length scale  $\approx H$  (using Taylor’s hypothesis). For both  $U_{uu}$  and  $E_{vv}$ , the LES spectral energy content is approximately 50% larger than the PIV energy content. Both PIV and LES spectra have an isotropic character; streamwise and transverse spectral energy levels are comparable. As in Section 3.6, it is assumed that near-field anisotropy of 2DCS is caused by lateral shear, whereas far-field isotropy is caused by quasi-2D flow behavior and gyre-vortex interaction. All spectra (especially the transverse  $E_{vv}$  components) clearly exhibit a  $-3$  power-law slope, which is associated with the presence and dissipation of quasi-2D turbulent kinetic energy (see Kraichnan [51]). Both PIV and LES results show this typical shallow-flow turbulence behavior. For  $f > 0.2$  Hz, the LES spectra exhibit another typical power-law slope, approximately equal to  $-1$ . This slope can be related to the  $-1$  spectral law reported by Nikora [68], which is typical for wall-bounded turbulence. In shallow flow cases, this nearby wall is obviously the bottom; hence a  $-1$  slope is often found in numerical experiments on shallow channel flows (see Van Balen [96]), whereas in the PIV experiments from Chapter 3 such a slope cannot be discerned.

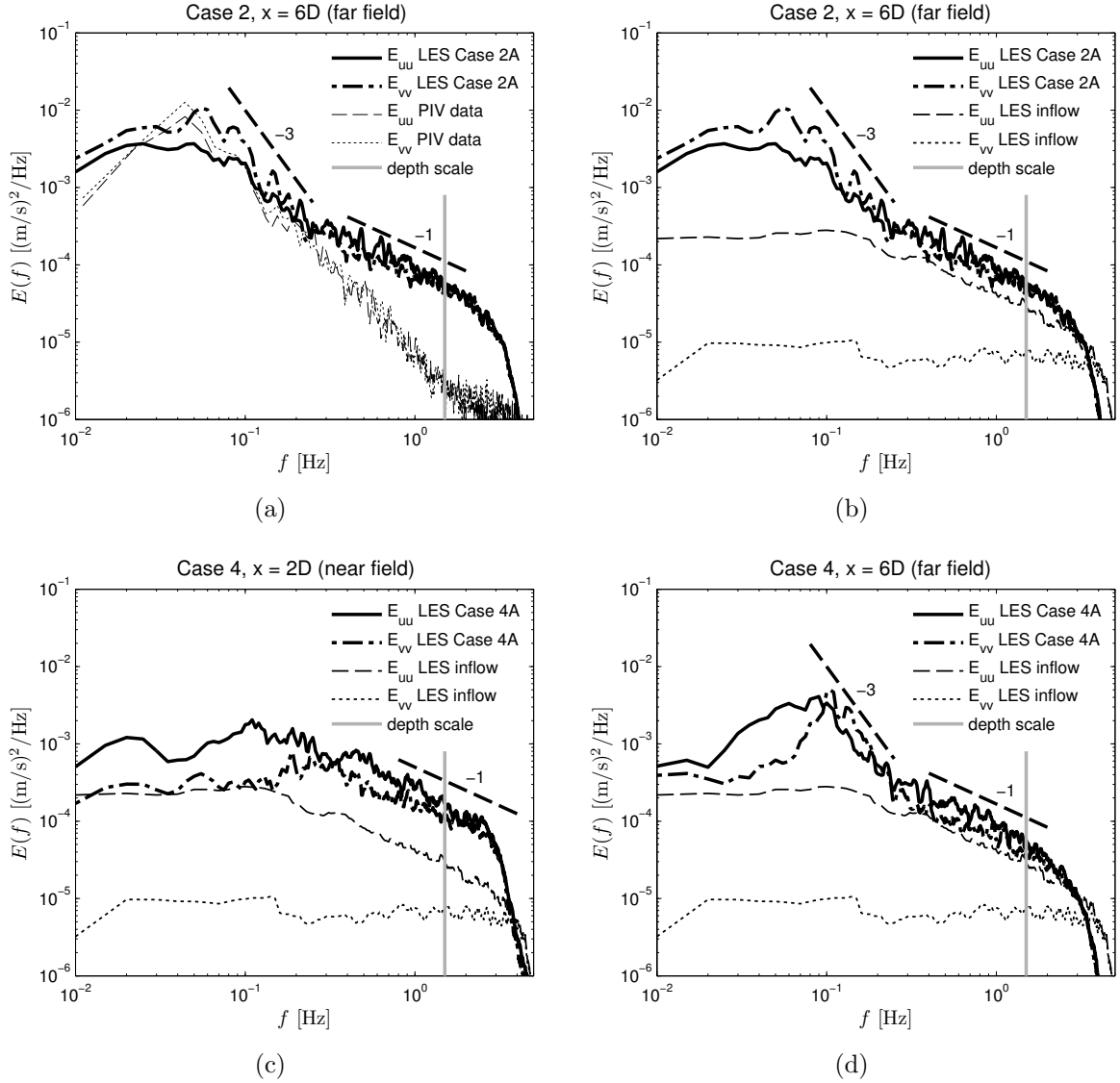


Figure 4.12: Comparison of streamwise and transverse energy density spectra for Cases 2 and 4. Upper panels: Case 2 (PIV versus unfiltered LES), lower panels: Case 4 (near field versus far field spectra).

In Figure 4.12(b), the LES results of panel (a) are compared with LES spectra at the center line of the uniform inflow section of Case 2A (with periodic boundary conditions). Obviously the energy content of these “inflow spectra” is much smaller than the far-field energy content, for these spectra do not contain energetic 2DCS but only components of 3D bottom turbulence. A considerable spectral anisotropy is observed, indicating that streamwise turbulent fluctuations are dominant in this uniform channel flow (see also [99]). It is confirmed here that the growth of 2DCS gives rise to more spectral isotropy. Furthermore, it is observed that the streamwise inflow spectrum  $E_{uu}$  obeys the same  $-1$  Nikora spectral law as the far-field spectra at the high-frequency side. No sign of a  $-3$  slope (associated with 2DCS) is present in the inflow spectra.

The uniform inflow section used for Case 2A has also been applied to the high-velocity inflow boundary of Case 4A. In Figures 4.12(c)-(d), the inflow spectra of panel (b) are subsequently compared to near-field and far-field spectra for Case 4A (at  $x = 2D$  and  $x = 6D$  respectively, and  $y = D$ ). No PIV data are available for this case (SML geometry).

Panel (c) shows a near-field increase of the spectral energy over the entire width of the spectrum: over the full frequency range, both  $E_{uu}$  and  $E_{vv}$  have considerably grown in energy level compared to the inflow spectra. The developing spectra continue to satisfy the  $-1$  Nikora spectral law; in the near field of Case 4A, no significant  $-3$  slope has developed yet. Meanwhile the ratio  $E_{uu}/E_{vv}$  in the low-frequency range is decreasing, which indicates for growing large-eddy isotropy. Finally, panel (d) shows the far-field spectra: a pronounced peak has eventually developed, including a clear  $-3$  slope. The energy at smaller scales is already decaying (in accordance with the linear stability analysis by [99]), while the  $-1$  slope remains valid in this frequency range. It is observed that  $E_{uu} > E_{vv}$  everywhere at the low-frequency side of the spectra; this indicates that the far-field still contains a slight spectral anisotropy, associated with a longitudinal elongation of the 2DCS in Case 4A (see Section 3.7). On the contrary, Panel (a) indicates that  $E_{uu} \approx E_{vv}$  for the PIV spectra (and even  $E_{uu} < E_{vv}$  for the LES spectra) of Case 2A. This difference in far-field isotropy underlines the role of gyre-vortex interaction in the SLE geometry, whereas the SML geometry is dominated by lateral shear over the entire flume length.

Although an exact fit between PIV and LES spectra is obviously impossible in the present case, the agreement between both for low frequencies (large eddy length scales) can be called satisfactory, whereas the LES spectra consistently exhibit a robust power-law behavior in the high-frequency range which is typical for shallow channel flows.

## 4.5 Influence of upstream perturbations

In the previous sections, some effects of upstream turbulence conditions on 2DCS behavior have already been encountered. In this section these effects are listed and summarized. It is concluded that a SLE geometry is less sensitive to upstream turbulence conditions than a SML geometry. Figures 4.5-4.6 and Table 4.3 have shown considerable sensitivity differences for Cases 1-3 (SLE) and Case 4 (SML), at least for low-resolution data. As mentioned in Section 4.4.1, well-resolved LES computations usually experience a correct transition to turbulence in the inflow section, which automatically provides the 3D bottom turbulence needed for 2DCS growth. In case of insufficient resolution, the prescription of explicit (turbulent) perturbations on the inflow boundary becomes necessary in order to induce 3D bottom turbulence.

In accordance with experiments and 2D depth-averaged simulations by Van Prooijen [99] on SML geometries, the present 3D LES data for Case 4 (low resolution) confirm that:

- A higher level of upstream perturbations results in wider mixing layers. The spreading rate of the mixing layer can be significantly larger, see Figure 4.5(f) and 4.6(f);
- Higher streamwise and transverse TKE levels and horizontal Reynolds stresses are found for cases with higher inflow perturbation levels.

As emphasized by [99], these effects are found predominantly in numerical results. This is due to the fact that developed 3D bottom turbulence is consistently found in experimental flow situations; it cannot be straightforwardly “switched off”. Within numerical context, on the other hand, natural perturbations like bottom turbulence are sometimes absent and should be explicitly accounted for by imposing perturbations; this enables the researcher to investigate the impact of these perturbations on the over-all flow. In the low-resolution LES results for Case 4 a large influence of inflow perturbations on the mixing layer development is found, as can be seen especially in the undisturbed Case 4C where the mixing layer is absent. In low-resolution LES results for Case 1-3, the effect of upstream perturbations



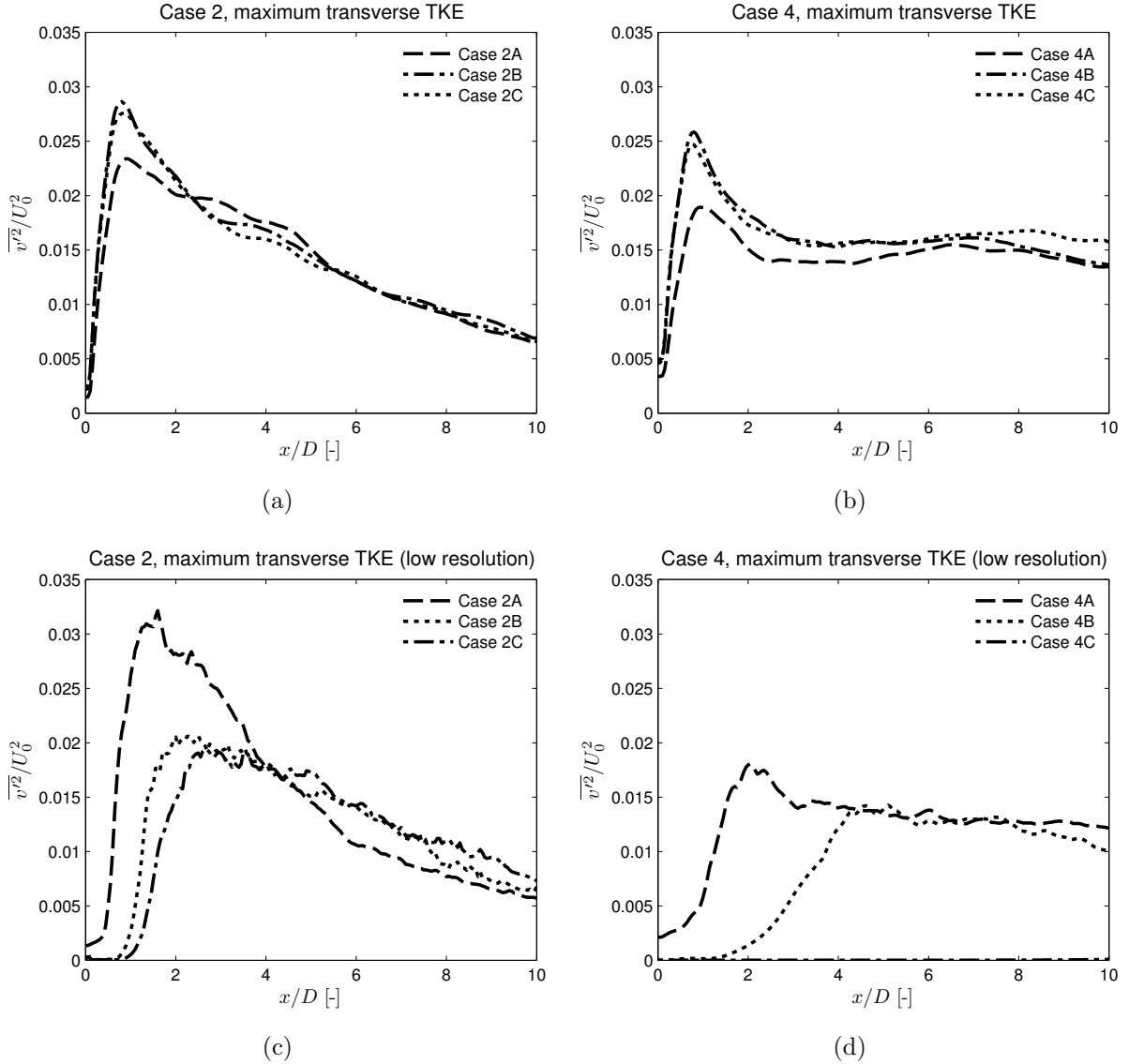


Figure 4.13: *Streamwise development of transverse (TKE) as a function of inflow condition A/B/C, for Cases 2 and 4 (high and low resolution).*

on the mixing layer is much smaller and predominantly restricted to the near field. The following is observed for these SLE cases:

- Each perturbation level (Condition A/B/C) gives rise to the same far-field mixing layer width  $\delta$  and approximately the same spreading rate (proportional to  $2\alpha$ , see Figure 4.5(e)). Only in the near field of Condition B/C cases,  $\delta$  is underpredicted due to damping and lack of perturbations. This underprediction gives rise to an increased value of the gyre lengths  $L_1$  and  $L_2$ ;
- Compared to Condition B/C, Condition A induces a larger near-field peak in the streamwise and transverse TKE and the horizontal Reynolds stress. This peak represents a large amount of small-scale 3D turbulence. The far-field energy levels of the cases A/B/C are virtually equal;
- Apart from slight variations in  $\delta$ ,  $L_1$  and  $L_2$ , the mean flow pattern is not fundamentally impacted by the inflow type, as confirmed by Table 4.3.

The longitudinal development of the transverse TKE as a function of inflow condition

(A/B/C) is illustrated by Figure 4.13, for Cases 2 and 4. The upper panels show high-resolution results; the lower panels depict low-resolution results. In panels (a)-(b), no significant influence of the inflow condition on the high-resolution TKE levels is observed. For the low-resolution results, the conclusions are quite different. The effect of Condition A on Case 1-3 and Case 4 (near-field energy peaks) is visible in panels (c) and (d) respectively. For Condition A, the low-resolution and high-resolution TKE levels are quite comparable. For the low-resolution Case 4B (panel (d)) the far-field TKE level is only triggered by the presence of small-scale white noise at the inflow boundary, whereas the TKE level of Case 4C is virtually zero.

Besides the effects on mixing layer width and energy levels, the inflow condition type also influences the vortex shedding process and 2DCS characteristics. It is observed that:

- A well-developed turbulent inflow profile induces slightly more regularity in the shedding frequency of 2DCS, causing them to be correlated over greater distances;
- A well-developed turbulent inflow profile shortens the transition process from near-field TKE anisotropy towards more isotropy in the far field.

The first observation is illustrated by Figures 4.14 and 4.15. The panels show conditionally averaged 2DCS patterns (vector potential functions) at the surface for Case 2 and 4 and Condition A/B/C (low resolution). The bold dashed vertical lines indicate the cross-section in which conditional averaging has been performed. For both Case 2 and 4, the longest and most pronounced series of conditionally averaged 2DCS are shown by inflow condition A. This indicates that for condition A large eddies are correlated over a greater distance than for the other two conditions. In Case 2B and 2C only a series of two or three significant large eddies is visible; eddies at a further distance from the cross-section are fading out. Apparently the spatial spreading of eddies at some distance of the cross-section is larger (i.e. more irregular) in these cases, so that the conditional averaged eddy is averaged away there and the spatial correlation tends to zero. The same effect is visible in Case 4B. Not surprisingly, the vector potential function of Case 4C shows no large eddies at all. All high-resolution results for Condition A/B/C are virtually equal to the low-resolution results for Condition A; this holds for Case 2 as well as Case 4. This implies that well-resolved 3D bottom turbulence has the same effect as inflow condition A. As high-resolution results are not distinctively different from the Condition A results presented here, they are not shown.

The second statement is illustrated by Figure 4.16. For all Cases 1-4 (low resolution), the ratio of streamwise over transverse TKE  $\overline{u'u'}/\overline{v'v'}$  along the center line of the mixing layer is shown. Inflow conditions A, B and C are compared with PIV results from Chapter 3 for Cases 1-3. For Case 4 (panel 4.16(d)), Conditions A and B are compared with experimental PTV results by Van Prooijen [99]. (No sensible  $\overline{u'u'}/\overline{v'v'}$  ratio can be computed for Case 4C.)

In all four panels of Figure 4.16, the near-field ratio  $\overline{u'u'}/\overline{v'v'}$  is large as streamwise TKE due to lateral shear is dominant. For all Condition A results the near-field value of  $\overline{u'u'}/\overline{v'v'}$  is within the range 3–4. This result is also found for all high-resolution results (not shown here). This is in agreement with the  $\overline{u'u'}/\overline{v'v'}$  ratio of approximately  $\approx 4$  which is often found in straight turbulent channel flows (see e.g. Nezu and Nakagawa [66] and Pope [71]). For low-resolution Conditions B and C, sometimes larger near-field values ( $\overline{u'u'}/\overline{v'v'} > 4$ ) are found as the inflow channel turbulence is not fully developed in these cases. Also for the PIV results much larger near-field values are found, because small-scale 3D bottom turbulence is not properly captured in these measurements.

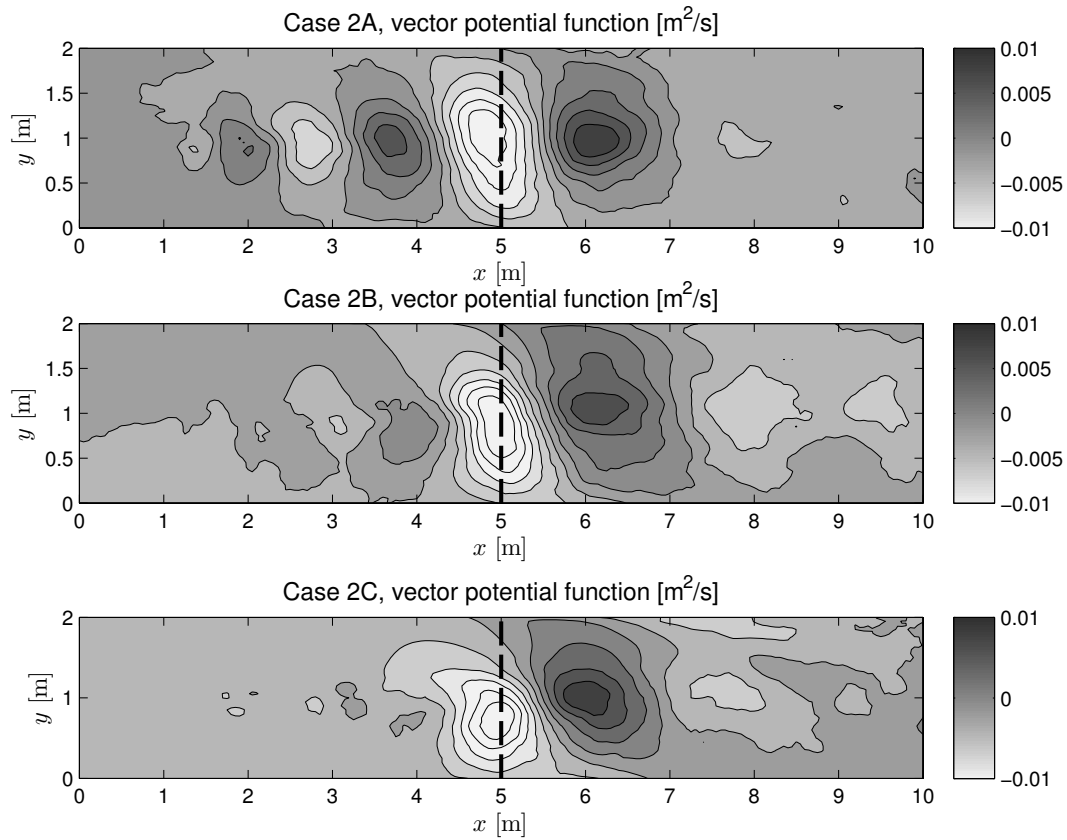


Figure 4.14: Sequences of conditionally averaged 2DCS, Case 2A/B/C (low resolution).

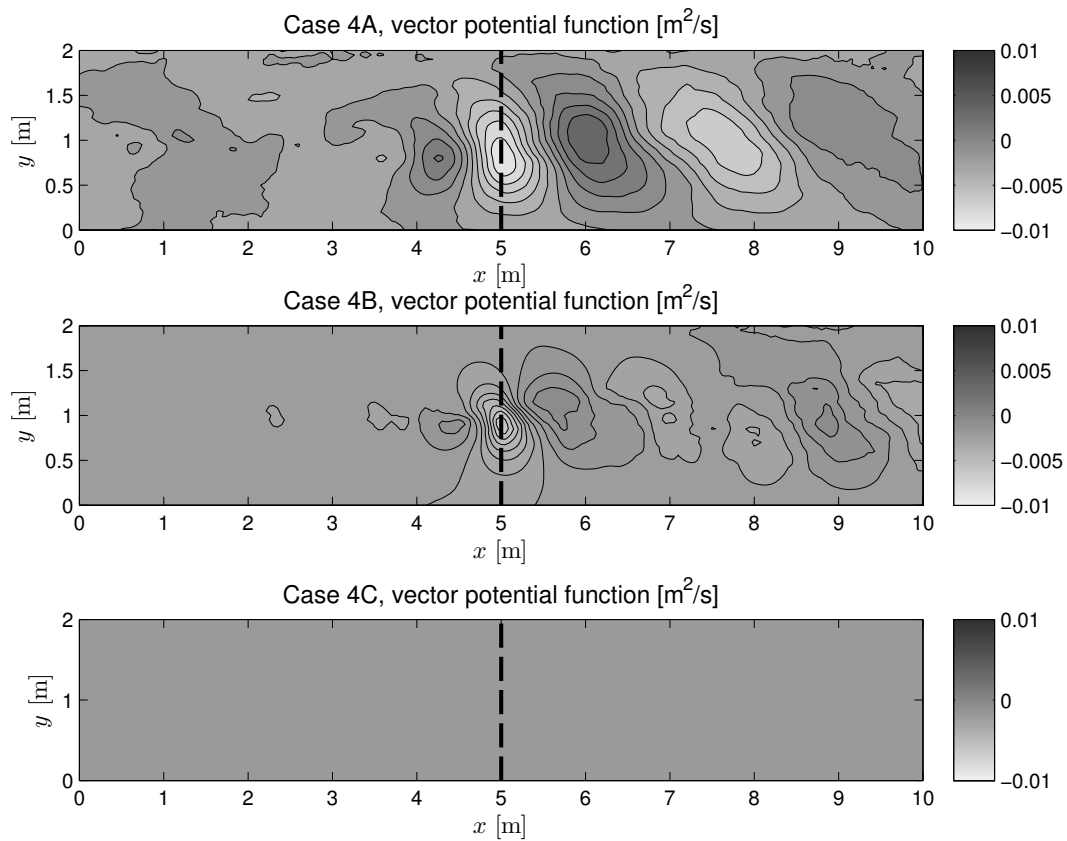


Figure 4.15: Sequences of conditionally averaged 2DCS, Case 4A/B/C (low resolution).

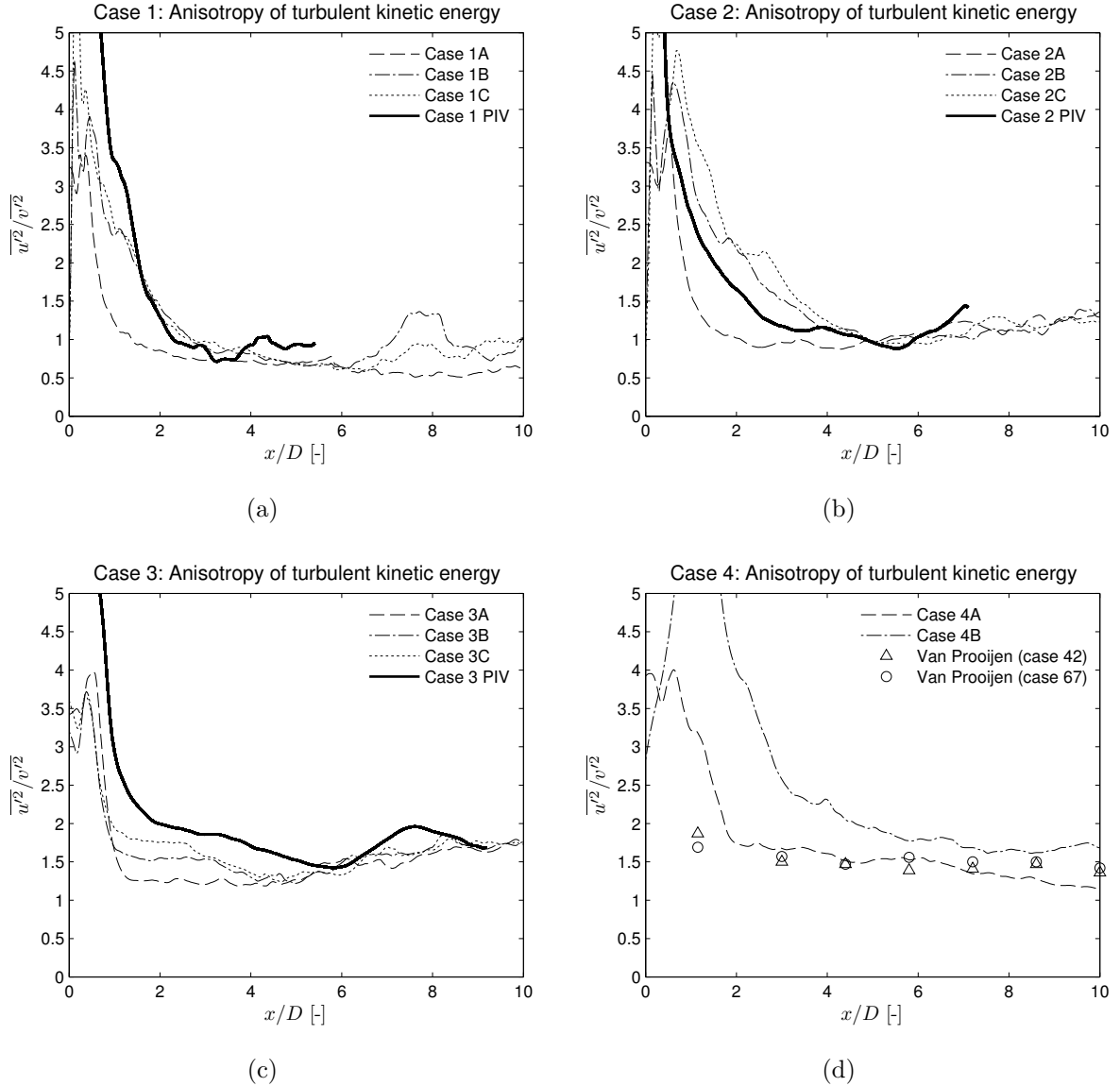


Figure 4.16: *Anisotropy of horizontal turbulent kinetic energy (TKE) components as a function of geometry (Case 1-4) and inflow condition A/B/C (low resolution).*

In the mixing-layer far field the ratio  $\overline{u'u'}/\overline{v'v'}$  reduces significantly. For Case 2 the far-field ratio is in the order of 1, for Case 1 even slightly below 1. These are the most “shallow” geometries and contain the most pronounced far-field isotropy. In Case 3 and Case 4, the far-field ratio is slightly larger than 1: approximately 1.5. This can be explained by the relatively “deep” geometry of Case 3 and the absence of steady gyres in Case 4: no quasi-2D gyre-vortex interaction is present and the mixing layer development is dominated throughout by lateral shear. Case 4A compares well with the experimental results by [99]. In all four cases, inflow condition A consistently causes the fastest near-field convergence to the far field limit of  $\overline{u'u'}/\overline{v'v'}$ . This can be explained by the fact that the well-developed 3D turbulence profile of condition A triggers near-field 2DCS growth more effectively than condition B and C. Again, all high-resolution results for Condition A/B/C are almost equal to the low-resolution results for Condition A: therefore, they do not need to be shown.

It can be concluded that the sensitivity of Case 4 to upstream perturbations complies to the linear stability analysis of SML geometries performed by Van Prooijen [101], whereas

the SLE Cases 1-3 do not comply to this linear analysis. The latter is explained by the presence of steady gyres, which are continuously disturbing the turbulent velocity field and force the development of 2DCS. Following the interpretation by Jirka [47], we can state that the development of 2DCS in Cases 1-3 is induced by *topographical forcing*, whereas Case 4 contains 2DCS caused by *internal transverse shear instabilities* (see Section 2.2.3).

## 4.6 Secondary flow

It is known that shallow shear flows can contain considerable secondary flow inside a vortex street, especially inside the near-field and middle-field (see e.g. Von Carmer et al. [107], Jirka [47] and Schnauder et al. [74]). Secondary flow enhances lateral transport of mass and momentum, which becomes larger than expected on the basis of quasi-2D turbulent transport mechanisms only. In Section 4.7, the contributions from various transport mechanisms to the lateral momentum transfer throughout the SML and SLE mixing layers will be compared.

Secondary flow can be defined in a Reynolds-averaged manner as the mean flow field minus the mean depth-averaged horizontal flow field:

$$\overline{\mathbf{u}^{3D}} = \left( \overline{u} - \widetilde{u}, \overline{v} - \widetilde{v}, \overline{w} \right) = \left( \overline{u''}, \overline{v''}, \overline{w} \right) \quad (4.26)$$

According to this definition, the secondary flow field  $\overline{\mathbf{u}^{3D}}$  includes the total vertical mean velocity  $\overline{w}$  (as explained by Hinterberger et al. [45]). It is also possible to decompose the turbulent kinetic energy and Reynolds stresses into a depth-averaged contribution and a secondary flow contribution, as has been shown in Equations (4.22)–(4.25). Also in this definition, the secondary flow component contains the entire vertical flow velocity fluctuation  $w'$ . Hence, as the vertical flow pattern is a good indicator for the presence of secondary flow structures, it receives special attention within this section.

At the water surface, secondary flow structures can be found by identifying divergent or convergent zones within the surface flow field. These zones of nonzero divergence are caused by local upwelling and downdraft regions, associated with net vertical velocities inside the mixing layer. Especially the depth-averaged mean vertical velocity  $\widetilde{w}$  and the depth-averaged vertical turbulence intensity  $\widetilde{w}' \equiv \sqrt{\overline{w'w'}}$  are considered useful indicators for the presence of such secondary flow structures.

Figure 4.17 shows the spatial distribution of  $\widetilde{w}$  and  $\widetilde{w}'$  for Case 2A (high-resolution data). As both quantities have dimension m/s, they can be easily compared. In the upper panel an elongated region of time-averaged upwelling is visible (along the approximate mixing layer center line), surrounded by two zones of downdraft (at the high and low velocity side of the mixing layer respectively). This result is in accordance with the conceptual sketch in Figure 3.9 (Section 3.4.4). The downdraft zones are approximately located along the mixing layer boundary. Inside the inflow region ( $x < 0$ ) long streaks of upwelling and downdraft are visible as well, indicating steady secondary recirculations inside each cross-section along the turbulent inflow section. The upwelling-downdraft circulation cell at the high-velocity side of the mixing layer can actually be seen as a continuation of this upstream secondary flow feature. The low-velocity downdraft region, however, is located inside the primary gyre and emerges from 3D flow structures inside the mixing layer. Downdraft is also observed along the sidewall boundary layer of the primary gyre backflow (along the line  $y = 0$ ) and along the interface between primary and secondary gyre (near  $x \approx 2$  m).

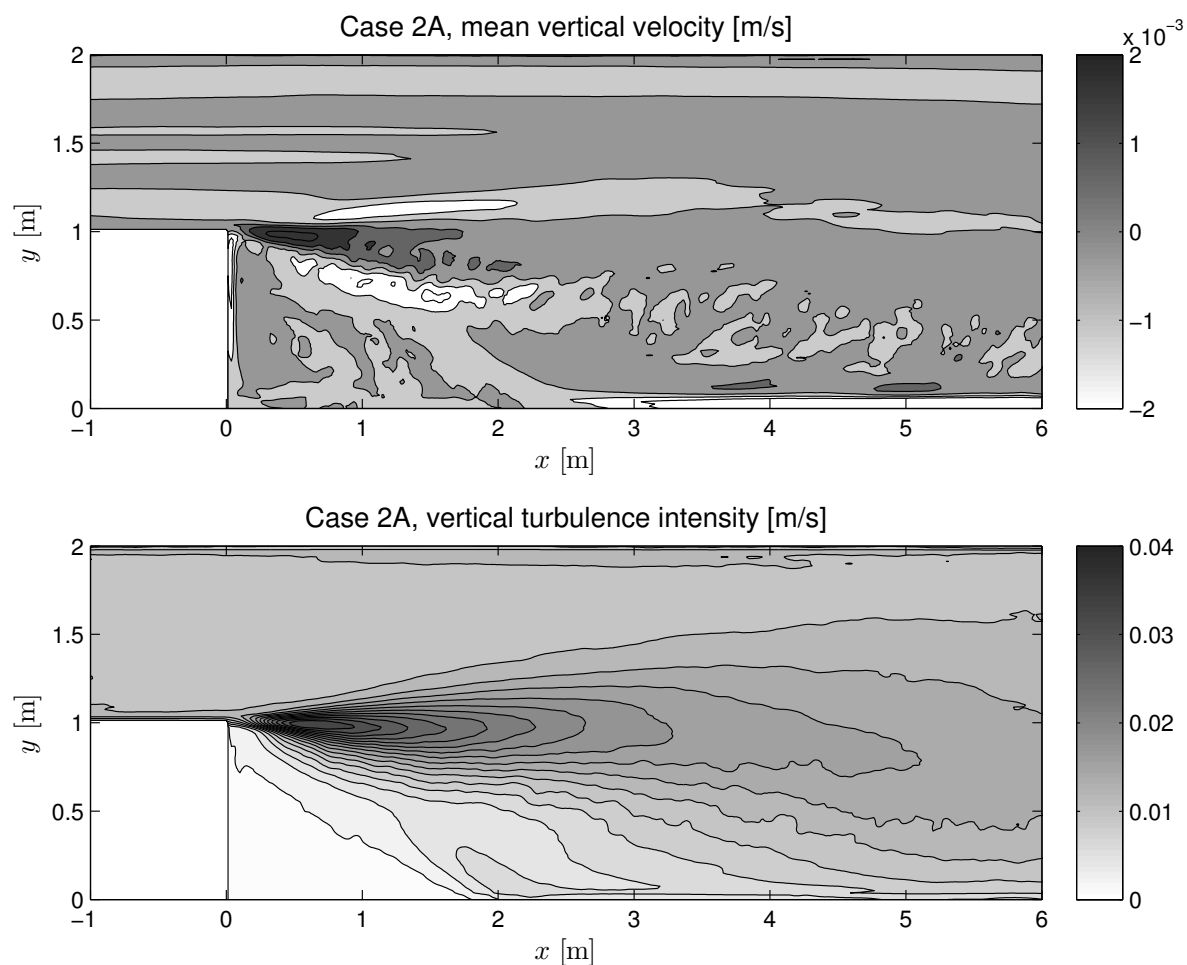


Figure 4.17: Secondary flow effects in Case 2A: mean vertical velocity (upper panel) and vertical turbulence intensity (lower panel).

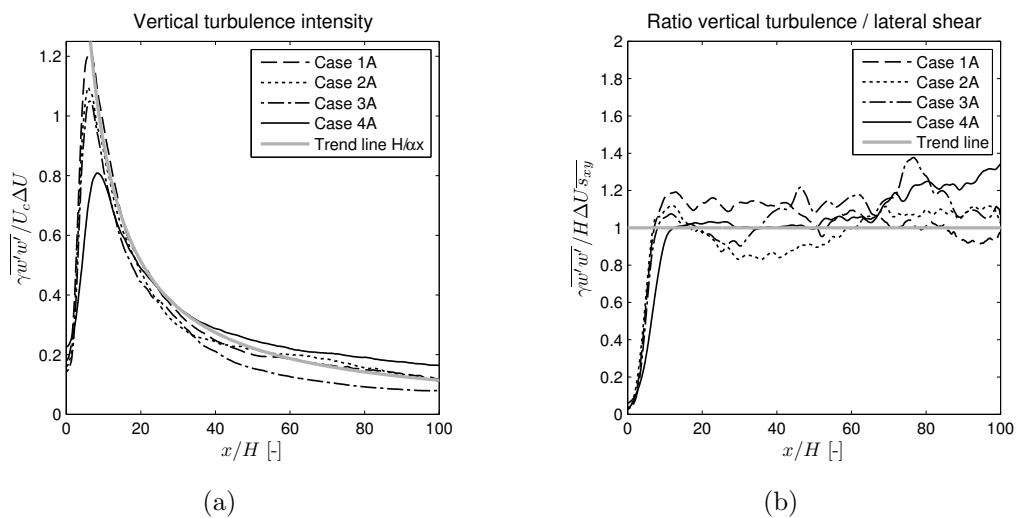


Figure 4.18: Proportionality of vertical turbulence intensity (in mixing layer center) to mean lateral shear.

It can be stated that, for the present flow cases, all regions with considerable net vertical flow (i.e. time-averaged secondary flow) also contain strong horizontal lateral shear.

The lower panel of Figure 4.17 shows a region of large vertical turbulence intensity  $\widetilde{w'}$  inside the mixing layer, widening in downstream direction while the peak value is located in the middle field. Apart from this region a basic level of vertical TKE is present almost everywhere, as the entire flow region somehow contains 3D bottom turbulence. Also in this panel a correlation can be found with the presence of lateral shear.

Looking at the scaling of both panels, it is observed that the maximum vertical turbulence intensity is approximately an order of magnitude larger than the maximum residual mean vertical flow (both in m/s). It is concluded that instantaneous regions of upwelling and downdraft are varying very quickly, which is not surprising as the entire mixing layer is a dynamic region containing 2DCS that move downstream. Apparently the residual mean secondary flow is weak compared to the over-all secondary flow activity.

The weakness of the mean secondary flow structure makes it difficult to find a proper scaling to correlate the mean vertical flow  $\widetilde{w}$  to other flow quantities. On the other hand, it is possible to relate the vertical turbulence intensity  $\widetilde{w'}$  inside the mixing layer to other mixing layer properties. Inspired by the correlations found above, it has been assumed that the vertical turbulent kinetic energy  $\overline{w'w'}$  along the mixing layer center line is proportional to the mean depth-averaged lateral shear  $\widetilde{s}_{xy}$  along the same line:

$$\overline{w'w'} \sim \nu_t \widetilde{s}_{xy} = \nu_t \left( \frac{\partial u}{\partial y} + \frac{\partial v}{\partial x} \right) \approx \nu_t \frac{\partial \widetilde{u}}{\partial y}, \quad (4.27)$$

where  $\nu_t$  is some representative eddy viscosity factor to translate the kinematic lateral shear  $\widetilde{s}_{xy}$  into a shear stress. Assuming that  $\nu_t$  is proportional to  $H\Delta U$  (where  $\Delta U$  is the lateral velocity difference over the mixing layer, see Section 3.5) and introducing a proportionality factor  $\gamma$  to compare between  $\overline{w'w'}$  and mean mixing layer quantities, we have:

$$\gamma \overline{w'w'} \approx H\Delta U \widetilde{s}_{xy} \quad (4.28)$$

This is the key assumption to be tested. Furthermore, as it is known that lateral shear is related to the mixing layer width  $\delta$ , the vertical TKE can be related to mixing layer growth as well. Equation (3.3) states that  $\widetilde{s}_{xy} = \Delta U/\delta$ , while from the self-similarity theory in Section 3.5 it follows that  $\delta(x) \approx \alpha(\Delta U/U_c)x$  in the near and middle field. Substitution of these expressions in (4.28) yields the following result:

$$\frac{\gamma \overline{w'w'}}{U_c \Delta U} \approx \frac{H}{\alpha x} \quad (4.29)$$

Hence, the streamwise development of this dimensionless form of the vertical TKE may be governed by the constant entrainment coefficient  $\alpha = 0.085$ .

We test assumptions (4.28) and (4.29) for all LES computations: Cases 1-4 and inflow conditions A/B/C (high-resolution data). The results are presented in Figure 4.18. Only Cases 1A-4A are depicted, but these results are fully representative for the B/C cases as well. Panel (a) compares the left-hand side and right-hand side of (4.29), taking  $\gamma = 60$ . Especially for the middle field a good agreement between the dimensionless vertical TKE and the dimensionless inverse mixing layer growth rate  $H/\alpha x$  is found. The far field exhibits slight deviations from this theoretical trend line. Furthermore a small adaptation length for  $\widetilde{s}_{xy}$  in the near field is found, because  $H/\alpha x$  obviously goes to infinity for the limit  $x \rightarrow 0$ . Panel (b) depicts the ratio between the left-hand and right-hand sides of (4.28),

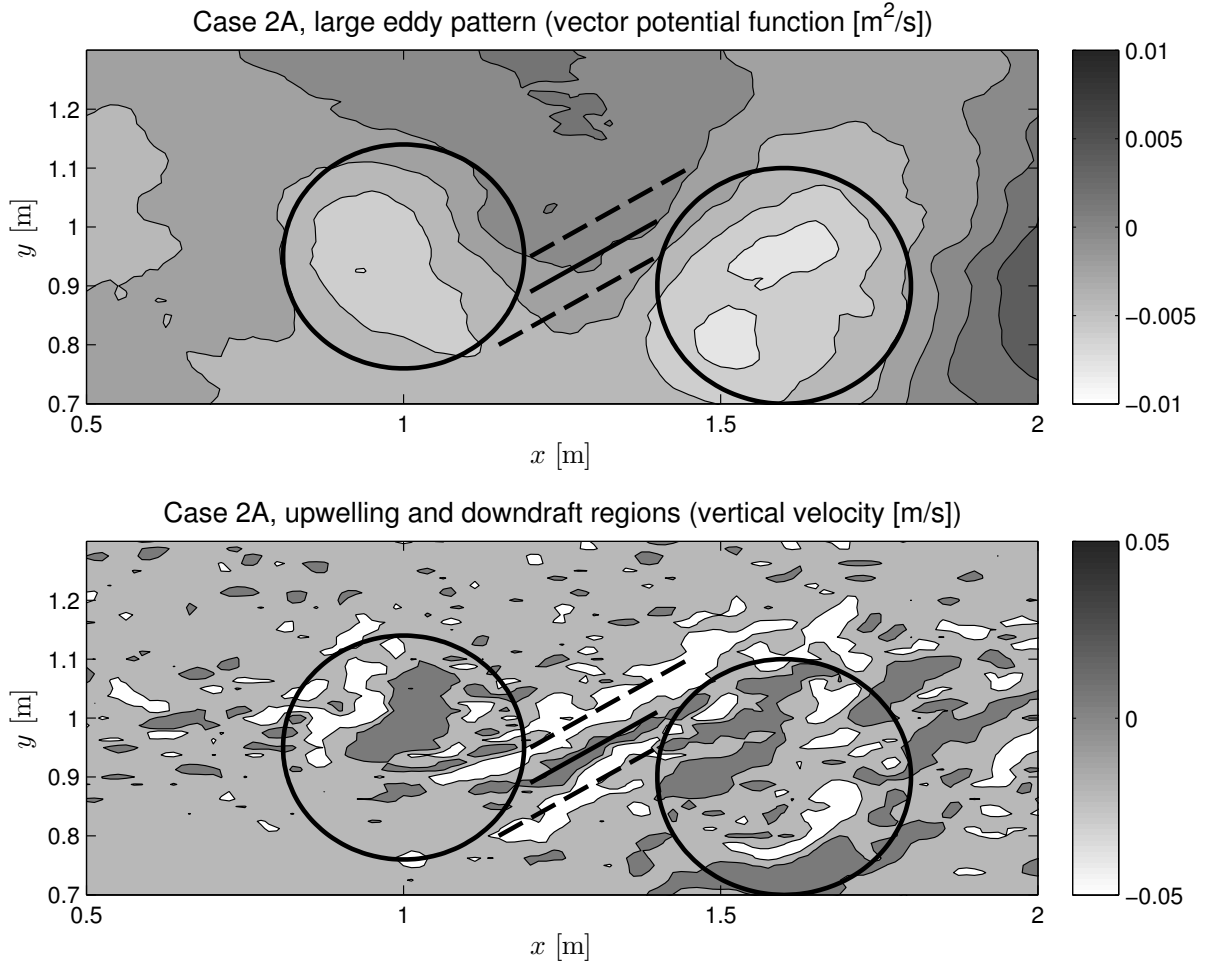


Figure 4.19: *Instantaneous patterns of upwelling and downdraft in the middle field of Case 2A. Location of two 2DCS and a region of strong deformation are indicated by bold lines.*

taking  $\gamma = 60$  again. Downstream of a short near-field adaptation length, the ratios found are satisfactorily close to unity for all LES cases.

From both panels it is concluded that all flow cases (both SML and SLE) comply to one single dimensionless scaling for the vertical TKE. The scaling with  $H$  seems somewhat arbitrary, as  $H$  is not varied in this study. However, scaling with  $H$  makes more sense in this case than scaling with a horizontal length scale, because the mean lateral shear is acting over the full water depth. A further improvement of the present scaling may yield better results for the near-field adaptation region. This could be achieved by considering a complete Reynolds-averaged balance equation for the vertical TKE instead of the present simple assumption (4.27).

Instantaneous secondary flow patterns are more complex than the mean vertical flow and vertical turbulence intensity patterns shown in Figures 4.17 and 4.18. Figure 4.19 illustrates an instantaneous secondary flow pattern between two consecutive 2DCS that move downstream. The middle-field of Case 2A ( $0.5D < x < 2D$ ) is shown for time level  $t = 2000$  s. The upper panel contains the instantaneous vector potential function at the surface (after subtraction of the mean flow field); the lower panel depicts depth-averaged instantaneous vertical velocities  $\tilde{w}$ , i.e. regions of local upwelling and downdraft. The locations of two 2DCS and a region of considerable lateral shear in between them (close to a saddle point, see Section 3.7) have been indicated by bold lines.



The lower panel shows that background vertical flow fluctuations due to 3D bottom turbulence are present in the entire domain. Besides, along the saddle point line in between the 2DCS a long streak of vertical upwelling can be discerned. When comparing this region with the surface velocity field (not shown here), it appears that horizontal flow divergence is present here. At both sides of the upwelling streak line two regions of downdraft are found, associated with horizontal flow convergence. These results are in accordance with PIV observations in Chapter 3: i.e. the presence of secondary flow was confirmed there by observing the black tracer particle distribution at the surface. Upwelling was visible by elongated empty regions and downdraft by streak lines with higher particle concentrations (see Section 3.4.4).

In experimental work on shallow wake flows, Von Carmer et al. [107] have observed that upwelling and downdraft regions are also present inside 2DCS themselves. Upwelling and flow divergence (due to centrifugal forces) were visible at the surface in the 2DCS kernels whereas downdraft was observed along the eddy boundaries. The effect was compared to the phenomenon of spiral flow along the outer bank of a shallow river bend. Upwelling inside 2DCS is visible as well in the lower panel of Figure 4.19; the left eddy contains a large region of upward vertical flow. However, this feature is not observed for every individual large eddy in the present LES data, whereas secondary flow patterns near saddle points in between two 2DCS are consistently found. The latter patterns have been observed by [107] as well. Von Carmer et al. claim that secondary flow effects are predominantly present in the near-field and middle-field of shallow wake flows, whereas they fade away in the far-field (approximately  $x/D > 5$ ). This observation is confirmed by the present LES results (see Figures 4.17 and 4.18).

## 4.7 Lateral momentum transfer

Mean advection, secondary flow and turbulent stresses are mechanisms that induce lateral transfer of momentum, which in turn impacts the mean flow pattern. In this section, momentum transfer patterns throughout the SLE and SML geometries are investigated in a depth-averaged sense.

Starting point is the LES momentum equation (4.2), supplemented with the Smagorinsky model (4.3). This momentum equation can be both Reynolds-averaged and averaged over a constant depth  $H$ , yielding equation (4.30). It should be noted that the LES filtering operator  $\overline{(\dots)}$  for resolved quantities (larger than subgrid) has been omitted throughout this chapter; the operator  $\widetilde{(\dots)}$  is used here to denote Reynolds averaging, while  $\overline{(\dots)}$  still represents depth-averaging. As the Reynolds-averaged momentum equation describes a stationary turbulent situation the time derivative vanishes, so we have:

$$\frac{\partial \widetilde{u_i u_j}}{\partial x_j} + \frac{\partial \widetilde{p}}{\partial x_i} - \frac{\partial}{\partial x_j} \nu \overline{\left( \frac{\partial u_i}{\partial x_j} + \frac{\partial u_j}{\partial x_i} \right)} = 0, \quad (4.30)$$

where  $\nu = \nu^{mol} + \nu^{SGS}$  contains both molecular and sub-grid scale eddy viscosity. The first term on the left-hand side contains the advective momentum fluxes  $\widetilde{u_i u_j}$ . These nonlinear fluxes  $T_{ij}$  can be decomposed into several contributions (see Vermaas et al. [106]):

$$\underbrace{\widetilde{u_i u_j}}_{T_{ij}} = \underbrace{\widetilde{u_i} \widetilde{u_j}}_{T_{adv}} + \underbrace{\widetilde{u_i'' u_j''}}_{T_{sec}} + \underbrace{\widetilde{u_i' u_j'}}_{T_{Rey}}, \quad (4.31)$$

	Normal transport	Lateral transport
Mean advection	$\overline{\tilde{u}\tilde{u}} \sim \mathcal{O}(10^{-2})$ $\overline{\tilde{v}\tilde{v}} \sim \mathcal{O}(10^{-3})$ $\overline{\tilde{w}\tilde{w}} \sim \mathcal{O}(10^{-5})$	$\overline{\tilde{u}\tilde{v}} \sim \mathcal{O}(10^{-3})$ $\overline{\tilde{u}\tilde{w}} \sim \mathcal{O}(10^{-4})$ $\overline{\tilde{v}\tilde{w}} \sim \mathcal{O}(10^{-5})$
Secondary flow	$\overline{\tilde{u}''\tilde{u}''} \sim \mathcal{O}(10^{-3})$ $\overline{\tilde{v}''\tilde{v}''} \sim \mathcal{O}(10^{-4})$ $\overline{\tilde{w}''\tilde{w}''} \sim \mathcal{O}(10^{-5})$	$\overline{\tilde{u}''\tilde{v}''} \sim \mathcal{O}(10^{-4})$ $\overline{\tilde{u}''\tilde{w}''} \sim \mathcal{O}(10^{-5})$ $\overline{\tilde{v}''\tilde{w}''} \sim \mathcal{O}(10^{-5})$
Reynolds stress (including TKE)	$\overline{u'u'} \sim \mathcal{O}(10^{-3})$ $\overline{v'v'} \sim \mathcal{O}(10^{-4})$ $\overline{w'w'} \sim \mathcal{O}(10^{-4})$	$\overline{u'v'} \sim \mathcal{O}(10^{-4})$ $\overline{u'w'} \sim \mathcal{O}(10^{-5})$ $\overline{v'w'} \sim \mathcal{O}(10^{-5})$
Subgrid stress  (molecular and eddy viscosity)	$\overline{2\nu\left(\frac{\partial u}{\partial x}\right)} \sim \mathcal{O}(10^{-6})$ $\overline{2\nu\left(\frac{\partial v}{\partial y}\right)} \sim \mathcal{O}(10^{-6})$ $\overline{2\nu\left(\frac{\partial w}{\partial z}\right)} \sim \mathcal{O}(10^{-6})$	$\overline{\nu\left(\frac{\partial u}{\partial y} + \frac{\partial v}{\partial x}\right)} \sim \mathcal{O}(10^{-5})$ $\overline{\nu\left(\frac{\partial u}{\partial z} + \frac{\partial w}{\partial x}\right)} \sim \mathcal{O}(10^{-5})$ $\overline{\nu\left(\frac{\partial v}{\partial z} + \frac{\partial w}{\partial y}\right)} \sim \mathcal{O}(10^{-5})$

Table 4.4: Global order of magnitude of normal and lateral momentum transport terms, in  $m^2/s^2$  (LES Cases 1, 2, 3 and 4).

where  $T_{adv}$  is the mean depth-averaged advective contribution,  $T_{sec}$  is the secondary flow contribution and  $T_{Rey}$  is the contribution due to Reynolds stresses.

Each contribution in (4.31) to the total momentum transfer  $T_{ij}$  is a symmetric  $3 \times 3$  tensor with 6 independent entries. As shallow shear flows are characterized by transverse exchange of streamwise momentum in the horizontal plane, we are mainly interested in the contributions to component  $T_{xy} = \overline{\tilde{u}\tilde{v}} + \overline{\tilde{u}''\tilde{v}''} + \overline{u'v'}$ . This is also motivated by estimating the order of magnitude of all contributions to  $T_{ij}$ . Table 4.4 is listing the global order of magnitude of normal and lateral depth-averaged momentum flux terms (all having dimension  $m^2/s^2$ ) in the present LES data. A comparison is also made with the importance of viscous subgrid stresses. (The orders of magnitude given here are equally valid for LES Cases 1, 2, 3 and 4.)

Looking at lateral momentum fluxes (right column in Table 4.4), it is observed that all contributions of  $T_{xy}$  are at least one order of magnitude larger than the corresponding contributions of  $T_{xz}$  and  $T_{yz}$ . In terms of normal fluxes (left column), the vertical contributions  $T_{zz}$  are negligible compared to the corresponding horizontal contributions  $T_{xx}$  and  $T_{yy}$ . Moreover, all viscous stresses can be neglected compared to the advective fluxes. The complete picture reveals  $T_{xx}$  and  $T_{xy}$  as dominant momentum flux contributions, with  $T_{xx}$  much larger than  $T_{xy}$ . The latter is not surprising, as streamwise transport of streamwise momentum is obviously indispensable to convey momentum from the inflow to the outflow boundary. For the analysis of momentum transfer by shallow mixing layers, however, the lateral component  $T_{xy}$  is most important. Taking the streamwise component of (4.30) and omitting negligible terms, we obtain:

$$\frac{\partial \tilde{u}}{\partial x} \tilde{u} + \frac{\partial \tilde{u}}{\partial y} \tilde{v} + \frac{\partial \tilde{u}''\tilde{v}''}{\partial y} + \frac{\partial \tilde{u}'v'}{\partial y} + \frac{\partial \tilde{p}}{\partial x} \approx 0 \quad (4.32)$$

Equation (4.32) is similar to the streamwise shallow-water equation by Schnauder et al. [74].

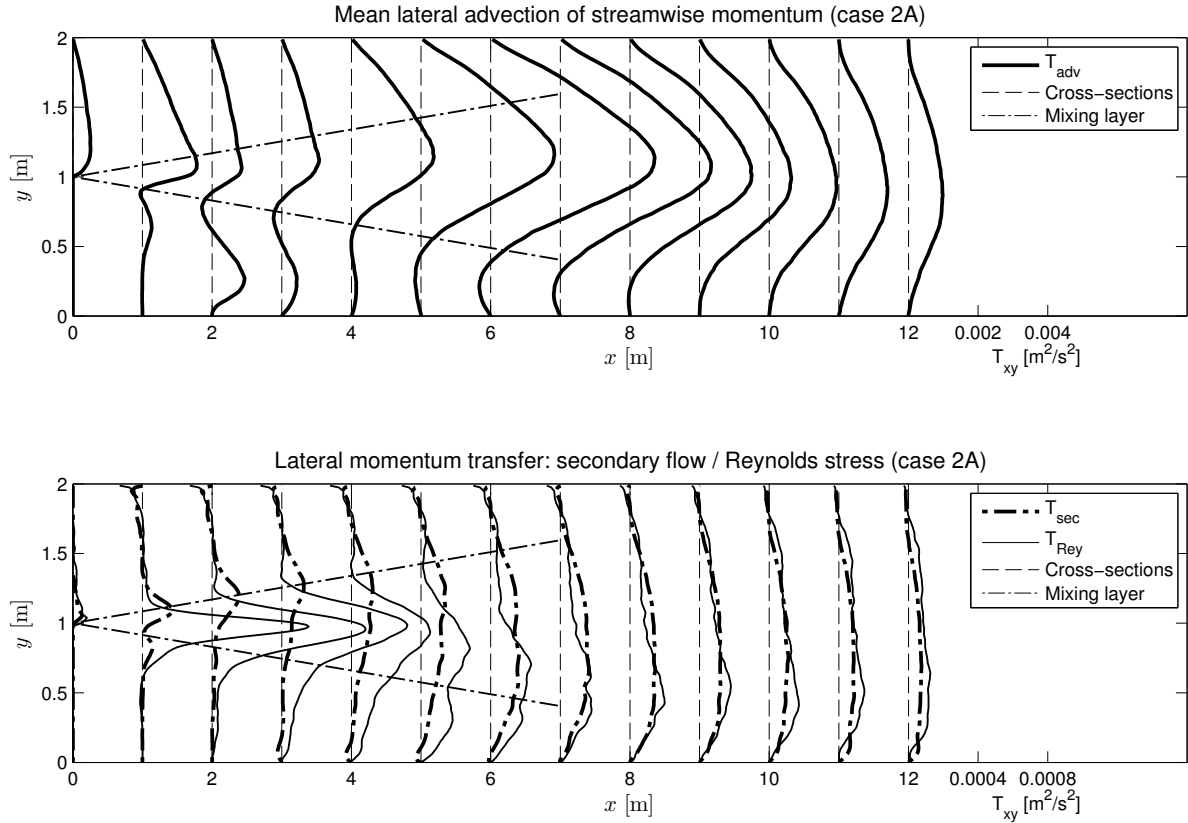


Figure 4.20: *Depth-averaged lateral transport of streamwise momentum (Case 2A): mean advective transport (upper panel), secondary flow and Reynolds stress transport (lower panel).*

Figures 4.20 and 4.21 show the spatial development of the separate contributions to  $T_{xy}$  ( $T_{adv}$ ,  $T_{sec}$  and  $T_{Rey}$ , see Equation (4.31)) for Cases 2A and 4A respectively (high resolution data). Because in the mixing layer region  $T_{adv}$  is an order of magnitude larger than  $T_{sec}$  and  $T_{Rey}$ , it has been depicted in a separate panel. In all panels the approximate location of the widening mixing layer has been indicated. As in the present geometries all dominant values of  $T_{xy}$  are negative, the transverse profiles in Figures 4.20 and 4.21 have been flipped about their  $y$ -axes in order to have a “natural” view on them.

The development of  $T_{adv}$  for Case 2A shows some interesting features (Figure 4.20, upper panel). The near-field main flow profile is almost a sawtooth function with a large momentum flux gradient near the primary separation point. When moving downstream, this narrow step-gradient region both broadens and flattens, which can be associated with the broadening of the mixing layer and decrease of the maximum lateral shear. Approximately between the cross-sections  $x = 4$  m and  $x = 8$  m, the mean advective lateral momentum transfer toward the low-velocity side of the SLE significantly increases. This is explained by the bending of the depth-averaged flow streamlines toward the low-velocity side of the SLE (see Figure 4.3). In the far field, streamlines are more straight again and the large peak in  $T_{adv}$  gradually decreases. In between  $x = 4$  m and  $x = 8$  m along the line  $y = 0$ , a momentum transfer in opposite direction (toward the high-velocity side) is visible; this is the region of primary gyre backflow. Its influence reaches no further downstream than about  $x = 8$  m, which is approximately the location of the primary reattachment point. Compared to Case 2A, Case 4A exhibits a more regular pattern (Figure 4.21, upper panel). A near-field sawtooth profile and a gradual spreading of the lateral gradient are visible.

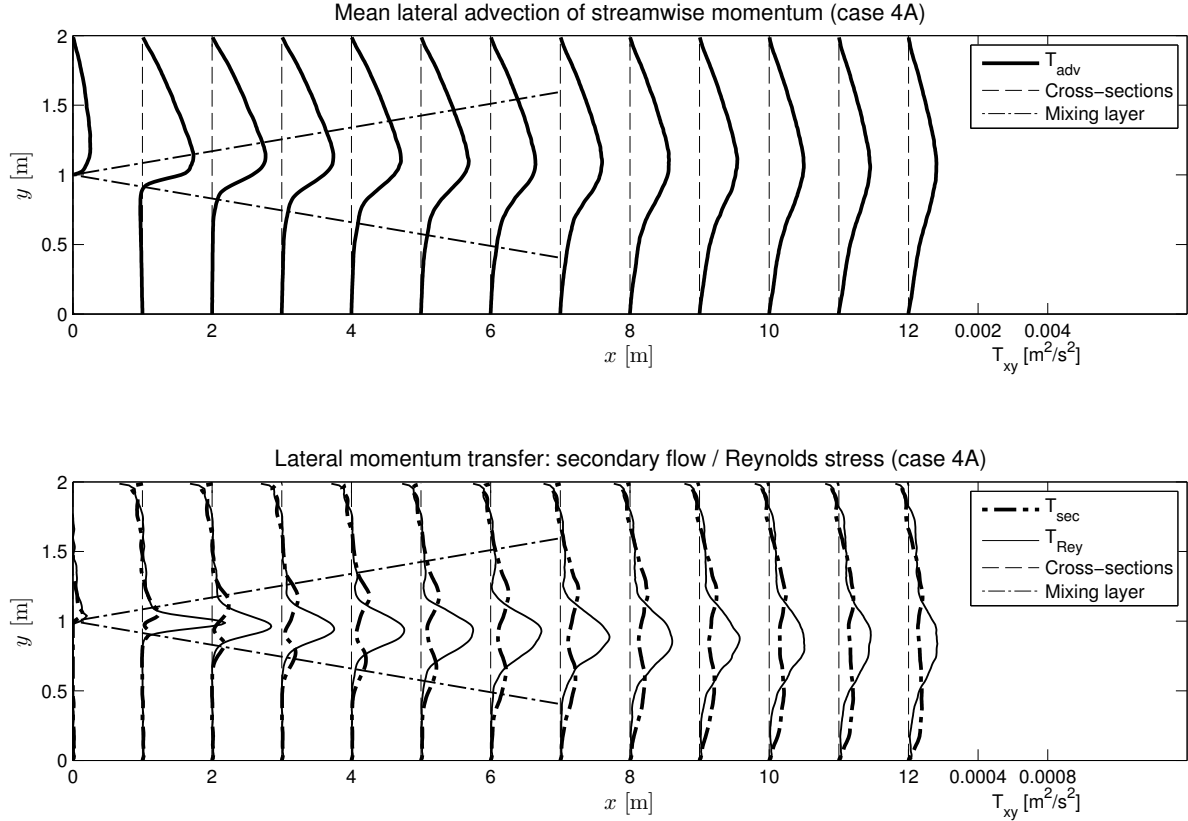


Figure 4.21: *Depth-averaged lateral transport of streamwise momentum (Case 4A): mean advective transport (upper panel), secondary flow and Reynolds stress transport (lower panel).*

However, no pronounced far-field increase of  $T_{adv}$  is found. This indicates that no significant streamline curvature is present here, in accordance with Figure 4.3. The widening process of the high-velocity side streamline pattern is much slower than for Case 2A.

For both Case 2A and Case 4A, the secondary flow transport  $T_{sec}$  (depicted in the lower panels of Figures 4.20 and 4.21) consists of two important contributions. Firstly, due to the presence of an over-all vertical velocity gradient (logarithmic velocity profile) combined with the broadening and deceleration of the high-velocity part of the flow, an over-all dispersive mechanism is present over the mixing layer width and eventually (in the far field) the entire flume width. Secondly, a contribution is made by the dynamic secondary flow events mentioned earlier in Section 4.6. The second contribution is mainly restricted to the middle field of the mixing layer and has its peak value near the high-velocity boundary of the mixing layer region. As indicated by Schnauder [74], the secondary flow stress must be larger here due to the higher mean streamwise velocity component (compared to the other side of the mixing layer). Another observation can be added: secondary flow plays an important role in the near-field and middle-field entrainment of main-stream fluid into the mixing layer region. This entrainment process obviously takes place at the high velocity side.

In both near-field and middle-field the secondary flow contribution  $T_{sec}$  is always smaller than the horizontal Reynolds stress  $T_{Rey}$ , which is approximately one order of magnitude larger there (lower panels of Figures 4.20 and 4.21). Reynolds stress profiles have their peaks along the mixing layer center line rather than along the high-velocity side of it. It should be noted that Reynolds stress profiles decay faster in streamwise direction for

Case 2A than for Case 4A. In the latter geometry, a pronounced velocity difference (lateral shear) remains intact over a longer distance than in the SLE geometry. On the other hand, the far-field secondary flow contribution for Case 4A is weaker than for Case 2A. This leads to the observation that  $T_{sec}$  and  $T_{Rey}$  become almost equal in the far-field of Case 2A, whereas  $T_{Rey}$  dominates over  $T_{sec}$  everywhere in Case 4A. It should however be kept in mind that far-field  $T_{sec}$  values are predominantly accounted for by dispersive effects, whereas the real “dynamic” secondary flow structures (associated with upwelling and downdraft patterns) are found in the middle-field region. This dynamic part of  $T_{sec}$  is small everywhere compared to  $T_{Rey}$  and  $T_{adv}$  inside the mixing layer. Hence, although the dispersive effect must be taken into account, the over-all flow pattern can still be called quasi-2D.

It is worthwhile noting that the mean advective momentum transport  $T_{adv}$  is not able to convey momentum across a streamline (by definition). Therefore, when looking at the depth-averaged flow streamlines in Figure 4.3, it can be stated that all momentum transfer from the main stream to the primary and secondary gyre (across streamlines) is accounted for by  $T_{sec}$  and  $T_{Rey}$ . This is an important observation for developing 2D modeling concepts. Not only turbulent stresses, but also secondary flow effects should be taken into account when modeling shallow shear flows in two dimensions.

## 4.8 Summary and discussion

Three-dimensional Large Eddy Simulations have been performed to investigate the influence of threedimensionality on quasi-2D turbulence development in shallow shear flows. Additional to the three SLE geometries investigated experimentally in Chapter 3 (Cases 1-3), a SML geometry has been simulated as well for comparison (Case 4). After comparing LES results with the experimental data, it has been clarified how the development of 2DCS depends on resolution as well as on the presence of upstream velocity perturbations. Furthermore, the influence of secondary flow on the shallow mixing layer structure and on lateral transfer of streamwise momentum has been investigated.

It is found that well-developed 3D bottom turbulence is needed to reproduce the correct mixing layer width and large-eddy length scales. If the over-all LES resolution is insufficient, the development of this 3D turbulence should be triggered by a fully developed turbulent inflow boundary condition. However, the sensitivity of Case 4 to upstream turbulence is much larger than for Case 1, 2 and 3. This is explained by the presence of steady gyres in the latter cases, which are responsible for a continuous perturbation of the shallow mixing layer. Such steady recirculations are absent in Case 4, causing this geometry to obey to the linear stability analysis for SML flows as derived by Van Prooijen [99, 101]. A consequence of this analysis is the absence of quasi-2D coherent structures in a completely undisturbed situation. For Case 1-3, such an undisturbed situation is never accomplished. It is concluded that this fundamental difference between SLE and SML flow behavior can be associated with two different mechanisms for the generation of 2DCS, as proposed by Jirka [47]: *topographical forcing* versus *internal transverse shear instabilities* (see Section 2.2.3).

Comparison of PIV and LES data yields a good agreement for time-averaged flow patterns and turbulence length scales, provided that either sufficient resolution has been applied or a proper turbulent inflow boundary condition (Condition A) has been provided. Also, it is confirmed that the emergence of large-scale vortex shedding is associated with the existence and growth of a steady secondary gyre (for SLE flow cases).

Due to the fact that surface PIV measurements and 3D LES computations are very different methods to generate data, it is not straightforward to properly compare the obtained turbulent kinetic energies and Reynolds stresses as well as the associated energy density spectra. The analysis in Sections 4.4.2 and 4.4.3 illustrates a shortcoming of large-scale surface PIV measurements, i.e. the inability to capture small-scale turbulence patterns (scales roughly below the order of the water depth  $H$ ). This however does not disqualify the PIV method to study large-scale patterns, which are captured quite well. Meanwhile LES is a relevant and suitable tool to investigate three-dimensional flow structures in addition to such free-surface measurements, especially when several different LES cases are mutually compared as well.

Pronounced dynamic secondary flow effects are present inside shallow mixing layers for both SML and SLE cases, giving rise to upwelling and downdraft regions near saddle points (in between consecutive 2DCS) in the middle field. The vertical turbulent kinetic energy associated with these secondary flow structures has been successfully scaled with the depth-averaged lateral shear. The residual time-averaged secondary flow patterns are relatively weak. Nevertheless, the contribution of secondary flow structures to the lateral transport of streamwise momentum (also due to mean flow dispersion) is not negligible in shallow shear flows and should be taken into account for 2D modeling purposes.

As lateral transport of streamwise momentum  $T_{xy}$  is a key characteristic of shallow turbulent shear flows, the spatial distribution of the various contributions to  $T_{xy}$  yields a lot of information about mixing layer development and mean depth-averaged flow patterns. In Chapter 5, the basic SLE geometry of Case 2A is systematically adapted in various ways in order to search for possibilities to manipulate the development of quasi-2D turbulence structures. Investigating the spatial structure of  $T_{xy}$  is a helpful tool in order to review the effects of these geometry adaptations.

# Chapter 5

## Influence of geometry variations

### 5.1 Introduction

As a spin-off from the previous LES computations, the original SLE geometry (analyzed in Chapter 4) is adapted in several ways in order to investigate how the emergence of large-scale turbulence is influenced by the horizontal geometry. The basic idea is attempting to manipulate the shape and size of the steady secondary gyre, so that its influence on 2DCS behavior can be analyzed by means of additional LES computations. The geometry variations adopted are mostly inspired by practical solutions which are sometimes encountered on prototype scale, e.g. in groyne fields. Although the flow geometries considered here are schematized and highly idealized, they provide some basic insights about the impact of geometry on quasi-2D turbulence, which are applicable for engineering purposes. The chapter concludes with the description of a practical application, which is an example of a full-scale shallow-flow turbulence problem: the adaptation of a groyne field on prototype scale. This has been a pilot project performed by the Dutch Ministry of Public Works<sup>1</sup>; the author of this thesis contributed to the associated laboratory experiments.

### 5.2 Strategies for geometry adaptations

In Figure 5.1 top views of a series of systematically adapted SLE geometries are shown. These new flow situations have been coined Cases 5 to 17. For all these geometries Case 2A from Chapter 4, depicted in Figure 5.1(a), is the reference case. It should be noted that all sidewalls remain fully vertical and the flume bottom remains horizontal, so that a top view is sufficient to outline each geometry. All flow cases share some basic scales identical to those of Case 2A: water depth  $H = 0.1$  m, inflow width  $B_1 = 1$  m, outflow width  $B_2 = 2$  m, expansion width  $D = 1$  m and mean inflow velocity  $U_0 = 0.30$  m/s. In all new computations, a fully 3D turbulent velocity profile is imposed at the inflow boundary (i.e. Condition A, see Section 4.3). Therefore, the suffix A for the Cases 5-17 will be omitted throughout this chapter.

Panels 5.1(b)-(g) illustrate various strategies to adapt the horizontal geometry in such a way that the secondary gyre could be influenced. In Cases 5-6 (b) a local splitter plate with length  $x_{split}$  is added downstream of the primary separation point, in order to reduce the near-field lateral shear. In Cases 7-8 (c), the space usually taken by the secondary gyre is now filled up by a smoothly contoured solid wall construction in order to “streamline”

---

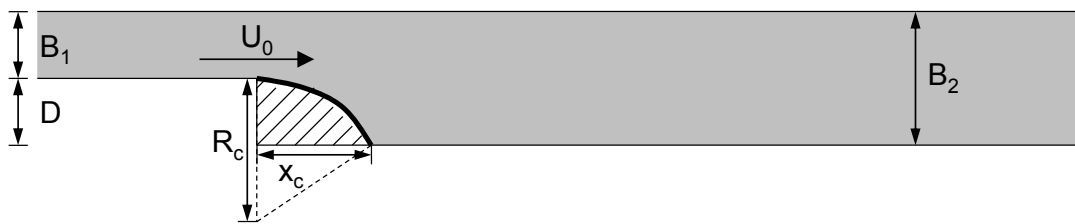
<sup>1</sup>Hydraulic survey “Bord voor de Kop”, performed by Rijkswaterstaat directorate for the Eastern Netherlands (see Sieben [76, 77]).



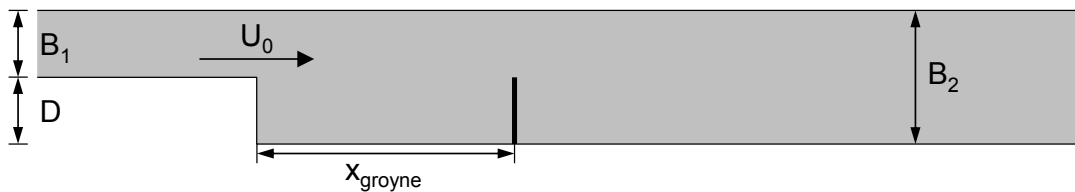
(a) Case 2A (reference)



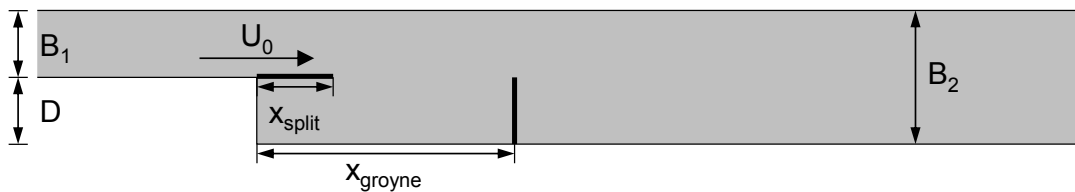
(b) Cases 5-6



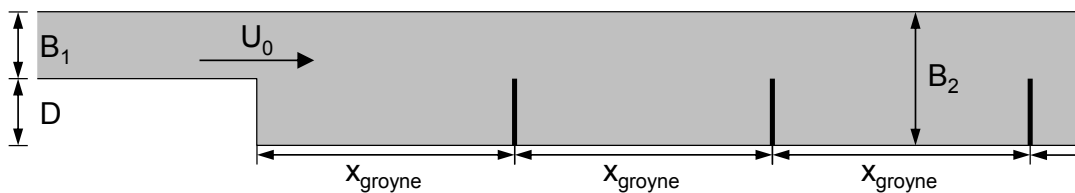
(c) Cases 7-8



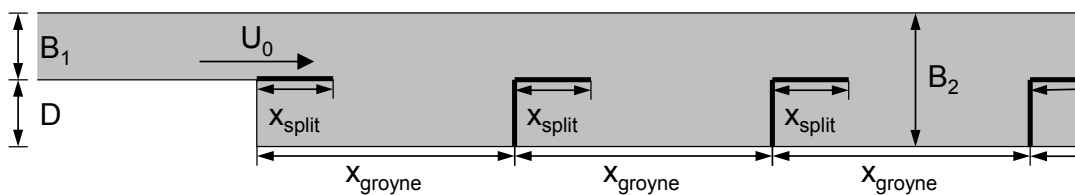
(d) Cases 9-13



(e) Cases 14-15



(f) Case 16



(g) Case 17

Figure 5.1: Schematic outlines of adapted LES geometries (including relevant length scales).



	$x_{split}$ [m]	$R_c$ [m]	$x_c$ [m]	$x_{groyne}$ [m]
Case 5	1.0			
Case 6	3.0			
Case 7		1.0	1.0	
Case 8		5.0	3.0	
Case 9				1.0
Case 10				3.0
Case 11				6.0
Case 12				10.0
Case 13				15.0
Case 14	1.0			3.0
Case 15	1.0			6.0
Case 16				3.0 (7x)
Case 17	1.0 (7x)			3.0 (7x)

Table 5.1: *Variable horizontal length scales in LES cases 5 to 17.*

the expansion area. This circular wall has a radius  $R_c$  and reaches downstream to a point  $x_c = \sqrt{(2DR_c - D^2)}$ . Another option is to compress the steady gyre pattern in streamwise direction (in order to reduce secondary gyre influence) by adding a downstream obstacle, e.g. a single groyne. This is done in Cases 9-13 (d). The groyne field length  $x_{groyne}$  can be varied and influences the effectiveness of the measure. Cases 14-15 (e) are in fact a combination of measures (b) and (d). In Case 16 (f), the effect of a series of 7 groyne fields on the 2DCS development is investigated. Finally, Case 17 (g) is a combination of measures (b) and (f).

Various new horizontal length scales occur in Cases 5-17. The relevant length scales for each case are listed in Table 5.1. By varying these scales, the sensitivity of large-scale turbulence to a certain geometrical adaptation can be estimated. The numerical grid resolution of Cases 5-17 is equal to that of Case 1A (see Table 5.2). For Cases 11-13 and 15, the computational domain length has been extended by 10 m or 15 m in order to have sufficient distance between the most downstream groyne and the outflow boundary.

Although it should be noted that all geometries are idealized (e.g. hydraulically smooth wall conditions, vertical walls and infinitesimally thin groynes), Cases 5-17 can be well compared to Case 2A and mutually. Furthermore, some cases can be considered a superposition of other cases: Case 14 = Case 5 + Case 10, Case 15 = Case 5 + Case 11, Case 16 is a spatial repetition of Case 10 and Case 17 is a repetition of Case 14. In this way the cumulative effect of some combined measures can be assessed as well.

	$L$	$B_2$	$H$	$N_x$	$N_y$	$N_z$	$\Delta x$ [m]	$\Delta y$ [m]	$\Delta z$ [m]	$N_{tot}$
Case 5-10	30	2	0.1	2400	160	32	0.0125	0.0125	0.003125	12,288,000
Case 11-12	40	2	0.1	3200	160	32	0.0125	0.0125	0.003125	16,384,000
Case 13	45	2	0.1	3600	160	32	0.0125	0.0125	0.003125	18,432,000
Case 14	30	2	0.1	2400	160	32	0.0125	0.0125	0.003125	12,288,000
Case 15	40	2	0.1	3200	160	32	0.0125	0.0125	0.003125	16,384,000
Case 16-17	30	2	0.1	2400	160	32	0.0125	0.0125	0.003125	12,288,000

Table 5.2: *Computational mesh sizes for LES cases 5 to 17.*

### 5.3 Geometry variations: 3D LES results

The next subsections discuss the effects of the geometry variations depicted in Figure 5.1 on large-scale turbulence behavior. The following selection of output quantities will be presented, showing relevant quasi-2D and 3D aspects of the 2DCS development:

- Time-averaged stream functions;
- Primary and secondary gyre lengths;
- Development of the mixing layer width;
- Development of conditionally averaged large-eddy length scale;
- Lateral momentum transfer due to mean secondary flow and Reynolds stresses;
- Anisotropy of horizontal turbulent kinetic energy (streamwise/transverse TKE ratio);
- Vertical turbulent kinetic energy (which is a measure of dynamic secondary flow effects inside the mixing layer).

All output results are presented in the order given by the classification of Figures 5.1(b)-(g), i.e. the order of Case labels 5 to 17.

#### 5.3.1 Mean flow patterns

The influence of geometry on the mean flow pattern is illustrated by time-averaged and depth-integrated stream functions  $\bar{\psi}$ . In Figures 5.2–5.3, contour plots of  $\bar{\psi}$  in the region  $-1 < x < 17$  m have been depicted for all flow cases. For comparison the reference Case 2A has been given as well. Furthermore, for Cases 2A and 5-17 the primary and secondary gyre lengths  $L_1$  and  $L_2$  are given by Table 5.3. For Cases 9-17 multiple values of  $L_1$  and  $L_2$  are listed as multiple gyre systems are present.

Comparing Case 5-6 to Case 2A, it occurs that the mean flow pattern is not substantially influenced by the presence of a single upstream splitter plate. The steady gyre pattern basically shifts in downstream direction, over a distance that is approximately equal to  $x_{split}$ . A different behavior is found in Cases 7-8: in both cases, the total reattachment length  $L_1$  shortens compared to reference Case 2A. When the circular contour length  $x_c$  is not taken into account, the shortening is even more pronounced (see Table 5.3). The presence of a secondary gyre depends on the local pressure gradient near the stagnation point  $(x, y) = (x_c, 0)$ , which is determined by the wall curvature  $R_c$ . The small value  $R_c = 1$  m in Case 7 induces an adverse pressure gradient acting against the primary gyre backflow, giving rise to a small secondary gyre. The value  $R_c = 5$  m in Case 8 yields a wall curvature smooth enough to suppress secondary separation. Basically the circular contour in Case 8 fills up the space which would be otherwise taken by the secondary gyre, which implies that  $x_c \approx L_2$ . For even milder a wall curvature (larger values of  $R_c$  and  $x_c$ ), the primary gyre would eventually disappear and the main flow would just broaden in a gradual way; presumably this is the case if  $x_c \approx L_1$ .

Cases 9-13 compared to Case 2A show the impact on the steady gyre pattern when the recirculation area is confined in streamwise direction by a single groyne. In most cases the value of  $L_1$  upstream of the groyne is bounded by the distance  $x_{groyne}$ , except for Case 13 where  $x_{groyne} = 15$  m and  $L_1 = 9.1$  m (close to  $L_1$  in Case 2A). With respect to Case 12, it is striking that  $L_1$  is not limited but even extended by the presence of the groyne at  $x = 10$  m. This is caused by the contraction of the flow bending around the groyne; this contraction interferes with the reattachment process and hinders a normal recovery of the boundary layer. With respect to  $L_2$ , it is observed that for small values of  $x_{groyne}$  (Cases 9 and 10) the near-field secondary gyre is compressed (Case 10) or even non-existent (Case

	Near field		Far field	
	$L_1$ [m]	$L_2$ [m]	$L_1$ [m]	$L_2$ [m]
Case 2A	8.90	2.04		
Case 5	8.9 (= 9.9 - $x_{split}$ )	1.8 (= 2.8 - $x_{split}$ )		
Case 6	9.2 (= 12.2 - $x_{split}$ )	1.6 (= 4.6 - $x_{split}$ )		
Case 7	7.7 (= 8.7 - $x_c$ )	1.0 (= 2.0 - $x_c$ )		
Case 8	4.7 (= 7.7 - $x_c$ )	–		
Case 9	1 (= $x_{groyne}$ )	–	9.6	1.4
Case 10	3 (= $x_{groyne}$ )	1.0	10.4	1.4
Case 11	6 (= $x_{groyne}$ )	2.2	10.9	1.4
Case 12	10 (= $x_{groyne}$ )	1.8	13.0	1.6
Case 13	9.1	1.9	14.6	1.8
Case 14	3 (= $x_{groyne}$ )	1.1	10.1	1.4
Case 15	6 (= $x_{groyne}$ )	3.2	10.9	1.4
Case 16	3 (= $x_{groyne}$ )	1.0	(7x)	(7x)
Case 17	3 (= $x_{groyne}$ )	1.1	(7x)	(7x)

Table 5.3: *Primary and secondary gyre lengths ( $L_1$  and  $L_2$ ) in Cases 5 to 17. If groynes are present, multiple gyre lengths have been listed.*

9). The presence of a nearby groyne gives rise to a pressure gradient in the direction of the primary gyre backflow, counteracting the adverse pressure gradient near the stagnation point at  $(x, y) = (0, 0)$ . For larger values of  $x_{groyne}$  (Cases 11-13), the groyne does not influence the size and intensity of the secondary gyre.

Downstream from the single groyne (far field), an additional recirculation area is present in Cases 9-13. From Figures 5.2–5.3 and Table 5.3, it follows that the far-field values of  $L_1$  consistently increase for increasing  $x_{groyne}$  (even up to  $L_1 = 14.6$  m). This effect is explained once more by flow contraction. As the main flow tends to penetrate into the near-field recirculation area for increasing aspect ratio  $x_{groyne}/D$  of the groyne field (see also Uijtewaal et al. [93]), it subsequently contracts around the tip of the downstream groyne. Due to this contraction the actual main flow width in Cases 9-13 is smaller than  $B_1$  directly downstream of the groyne. This gives rise to larger width of the gyre area and a longer reattachment length; it also causes larger main flow velocities and, hence, a stronger lateral shear and enhanced turbulence intensities. The far-field values of  $L_2$  are only slightly influenced by the value of  $x_{groyne}$ . Compared to the reference Case 2A, Cases 9-11 yield slightly shorter values of  $L_2$  (1.4 m). This can be explained by the increased mixing layer turbulence intensity downstream of the groyne due to the disturbing effect of 2DCS coming from upstream. The slightly larger values of  $L_2$  (up to 1.8 m) found in Cases 12-13 can be ascribed to the effect of flow contraction.

The combination of a groyne with an upstream splitter plate (Cases 14-15) affects the near-field secondary gyre. In Case 14, the secondary gyre is fully sheltered by the splitter plate and does not affect the main flow. The primary gyre with  $L_1 = x_{groyne}$  fills the entire interface between main flow and groyne field; hence, near the apex of the splitter plate the lateral velocity gradient is small. Case 15, on the contrary, exhibits a secondary gyre size similar to Case 5; in those cases, the secondary flow is exposed to the main flow and induces a strong lateral shear near the splitter plate apex. Compared to Case 14,  $x_{groyne}$  in Case 15 is not small enough to compress the secondary gyre pattern (see also Case 11 compared to

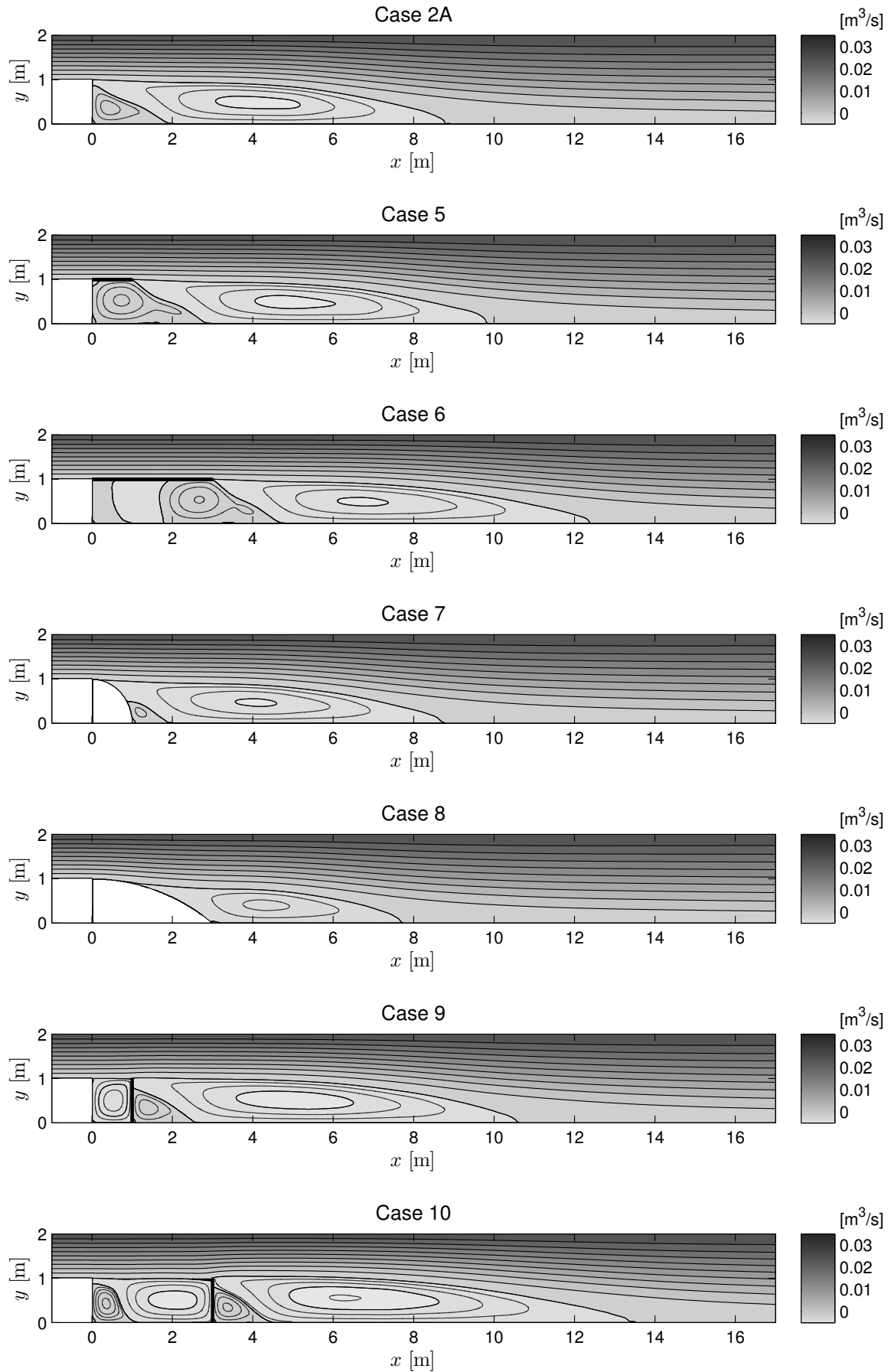


Figure 5.2: Mean depth-integrated stream function of LES Cases 5 to 10, compared to 2A.

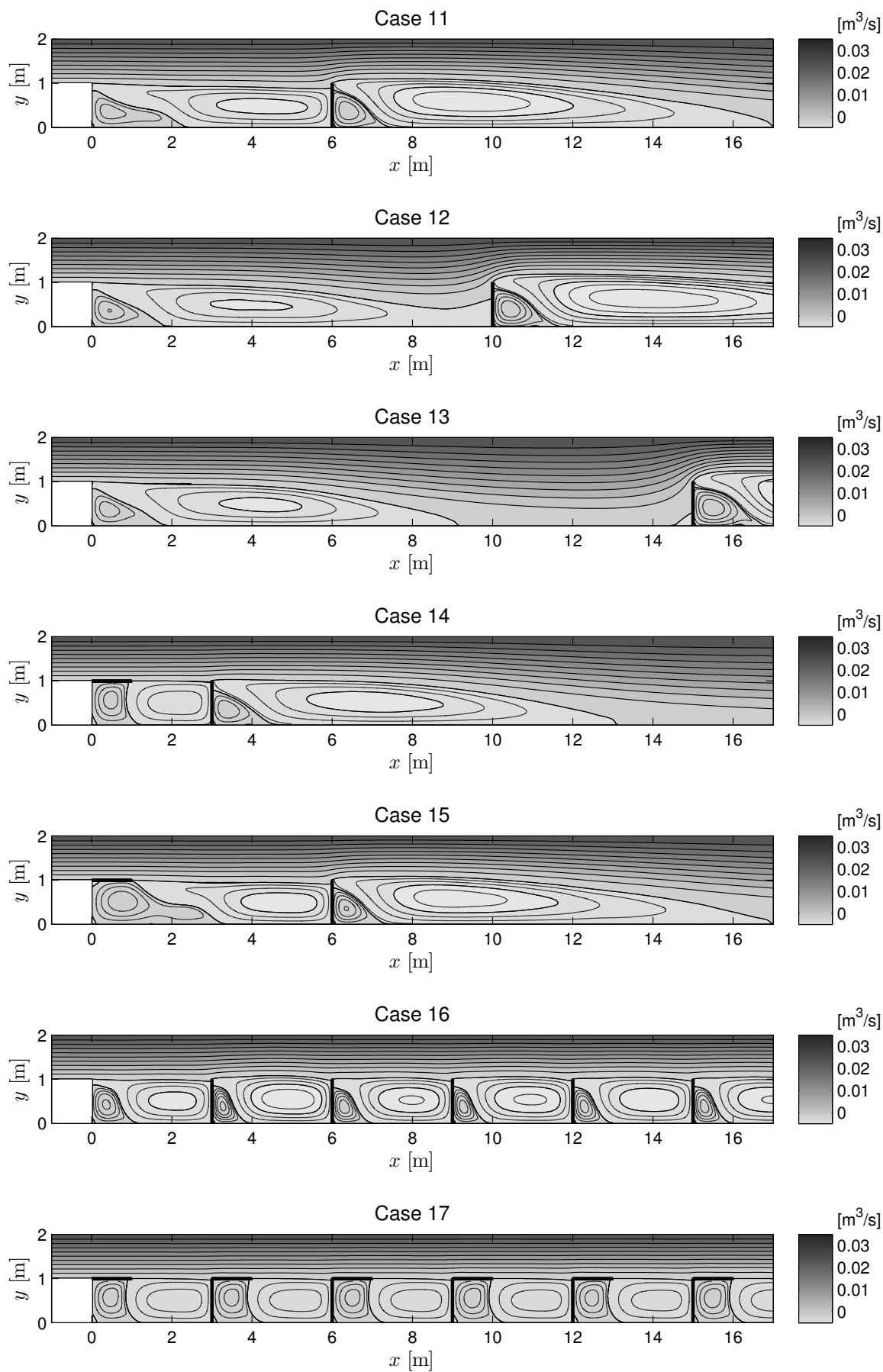


Figure 5.3: Mean depth-integrated stream function of LES Cases 11 to 17, compared to 2A.

Case 10). Apparently a groyne field aspect ratio  $x_{groyne}/D$  in between 3 : 1 and 6 : 1 is the limiting case which determines whether the downstream groyne influences the upstream gyre pattern or not. In the groyne field series of Case 16, the aspect ratio  $x_{groyne}/D$  is 3 : 1 (as it is in Case 10 and 14). The secondary gyre sizes are effectively compressed; a virtually constant value of  $L_2$  is found. At the same time, a slight contraction of the main flow is visible downstream from each groyne (bending streamlines). Finally, Case 17 shows secondary gyres that are fully sheltered by the splitter plates, while the main flow exhibits virtually straight streamlines; no flow contraction is visible here.

### 5.3.2 Horizontal length scales

Figures 5.4 and 5.5 show the streamwise development of two horizontal turbulence length scales: the mixing layer width  $\delta$  and the 2DCS length scale  $\lambda_{eddy}$  respectively, which have the same order of magnitude (see Sections 3.7.2 and 4.4.1). As the first quantity is derived from time-averaging and the second from conditional averaging operations, some differences can be observed. The value of  $\delta$  as a function of  $x$  is given for  $0 < x < 20$  m; values of  $\lambda_{eddy}(x)$  are available only within the domain  $0 < x < 10$  m.

In all flow cases with groynes (Cases 9-17, panels (c)-(f) in both figures),  $\delta$  tends to almost zero directly downstream of each groyne whereas  $\lambda_{eddy}$  remains significantly larger than zero in those regions. This difference between both quantities is explained by their definition. The mixing layer width is defined by the mean local shear, whereas the characteristic large eddy length scale depends on non-local quantities too, e.g. the upstream turbulence level: 2DCS developing in the upstream groyne field can be conveyed along the groyne tip and subsequently trigger the growth of 2DCS downstream of it. In general  $\lambda_{eddy}(x)$  seems to have a practical upper limit  $\approx \delta(x)$ . In Figures 5.5(c)-(f),  $\lambda_{eddy}$  reaches a local maximum directly upstream of each groyne and a local minimum directly downstream of it.

Both  $\delta$  and  $\lambda_{eddy}$  have a similar near-field growth rate, proportional to  $\approx 2\alpha$  (see Sections 3.5 and 4.4.1). In Figures 5.4-5.5, the theoretical mixing layer growth rate according to Van Prooijen [99] and its near-field trend line have been indicated. Compared to Figures 4.5 and 4.6, a larger section of the far field is shown here. Figure 5.4 shows that all cases (except the groyne field Cases 16-17) have an identical far-field limit of the mixing layer width, equal to  $\delta_\infty/D \approx 0.8$ . This restriction is due to the flume width  $B_2$ . The middle-field growth rate of  $\lambda_{eddy}$  is observed to be slightly lower than for  $\delta$ ; on the other hand,  $\lambda_{eddy}$  still increases near  $x/D = 10$  and has not yet reached a far-field limit (Figure 5.5). Cases 5-8 show values of  $\delta(x)$  and  $\lambda_{eddy}(x)$  close to reference Case 2A; in Case 5 and 6, these profiles are shifted downstream over a distance  $x_{split}$  as expected. Cases 9-13 exhibit a near-field length scale growth, a sudden break-down near the groyne tip (as not all 2DCS kinetic energy can pass along the groyne) and a far-field recovery. From Figures 5.4(c)-(f), it occurs that for  $x_{groyne}/D < 6$  the mixing layer width  $\delta$  does not reach its far-field limit. Especially when the secondary gyre size is compressed (e.g. Cases 10 and 14), the near-field mixing layer growth is reduced. The groyne-field Cases 16-17 show far-field limits for  $\delta$  and  $\lambda_{eddy}$  that lie consistently below all other cases.

### 5.3.3 Lateral momentum transfer

In analogy with Section 4.7, Figures 5.6-5.7 show the contributions of time-averaged secondary flow ( $T_{sec}$ ) and horizontal Reynolds stress ( $T_{Rey}$ ) to the transverse exchange of streamwise momentum  $T_{xy}$ . Compared to Figures 4.20 and 4.21, these transport quantities are given here in a more concise way. The mean depth-averaged advective transport

$T_{adv}$  has been omitted and no transverse profiles of  $T_{sec}$  and  $T_{Rey}$  are given; instead, both quantities are given as a function of  $x$  along the mixing layer. The maxima of  $T_{Rey}$  are situated along the mixing layer center line, whereas maxima of  $T_{sec}$  profiles are located near the high velocity side of the mixing layer, especially in the near-field region where entrainment plays an important role (see Section 4.7 and Schnauder et al. [74]). The vertical scaling of Figures 5.6 and 5.7 is identical, so that  $T_{sec}$  and  $T_{Rey}$  are easily compared.

The Reynolds stress profiles of Cases 5-17 depicted by Figure 5.6 all exhibit a near-field peak and a far-field decaying behavior, in accordance with the LES results of reference Case 2A (see e.g. Figure 4.7). The local level of  $T_{Rey}$  depends on local lateral shear and the upstream turbulence level (non-local). Case 5 and 6 show a downstream shift of the  $T_{Rey}$  profiles over a distance  $x_{split}$ . A slightly smaller shift is found for Case 7 and 8 due to the presence of the circular wall contour. As the secondary gyre is absent in Case 8 (but flow separation still occurs), the near-field lateral shear is smaller than for the reference case, resulting in a slight decrease of the Reynolds stress peak.

The large peak values found for Cases 9-13 have two causes. Firstly, 2DCS from upstream trigger the growth of 2DCS downstream of the groyne. Secondly, especially for Cases 11-13, main flow contraction plays an important role. This contraction causes higher main flow velocities, inducing enhanced lateral shear and hence higher levels of TKE and  $T_{Rey}$ . The results for Cases 14 and 15 show that the presence of a splitter plate mainly affects the mixing layer upstream of the groyne. Compared to Case 10, Case 14 exhibits a considerable decrease of  $T_{Rey}$  for  $0 < x < 3$  m. This is explained by the breakdown of the lateral shear, as the secondary gyre is fully sheltered by the splitter plate. Case 15 shows no decrease of  $T_{Rey}$ , only a downstream shift comparable to Case 5. In this case the near-field lateral shear is not influenced by the groyne. The groyne-field Case 16 exhibits a sequence of near-field  $T_{Rey}$  peaks, slightly enhanced by main flow contraction. Finally, for Case 17 (with sheltered secondary gyres) the flow contraction effect is absent and 2DCS growth is limited due to the small lateral shear, resulting in  $T_{Rey}$  peaks that lie consistently below all other cases (including the reference Case 2A).

Compared with Figure 5.6, Figure 5.7 shows near-field values for  $T_{sec}$  that are much smaller than the near-field maxima for  $T_{Rey}$  inside the mixing layer. This underlines the quasi-2D character of these shallow shear flows. In the far field, values of  $T_{sec}$  are approximately equal to  $T_{Rey}$ . As explained in Section 4.7, these far-field values of  $T_{sec}$  are mainly accounted for by dispersion due to velocity variation over the water depth (logarithmic velocity profile) combined with the effect of a broadening and decelerating main flow. Apart from this dispersive contribution, dynamic secondary flow effects are small in the greater part of the domain of Cases 5-17. An important exception are obviously the large peaks in  $T_{sec}$  directly downstream of each groyne (Cases 9-17). These peaks are accounted for by considerable spiral flow around each groyne tip (“horseshoe vortex”). Mainly due to flow contraction and strong lateral shear (combined with velocity variations over the water depth),  $T_{sec}$  makes a significant contribution here to the entrainment of mass and momentum into the mixing layer behind a groyne.

### 5.3.4 Horizontal anisotropy

For the sake of brevity, no longitudinal profiles of the streamwise and transverse TKE ( $\overline{u'u'}$  and  $\overline{v'v'}$ ) are shown in the present sections. These quantities follow the same trend as the horizontal Reynolds stress  $T_{Rey} = \overline{u'v'}$  depicted in Figure 5.6, although the peak values of  $\overline{u'u'}$  and  $\overline{v'v'}$  are somewhat higher (see also Figure 4.7). In order to illustrate the anisotropy of horizontal turbulence intensities, the ratio  $\overline{u'u'}/\overline{v'v'}$  along the mixing layer center line

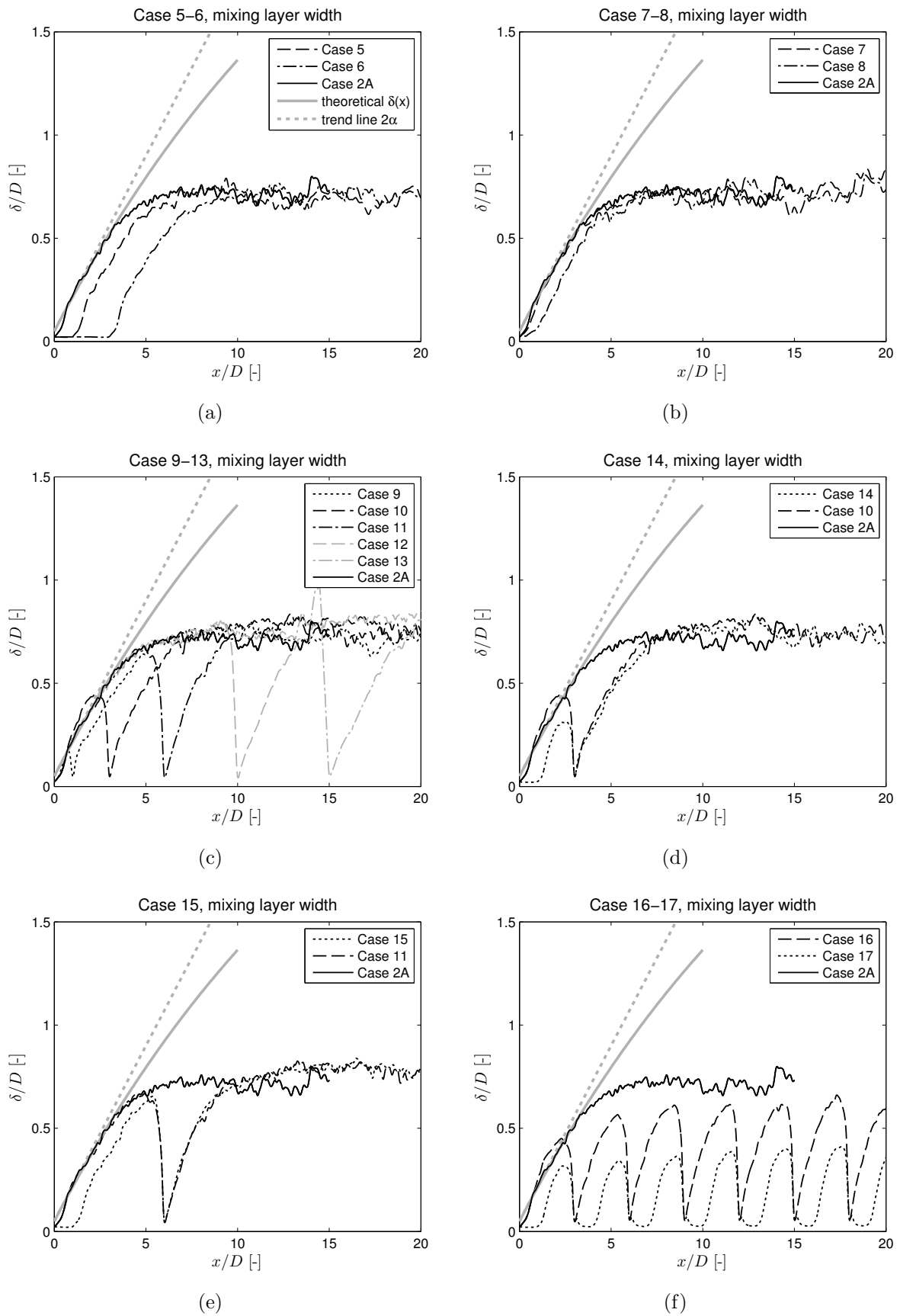
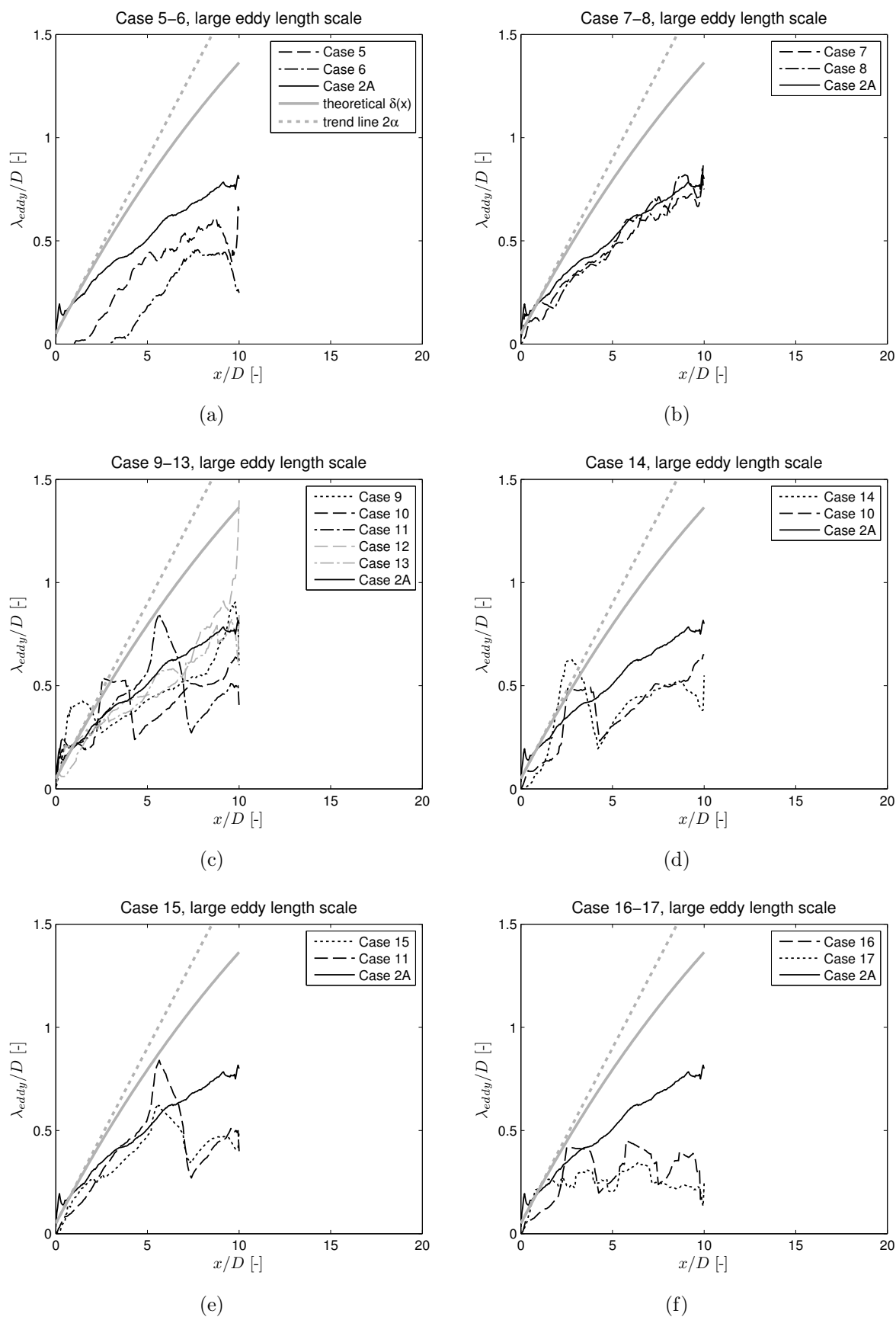


Figure 5.4: *Mixing layer width  $\delta(x)$  for Cases 5-17.*



Figure 5.5: Large eddy length scale  $\lambda_{eddy}(x)$  for Cases 5-17.

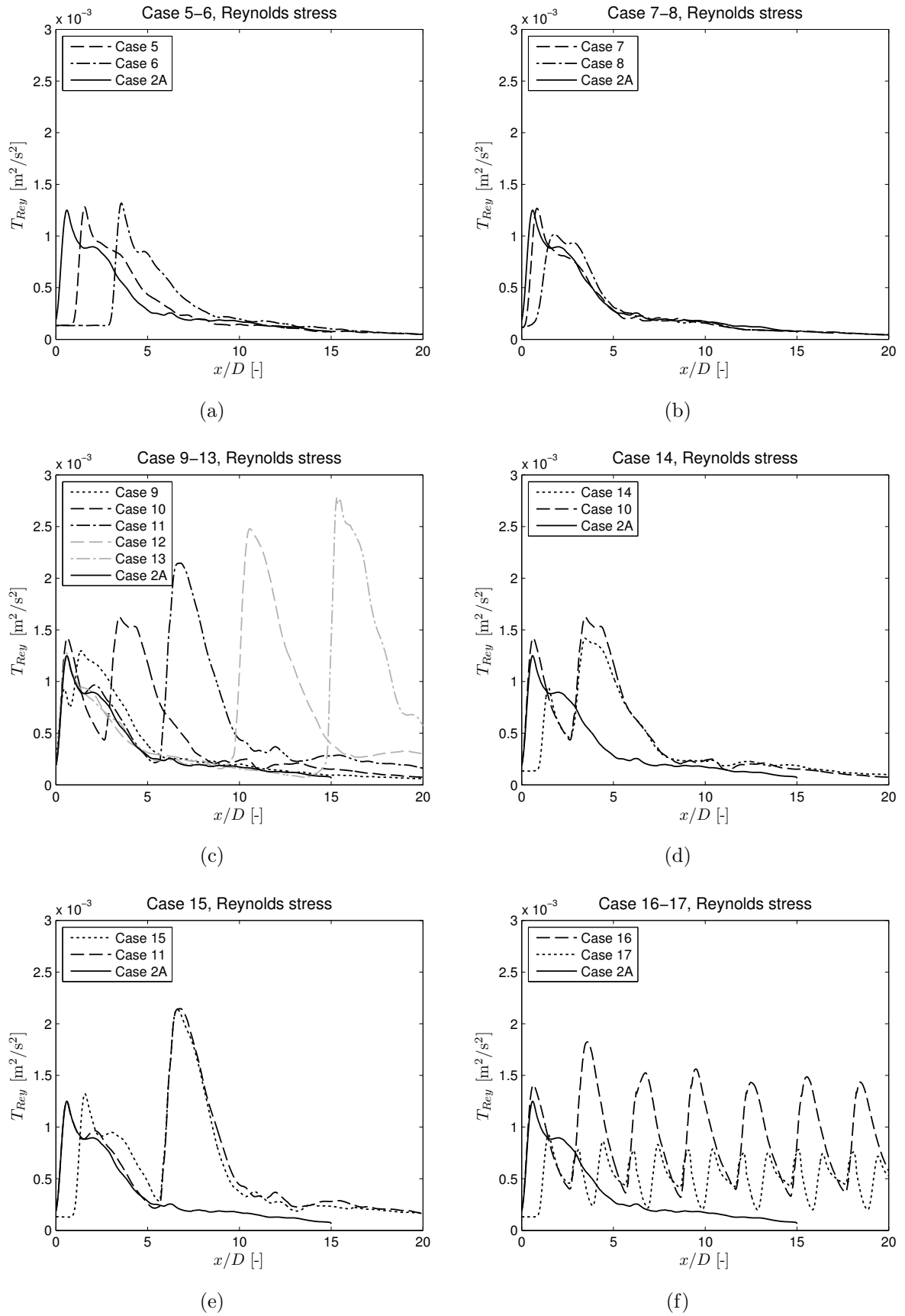


Figure 5.6: Lateral momentum transport by Reynolds stress  $T_{Rey} = \overline{u'v'}$  for Cases 5-17.

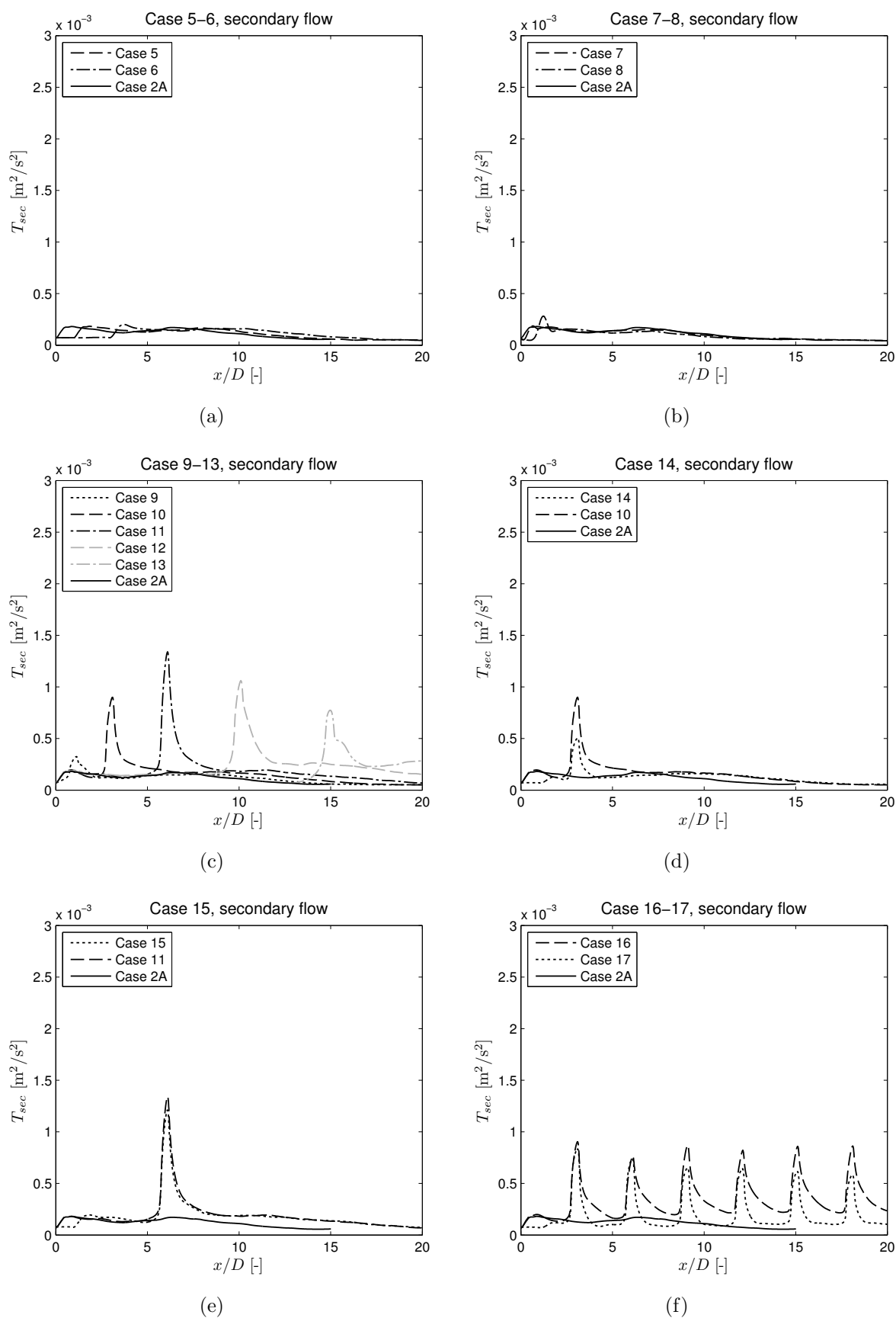


Figure 5.7: Lateral momentum transport by secondary flow  $T_{sec} = \overline{u''v''}$  for Cases 5-17.

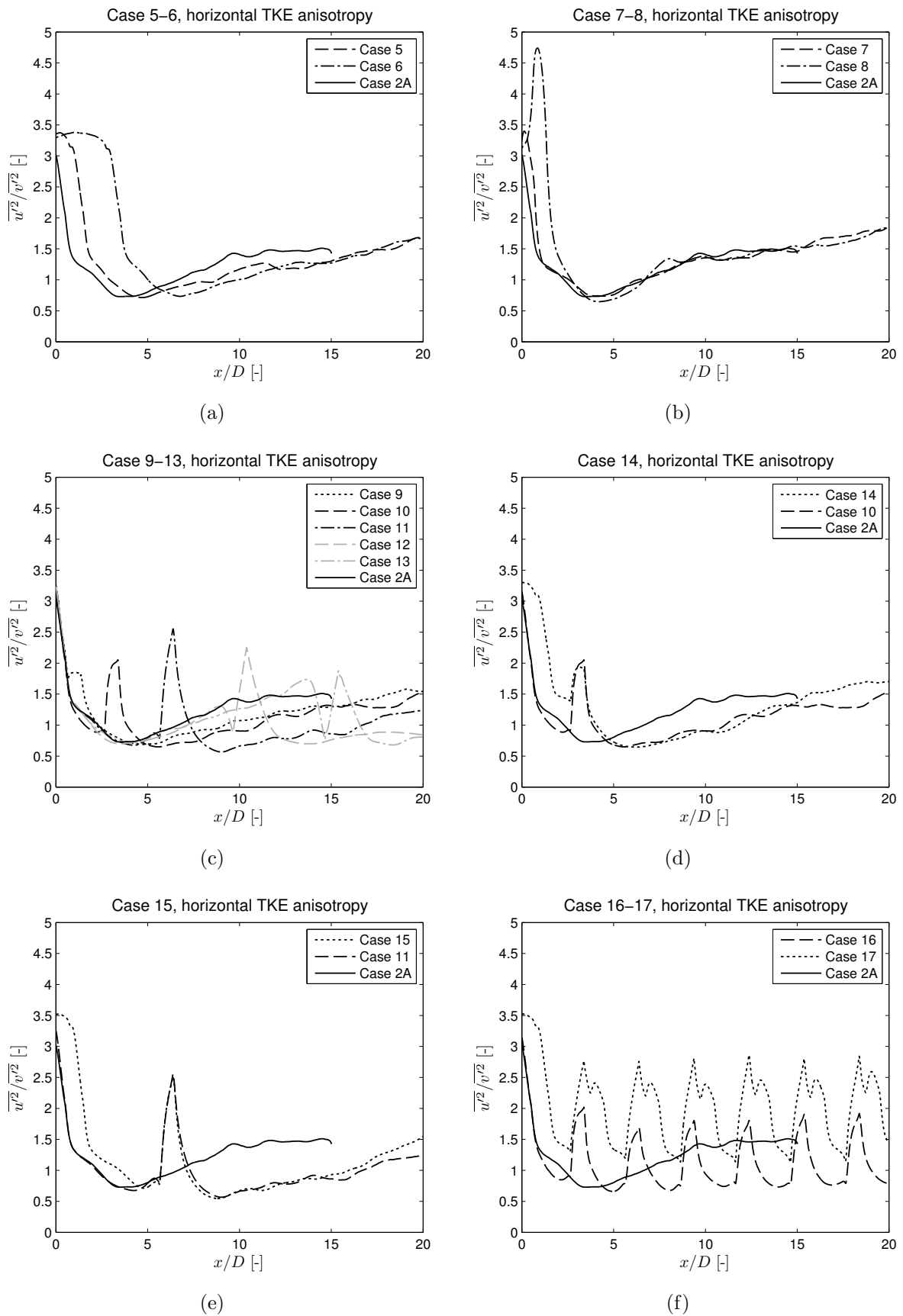


Figure 5.8: Anisotropy of horizontal TKE  $\overline{u'u'}/\overline{v'v'}$  for Cases 5-17.

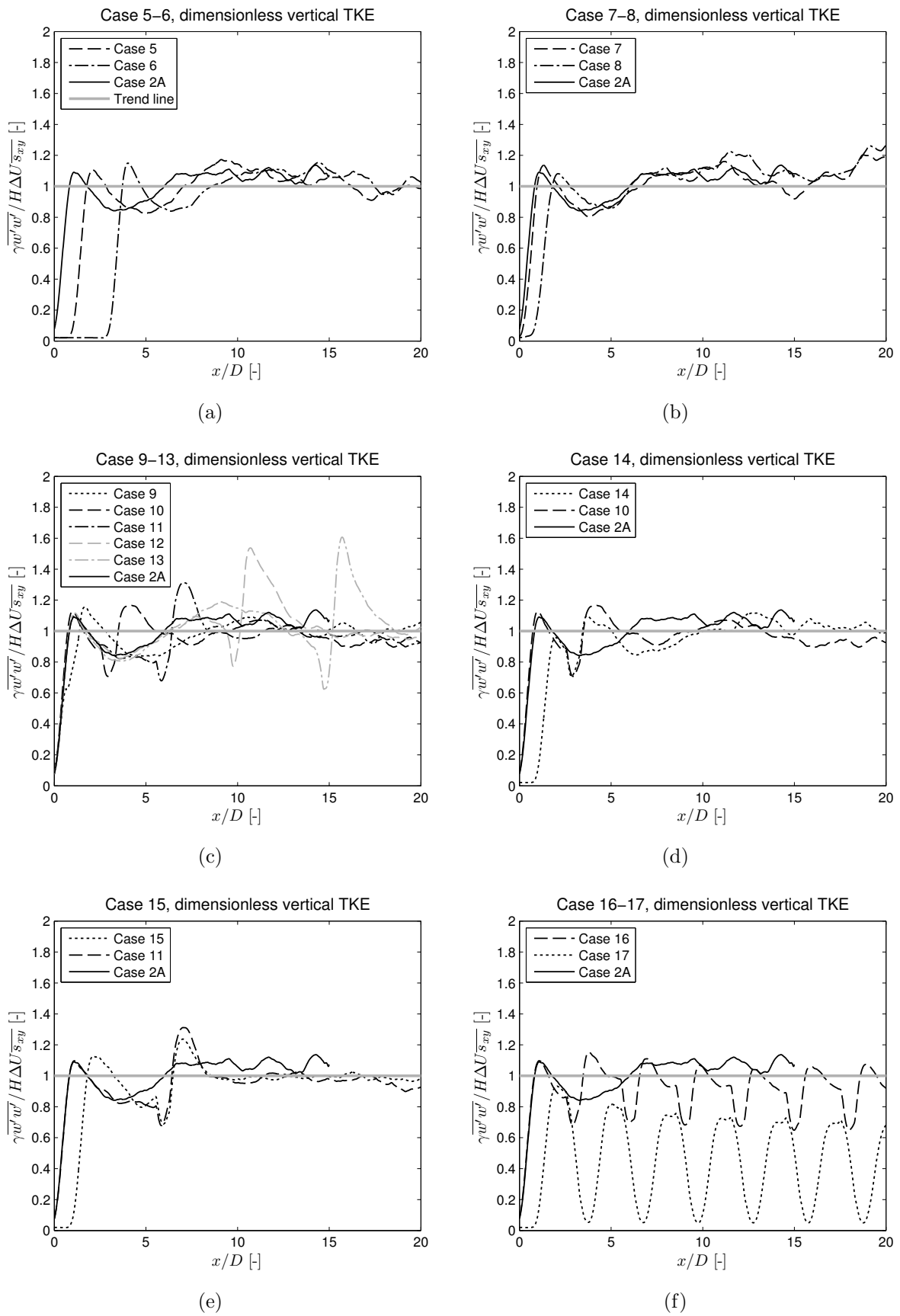


Figure 5.9: Dimensionless vertical TKE  $\overline{\gamma w'w'}/H\Delta U\tilde{s}_{xy}$  for Cases 5-17.

is shown in Figure 5.8 (see also Figure 4.16). The trend from anisotropy toward more isotropy for Case 2A, depicted in Figure 4.16(b), is also visible for Cases 5-17.

All cases consistently show a near-field value of  $\overline{u'u'}/\overline{v'v'}$  within the range 3–4. A global minimum is located approximately at 2–3 m downstream of each separation point, indicating a growing isotropy of the large energy-containing turbulence scales. This development is governed by the widening of the mixing layer and the transfer of small-scale TKE to larger (quasi-2D) length scales, as well as the disturbing influence of the steady gyre pattern (gyre-vortex interaction). It is striking that all cases with groynes (Cases 9-17 in Figures 5.8(c)-(f)) show pronounced peaks directly downstream of each groyne. The near-field anisotropy of the 2DCS is restored here, under the influence of both contraction and strong lateral shear. These peaks are always lower than the near-field global maximum of  $\approx 3-4$ , which indicates that (isotropic) 2DCS from upstream are penetrating into the downstream mixing layer and hinder the full recovery of anisotropy.

After the emergence of isotropy due to 2DCS growth, all far fields of Figure 5.8 (except groyne-field Cases 16-17) exhibit a gradual recovery of TKE anisotropy in downstream direction, up to  $\overline{u'u'}/\overline{v'v'} \approx 2$  for Case 2A. This is explained by a gradual large-eddy decay, after which the turbulent flow will gradually evolve toward a uniform channel flow with weaker 2DCS (secondary instability of base flow, see Jirka [47] and Moser et al. [61]). Such a uniform channel flow is known to include a ratio  $\overline{u'u'}/\overline{v'v'}$  that is approximately  $\approx 3-4$  (see e.g. Nezu and Nakagawa [66] and Pope [71]). In the results of Cases 16-17, this far-field anisotropy is prohibited by the sequence of groyne fields, repetitiously enforcing a trend toward more isotropy. Nevertheless, also in these groyne-field cases the near-field anisotropy remains significant.

### 5.3.5 Vertical turbulence intensities

In analogy with Figure 4.18, the maximum vertical turbulent kinetic energy along the mixing layer is shown in Figure 5.9. For Case 2A the vertical TKE  $\overline{w'w'}$  yields more significant information about the vertical flow structure than the time-averaged residual vertical (secondary) velocity  $\tilde{w}$ , which is rather weak inside the mixing layer (see Figure 4.17); this holds for Cases 5-17 as well. The vertical TKE is presented here in dimensionless form according to Equation (4.28), taking again  $\gamma = 60$ ; in this way the vertical turbulence intensity can be scaled with the local lateral shear  $\tilde{s}_{xy}$  inside the mixing layer.

From Figure 5.9, it is observed that the dimensionless quantity  $\gamma\overline{w'w'}/H\Delta U\tilde{s}_{xy}$  is close to a far-field trend line  $\approx 1$ . Cases 5-8 (without groynes) show a rather satisfactory agreement with this limit, whereas the local presence of groynes in Cases 9-16 induces deviations from the trend line (presumably due to the presence of horseshoe vortices, see Section 5.3.3). These observations hold for all cases except Case 17, where the combination of short groyne fields ( $x_{groyne}/D = 3$ ) and near-field splitter plates hinders the full spatial development of dynamic secondary flow. In this case, the relatively small lateral shear along the interface between main flow and groyne fields causes a reduction of vertical (secondary) turbulence intensity.

## 5.4 Review of geometry variations: effectiveness

Based on the results presented in Figures 5.2 to 5.9, the various strategies presented in Section 5.1 for the manipulation of 2DCS development by adapting the horizontal flow geometry can be reviewed for their effectiveness. The following conclusions can be drawn:

- *Case 5-6.* It is concluded that the addition of a stand-alone splitter plate of arbitrary length  $x_{split}$  has no effect on 2DCS development. The near-field region sheltered by the splitter plate becomes a large dead zone and does not contain the full steady secondary gyre. The “equilibrium gyre pattern” of Case 2A simply shifts in downstream direction, maintaining its large near-field lateral shear. No significant change of any relevant turbulence quantity has been observed.
- *Case 7-8.* Filling up the region of a secondary gyre by a “streamlined” solid sidewall has only a limited influence on 2DCS development. Slightly lower turbulence intensities and horizontal Reynolds stresses are found in these cases, whereas all turbulence length scales remain unchanged. Although the secondary gyre is significantly weaker than in the reference case or even absent, the near-field lateral shear hardly decreases. In combination with the disturbing presence of the primary gyre (gyre-vortex interaction), the shallow mixing layer development is virtually identical to that of Case 2A. A real reduction of turbulence intensities and length scales is only achieved if the contour length  $x_c$  is chosen very large so that the primary gyre size becomes considerably smaller. In the most extreme case, no flow separation will occur at all. In real-life engineering practice, however, it is unfeasible (and undesirable) to streamline every shallow flow in such a way that separation would be prohibited.
- *Case 9-13.* Systematic variation of groyne field length  $x_{groyne}$  shows that a single groyne influences the upstream gyre pattern and mixing layer development up to a certain distance. Based on the observations made in this chapter, this limit lies within the range  $3 < x_{groyne}/D < 6$ . A confinement of the recirculation area in streamwise direction effectively compresses the steady gyre pattern, giving rise to a smaller final mixing layer width  $\delta$ ; the horizontal Reynolds stress is however hardly influenced. A reduction with respect to  $\delta$  is especially observed for Case 10 ( $x_{groyne}/D = 3 : 1$ ), whereas downstream contraction and consequently enhanced TKE and Reynolds stress levels remain limited in this case. Groyne field aspect ratios of  $\approx 3 : 1$  are often found along low-land rivers; we may conclude that such a ratio makes sense, in spite of the much greater complexity of environmental river flow geometries.
- *Case 14-15.* A combination of an upstream splitter plate and a downstream groyne yields the greatest impact on 2DCS development, provided again that the groyne field length is not too large:  $x_{groyne}/D < 6$ . Case 14 is a combination of Cases 5 and 10; in this case the upstream lateral shear is strongly reduced and the shallow mixing layer development is effectively hindered. With respect to Case 15 (a combination of Cases 5 and 11), it is observed that a groyne field aspect ratio of  $6 : 1$  is actually too large to have an impact on the secondary gyre.
- *Case 16-17.* A drawback of groynes worth noticing is the following point: although mixing layer development inside the upstream groyne field can be effectively controlled (e.g. Cases 10 and 14), turbulence intensities downstream of this groyne can be strongly enhanced by both flow contraction and the triggering effect of upstream large-scale turbulence. Hence, the “problem” (i.e. undesirably large turbulence length scales and/or energy content) shifts in downstream direction. Obviously, this is only a problem if it is aimed to reduce the influence of large-scale turbulence. A remedy often used in this case is the construction of long sequences of groynes in order to keep the large-scale turbulence development in each groyne field within certain bounds, as has been done in Case 16. The results for Case 17 presented in Figures 5.4-5.9 indicate that the combination of such groyne sequences with upstream splitter plates is very effective for the reduction of quasi-2D turbulence length scales and energy levels.

It must be emphasized that all geometries considered here are idealized and hence quite different from realistic shallow-flow situations like a separating river flow. Nevertheless, some of the conclusions drawn above have a generic character.

The intensity of 2DCS development in a mixing layer is strongly correlated to near-field lateral shear directly downstream of the separation point. Especially the combination of a large near-field shear and a steady primary gyre further downstream (interacting with the mixing layer) may induce large length scales and energy content of 2DCS. Regardless of geometrical details, it can be stated that the confinement of shallow recirculation areas has a mitigating influence on 2DCS development, in particular if this confinement can be combined with a measure to reduce the upstream lateral shear. This can be done by somehow weakening the secondary gyre or by sheltering it from the main flow, such that the largest near-field lateral velocity difference is removed from the flow situation. These conclusions are illustrated by the observation that Case 14 and Case 17 are the most effective geometry adaptations to control large-scale turbulence development.

These conclusions have been kept in mind while performing a laboratory experiment on groyne fields which contained some analogy with the idealized geometries of 3D LES Cases 14 and 16/17. In the next section the results of this experiment and its context are described.

## 5.5 Application to groyne fields: experimental data

The main purpose of this chapter is to assess the effects of geometry variations on large-scale flow and turbulence patterns. So far, we have adopted idealized laboratory geometries: hydraulic smooth wall conditions, a fixed horizontal bottom and vertical sidewalls (which actually imply infinitely thin groynes). It is a challenge to apply the insights stemming from previous sections to a real-life shallow-flow situation. This is not straightforwardly done as the associated flow geometries are more complex with respect to e.g. bathymetry and roughness. Especially 3D flow effects like secondary flow play a more prominent role due to this enhanced complexity.

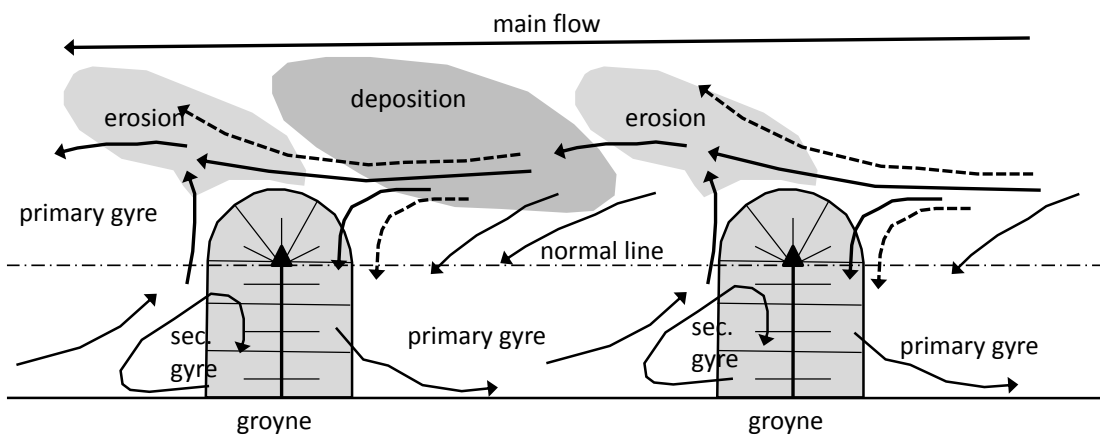
This section presents and discusses a practical test case: a geometry adaptation in a realistic groyne field flow. Experimental data on both laboratory scale and prototype scale are presented. No additional LES data have been generated, as the LES implementation adopted in this thesis is not suitable for modeling the complex geometry of the present test case (especially not on prototype scale). The experimental data presented here stem from a pilot project that the author of this thesis made a contribution to; this pilot project was initiated by the Dutch Ministry of Public Works<sup>2</sup>, which will be abbreviated RWS throughout this section. The full results of the pilot project are reported by Sieben [76,77]. Effects of the geometry adaptation on both 3D and quasi-2D flow as well as bed morphology are presented.

The dynamics of groyne fields along lowland rivers are a relevant test case for civil engineering practice. Their complexity involves e.g. large variations in bathymetry, discharge and hydraulic roughness, the interaction of flow dynamics with bed morphology and the presence of sloping groynes. Especially the latter can have an impact on the emergence of 2DCS and their interaction with steady gyres inside a groyne field. Last but not least, the differences between laboratory-scale and field-scale results can be significant; at present, it is not possible in practice to assess these differences by means of Large Eddy Simulations, as the computational cost of LES on field scale is usually far too demanding. In order to gain reliable insights into field situations, it is preferable to acquire both laboratory-scale

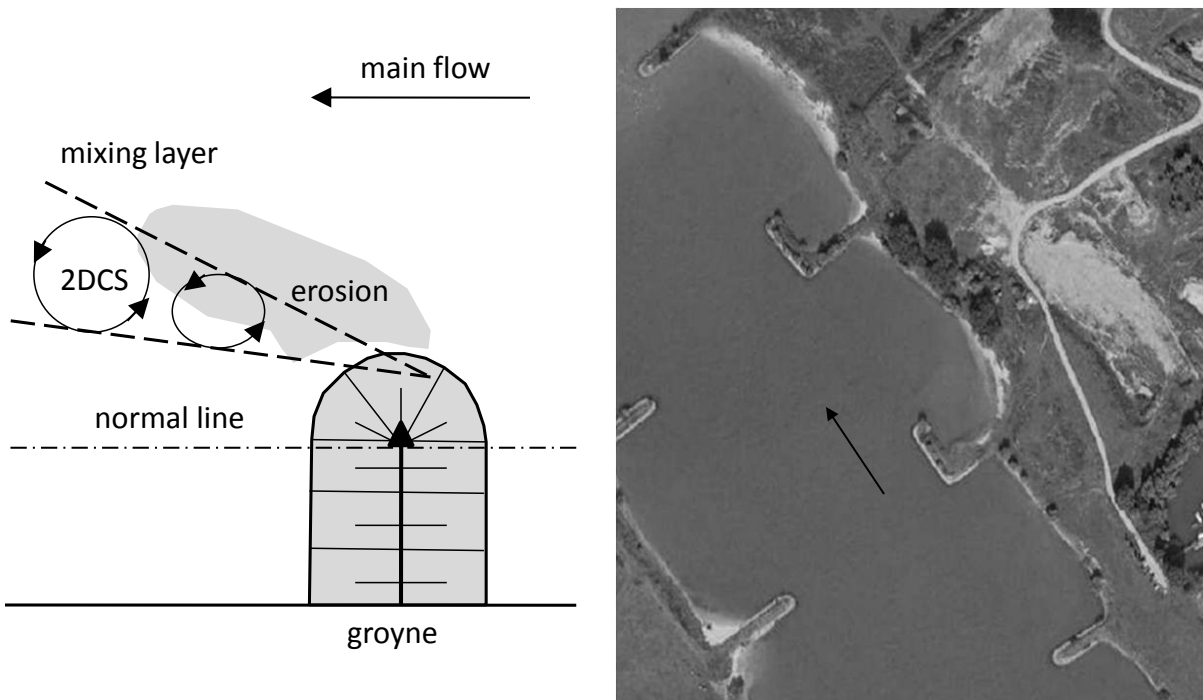
---

<sup>2</sup>Rijkswaterstaat directorate for the Eastern Netherlands.



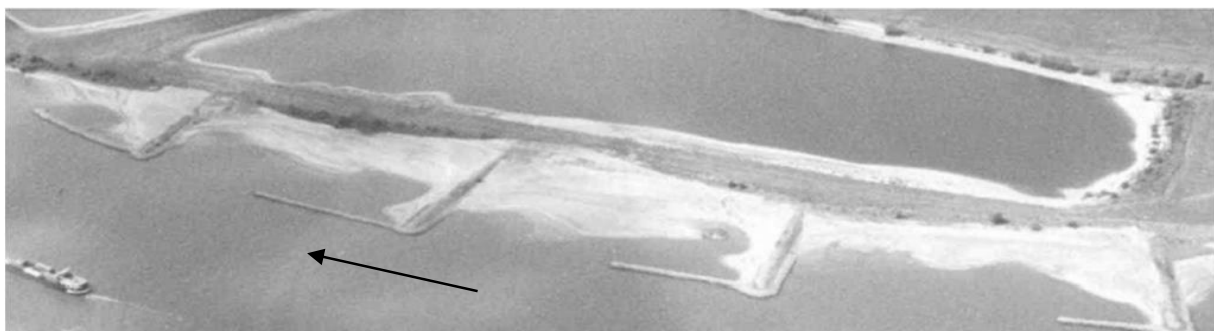


(a) Characteristic flow and morphology patterns induced by sloping groynes.



(b) Inclined mixing layer from groyne tip.

(c) Extended groyne heads (Pannerdensch Kanaal).



(d) Extended groyne heads near Sint Andries (River Waal).

Figure 5.10: *Impact of groynes on flow and turbulence patterns (and a possible geometry adaptation which is similar to LES Case 17).*

data (either experimental or computational) and field data; from the combination of both, conclusions must be drawn with the use of expert judgment.

The pilot project initiated by RWS has investigated the influence of a splitter plate (placed in front of a groyne head) on downstream flow dynamics and morphology along the interface between river and groyne field. Field data have been generated in the Dutch River Waal, along a groyne field near the village of Brakel, which was monitored by RWS in the period between August 2006 and September 2009. Results are reported in [77]. It has been concluded that the splitter plate near the groyne tip regulates both mean flow and turbulence patterns, which has an advantageous effect on river morphology and hence the navigation channel depth.

Anticipating on the field experiment, orientating laboratory experiments on a groyne field series were conducted by Wageningen University and Delft University of Technology. The latter experiment<sup>3</sup> has been conducted in the experimental flume used before in Chapter 3, applying qualitative flow visualization techniques (dye injection and seeding with tracer particles, see Section 3.3.1); it was coined *Hydraulic Survey “Bord voor de Kop”*<sup>4</sup>. Results have been reported in [76].

Although originally designed to regulate the flow field (e.g. on behalf of navigation depth) and to keep river beds at a fixed location, groynes have a profound impact on local river morphology as well. This influence is obvious from abundant field data of lowland-river bottom levels. A regular pattern of alternating scour holes and deposition areas (see Figures 5.10(a) and 5.14(c)-(d)) is often found in the neighborhood of the *normal line* (i.e. the imaginary line that connects the groyne heads and virtually marks the border between main channel and groyne fields). The combination of shallow-flow separation (inducing the shedding of 2DCS) and deformation of the flow field by the sloping groyne head results in quite a complex flow pattern, which impacts the bottom level in turn.

Figure 5.10(a) outlines a typical flow pattern that is found in groyne fields along lowland rivers in the Netherlands. The flow field near the free surface has been indicated by solid lines; the dashed lines represent flow directions near the bottom. (The normal line is given by the dash-dot line.) When passing a groyne the main flow contracts and accelerates, giving rise to a region of erosion. Further downstream the flow widens again, which leads in turn to deceleration and deposition of the eroded material. This process of repetitive main flow contraction and widening is also visible in the streamline patterns of LES Cases 10-16 (see Figures 5.2-5.3). It is recognized by Sieben [77] as the primary cause of scour and deposition patterns found along groyne fields. Besides this, a number of secondary causes are discerned by [77]:

1. Flow contraction past each groyne (in combination with the vertical gradient of streamwise velocity) gives rise to a horseshoe vortex (see Figure 5.7) around the toe of the entire groyne head, which is responsible for the import of sediment from the scour hole into adjacent groyne fields. Sometimes the horseshoe vortex tends to undermine the groyne toe.
2. Due to the groyne tip slope (which is typically of the order 1 : 3), flow contraction near the bottom is relatively strong: transverse velocities toward the river axis are slightly larger than near the surface. This leads to a distortion of velocity profiles in transverse direction and induces an even intensified horseshoe vortex, which enhances

---

<sup>3</sup>The experiment was performed by the author of this thesis and W.S.J. Uijttewaal in cooperation with J. Sieben and fellow-workers from RWS.

<sup>4</sup>“Bord voor de Kop” is a Dutch word play: it can be interpreted as “splitter plate in front of a groyne tip”, as well as “limited vision due to pride or prejudice”.

the primary erosion process. The spiral flow points toward the river axis near the bottom and toward the river bank near the free surface.

3. Finally, the well-known process of flow separation and quasi-2D vortex shedding is present. Due to main flow contraction and depth differences between main channel and groyne fields, the character of 2DCS in groyne field flow is different from the situation in a Shallow Lateral Expansion (SLE). It is often observed (see Figure 5.10(b)) that the shallow mixing layer is not fully parallel to the normal line but is inclined toward the river axis, making an angle of approximately 20-30° with the normal line. Due to this inclination and the fact that groyne fields are often more shallow than the main channel, there exists a “sheltered” room for 2DCS to develop directly downstream of the groyne tip, while staying in place under the action of both the separating main flow and the secondary gyre (opposite forces). When the eddy has grown sufficiently in size to sense the main flow and primary gyre, it is shed from the groyne tip and is entrained into the shallow mixing layer. This type of vortex shedding has been coined *direct vortex shedding* in Section 2.4. Although this mechanism has not been observed within the PIV and LES data on the SLE geometry presented in previous chapters (see Section 3.8), it is often found in groyne field data, especially in the presence of groyne head slopes; see e.g. Uijttewaal et al. [90,93], Van Schijndel and Jagers [103] and Yossef [119]. The shedding of 2DCS enhances bottom friction inside the mixing layer and contributes to local erosion. The inclination of the scour hole is therefore roughly aligned with the mixing layer inclination from the normal line.

Due to the combination of main-flow contraction and the dynamic vortex shedding process described above, considerable transverse velocities are often found directly downstream of each groyne head (see [77]). Fluid from the primary gyre is virtually “launched” into the inclined mixing layer here, in a very concentrated manner (see Figures 5.10(a) and 5.14(a)), while the widening flow further downstream feeds the primary gyre with mass and momentum over the full length of the groyne field. The impact of navigation and high-water (flood wave) circumstances on groyne field dynamics is briefly described by [77], but is not included in the present discussion.

Based on the above observations, it has been conjectured that preventing contraction of the separating flow near groyne heads should result in less complex flow dynamics and hence a smoother bottom level (reduction of erosion and deposition areas). Innovative ideas to improve the normalizing function of groynes (thus reducing maintenance and dredging costs) have been collected by RWS within the context of the project *Innovative groynes* and the design contest *Groynes of the Future* (see [104]).

Various pilot projects involving groyne field adaptations have been initiated along Dutch rivers in order to test such innovative concepts. Along the river Neder-Rijn the effect of a complete groyne field closure is currently investigated. Along the River Waal (near Sint Andries) and Pannerdensch Kanaal (near Huissen) groyne heads have been extended in perpendicular direction (parallel to the normal line) in order to prevent near-field flow contraction and vortex shedding, see Figure 5.10(c)-(d). This type of solution is actually similar to the geometry of LES Cases 14 and 17 depicted in Figure 5.1. The final results of these pilot projects are not available at present.

Furthermore, it has been found by Uijttewaal et al. [90,93] that applying a gentler groyne head slope (e.g. 1 : 6 instead of 1 : 3) is advantageous to mitigate turbulence intensities and hence possibly the local erosion. Flow separation in a vertical instead of a horizontal plane is induced, which effectively suppresses the quasi-2D vortex shedding phenomenon,

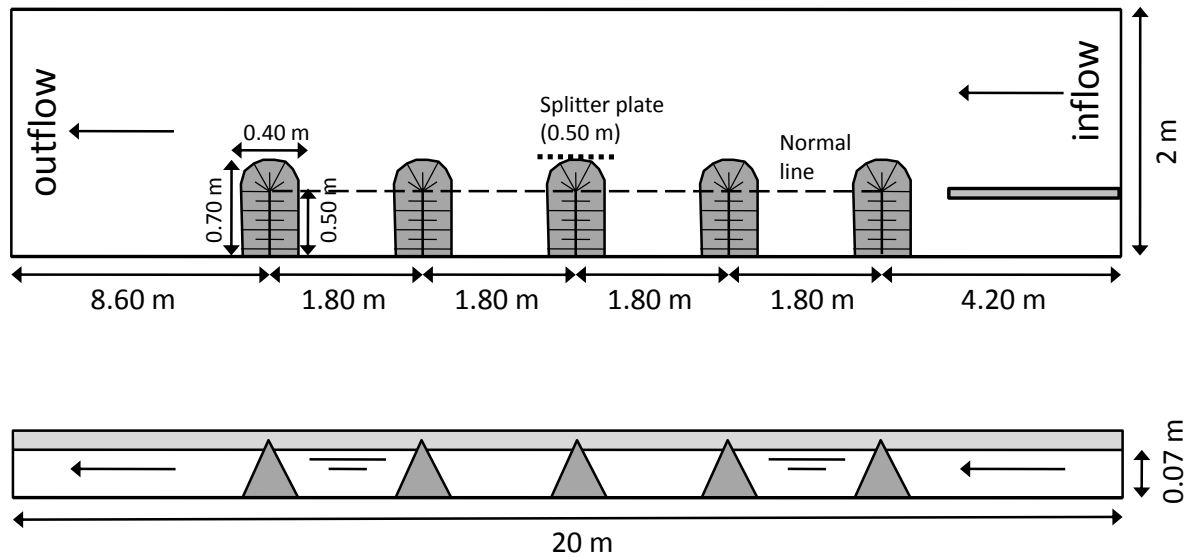


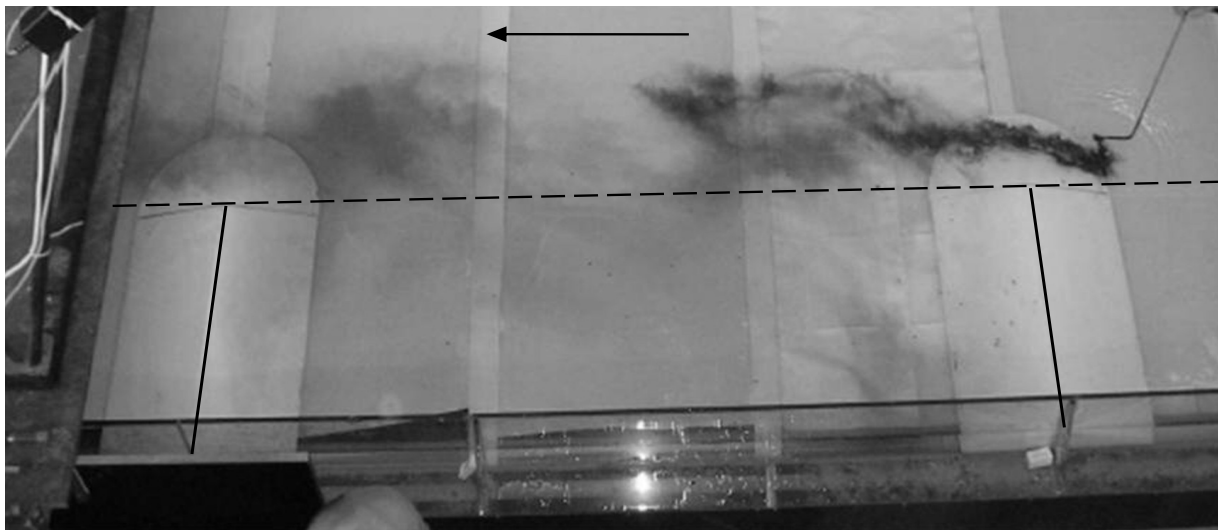
Figure 5.11: *Top view and side view of the experimental setup (distorted scales) for Hydraulic Survey “Bord voor de Kop”. Main flow direction is from right to left (see arrows). The normal line has been indicated (dashed line). A splitter plate (dotted line) is located in front of the 3<sup>rd</sup> groyne.*

broadens the shallow shear layer and possibly weakens the secondary flow intensity due to contraction. Equipping existing groynes with much gentler slopes, however, is quite a costly operation and could narrow the river cross-section; the latter would enhance the over-all flow resistance of the river, giving rise to higher water levels.

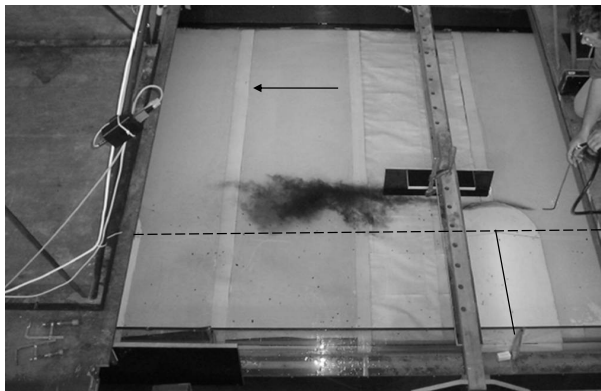
The present pilot project supported by the “Bord voor de Kop” experiments involves the placement of a pile sheet (splitter plate) in front of a groyne head (or slightly upstream or slightly downstream of it). If effective, such a structure would certainly be a cheaper and less cumbersome measure than adaptations of groyne constructions themselves. The pile sheet is intended to regulate the main flow direction near the groyne tip and to align it with the normal line as much as possible. Also, 2DCS shed from the groyne tip may be hindered or changed in traveling direction which may reduce the mixing layer inclination. The ultimate objective is to prevent flow contraction and widening, effectively enhancing flow velocities and bottom friction along the groyne field border and removing the shallow deposition area; this could produce a wider navigation channel. An important requirement is that the regulated flow should not threaten the groyne head stability.

Key purpose of the laboratory experiments “Bord voor de Kop” has been to assess (in a qualitative way) the sensitivity of large-scale turbulence patterns to the exact pile sheet location and orientation.

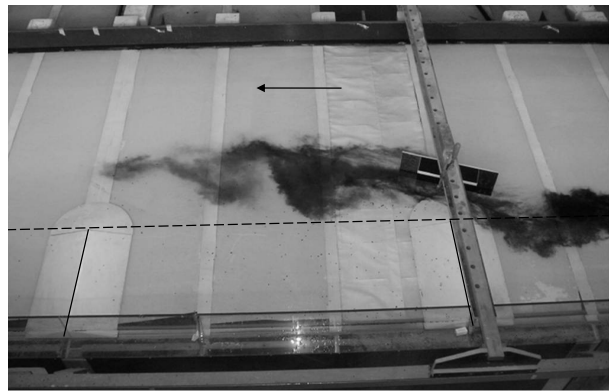
Figure 5.11 depicts a top view and side view of the experimental flume employed, with slightly distorted scales. The setup had a length of 20 m and a width of 2 m; a water depth of 0.07 m was adopted. Four groyne fields have been constructed, using five identical wooden groynes with hydraulic smooth surface and circular groyne head. The crest had a length of 0.50 m and a height of 0.08 m; the groyne slope was 1 : 2.5, implying a total groyne width of 0.40 m and a total length of 0.70 m. The normal line (dashed line) connects all groyne heads (locations of the groyne beacons). Main flow direction is from the right to the left. Close to the inflow boundary, an additional splitter plate was applied in order to prevent too severe a flow contraction near the first groyne.



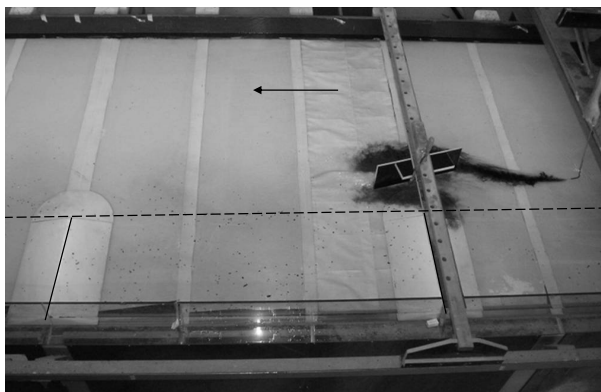
(a)



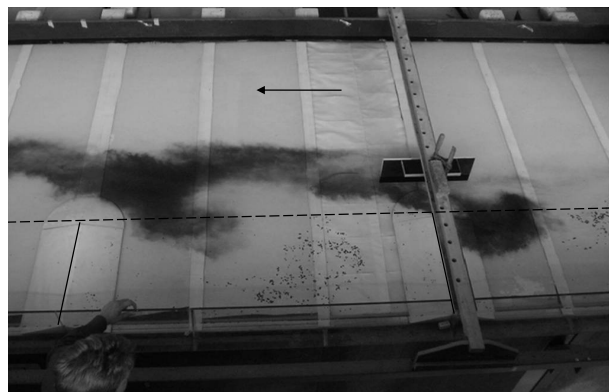
(b)



(c)



(d)



(e)

Figure 5.12: *Hydraulic Survey “Bord voor de Kop”*: laboratory experiments at Delft University of Technology. Groyne crests are indicated by solid lines. Main flow direction is from right to left (see arrows). Some cases considered: reference case (a); splitter plate downstream of 3<sup>rd</sup> groyne (b); splitter plate in front of 3<sup>rd</sup> groyne, inclined toward river axis (c), or inclined toward the river bank (d), or positioned parallel to the (dashed) normal line (e).

The pile sheet was represented by a vertical wooden plate of length 0.50 m, height 0.15 m and thickness 0.01 m. It was placed directly adjacent to the third groyne (dotted line in Figure 5.11). Three positions have been tested: slightly upstream (1), slightly downstream (2) and straight in front of (3) the groyne tip. Furthermore, three pile sheet orientations were applied: an inclination of  $\pm 20^\circ$  toward the river axis (A), respectively  $\pm 20^\circ$  toward the river bank (B), or an orientation parallel to the normal line (C). As a reference case, an experiment without pile sheet was performed first. Hence 10 flow cases have been examined in total.

Figure 5.12 shows shallow-flow turbulence patterns for several cases, visualized by dye. Photographs have been taken by Sieben [76]. Only the most relevant flow cases are shown: the reference case in panel (a), Case 2C (b), Case 3A (c), Case 3B (d) and Case 3C (e). The reference case (a) without pile sheet shows flow contraction near the upstream groyne, as well as a considerable dispersion in downstream direction (low downstream dye concentrations). The over-all flow pattern has quite a 3D character. In all experiments with pile sheet, the large-scale turbulence patterns observed exhibit a more two-dimensional character; this is expressed by either quasi-2D eddies or by more or less straight streamlines, as well as only a limited lateral dispersion (higher downstream dye concentrations).

Nevertheless, quite different results are found for the various pile sheet locations and orientations. In general an upstream pile sheet (Case 1A-B-C) tends to “catch” too much upstream fluid, inducing high flow velocities in between pile sheet and groyne tip. In spite of the effective way in which flow contraction is prohibited, too high velocities may cause erosion and threaten the groyne head stability. Furthermore, all cases with an inclined pile sheet (orientations A and B) give rise to additional flow separation and vortex shedding from the pile sheet tip, which is not a desirable effect (panels (c) and (d)). The most regular flow patterns are found for Cases 2C and 3C: a pile sheet parallel to the normal line, slightly downstream or in front of the groyne head (panels (b) and (e)). In both cases flow contraction, as well as dynamic vortex shedding and the “launching” of primary gyre fluid into the mixing layer, is effectively reduced. Furthermore, all upstream 2DCS are effectively caught by the splitter plate, which partially prevents them from feeding the downstream mixing layer with turbulent kinetic energy.

It has been concluded that an optimal configuration is given by the combination of Case 2C and 3C: a straight pile sheet over the full width of the groyne, extending slightly downstream of it, aligned with the normal line and placed inside the mixing layer region. (An option which was not considered here is the application of curved pile sheets, as these are not as easily constructed as straight pile sheets and hence will be more expensive to implement in practice.)

The recommendations stemming from the “Bord voor de Kop” experiments have been followed for the implementation of the actual pilot project. A splitter plate with length 75 m was placed in front of a representative groyne near Brakel (groyne no. 946.625), along an inner bend of the river Waal. The design and construction of this pile sheet is shown in Figure 5.13 (pictures taken by Sieben [77]). The pile sheet was placed at a distance of 30 m from the groyne beacon and extended to locations 25 m upstream and 50 m downstream of it (see panel (a)). The upper part of the pile sheet has been made semi-permeable (see panel (c)-(d)) in order to reduce flow velocities and wave forces due to ships passing by. Monitoring of velocity maps and bottom level was performed by RWS during several campaigns between August 2006 and September 2009. Some results are briefly shown in Figure 5.14 (see [77]). In panels (b) to (d), the location of the pile sheet has been indicated by a dotted bold line.

Comparing the initial velocity map (a) with instantaneous velocities after 4 weeks (b), we

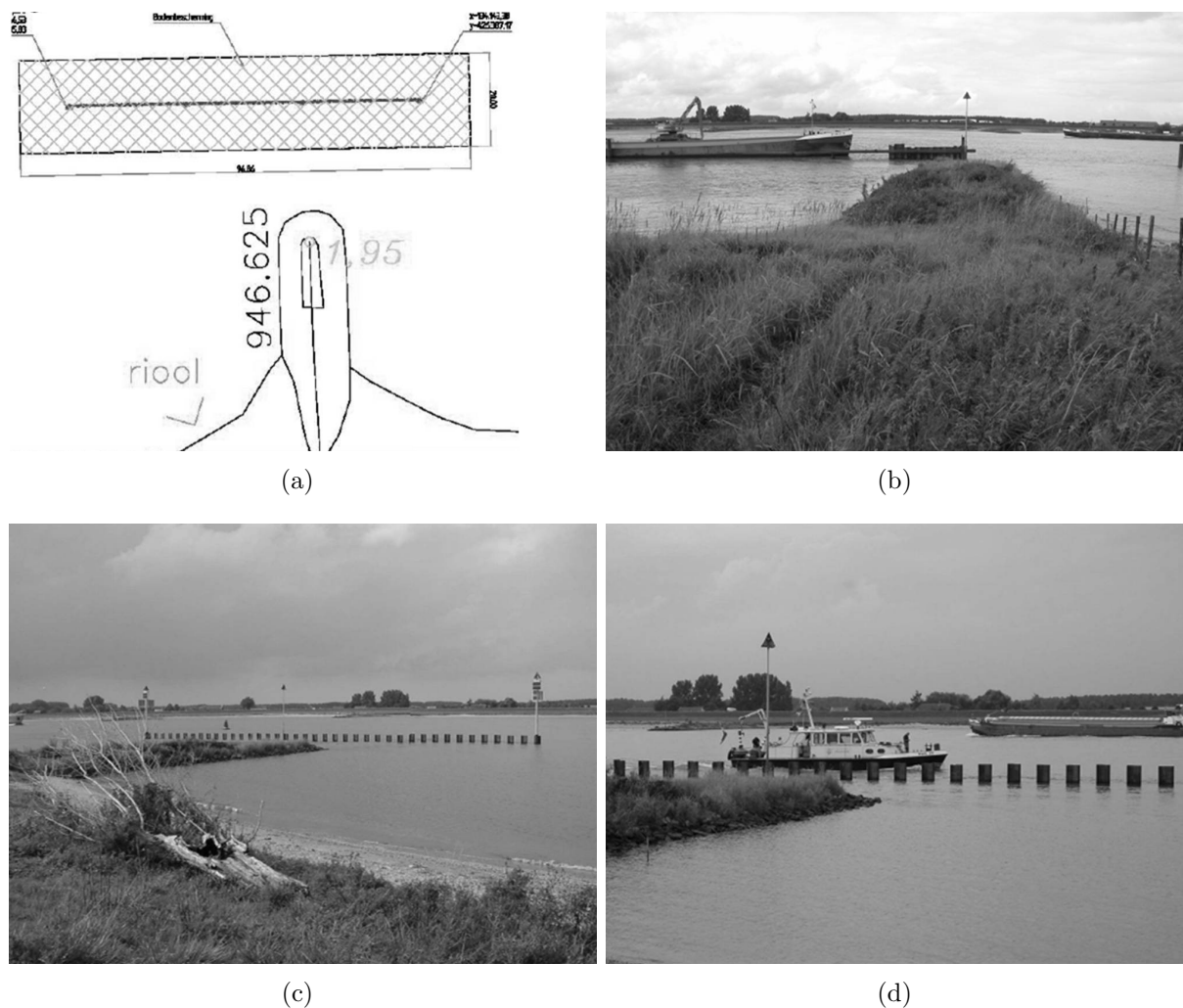


Figure 5.13: *Pilot project near Brakel: splitter plate in front of groyne head. Design of pile sheet and river bed protection (a); under construction, August 2006 (b); Situation after construction, August 2006 (c); monitoring work by RWS (d).*

observe that the general flow pattern has become much more aligned with the normal line, and that the considerable contraction and widening of the main flow has been reduced. Especially the disappearance of the huge transverse entrainment velocities directly downstream of the groyne tip is obvious and can be ascribed to the presence of the pile sheet. It is concluded that the shallow mixing layer has moved toward the direction of the normal line (smaller mixing layer inclination). Comparison of the initial bottom level (c) and the bottom level after 7 months (d) indicates that the scour hole adjacent to the pile sheet has partially filled up, whereas the shallow deposition area further downstream has partially eroded. As a guideline to the eyes, the contour line corresponding with an initial bottom level of NAP -3.0 m has been plotted in both figures (bold solid line). Panel (d) clearly shows that downstream of the pile sheet the NAP -3.0 m depth line has moved toward the river bank (over a distance of 25–50 m), indicating local erosion. Inside this erosion region, the average bottom level lowered by approximately 0.2–0.3 m. This implies a slight widening of the navigation channel, which may prove to be useful in the near future (especially along inner river bends) when RWS would aim to achieve a wider over-all navigation channel in the river Waal.

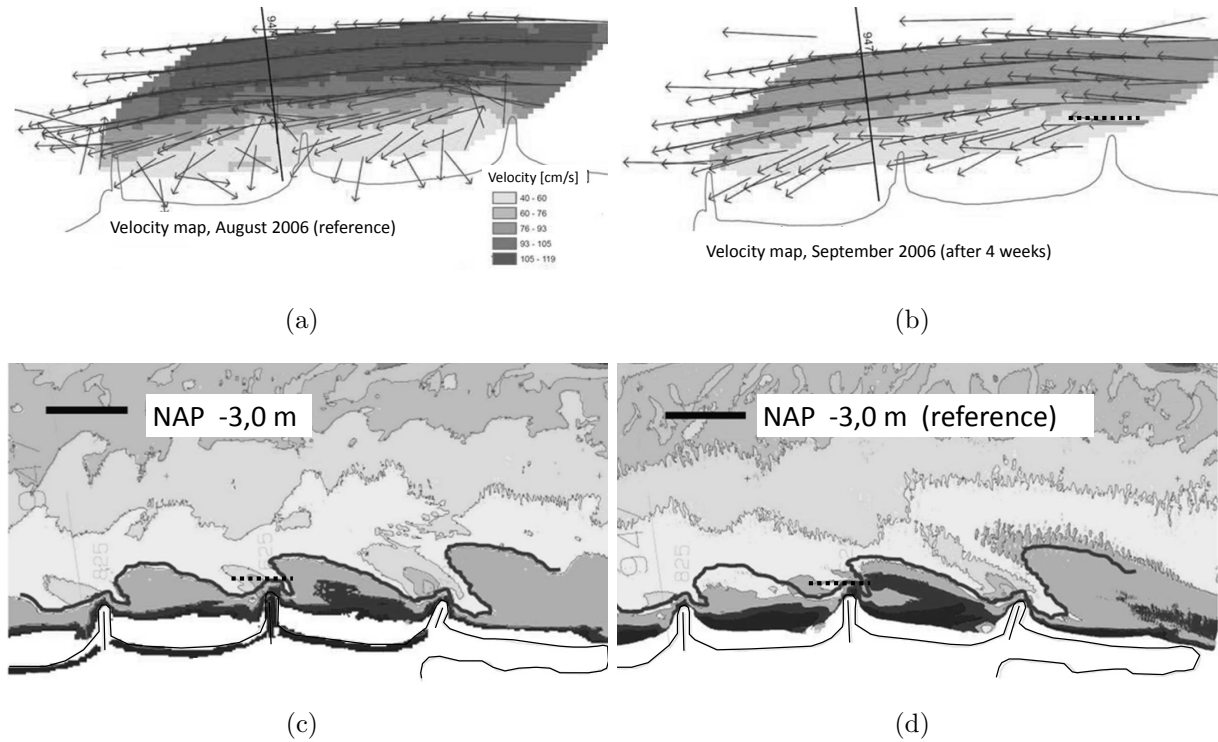


Figure 5.14: *Pilot project near Brakel: impact of splitter plate in front of groyne head. Reference velocity map (August 2006) (a), velocity map after 4 weeks (September 2006) (b), initial bottom level (August 2006) (c), bottom level after 7 months (March 2007) (d).*

From the above field data we can conclude that the pile sheet construction gives rise to the effects which were desired: flow and morphology regulation. Furthermore, the qualitative recommendations stemming from the “Bord voor de Kop” laboratory experiments have proven very useful for application to the prototype-scale river situation.

## 5.6 Summary and discussion

In this chapter, the impact of geometry variations on large-scale turbulence patterns has been investigated in two quite different ways. Firstly, the idealized SLE flow geometry investigated in Chapters 3 and 4 has been varied systematically in order to computationally assess the influence of mean flow characteristics (especially the secondary gyre) on 2DCS dynamics. Secondly, a realistic groyne field flow case stemming from civil engineering practice has been examined experimentally on both laboratory and field scale, with satisfactory results.

Although both types of analysis cannot be straightforwardly compared (as they refer to very different scales and hydraulic conditions), they give rise to rather similar solutions.

The results of LES Cases 14 and 17 provide the insight that the presence of an upstream splitter plate inside an idealized groyne field is useful to reduce near-field lateral shear (by sheltering the secondary gyre); this leads to a reduction of 2DCS length scales en turbulence intensities. It has also been found that such splitter plates are helpful to reduce main flow contraction and near-field secondary flow effects like the horseshoe vortex, as can be seen by comparing Case 17 with results for Case 16 (see Figures 5.3 to 5.9).



The experimental results presented in Section 5.5 show that flow contraction and dynamic secondary flow play a prominent role within realistic groyne field flows, mainly due to their complex bathymetry, and subsequently have a large impact on 2DCS behavior and morphology. Both the “Bord voor de Kop” laboratory experiments and the acquired field data indicate that these effects of contraction and dynamic secondary flow can be effectively regulated by an upstream splitter plate. Additional advantages of this solution are probably a lowered near-field lateral shear and the reduction of the exchange of mass and momentum between groyne field and main channel (see Figure 5.14(a)-(b)). The construction of a pile sheet in front of a groyne head is a cheap and practical way to realize an effective geometry adaptation without the need to rebuild the entire groyne structure.

Hence, despite the very different level of complexity of both types of geometries studied, the same type of engineering solution provides satisfactory results for both the idealized and the realistic groyne field case. Somehow regulating the near-field flow by means of a splitter plate or pile sheet (redirecting streamlines and hindering the emergence of large-scale instabilities) turns out to be effective both in theory and practice. Furthermore, we can state that theoretical (both computational and experimental) investigations on laboratory scale are a helpful tool to find effective ways of influencing real-life large-scale turbulence behavior.

For hydraulic engineering purposes, however, full 3D computations will often be practically unfeasible or undesirable due to the large computational cost (in contrast with limited project budgets, both in terms of time and funding). For use in engineering practice, it is often required to adopt a two-dimensional depth-averaged (2DH) approach to solve hydraulic problems which may involve large-scale turbulence. Therefore, the final part of this thesis is mostly dedicated to the 2DH modeling of shallow flow situations including 2DCS. Chapter 6 will elaborate on the issue how to properly incorporate quasi two-dimensional turbulence dynamics into the 2D Shallow Water Equations (SWE).



# Chapter 6

## 2D depth-averaged computations

### 6.1 Introduction

This chapter describes the two-dimensional depth-averaged (2DH) modeling of the shallow turbulent flow types treated in previous chapters. We employ numerical models in which the large-scale quasi-2D turbulence (at supra-depth scale) is actually resolved on the computational grid, whereas smaller-scale 2D and 3D fluctuations (roughly at sub-depth scale) are accounted for by a turbulence model. The interaction between resolved and unresolved scales has to be modeled as well; this is achieved by means of a so-called *backscatter model*. In this chapter, after a formal depth-integration of the 3D Navier-Stokes Equations, a new 2D backscatter formulation is proposed which integrates several existing models for 2D turbulence. The unified model is calibrated against 3D LES data of a basic shallow flow geometry: a Straight Channel Flow, which is abbreviated here as SCF. The calibrated model is applied to two shallow-flow geometries that have been encountered in previous chapters: the Shallow Mixing Layer (SML) and Shallow Lateral Expansion (SLE). The results are compared with 3D LES results of these geometries, as well as with results acquired by the existing 2D turbulence models. Based on this analysis the suitability of the models for practical applications can be assessed. Finally, the sensitivity of the 2D results to vertical resolution is investigated by means of a brief excursion to 3D modeling.

### 6.2 Background; importance of a backscatter model

In spite of the increasing feasibility of 3D simulations for prediction and design purposes in environmental hydraulics, the majority of numerical models used in hydraulic engineering practice are still two-dimensional. Many 3D turbulence problems in practice are solved by means of Reynolds Averaged Navier-Stokes (RANS) equations, using a closure model (like a  $k-\epsilon$  formulation) which basically models all turbulence scales. However, if one aims to directly resolve the larger-scale turbulent motion while modeling only the smaller-scale turbulence, Large Eddy Simulation (LES) is much better suited than RANS-type modeling. This is especially relevant for flow problems that involve a wide range of turbulence scales, e.g. shallow flows that contain both large-scale 2DCS and smaller-scale 3D turbulence. The applicability of LES to environmental shallow flow problems is however quite limited. The increase of computer power and storage capacity in recent decades has enabled researchers to perform a 3D LES of laboratory-scale problems on parallel clusters or even desktop computers. However, due to the resolution needed for a full 3D LES computation of prototype-scale flow situations (at least 80% of the turbulent motion needs to be

resolved, see Pope [71]), LES is not a workable tool for real-life engineering problems, and is not likely to become such a tool for the next decades.

In the context of 3D modeling, it is often aimed to simulate prototype-scale or laboratory-scale turbulence at an intermediate level of detail, containing less detail than LES but more detail than a RANS model. A variety of formulations has been proposed for this purpose; consequently, some of these methods are based on the LES philosophy whereas others rely on the RANS approach. The first category includes the concept of VLES (Very Large Eddy Simulation, see Pope [71]); the second category includes e.g. TRANS (Transient RANS) and URANS (Unsteady RANS, see Spalart [80]). Basically all LES-type methods maintain the basic principle of spatially filtering the velocity field, whereas RANS-type methods involve time-averaging over a time interval which is larger than the time scale of the 3D bottom turbulence but smaller than the time scale of the large-scale 2D motion (see [96]).

In depth-averaged 2DH methods, it is often aimed to resolve horizontal quasi-2D large eddies and to model all other turbulent motion. The turbulent scales which are modeled are either smaller than a certain low-pass filter width (LES-based approaches, see Sagaut [72]) or smaller than a certain intermediate time scale (RANS-based approaches). As it is aimed to resolve the quasi-2D large eddies only, the low-pass filter width for LES-based methods is usually of the order of the water depth  $H$ . It should be noted that, for 2DH models, the “modeled or unresolved scale” is not a synonym of “sub-grid scale”, as would be the case in the context of full 3D Large Eddy Simulations. Hence, not only the sub-grid scale but also the sub-depth scale is of importance.

The modeling of unresolved scales is usually accounted for by an expression for the turbulence viscosity. Yet, in the case of 2DH models, this modeling concept is generally not sufficient for the generation of 2D turbulence because it has a merely dissipative character. Ghidaoui and Kolyshkin [38] have demonstrated the fundamental ability of the 2D Shallow Water Equations to capture patterns of 2D coherent structures. Nevertheless, the generation of these 2DCS often emerges from 3D bottom turbulence at sub-depth scale, induced by vertical shear, and exactly these physical mechanisms are not resolved within a 2D model. The essential dynamic interaction between 2DCS and 3D bottom turbulence is lacking. Also larger-scale components of the bottom turbulence (as found by Kim and Adrian [50]) are absent. The triggering effect of 3D motions on 2D large eddies should therefore be modeled explicitly. Such a model is called a backscatter model. This is because the growth of 2DCS is often (at least partially) caused by “backscatter” of turbulent kinetic energy, i.e. the transfer of energy from smaller to larger scales (according to the inverse energy cascade, see Sections 2.2.2 and 2.2.3).

A variety of 2D shallow-flow turbulence models is available in literature. In several models large-scale 2D turbulent motions are imposed as inflow boundary conditions and spread over the flow domain by advection, in combination with an eddy viscosity-type model that accounts for the dissipation of 2D and 3D motions. Such a model is HLES (Horizontal Large Eddy Simulation, see Uittenbogaard and Van Vossen [95]). Other models contain an explicit backscatter formulation: they locally generate 2D turbulent motions throughout the domain by means of a direct forcing mechanism. The models DA-LES (Depth-Averaged Large Eddy Simulation, see Hinterberger et al. [43, 44]) and 2D-TRANS+KS (2D Transient RANS with Kinematic Simulation, see Van Prooijen [99, 102]) belong to this category.

The shallow-flow turbulence models listed here (HLES, DA-LES and 2D-TRANS+KS) will be described in more detail throughout the next sections, where they are used to inspire a new backscatter model which integrates the existing models. The newly proposed model is coined DANSLES (Depth-Averaged Navier-Stokes with Large Eddy Stimulation) and is applied to several shallow flow geometries encountered in earlier chapters.

## 6.3 Basic equations

### 6.3.1 2D Shallow Water Equations

In analogy with 3D turbulence closure formulations, any 2DH turbulence model should follow from a suitable closure of residual terms within the basic equations of motion. Although one cannot escape from making a number of crude assumptions when closing such residual terms, it should be clear in which way each term is closed and whether these closures are appropriate. Therefore, the 2DH turbulence models treated in this chapter are explicitly linked to residual terms within the 2DH equations of motion, the 2D depth-averaged Shallow Water Equations (SWE).

A full formal derivation of the 2D Shallow Water Equations, based on the 3D incompressible Navier-Stokes Equations and applying the Boussinesq approximation for small density variations, can be found in Vreugdenhil [108]. For the present study it is sufficient to adopt a constant density  $\rho$  (fresh water); furthermore, the influences of earth rotation (Coriolis force), wind stresses and atmospheric pressure gradients are not taken into account. The derivation of the 2D SWE involves three basic steps (see [108]):

1. Low-pass filtering of the 3D Navier-Stokes Equations (2.1) and (2.3) by means of a Transient (Unsteady) Reynolds averaging operation in time or a LES filtering operation in space;
2. Applying the hydrostatic pressure assumption to the low-pass filtered equations and replacing the pressure  $p$  by the piezometric level  $h$ ;
3. Integration of the resulting equations over the water depth  $H$  using Leibniz' integral rule, adopting a movable free surface level  $h$  and a fixed bottom level  $z_b$ .

The first step yields the low-pass filtered 3D Navier-Stokes Equations:

$$\frac{\partial \bar{u}_i}{\partial x_i} = 0 \quad \text{and} \quad (6.1)$$

$$\frac{\partial \bar{u}_i}{\partial t} + \frac{\partial \bar{u}_i \bar{u}_j}{\partial x_j} + \frac{\partial \bar{p}}{\partial x_i} - \frac{\partial}{\partial x_j} \nu \left( \frac{\partial \bar{u}_i}{\partial x_j} + \frac{\partial \bar{u}_j}{\partial x_i} \right) + \frac{\partial \overline{u'_i u'_j}}{\partial x_j} = 0, \quad (6.2)$$

in which the operator  $\overline{(\dots)}$  denotes either spatial LES-filtering (see Section 4.2.1) or ensemble averaging (TRANS/URANS-filtering). Both types of filtering yield the same result in terms of mathematical form. The residual term  $\overline{u'_i u'_j} = \overline{u_i u_j} - \bar{u}_i \bar{u}_j$  represents either a sub-grid scale (SGS) residual stress, or a Reynolds stress including all turbulent scales below a certain TRANS-filtering time scale. In practice both types of residual terms are often closed in a similar way, as Equations (6.1)-(6.2) are usually only implicitly filtered due to the numerical discretization (both in space and time).

The second step implies the assumption that the low-pass filtered turbulent motion (i.e. the large-scale motion which is resolved on a 3D computational grid) has a quasi-2D hydrostatic character whereas the high-pass filtered non-resolved motion has a predominantly 3D non-hydrostatic character. This assumption is justifiable if secondary flow components (both fluctuating and time-averaged contributions) are either negligible or non-resolved; the latter can be achieved if the LES or TRANS low-pass filter corresponds with a filtering length scale of the order of the water depth. This implies that the horizontal grid resolution should be such that quasi-2D structures with roughly a length scale  $\mathcal{L} > H$  are resolved.

The third step involves the formal integration of (6.1)-(6.2) over the water depth  $H = \bar{h} - z_b$  under the hydrostatic pressure assumption, adopting the operator  $(\overline{\cdot\cdot\cdot})$  to denote depth-averaging. All details of the derivation can be found in Vreugdenhil [108]. The resulting system of equations (also given by Hinterberger et al. [43,44]) reads:

$$\frac{\partial \bar{h}}{\partial t} + \frac{\partial H \widetilde{u}_i}{\partial x_i} = 0 \quad \text{and} \quad (6.3)$$

$$\frac{\partial H \widetilde{u}_i}{\partial t} + \frac{\partial H \widetilde{u}_i \widetilde{u}_j}{\partial x_j} + gH \frac{\partial \bar{h}}{\partial x_i} + \frac{\bar{\tau}_{bi}}{\rho} - \frac{\partial}{\partial x_j} H \nu \left( \frac{\partial \widetilde{u}_i}{\partial x_j} + \frac{\partial \widetilde{u}_j}{\partial x_i} \right) + \frac{\partial H (\overline{\widetilde{u}_i \widetilde{u}_j} - \widetilde{u}_i \widetilde{u}_j)}{\partial x_j} = 0, \quad (6.4)$$

where the low-pass filtered water level  $\bar{h}$  and filtered depth-averaged 2D velocity field  $\widetilde{u}$  are the quantities that are actually resolved by a 2DH numerical model. The bottom shear stress  $\tau_{bi}$  is straightforwardly modeled by the well-known quadratic friction law:

$$\bar{\tau}_{bi} = c_f \rho |U| \widetilde{u}_i, \quad (6.5)$$

where  $|U| = \sqrt{\widetilde{u}_k \widetilde{u}_k}$  is the Euclidean norm of the horizontal velocity vector. The computation of the friction coefficient  $c_f$  depends on hydraulic roughness conditions. For the present laboratory-scale geometries with hydraulic smooth wall conditions,  $c_f$  can be found iteratively by the following expression (see Uijttewaal and Booij [91]):

$$\frac{1}{\sqrt{c_f}} = \frac{1}{\kappa} [\ln(Re \sqrt{c_f}) + 1], \quad (6.6)$$

where  $Re = |U|H/\nu$  is the Reynolds number and  $\kappa \approx 0.4$  is the Von Kármán constant.

### 6.3.2 Residual closure terms

According to Hinterberger [42], the operators  $(\overline{\cdot\cdot\cdot})$  and  $(\widetilde{\cdot\cdot\cdot})$  are commutative for constant water depth  $H$ , hence  $\overline{\widetilde{u}} = \widetilde{\overline{u}}$ ; this is explained by the linear character of both operators. Variable water levels or bottom levels, however, introduce additional nonlinear terms at the integration boundaries which means that the commutativity is not valid in those cases. For sufficiently small variations of  $H$  (i.e. small at the scale of the LES or TRANS low-pass filter width), these nonlinear terms can be neglected.

The quantity  $R_{ij} = \overline{\widetilde{u}_i \widetilde{u}_j} - \widetilde{u}_i \widetilde{u}_j$  in Equation (6.4) represents a total residual stress that stems from the combination of low-pass filtering and depth integration. By approximation it can also be stated that  $R_{ij} = \overline{\overline{u}_i \overline{u}_j} - \overline{\overline{u}_i} \overline{\overline{u}_j}$ , which is exact for constant water depth  $H$  (see [42]). The combined residual  $R_{ij}$  can be decomposed into three contributions (A), (B) and (C); again, this decomposition is exact for constant water depth and sufficiently accurate for small variations of  $H$ . Irrespective which operator is applied first, both definitions of  $R_{ij}$  equally give rise to the same approximate decomposition, which reads:

$$R_{ij} = \underbrace{\left( \overline{\widetilde{u}_i \widetilde{u}_j} - \widetilde{u}_i \widetilde{u}_j \right)}_{(A)} + \underbrace{\left( \overline{\overline{u}_i \overline{u}_j} - \overline{\overline{u}_i} \overline{\overline{u}_j} \right)}_{(B)} + \underbrace{\left( \overline{u'_i u'_j} - \overline{u'_i} \overline{u'_j} \right)}_{(C)} \quad (6.7)$$

This is a generalization of the similar decomposition given by Hinterberger et al. [42,43]; it is equally applicable to 2D LES as well as 2D TRANS model types, and it is found irrespective of the order of the low-pass filtering and depth-averaging operations. The residual terms (A), (B) and (C) need to be closed and can be interpreted as follows:

- Term (A) is a mean dispersive stress, which represents the effect of the unresolved 3D mean or large-scale motion (secondary flow) on the resolved 2D motion;
- Term (B) is a 2D subgrid stress (or Reynolds stress), which represents the effect of unresolved 2D turbulence on the resolved 2D motion;
- Term (C) is a 3D subgrid stress (or Reynolds stress), which represents the effect of unresolved 3D turbulence on the resolved 2D motion. Alternatively, term (C) can be equivalently defined as a dispersive stress which represents the effect of unresolved 3D secondary flow fluctuations.

It has been stated by Hinterberger [42,43] that term (A) could be neglected. However, the results from Sections 4.7 and 5.3.3 indicate that this secondary flow term plays an important role for the lateral transfer of streamwise momentum throughout shallow shear flows, see Figures 4.20-4.21 and 5.7. Term (A) is equivalent to the term  $T_{sec}$  in Equation (4.31), which represents momentum transfer by mean secondary flow; this contribution can be important both in near-field situations with strong lateral shear (due to upwelling/downdraft and horseshoe vortices) and in far-field situations (flow dispersion due to vertical velocity differences). In order to account for momentum transfer associated with these effects, term (A) cannot be neglected and should be appropriately closed.

Basically, term (B) describes the influence of 2D unresolved turbulence on the 2D resolved flow, whereas term (C) accounts for the 3D unresolved turbulence. The closure formulations for (B) and (C) should reflect this distinction.

### 6.3.3 Eddy viscosity-type models: Elder's term and HLES

It is important to note that the effect of closure terms (A), (B) and (C) can be both productive and dissipative in terms of energy; the respective residuals can account for both the generation and decay of resolved 2D turbulence fluctuations. In other words, these residuals include both the standard energy cascade (transfer of energy toward smaller scales) and the inverse energy cascade (backscatter of energy toward larger scales). The first cascade is often straightforwardly closed by means of an eddy viscosity-type model, whereas the second cascade can be accounted for by a backscatter model. These models may be applied in a combined fashion. In the present subsection two types of eddy viscosity closures are presented, while Section 6.4 discusses backscatter models.

A simple and well-known closure formulation to account for 3D turbulence effects on a 2DH flow is the Elder formulation, also called Elder's term. This eddy viscosity model has a merely dissipative character; in principle, it can be used to close term (C). The dissipative effect of 3D turbulence on the resolved flow is modeled by an additional viscosity term, using an eddy viscosity  $\nu_t$  that is based on the law-of-the-wall principle:

$$\underbrace{\left(\overline{u'_i u'_j} - \overline{\tilde{u}'_i \tilde{u}'_j}\right)}_{(C)} = -\nu_t \left( \frac{\partial \tilde{u}_i}{\partial x_j} + \frac{\partial \tilde{u}_j}{\partial x_i} \right) = -\nu_t \tilde{s}_{ij} \quad \text{with} \quad \nu_t = c_h u_* H, \quad (6.8)$$

where  $u_* = \sqrt{c_f} |U|$  is the friction velocity. Elder's term is straightforwardly implemented by adding  $\nu_t$  to the molecular viscosity  $\nu$  in Equation (6.4). The coefficient  $c_h$  is a dimensionless parameter; following the mixing length theory by Prandtl for turbulent wall flows (see Pope [71]), its theoretical value is  $c_h = \frac{1}{6} \kappa \approx 0.07$ . Nonetheless, values between 0.07 and 0.20 can be found in literature, see Hinterberger et al. [43] and Van Prooijen and Uijttewaai [102]: in the latter work a value  $c_h = 0.15$  is adopted. This relatively large value is motivated by the idea that the dissipative part of other closure terms can be closed by

the Elder formulation as well, although the formal derivation of Elder's term is intended to close term (C) only. It is especially relevant to close the dispersive term (A) by means of an eddy viscosity formulation, as term (A) and (C) are often important in the same regions, i.e. regions with strong lateral shear (see Figures 5.6-5.7). It is common practice to model dispersion terms by means of a diffusion-type model. In the present study, it is assumed that the dissipative parts of term (A) and (C) can both be closed by Elder's term according to (6.8), with  $c_h > \frac{1}{6}\kappa$ .

In order to close the two-dimensional stress term (B), a subgrid-scale (SGS) model for quasi-2D turbulence by Van Vossen [105], Kernkamp and Uittenbogaard [49] and Uittenbogaard and Van Vossen [95] can be used. This SGS model is named *Horizontal Large Eddy Simulation* (HLES). Although the authors do not explicitly mention which residual term is closed by HLES, it is clear from the context that term (B) is the term actually closed. In literature HLES is always used in combination with Elder's term (with  $c_h = \frac{1}{6}\kappa$ ) in order to close term (C). Apparently term (A) is not taken into account by [49, 95, 105]. It should be noted that HLES can be applied in a multi-layered model, although the formulation is depth-averaged. In such cases Elder's term can be replaced by a  $k$ - $\epsilon$  approach, see e.g. Bijlsma et al. [11].

The basic form of the 2D SGS model is given by:

$$\underbrace{\left(\overline{\widetilde{u}_i \widetilde{u}_j} - \widetilde{u}_i \widetilde{u}_j\right)}_{(B)} = -\nu_{2D} \left( \frac{\partial u_i^*}{\partial x_j} + \frac{\partial u_j^*}{\partial x_i} \right) = -\nu_{2D} s_{ij}^*, \quad (6.9)$$

where  $\nu_{2D}$  is a 2D subgrid eddy viscosity, and the asterisk  $*$  denotes high-pass filtering of the resolved velocity field. It is emphasized by [49, 95] that an SGS model for unresolved 2D turbulence should be sensitive to turbulent velocities only and *not* to the total resolved velocity signal  $\widetilde{u}$ ; otherwise, the rate of energy dissipation would be too high (as is often the case in Smagorinsky-based SGS models). A spatial high-pass filtering operation (as applied by Germano et al. [37]) is however not applicable on arbitrary grids and geometries. For use in HLES, therefore, the mean flow contributions to  $\widetilde{u}$  are removed by means of a temporal high-pass filter  $u^* = \widetilde{u} - \widetilde{u}^{temp}$ , where  $\widetilde{u}^{temp}$  is recursively updated at each time step  $n$ :

$$\widetilde{u}_{n+1}^{temp} = (1 - \exp^{-\Delta t/\tau}) \widetilde{u}_{n+1} + (\exp^{-\Delta t/\tau}) \widetilde{u}_n^{temp}, \quad (6.10)$$

in which  $\Delta t$  denotes the time step. The filtering time scale  $\tau$  determines the width of the temporal filter and is specified by the user; it should be larger than the characteristic time scale of 2DCS but smaller than long-term velocity variations (e.g. tidal flow). See [95] for the full description of the high-pass filter. This filtering operation has the effect that, for a *steady* resolved flow field, the 2D subgrid stress of HLES in (6.9) is exactly zero whereas the contribution of Elder's term in (6.8) is generally nonzero. This is logical as a steady resolved flow does not contain large-scale 2D turbulence (i.e. term (B) is zero), while 3D non-resolved bottom turbulence is always present (i.e. term (C) is nonzero).

An expression for the 2D eddy viscosity  $\nu_{2D}$  is derived by Uittenbogaard and Van Vossen [95], based on a depth-averaged balance of kinetic energy of homogeneous and stationary quasi-2D turbulence. The work done by 2D turbulent motion against bed friction has been taken into account. Bed friction drains energy from the resolved 2D motions and converts it into energy of unresolved 3D motions. In HLES this direct dissipation is modeled by a so-called "short-cut cascade": energy dissipation by the 2D SGS model is reduced as this energy is already dissipated by the action of bottom friction. The resulting expression for  $\nu_{2D}$  (in slightly summarized notation, see [95]) reads:



$$\nu_{2D} = \frac{\Delta^2}{\pi^2 f_{lp}^2} \left( \sqrt{\gamma^2 s_{ij}^* s_{ij}^* + b^2} - b \right), \quad (6.11)$$

where  $b = \frac{3}{4} c_f |U|/H$  accounts for the effect of bottom friction,  $\Delta$  is a characteristic horizontal mesh size, and  $\gamma$  is a model constant which has a value  $\approx 0.236$  for homogeneous and stationary quasi-2D turbulence (see [95] for a detailed description). The calibration parameter  $f_{lp}$  depends on the amount of artificial dissipation by the numerical scheme; its default value is  $f_{lp} \approx 0.3$  for the applications of HLES described by e.g. Kernkamp and Uittenbogaard [49], Bijlsma et al. [11] and Van Schijndel and Jagers [103] (all applying the numerical solver DELFT3D-FLOW [46]).

Essentially, HLES can be considered as a 2D Smagorinsky-type subgrid model which fine-tunes the dissipation rate of turbulent kinetic energy. This is a property the model has in common with well-known 3D LES approaches like the SGS model by Smagorinsky [79] or Germano et al. [37]. Basically Elder’s term is about fine-tuning a dissipation rate as well, although its algebraic shape is different from HLES (it is not a subgrid model). It should be kept in mind that HLES represents dissipation by down-cascading of *resolved* turbulent kinetic energy (term (B)), while Elder’s term represents the dissipation of resolved energy due to the action of *unresolved* 3D turbulence (term (C)). The application of pure HLES with Elder’s term (without any backscatter model) implies that all turbulence within the model domain is either generated by topographical forcing or imposed as inflow boundary conditions.

## 6.4 The DANSLES backscatter model

As explained in Section 6.2, the generation of 2DCS by unresolved 3D turbulent motion can essentially not be captured by eddy viscosity-type models due to their dissipative character. The Elder formulation is an example of an eddy viscosity model that is purely dissipative, while HLES is a predominantly dissipative model. Theoretically, HLES may give rise to a slight backscatter effect (as explained by [95]); mathematically this is a direct consequence of the high-pass filtering operation applied to the resolved velocity field. However, this backscatter effect only concerns unresolved 2D kinetic energy; the principal backscatter mechanism given by the transfer of unresolved 3D energy toward 2D resolved scales is still lacking. This implies that neither Elder’s term nor HLES is able to reproduce 2DCS in an otherwise uniform base flow, as described by e.g. Jirka [47].

The energy-producing part of the residual stress terms within  $R_{ij}$  given in Equation (6.7) can be accounted for by an explicit backscatter model, based on assumptions about the 2D kinetic energy production (and its spectral distribution) that can be caused by backscatter. Generally a backscatter model is implemented by imposing body forces on the resolved 2D flow field. The body force vector field is denoted by  $F_i$  in index notation (or  $\mathbf{F}$  in vector notation); it is a function of 2D space and time. The two existing backscatter models discussed in the present chapter both apply such a body force field; these methods are named *Depth-Averaged Large Eddy Simulation* (DA-LES) and *Two-Dimensional Transient RANS with Kinematic Simulation* (2D-TRANS+KS).

In this section a new 2D backscatter formulation is proposed, which is basically a unification of both existing models. Inspired by DA-LES, the combined method is coined *Depth-Averaged Navier-Stokes with Large Eddy Stimulation* (DANSLES)<sup>1</sup>. Although this

<sup>1</sup>The acronym DANSLES is a word play: the Dutch word “dansles” means “dance lesson”.

backscatter model mainly concerns integration of DA-LES and 2D-TRANS+KS, the Elder formulation and HLES do fit in the total model framework as well. One may note that the acronym DANSLES contains the word “stimulation” instead of “simulation”; this is because application of a backscatter forcing field  $F_i$  obviously stimulates rather than simulates the generation of 2DCS.

Starting point for DANSLES are the 2D SWE given by (6.3)-(6.4), in which the residual stress terms are appropriately closed. We assume that Elder’s term can be applied for the dissipation by both terms (A) and (C) (with  $c_h > \frac{1}{6}\kappa$ ), while HLES is used to close term (B). The productive part of all residual stress terms is accounted for by the body force field  $F_i$ , which is still to be specified. Substituting all closure expressions into (6.4) and adopting (6.5) to model bottom friction, we obtain:

$$\frac{\partial \bar{h}}{\partial t} + \frac{\partial H \tilde{u}_i}{\partial x_i} = 0 \quad \text{and} \quad (6.12)$$

$$\frac{\partial H \tilde{u}_i}{\partial t} + \frac{\partial H \tilde{u}_i \tilde{u}_j}{\partial x_j} + gH \frac{\partial \bar{h}}{\partial x_i} + c_f |U| \tilde{u}_i - \frac{\partial}{\partial x_j} H (\nu + \nu_t) \tilde{s}_{ij} - \frac{\partial}{\partial x_j} H \nu_{2D} s_{ij}^* = HF_i \quad (6.13)$$

In the following subsections expressions for  $F_i$  are derived. In DA-LES,  $F_i$  is given by a fully stochastic model without spectral information; this method is both fast and flexible in use. In 2D-TRANS+KS, on the other hand,  $F_i$  is derived from a detailed kinematic simulation based on 2D energy density spectra; this method is however slow and only valid for one type of uniform channel flow. In DANSLES the advantages of both approaches are combined, giving rise to a fast implementation with generalized spectral information that is easy to apply. All backscatter models listed here require a constant water depth  $H$ .

### 6.4.1 DA-LES

The DA-LES model has been introduced by Hinterberger et al. [43–45], see also Hinterberger [42]; it consists of a stochastic backscatter model (BSM) to account for the body force field  $\mathbf{F}$ , supplemented with a simple eddy viscosity model (Elder’s term) to close residual term (C). The general framework of DA-LES as presented by [42–45] is basically given by Equations (6.12)-(6.13) and (6.8), without HLES and with  $c_h = \frac{1}{6}\kappa$ . The BSM formulation is meant to model energy production by term (C), i.e. the local generation of resolved 2D turbulence by the 3D unresolved motion.

The stochastic BSM makes use of *white noise* to disturb the resolved 2D flow field at all time and length scales. A random 2D white noise vector field  $\mathbf{r}(x, y, t)$  as a function of space and time is generated, satisfying a standard normal distribution (zero mean and unit variance). For this purpose, Hinterberger et al. employ an advanced Gaussian random generator by Marsaglia and Bray [59]<sup>2</sup>. The dimensionless field  $\mathbf{r}$  is scaled to the dimension of a body force, using the scaling factor  $F_{rms}$ :

$$\mathbf{F} = F_{rms} \mathbf{r} \quad (6.14)$$

Hence the resulting field  $\mathbf{F}$  has zero mean and variance  $F_{rms}^2$  everywhere, in all directions. The forcing scale  $F_{rms}$  is derived as follows. Hinterberger [42] supposes that the production

<sup>2</sup>In the present study a slightly simpler Gaussian random generator is used, producing sufficiently accurate results. Each normally distributed random number  $r$  is constructed using twelve standard uniformly distributed random numbers  $R_k$ :  $r = \sum_{k=1}^{12} R_k - 6$ . The resulting field  $r$  has zero mean and unit variance.

rate  $P_{2D}$  of 2D turbulent kinetic energy (TKE) by the action of  $\mathbf{F}$  is proportional to the squared norm of the body force, according to:

$$P_{2D} \sim F_{rms}^2 \Delta t, \quad (6.15)$$

where  $\Delta t$  is the numerical time step. Furthermore,  $P_{2D}$  is assumed to be proportional to the production rate  $P_{3D}$  of 3D TKE:

$$P_{2D} \sim \frac{P_{3D}}{Re_*} = \frac{|U|u_*^2}{HRe_*} = \frac{|U|^2\nu\sqrt{c_f}}{H^2}, \quad (6.16)$$

where  $Re_* = u_*H/\nu$  is the Reynolds number based on the friction velocity. Combination of (6.15) and (6.16) yields:

$$F_{rms} = c_B \frac{|U|}{H} \sqrt{\frac{\nu\sqrt{c_f}}{\Delta t}}, \quad (6.17)$$

where  $c_B$  is a dimensionless model constant. Calibration against a high-resolution 3D LES computation of a uniform channel flow by Hinterberger [43] resulted in a recommended value  $c_B = 55$ . Adopting this value, the 2D TKE level  $k_{2D}$  computed by DA-LES compared well to the level computed by 3D LES. In the uniform channel flow,  $k_{2D}$  was found to be approximately 15% of the 3D TKE level  $k_{3D}$  (see [42, 45]).

According to Hinterberger et al. [42, 43], the random field  $\mathbf{r}$  should be filtered both spatially and temporally (the so-called BSM filter) for the sake of numerical stability. (The necessity of this filter operation is disputed in this thesis, as will be discussed later.) The BSM filter is a simple temporal and spatial bandpass filter that removes the largest and smallest time and length scales from  $\mathbf{r}$ . Provided that  $\mathbf{r}$  is defined on a structured rectangular grid with spatial indices  $i, j$  and time index  $n$ , the filter reads:

$$\begin{aligned} \mathbf{Z}_{i,j}^n = \frac{1}{4} \{ & \mathbf{r}_{i+1,j+1}^{n+1} - \mathbf{r}_{i-1,j+1}^{n+1} - \mathbf{r}_{i+1,j-1}^{n+1} + \mathbf{r}_{i-1,j-1}^{n+1} \\ & - \mathbf{r}_{i+1,j+1}^{n-1} + \mathbf{r}_{i-1,j+1}^{n-1} + \mathbf{r}_{i+1,j-1}^{n-1} - \mathbf{r}_{i-1,j-1}^{n-1} \}, \end{aligned} \quad (6.18)$$

where  $\mathbf{Z}$  is the BSM-filtered random field (see [42]). The resulting body force field is then given by  $\mathbf{F} = F_{rms}\mathbf{Z}$  instead of  $\mathbf{F} = F_{rms}\mathbf{r}$ . The spectral amplitude ratio between  $\mathbf{Z}$  and  $\mathbf{r}$  satisfies the following transfer function  $\hat{G}$ :

$$\hat{G}(f, k_x, k_y) = 2 \sin(2\pi f \Delta t) \sin(k_x \Delta x) \sin(k_y \Delta y) \quad (6.19)$$

This is a function of frequency  $f$  and wave numbers  $k_x$  and  $k_y$ ; it reaches a maximum at frequency  $f = 1/4\Delta t$  resp. at wave numbers  $k_x = \pi/2\Delta x$  and  $k_y = \pi/2\Delta y$ . This implies that time scales  $\approx 4\Delta t$  and length scales  $\approx 4\Delta x$  or  $\approx 4\Delta y$  become dominant whereas smaller and larger scales are partially filtered out. The effect of BSM filtering on DA-LES results will be discussed in Section 6.6.

Another important aspect of the noise field  $\mathbf{r}$  is that it is not divergence-free:  $\nabla \cdot \mathbf{r} \neq 0$ , hence also  $\nabla \cdot \mathbf{F} \neq 0$ . If a rigid-lid assumption is applied (recommended by [43]) this is not a problem, as only the solenoidal part of the body force  $\mathbf{F}$  will affect the flow field; the divergent part of  $\mathbf{F}$  is immediately compensated by a modified pressure field  $p_{new} = p + p^*$ , where  $\nabla^2 p^* = \rho \nabla \cdot \mathbf{F}$ . However, in case of a movable free surface (which is standard for the 2D SWE), the divergent part of  $\mathbf{F}$  will induce unphysical and unwanted oscillations of the water level.

A solution to this problem may be to derive 2D noise from a vector potential function  $\Phi$ , yielding a solenoidal vector field  $\mathbf{r} = \nabla \times \Phi$ . If  $\Phi$  is not made up by white noise (equal energy density for all wave numbers  $k$ ) but by so-called “red noise” or “Brownian noise” (energy density satisfies a power-law  $E(k) \sim k^{-2}$ ), the spatial derivative  $\mathbf{r}$  renders exactly white noise in one dimension. In two dimensions, however, this operation always induces anisotropy: white noise in one dimension, red noise in the other. Hence, this approach is not helpful. A better approach is to modify  $\mathbf{r}$  by a projection step (see Schumann [75]):

$$\mathbf{r}_{new} = \mathbf{r} - \nabla\phi, \quad (6.20)$$

where the scalar potential field  $\phi$  is derived from the Poisson equation

$$\nabla^2\phi = \nabla \cdot \mathbf{r} \quad (6.21)$$

It is easily verified that  $\nabla \cdot \mathbf{r}_{new} = 0$ . (If the BSM filter has been applied, obviously  $\mathbf{Z}$  should be corrected instead of  $\mathbf{r}$ .) An advantage of this projection step is that the original white noise properties of  $\mathbf{r}$  are maintained. A drawback mentioned by [43] is the fact that solving an extra Poisson equation is computationally expensive; the additional computational cost is comparable to that of a pressure correction solver. This drawback is especially relevant for problems on unstructured meshes; if however a rectangular mesh is used, the solution of (6.20) and (6.21) can be significantly accelerated by means of a Fast Fourier (FFT) Poisson solver, which takes only a minimum of computational effort.

In fact, both the BSM filter and the divergence correction according to Schumann [75] are needed within DA-LES because the white noise field  $\mathbf{r}$  does not contain proper spectral information. The white noise generator provides equal energy density to all frequencies and wave numbers that are provided by the discretization, and there is no spatial correlation between these energy modes. The BSM-filter and divergence correction are required to construct a forcing field  $\mathbf{F}$  with acceptable properties. The effect of these operations on numerical results is discussed in Section 6.6.

The main advantage of the DA-LES backscatter model is that the formulation is both generic and easy to implement. The model is generic in the sense that it does not contain specific information about the flow geometry or main flow direction: it is fully isotropic, and all parameters needed in expressions (6.14)-(6.17) to compute  $\mathbf{F}$  are readily provided by the flow solver without the need to know detailed local turbulence properties. Equations (6.14)-(6.17) are applicable to arbitrary computational grids, but both the BSM filter and the divergence correction are best suited for structured rectangular meshes. In order to have an effective backscatter model, the horizontal resolution should be sufficiently fine: e.g. a mesh size  $\Delta x = \frac{1}{4}H$  is required in order to resolve 2DCS with length scales  $\mathcal{L} \approx 2H$ . The model has been tested by [42–45] for flow geometries with constant water depth  $H$ .

A number of improvements to DA-LES are desirable:

1. We aim at a more elegant way to obtain a divergence-free forcing field  $\mathbf{F}$ , without the need for solving an additional Poisson equation;
2. As the current white noise spectrum (without any scale-dependence or correlation of velocity modes) requires a lot of post-processing to make it acceptable, it is desirable to introduce a more proper turbulence length scaling (and possibly also directional anisotropy) into the spectrum of  $\mathbf{F}$ ;
3. The correctness of the scaling for  $F_{rms}$  in Equation (6.17) is questionable (especially the presence of the quantities  $\nu$ ,  $\Delta t$  and  $\sqrt[4]{c_f}$ ) and it should possibly be changed.

The three improvements listed here are addressed in Section 6.4.3.

### 6.4.2 2D-TRANS+KS

As a next step in the derivation of the DANSLES formulation for  $\mathbf{F}$ , we treat the 2D-TRANS+KS model proposed by Van Prooijen [99] and Van Prooijen and Uijttewaal [102]. Although this model has been originally derived from a transient RANS approach instead of a LES approach, its basic equations are virtually identical to DA-LES (except for the formulation of  $\mathbf{F}$ ). As in DA-LES and HLES, a simple eddy viscosity model (Elder's term) is adopted to model dissipation by 3D turbulence. The general framework of 2D-TRANS+KS is given by Equations (6.12)-(6.13) and (6.8), without HLES and with  $c_h = 0.15$  in order to account for terms (A) and (C).

The model for the backscatter term  $\mathbf{F} = (F_x, F_y)$  uses a 2D Kinematic Simulation (KS): an artificial 2D time-dependent velocity field  $\mathbf{u}_{ks} = (u_{ks}, v_{ks})$  is constructed, which mimicks the 2D turbulence components that would be generated by backscatter in a real 3D shallow flow. This artificial turbulence field determines the forcing term  $\mathbf{F}$ , which is used to trigger such 2D turbulence locally throughout the resolved flow field. The principle of KS-type modeling has been described by Fung et al. [36]; this principle is applied by [99, 102] in a 2DH context. The 2D-TRANS+KS model was calibrated by Van Prooijen [99] against a 3D LES computation of a uniform channel flow and a Direct Numerical Simulation (DNS) by Moser et al. [61] of the same flow type; the calibrated model has been applied to a SML geometry. Van Balen [96] re-calibrated 2D-TRANS+KS and applied it to shallow grid turbulence (see Uijttewaal and Jirka [92]).

The basic idea of 2D-TRANS+KS with respect to generation of 2D turbulence in shallow flows is the assumption of *local equilibrium* between production and dissipation of 2D turbulent kinetic energy. This equilibrium enables 2DCS to be maintained in a steady-state turbulent flow without other forcing mechanisms. In order to resolve eddies with scales  $\mathcal{L} \approx 2H$ , a sufficiently fine mesh resolution of e.g.  $\Delta x = \frac{1}{4}H$  is needed (similar to DA-LES). In case of sufficient resolution, two principal dissipation mechanisms for 2DCS can be identified within the basic equations (6.12)-(6.13): bottom friction and 3D eddy viscosity (Elder's term). These two terms should be balanced by production terms of similar form.

If  $\mathbf{u}_{ks}$  represents the 2D turbulent fluctuations which are desired, the production terms in  $\mathbf{F}$  should equal the two dissipation terms with opposite sign, with the resolved velocity  $\tilde{\mathbf{u}}$  replaced by the prescribed fluctuations  $\mathbf{u}_{ks}$ . To this end the nonlinear bottom friction term needs to be linearized; this is formally done by Van Prooijen for the case of a uniform turbulent channel flow with constant depth  $H$  and mean flow direction along the  $x$ -axis (see [99]). In order to generalize this result for application to general shallow flow domains (still with constant  $H$ ), the linearization of the friction term has to be slightly simplified. The associated error is only small because the eddy viscosity term dominates over bottom friction for most eddy length scales within  $\mathbf{u}_{ks}$  (as will be shown in Section 6.4.3). Adopting this simplified linearization, the resulting forcing term  $\mathbf{F}$  reads:

$$\mathbf{F} = \frac{c_f |U|}{H} \mathbf{u}_{ks} - \nu_t \left( \frac{\partial^2 \mathbf{u}_{ks}}{\partial x^2} + \frac{\partial^2 \mathbf{u}_{ks}}{\partial y^2} \right), \quad (6.22)$$

where  $|U|$  is the Euclidean norm of the resolved velocity vector field. The bottom friction production term is mainly effective on relatively large length scales whereas the viscosity term (due to its double spatial derivatives) acts on smaller scales. Equation (6.22) is linear in the prescribed KS velocity field  $\mathbf{u}_{ks}$ . Although this field is time-dependent, we look at the spatial structure first. Omitting time-dependency for the moment,  $\mathbf{u}_{ks} = (u_{ks}, v_{ks})$  is made up by a summation of 2D harmonic components according to:

$$\mathbf{u}_{ks}(x, y) = \frac{1}{\sqrt{N}} \sum_{n=1}^N \hat{\mathbf{u}}^n \sin(k_x^n x + k_y^n y + \phi^n), \quad (6.23)$$

where each component  $n$  has wave number  $\mathbf{k}^n = (k_x^n, k_y^n)$ , random phase  $\phi^n$  and prescribed amplitude  $\hat{\mathbf{u}}^n = (\hat{u}^n, \hat{v}^n)$ . In the implementations by Van Prooijen [99] and Van Balen [96], random wave numbers are generated by taking  $N$  uniformly distributed absolute values  $k^n$  within the range  $[0, k_{max}]$  (with resolution-dependent maximum wave number  $k_{max} \approx 2\pi/\Delta$ ) and  $N$  uniformly distributed wave direction angles  $\psi^n$  in the range  $[0, 2\pi]$ , after which we have  $k_x^n = k^n \cos \psi^n$  and  $k_y^n = k^n \sin \psi^n$ . The factor  $\frac{1}{\sqrt{N}}$  in (6.23), instead of the factor  $\frac{1}{N}$  used by the former authors, is necessary to keep the variance of  $\mathbf{u}_{ks}$  independent from  $N$ . Otherwise, the turbulent kinetic energy level induced by the KS model would be dependent on the number of harmonic components, which is inconvenient for practical applications.

The total computational effort of KS is proportional to  $N$  and to the computational mesh size; for values of  $N$  larger than  $\approx 1000$ , the KS method consumes the vast majority of all computational time, which makes 2D-TRANS+KS a costly method to apply. (The DANSLES model significantly reduces this large computational cost, see Section 6.4.3). When 2D-TRANS+KS is applied in the present study, the number of harmonic components is limited to  $N = 500$ .

The amplitudes  $\hat{u}$  and  $\hat{v}$  in (6.23) are determined by prescribed 2D spatial spectra of the streamwise and transverse turbulent kinetic energy. Following [96, 99], these spectra are given by the following 2D functions of dimensionless wave numbers  $k_x H$  and  $k_y H$ :

$$E_{uu}(k_x H, k_y H) = \frac{1}{2} \left\{ \underbrace{\alpha u_*}_{(A)} \underbrace{(\lambda k H) \exp(-\lambda k H)}_{(B)} \underbrace{\left(\frac{k_y}{k}\right)^\beta}_{(C)} \underbrace{\left(\frac{k_y}{k}\right)}_{(D)} \right\}^2 \quad \text{and} \quad (6.24)$$

$$E_{vv}(k_x H, k_y H) = \frac{1}{2} \left\{ \underbrace{\alpha u_*}_{(A)} \underbrace{(\lambda k H) \exp(-\lambda k H)}_{(B)} \underbrace{\left(\frac{k_y}{k}\right)^\beta}_{(C)} \underbrace{\left(-\frac{k_x}{k}\right)}_{(D)} \right\}^2, \quad (6.25)$$

in which  $\alpha$ ,  $\beta$  and  $\lambda$  are calibration constants and  $k = \sqrt{k_x^2 + k_y^2}$ . Calibration of the spectra by Van Balen [96] against 3D LES and DNS data resulted in  $\alpha = 1.0$ ,  $\beta = 3.0$  and  $\lambda = 0.4$  for a uniform channel flow (with friction Reynolds number  $Re_* = u_* H / \nu = 1000$ ). This calibration is considered representative for the laboratory-scale turbulent shallow flows discussed in the present thesis (with approximately the same value of  $Re_*$ ) and is therefore adopted here. The current calibration is sufficient for application in the present study, although Van Prooijen [99] indicates that improvements in the mathematical form of the prescribed spectra are possible.

The calibrated spectra  $E_{uu}$  and  $E_{vv}$ , normalized by the water depth, are shown in Figure 6.1. The total spectral energy can be found by analytical integration: the result of this operation can be found in Appendix C. It is only remarked here that a practical limit for the integration is given by the maximum wave number that can be resolved on the computational grid. For instance, a grid resolution  $\Delta x = \frac{1}{4}H$  allows for a maximum resolvable (dimensionless) wave number  $k_{max} H = 4\pi$ . If this value is applied as upper integration limit in Appendix C, approximately 99% of the theoretical spectral kinetic energy is resolved.

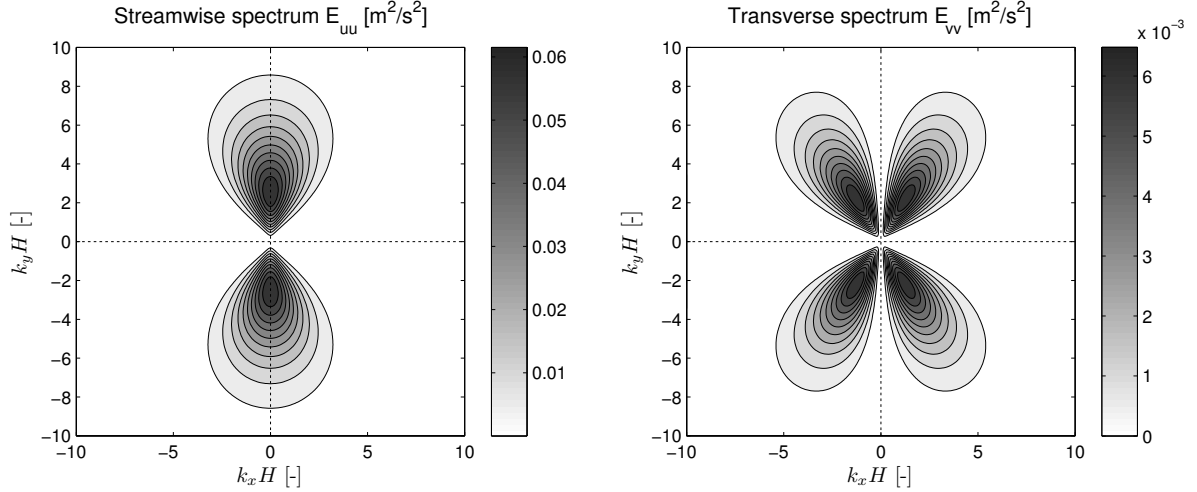


Figure 6.1: *Streamwise and transverse energy density spectra of  $\mathbf{u}_{ks} = (u_{ks}, v_{ks})$ .*

The amplitudes  $\hat{u}$  and  $\hat{v}$  are derived from the spectra as follows:

$$\hat{u} = k_{max}H \sqrt{2E_{uu}(k_xH, k_yH)} \quad \text{and} \quad \hat{v} = k_{max}H \sqrt{2E_{vv}(k_xH, k_yH)}, \quad (6.26)$$

where  $k_{max}$  is the resolution-dependent maximum wave number applied before. The factor  $k_{max}H$  is erroneously omitted in the implementations by [96, 99], but is essential to retrieve a kinetic energy level for  $\mathbf{u}_{ks}$  that is equal to the spectral energy content defined by  $E_{uu}$  and  $E_{vv}$ ; this is further explained in Appendix B.<sup>3</sup>

The expressions for the spectra  $E_{uu}$  and  $E_{vv}$  (as well as amplitudes  $\hat{u}$  and  $\hat{v}$ ) contain four contributions with an explicit physical meaning, denoted by factors (A)-(D) in Equations (6.24)-(6.25). Factor (A) is a velocity scaling factor, implying that the amplitude of  $\mathbf{u}_{ks}$  is proportional to the friction velocity  $u_*$ . The length scaling factor (B) implies that the 2D spectra have a global maximum at wave number  $k = 1/\lambda H$ , associated with a dominant wave length  $\mathcal{L} = 2\pi\lambda H \approx 2.5H$ . At lower wave numbers the amplitude scales linearly with  $kH$ . Hence the bulk of 2D forcing takes place at supra-depth length scales, in accordance with observations by Kernkamp and Uittenbogaard [49] and Uijttewaald and Booij [91]. The factor (C) introduces anisotropy between streamwise and transverse turbulence intensities, which is often present in uniform channel flows as well as shallow shear flows; for a calibration value  $\beta = 0$  this anisotropy would vanish and  $E_{uu}$  and  $E_{vv}$  would contain equal spectral energy. Finally, factor (D) ensures that  $\mathbf{u}_{ks}$  is divergence free. This can be seen as follows. Taking the divergence of Equation (6.23) yields:

$$\nabla \cdot \mathbf{u}_{ks} = \frac{1}{\sqrt{N}} \sum_{n=1}^N (\hat{u}^n k_x^n + \hat{v}^n k_y^n) \cos(k_x^n x + k_y^n y + \phi^n), \quad (6.27)$$

which shows that the requirement  $(\hat{u}^n k_x^n + \hat{v}^n k_y^n) = \hat{\mathbf{u}}^n \cdot \mathbf{k}^n = 0$  (satisfied by factor (D)) is sufficient to have  $\nabla \cdot \mathbf{u}_{ks} = 0$ , and also approximately  $\nabla \cdot \mathbf{F} \approx 0$ ; the latter is a desirable property for a backscatter model.

<sup>3</sup>For structured grids and associated structured discrete wave number space, an exact version of (6.26) is straightforwardly given by Equation (B.10) in Appendix B. In the present case of randomly generated wave numbers, (B.10) is sufficiently approximated by (6.26), which was confirmed by some tests.

Time-dependency within  $\mathbf{u}_{ks}$  can be introduced in several ways. The classical approach (see Fung et al. [36]) is to let all harmonic components be advected by the mean flow field, along fluid particle trajectories. This approach is coined Method 1 here, and reads:

$$\mathbf{u}_{ks}(x, y, t) = \frac{1}{\sqrt{N}} \sum_{n=1}^N \hat{\mathbf{u}}^n \sin \left( k_x^n \left( x - \int_0^t \bar{u} dt \right) + k_y^n \left( y - \int_0^t \bar{v} dt \right) + \phi^n \right) \quad (6.28)$$

Method 1 suggests that 2D turbulence is mainly advected from inflow to outflow boundary, rather than generated locally. Therefore, Van Prooijen [99, 102] proposes to make the amplitudes  $\hat{\mathbf{u}}^n$  time-dependent instead. This approach is coined Method 2:

$$\mathbf{u}_{ks}(x, y, t) = \frac{1}{\sqrt{N}} \sum_{n=1}^N \sqrt{2} \sin \left( \int_0^t (k_x^n \bar{u} + k_y^n \bar{v}) dt + \theta^n \right) \hat{\mathbf{u}}^n \sin (k_x^n x + k_y^n y + \phi^n), \quad (6.29)$$

where  $\theta^n$  (like  $\phi^n$ ) is another random phase vector. Method 2 involves actually a summation of standing waves, whereas Method 1 involves traveling waves only.

It is essential to Methods 1-2 that some mean velocity  $\bar{\mathbf{u}}$  is adopted for advection purposes; otherwise, kinematic perturbations within  $\mathbf{u}_{ks}$  would be advected by themselves and distort themselves, eventually turning the velocity field into uncorrelated noise. As  $\bar{\mathbf{u}}$  is not known a priori, the low-pass filtered HLES velocity field  $\bar{\mathbf{u}}^{temp}$  can be used instead, see Equation (6.10). However, it is observed by [99] that spatial variations in  $\bar{\mathbf{u}}$  or  $\bar{\mathbf{u}}^{temp}$  can distort the field  $\mathbf{u}_{ks}$  as well. Especially lateral velocity differences (lateral shear) induce spurious beat effects. This is why [96, 99] apply a constant advective velocity  $\mathcal{U}$  (in  $x$ -direction only) in the entire flow domain. Although this solution may be sufficient for uniform channel flows and relatively simple shallow shear flows, it is not suitable or realistic for general geometries. Therefore, a different approach is recommended in the present study. We let go of all temporal coherence of  $\mathbf{u}_{ks}$  by advection, and introduce time variation via the random phase vector  $\phi^n$  only. This approach is coined Method 3:

$$\mathbf{u}_{ks}(x, y, t) = \frac{1}{\sqrt{N}} \sum_{n=1}^N \hat{\mathbf{u}}^n \sin (k_x^n x + k_y^n y + \phi^n(t)) \quad (6.30)$$

It should be noted that Equation (6.30) resembles (6.23), except for the fact that  $\mathbf{u}_{ks}$  and  $\phi^n$  have become time-dependent. Method 3 is a robust solution for general domains with non-uniform flow fields, as it does not induce flow distortion effects.

An important effect of the loss of temporal coherence in Method 3 is the fact that the resulting kinetic energy content of the resolved velocity field  $\tilde{\bar{u}}$  becomes smaller; at two subsequent time levels, the kinematic fields  $\mathbf{u}_{ks}$  may contain harmonic components with opposite random phases  $\phi^n$  (i.e.  $\Delta\phi^n \approx \pm\pi$ ) which therefore will cancel out (at least partially). Hence, the 2D-TRANS+KS model requires some re-calibration when Method 3 is applied: the calibration factor  $\alpha$  should be larger. Computational tests showed that a value  $\alpha \approx 15$  for Method 3 yields approximately the same kinetic energy level as a value  $\alpha = 1.0$  for Methods 1-2.

Finally, a few other simplifications must be addressed which make the 2D-TRANS+KS model suitable for general flow situations. Originally the friction velocity  $u_*$  in (6.24)-(6.25) was a constant velocity (in  $x$ -direction only) applied in the entire flow domain (see [99]). For the sake of generality this constant must be replaced by a variable  $u_*$  that depends on the locally resolved velocity  $\tilde{\bar{u}}$ . Obviously this replacement will affect the results; however,



as  $u_*$  is only a scaling factor here and no advective velocity (like  $\bar{\mathbf{u}}$  in Methods 1-2), the variability of  $u_*$  will not induce significant distortion of the flow field.

The only remaining geometry-dependent element in the final 2D-TRANS+KS model is given by the anisotropy factor  $\beta = 3$ . This factor can be maintained for relatively simple flow cases with main flow direction along the  $x$ -axis; this includes not only straight channel flows but also relatively simple shallow shear flows like the SML and SLE geometries. For general shallow flow domains, a nonzero anisotropy factor  $\beta$  is obviously incorrect and hence  $\beta = 0$  should be adopted here. In Appendix C, the total spectral energy of  $E_{uu}$  and  $E_{vv}$  is derived for both  $\beta = 3$  and  $\beta = 0$ . In Section 6.6, the sensitivity of the numerical results to the value of  $\beta$  will be investigated.

It has been concluded by Van Prooijen [99,102] and Van Balen [96] that 2D-TRANS+KS is a suitable backscatter model for the type of shallow shear flows against which it has been tested. In the present section, the model has been slightly adapted in order to make it suitable for general flow situations; special attention has been paid to the time-dependency of the kinematic velocity field.

The key advantage of the KS-type formulations is the possibility to use detailed spectra to construct the velocity fluctuations needed; these spectra offer a very natural way to achieve a divergence-free forcing field and a proper length scaling. Although the backscatter model is based upon a few crude assumptions, both the structure of the fluctuations  $\mathbf{u}_{ks}$  and their relation to the forcing field  $\mathbf{F}$  have a certain physical basis. A disadvantage of 2D-TRANS+KS (apart from its high computational cost) is the fact that its original derivation and calibration was only valid for one specific flow case: a straight uniform channel flow. The generalization to shallow shear flows on general domains (as performed in this section) is not completely straightforward: it involves some additional assumptions as well as a recalibration of the model, which may lead to loss of accuracy. Nevertheless, this does not affect the advantages of the model.

Three desired improvements on DA-LES were listed at the end of Section 6.4.1. In fact, the first two improvements are accomplished by the present 2D-TRANS+KS model. In order to fully exploit these improvements, the computational effort of 2D-TRANS+KS should be significantly reduced and its relation to DA-LES should be clarified, in order to bridge the theoretical gap between both methods. Section 6.4.3 will address these topics.

### 6.4.3 The unified DANSLES formulation

This section treats the mathematical integration of DA-LES and 2D-TRANS+KS, yielding the DANSLES backscatter model. As before, the general framework of DANSLES is given by the Shallow Water Equations (6.12)-(6.13). These equations are supplemented with HLES to account for dissipation by term (B), and Elder's term (with  $c_h > \frac{1}{6}\kappa$ ) to account for dissipation by terms (A) and (C). The unification of DA-LES and 2D-TRANS+KS basically involves the integration of their respective expressions for  $\mathbf{F}$ .

DANSLES is motivated in multiple ways. First, we wish to "color" the white noise used in DA-LES in order to give it a more proper physical basis. Appropriate length scaling and optional anisotropy can be added to  $\mathbf{F}$  by adapting the spectrum of the noise, simultaneously enforcing solenoidality. Second, 2D-TRANS+KS should be accelerated for large values of  $N$ . Finally, it is desired to bridge the theoretical gap between DA-LES and 2D-TRANS+KS by examining the scaling for  $\mathbf{F}$ . The basic idea is to construct  $\mathbf{F}$  and  $\mathbf{u}_{ks}$  by means of 2D Inverse Fast Fourier Transformations (IFFT). This tool is very efficient in deriving coherent vector fields directly from a 2D energy density spectrum, while only adding random phase information (see Appendix B).

We start out with applying IFFT to 2D-TRANS+KS. To this end, the random wave numbers applied in 2D-TRANS+KS must be replaced by a 2D rectangular grid of wave numbers  $\mathbf{k} = (k_x, k_y)$  in order to resolve the spectral energy more accurately. This wave number domain is related to an associated 2D spatial rectangular mesh on which  $\mathbf{u}_{ks}$  is defined. This would imply that DANSLES, due to the IFFT operations, can be only applied to flows on rectangular grids, which is inconvenient for general shallow flow problems. A practical work-around however exists: the backscatter model can be defined on an *auxiliary* rectangular grid which covers the entire computational domain. Each time step the computation of  $\mathbf{u}_{ks}$  is performed on this auxiliary grid, after which the resulting quantities are interpolated toward the “real” computational mesh. (This interpolation procedure induces only small errors that are negligible for practical cases, given the over-all empirical character of backscatter models.)

For use in the present chapter, we define an auxiliary rectangular grid with length  $L_x$  and width  $L_y$ , using a local reference frame with  $(x, y) = (0, 0)$  in the lower left corner. We adopt  $\Delta x = \Delta y = H/4$  in order to resolve 2D structures with length scales  $\mathcal{L} > 2H$ . The grid size is  $(M, N)$  with  $M = L_x/\Delta x$  and  $N = L_y/\Delta y$ . Local coordinates are given by:

$$x = j\Delta x \quad (j = 0, 1, 2, \dots, M-1) \quad \text{and} \quad y = k\Delta y \quad (k = 0, 1, 2, \dots, N-1) \quad (6.31)$$

Associated with the spatial domain  $(x, y)$ , a wave number domain  $(k_x, k_y)$  is defined having the same size  $(M, N)$ . The wave numbers are given by:

$$k_x = 2\pi m/L_x \quad (m = 0, 1, \dots, M-1) \quad \text{and} \quad k_y = 2\pi n/L_y \quad (n = 0, 1, \dots, N-1) \quad (6.32)$$

The upper bounds of the wave number domain are given by  $\hat{k}_x = 2\pi/\Delta x$  and  $\hat{k}_y = 2\pi/\Delta y$ . A basic property of 2D-TRANS+KS is the use of  $N$  random wave numbers, after which  $N$  harmonic components must be summed (see Section 6.4.2). The associated computational cost can become unacceptable for large values of  $N$ . This limits the ability of 2D-TRANS+KS to accurately represent the spectrum of perturbations. In contrast, DANSLES uses the entire non-random wave number space given by (6.32). In this way not only the full energy density spectrum for  $\mathbf{u}_{ks}$  is accurately covered, but also a Fast Fourier approach can be applied which accelerates the summation of harmonic components (it requires only  $\mathcal{O}(N \log N)$  operations instead of  $\mathcal{O}(N^2)$ ).

We revisit Equation (6.23), in which  $\mathbf{u}_{ks}$  was defined. Without loss of generality we may replace the sine operator by a cosine operator. Furthermore, the number of harmonic components is equal to  $MN$  here instead of  $N$ . Then, adopting indices  $(m, n)$  instead of  $n$  and using Method 3 from Equation (6.30) for time-dependency, we obtain:

$$\mathbf{u}_{ks}(x, y, t) = \frac{1}{\sqrt{MN}} \sum_{m=0}^{M-1} \sum_{n=0}^{N-1} \hat{\mathbf{u}}^{m,n} \cos(k_x^m x + k_y^n y + \phi^{m,n}(t)) \quad (6.33)$$

Substitution of (6.31) and (6.32) into (6.33) yields:

$$\mathbf{u}_{ks}(x, y, t) = \frac{1}{\sqrt{MN}} \sum_{m=0}^{M-1} \sum_{n=0}^{N-1} \hat{\mathbf{u}}^{m,n} \cos(2\pi\{jm/M + kn/N\} + \phi^{m,n}(t)), \quad (6.34)$$

As explained in Appendix B, expression (6.34) is equal to the real part of the 2D IFFT transform ( $\mathcal{F}_2^{-1}$ ) of  $\tilde{\mathbf{u}}$ , where  $\tilde{\mathbf{u}}^{m,n} = \hat{\mathbf{u}}^{m,n} \exp(i\phi^{m,n})$  is a complex amplitude for  $\mathbf{u}_{ks}$  including the time-dependent random phase  $\phi$ . This relation is denoted by:  $\mathbf{u}_{ks} = \Re(\mathcal{F}_2^{-1}\{\tilde{\mathbf{u}}\})$ . For a proper choice of  $\phi$ , the imaginary part vanishes and (6.34) reduces to:

$$\mathbf{u}_{ks} = \mathcal{F}_2^{-1}\{\tilde{\mathbf{u}}\} = \mathcal{F}_2^{-1}\{\hat{\mathbf{u}}e^{i\phi}\} \quad (6.35)$$

In order to have zero imaginary part, one must consider the important role of the Nyquist wave numbers which are related to wave aliasing:  $k_x^* = \pi/\Delta x = \frac{1}{2}\hat{k}_x$  and  $k_y^* = \pi/\Delta y = \frac{1}{2}\hat{k}_y$ . The Nyquist wave numbers correspond with the lines  $m = M/2$  and  $n = N/2$  inside the 2D wave number domain  $(k_x, k_y)$ ; these lines divide this domain into four quadrants. In two adjacent quadrants, the random phases  $\phi^{m,n}$  may be chosen freely within the range  $[0, 2\pi]$  for each index pair  $(m, n)$ . It is convenient to choose the lower-left and lower-right quadrant for this. The predefined amplitudes  $\hat{\mathbf{u}}$  in both quadrants should mirror one another:  $\hat{\mathbf{u}}^{M-m, n} = \hat{\mathbf{u}}^{m, n}$ . Next, the complex amplitudes are made up by  $\tilde{\mathbf{u}}^{m, n} = \hat{\mathbf{u}}^{m, n} \exp(i\phi^{m, n})$ . The upper two quadrants must contain the complex conjugates of  $\tilde{\mathbf{u}}$  in the lower two quadrants. Each phase  $\phi$  should exactly mirror the corresponding value of  $\phi$  in the opposite quadrant, with negative sign, whereas the values for  $\hat{\mathbf{u}}$  are unaltered:

$$\hat{\mathbf{u}}^{M-m, N-n} = \hat{\mathbf{u}}^{m, n} \quad \text{and} \quad \phi^{M-m, N-n} = -\phi^{m, n} \quad (6.36)$$

These conditions are sufficient to obtain a fully real IFFT transform. A more elaborate explanation about the role of Nyquist wave numbers can be found in Appendix B.

In the above expressions, Method 3 has been adopted for time-dependency. Instead, also Method 1 could have been implemented by making the phases  $\phi^{m, n}$  a function of time (inducing traveling waves), or Method 2 by making the amplitudes  $\hat{\mathbf{u}}^{m, n}$  time-dependent (inducing standing waves). These methods are however not applicable to general shallow flow problems, as explained in Section 6.4.2. Moreover, making  $\hat{\mathbf{u}}$  or  $\phi$  time-dependent requires an advective velocity field  $\bar{\mathbf{u}}$  which can be spatially varying, see Equations (6.28)-(6.29); but  $\hat{\mathbf{u}}$  and  $\phi$  are quantities in a spectral domain, not in a spatial domain. This implies that within DANSLES only a spatially constant advective velocity  $\mathcal{U}$  is allowed. Because such constant advective fields are not workable for general flow domains, Method 1 and 2 cannot be applied. Hence, Method 3 is the only workable approach for time-dependency within DANSLES; this approach is consistent with DA-LES as well.

Analogous to 2D-TRANS+KS, the amplitudes  $\hat{\mathbf{u}} = (\hat{u}, \hat{v})$  are derived from calibrated 2D spectra  $E_{uu}$  and  $E_{vv}$  given by Equations (6.24)-(6.25). The energy content of these spectra has been elaborated in Appendix C. Following Equation (B.10) in Appendix B, the amplitudes  $\hat{\mathbf{u}}$  can be derived from the spectra (for all  $m, n$ ) as follows:

$$\hat{u} = \sqrt{(\hat{k}_x H)(\hat{k}_y H)} \sqrt{2E_{uu}(k_x H, k_y H)}, \quad \hat{v} = \sqrt{(\hat{k}_x H)(\hat{k}_y H)} \sqrt{2E_{vv}(k_x H, k_y H)} \quad (6.37)$$

When substituting (6.24) and (6.25) into (6.37), we can write  $\hat{u}$  and  $\hat{v}$  in a compact manner:  $\hat{\mathbf{u}} = \hat{\mathbf{A}}u_*$ , where  $\hat{\mathbf{A}} = (\hat{A}_x, \hat{A}_y)$  is given by

$$\begin{aligned} \hat{A}_x &= \sqrt{(\hat{k}_x H)(\hat{k}_y H)} \left\{ \alpha(\lambda k H) \exp(-\lambda k H) (k_y/k)^\beta (k_y/k) \right\} \quad \text{and} \\ \hat{A}_y &= \sqrt{(\hat{k}_x H)(\hat{k}_y H)} \left\{ \alpha(\lambda k H) \exp(-\lambda k H) (k_y/k)^\beta (-k_x/k) \right\}, \end{aligned} \quad (6.38)$$

Now we encounter a problem that did not occur within 2D-TRANS+KS:  $u_*$  is a variable within the spatial domain  $(x, y)$  only, whereas  $\hat{\mathbf{A}}$  is merely a function of the spectral domain  $(k_x, k_y)$ . This problem can be circumvented by the assumption that the spatial variability of  $u_*$  and the spectral variability of  $\hat{\mathbf{A}}$  are not correlated. Assuming this, the 2D IFFT operation (6.35) can be rewritten as:

$$\mathbf{u}_{ks} = u_* \mathcal{F}_2^{-1} \{\tilde{\mathbf{A}}\}, \quad (6.39)$$

where we have defined  $\tilde{\mathbf{A}} = \hat{\mathbf{A}}e^{i\phi}$ . Hence, the operator  $\mathcal{F}_2^{-1}$  acts on a fully spectral quantity  $\tilde{\mathbf{A}}$  whereas the output is a fully spatial quantity  $\mathbf{u}_{ks}/u_*$ .

We are now able to construct  $\mathbf{u}_{ks}$  using 2D IFFT operations; subsequently,  $\mathbf{F}$  could be computed using Equation (6.22). However, it is also possible to construct  $\mathbf{F}$  directly with the help of 2D IFFT operations. This is done as follows. When we substitute the Elder formulation  $\nu_t = c_h u_* H$  into (6.22), as well as the identity  $c_f |U| = \sqrt{c_f} u_*$ , we obtain:

$$\mathbf{F} = \frac{\sqrt{c_f} u_*}{H} \mathbf{u}_{ks} - c_h u_* H \nabla^2 \mathbf{u}_{ks} \quad (6.40)$$

Now, if we assume that  $u_*$  and  $\hat{\mathbf{A}}$  are not correlated (as before), we can derive the Laplacian of  $\mathbf{u}_{ks}$  from another 2D IFFT operation:

$$\nabla^2 \mathbf{u}_{ks} = -u_* \mathcal{F}_2^{-1} \{k^2 \tilde{\mathbf{A}}\} \quad (6.41)$$

Substitution of (6.39) and (6.41) into (6.40) and assuming an approximately constant water depth  $H$  finally yields:

$$\mathbf{F} = \frac{u_*^2}{H} \left[ \underbrace{\sqrt{c_f} \mathcal{F}_2^{-1} \{\tilde{\mathbf{A}}\}}_{(A)} + \underbrace{c_h \mathcal{F}_2^{-1} \{(kH)^2 \tilde{\mathbf{A}}\}}_{(B)} \right] \quad (6.42)$$

This expression represents the complete DANSLES backscatter model. The factor between square brackets contains two terms: term (A) represents the production of 2D turbulence by bottom friction, whereas term (B) accounts for the contribution by eddy viscosity. The KS calibration constants  $\alpha$ ,  $\beta$  and  $\lambda$  have been incorporated into the quantity  $\tilde{\mathbf{A}}$ ; in the present calibration, we have  $\alpha = 15$  (see the final part of Section 6.4.2),  $\beta = 3$  and  $\lambda = 0.4$ . For general shallow flow problems, in the absence of one dominant flow direction, it has been argued that spectral anisotropy should be discarded ( $\beta = 0$ ). Comparing DANSLES results for  $\beta = 3$  and  $\beta = 0$  can provide some useful insight into the sensitivity of 2DH turbulence to prescribed anisotropy (see Section 6.6).

Practically, Equation (6.42) is implemented as follows: the terms  $\tilde{\mathbf{A}}$  and  $(kH)^2 \tilde{\mathbf{A}}$  are constructed within the wave number domain, on the auxiliary grid given by (6.31)-(6.32). Each time step only the random phase information needs to be replaced, whereas the amplitude information remains unchanged. The results of the IFFT operations  $\mathcal{F}_2^{-1} \{\tilde{\mathbf{A}}\}$  and  $\mathcal{F}_2^{-1} \{(kH)^2 \tilde{\mathbf{A}}\}$  are interpolated from the auxiliary grid toward the computational mesh, after which finally  $\mathbf{F}$  can be computed in the spatial domain.

For each separate wave number  $k$ , the ratio between terms (A) and (B) is given by:  $F_{visc}/F_{fric} = c_h (kH)^2 / \sqrt{c_f}$ , which is of the order  $\approx (kH)^2$  (as  $c_h$  and  $\sqrt{c_f}$  often share equal order of magnitude). This implies that eddy viscosity dominates over friction for all wave numbers  $kH > 1$ , i.e. all wave lengths  $L < 2\pi H \approx 6.3H$ . As the calibrated 2D spectra have global maxima at wave length  $\mathcal{L} = 2\pi\lambda H \approx 2.5H$ , we can conclude that eddy viscosity is the dominant contribution within (6.42). The bottom friction term only dominates at the largest length scales, in the range  $0 < kH < 1$  which represents less than 1% of the total spectral energy.

The dominance of eddy viscosity also follows from the spectral energy contents derived in Appendix C. If we divide the energy content of  $H^2 \nabla^2 \mathbf{u}_{ks}$  (derived in Equations (C.13)-(C.14)) by the energy content of  $\mathbf{u}_{ks}$  (computed in Equations (C.10)-(C.11)) for  $\beta = 3$  and

$\beta = 0$ , we consistently find a ratio  $\frac{8257.88}{4.027} = \frac{1179.70}{0.575} = \frac{15100.12}{7.363} = 840/(2\lambda)^4 \approx 2050.8$ . This implies that the total energy contributed by eddy viscosity is over 3 orders of magnitude larger than the total contribution by bottom friction.

A measure for the total production rate of 2D turbulent kinetic energy for each dimension is given by the quantities  $F_{rms,x}^2$  and  $F_{rms,y}^2$ , where  $F_{rms,x}$  and  $F_{rms,y}$  are the root-mean-square (RMS) values of the amplitudes of the forcing field  $\mathbf{F}$ . These values equal the square root of the the energy content of the associated spectra (see Equation (B.9) in Appendix B). When we neglect term (A) in (6.42) and substitute expressions (C.13)-(C.14), we find the following RMS values for  $\mathbf{F}$  for  $\beta = 3$  (anisotropic model):

$$F_{rms,x} = \frac{u_*^2}{H} c_h \alpha \sqrt{8257.88} \quad \text{and} \quad F_{rms,y} = \frac{u_*^2}{H} c_h \alpha \sqrt{1179.70} \quad (6.43)$$

A dimensionally averaged RMS value is then given by:

$$F_{rms} = \frac{u_*^2}{H} c_h \alpha \sqrt{(8257.88 + 1179.70)/2} = \frac{u_*^2}{H} c_h \alpha \sqrt{4718.79} \quad (6.44)$$

Equivalently, we find for  $\beta = 0$  (isotropic model):

$$F_{rms} = F_{rms,x} = F_{rms,y} = \frac{u_*^2}{H} c_h \alpha \sqrt{15100.12} \quad (6.45)$$

Comparing (6.45) with (6.43)-(6.44) shows that  $\alpha$  should be slightly adjusted if  $\beta = 0$  is adopted, as the isotropic model contains more spectral energy by itself. While we have  $\alpha = 15$  for  $\beta = 3$ , we find that  $\beta = 0$  requires  $\alpha = 15\sqrt{4718.79/15100.12} = 15\sqrt{5/16} \approx 8.4$  in order to have the same total energy content in both cases (see Appendix C).

The DANSLES backscatter model derived so far is actually a version of 2D-TRANS+KS, adjusted in such a way that IFFT operations can be applied. It will be shown now that IFFT's are applicable to DA-LES as well. To this end we revisit the basic (unfiltered) DA-LES formulations (6.14)-(6.17):  $\mathbf{F} = F_{rms}\mathbf{r}$ , where  $\mathbf{r}$  is random 2D white noise and  $F_{rms}$  satisfies

$$F_{rms} = F_{rms,x} = F_{rms,y} = c_B \frac{|U|}{H} \sqrt{\frac{\nu\sqrt{c_f}}{\Delta t}}, \quad (6.46)$$

with calibration constant  $c_B = 55$  (see Hinterberger [42]), and  $F_{rms}$  having precisely the same physical interpretation as  $F_{rms}$  in Equations (6.43)-(6.45).

Now, it is possible to derive  $\mathbf{r}$  from a 2D IFFT operation, according to:

$$\mathbf{r} = \mathcal{F}_2^{-1}\{\tilde{\mathbf{r}}\}, \quad (6.47)$$

where we have defined  $\tilde{\mathbf{r}} = \hat{\mathbf{r}}e^{i\phi}$ . The amplitude field is simply a constant function  $\hat{\mathbf{r}} = 1$ , whereas the random phase field  $\phi$  satisfies the requirements given in (6.36) to render  $\mathbf{r}$  fully real. Following Appendix B, we find that  $\text{var}(\mathbf{r}) = 1$  exactly.

Paradoxically, calibration of  $\hat{\mathbf{r}}$  via the spectrum is not possible in this case. This is due to the fact that, for white noise, the spectral energy of  $\mathbf{r}$  is not invariant but resolution-dependent. Whereas the total energy content of 2D-TRANS+KS spectra is finite and bounded for  $k_{max} \rightarrow \infty$  (implying infinite resolution), the spectral energy content of white noise is proportional to  $k_{max}$  and thus becomes infinite in the continuous limit. This remains true if the BSM filter (see Section 6.4.1) is applied. Therefore calibration of white noise spectra is of no use; nonetheless, setting  $\hat{\mathbf{r}} = 1$  is fully sufficient here to obtain  $\text{var}(\mathbf{r}) = 1$  and thus to have a finite and invariant total energy content after all.

The application of IFFT's to DA-LES provides the opportunity to “color” the white noise in the spectral domain, leading to spectra such as given by Figure 6.1. Anisotropy and dominant wave lengths can be added, as well as a natural constraint to obtain a divergence-free vector field, see (6.27). In fact, all this has already been achieved for the 2D-TRANS+KS and DANSLES models and there is no need to repeat it here. A relevant topic however is the question why the scaling factors  $F_{rms}$  for DANSLES and DA-LES (given by (6.43)–(6.45) and (6.46) respectively) have such different mathematical forms.

It is conjectured here that the scaling for  $F_{rms}$  in Equation (6.46) contains several unphysical elements. Firstly, the molecular viscosity  $\nu$  is expected to play a role in micro-scale 3D energy dissipation, rather than in the generation of macro-scale 2D eddies. Secondly, a numerical quantity like  $\Delta t$  (related to discretization) should not be applied in the context of a formulation that models a physical process. Finally, although the bottom friction coefficient  $c_f$  obviously plays a role in backscatter models, the 4<sup>th</sup> root of it is unlikely to have a reliable physical meaning.

In order to improve the factor  $F_{rms}$  for DA-LES in (6.46), the assumptions given by Equations (6.15) and (6.16) need to be revisited. Hinterberger et al. [42, 43] assume that the production rate  $P_{2D}$  of 2D turbulent kinetic energy is proportional to  $F_{rms}^2$ , see (6.15). However, although this square proportionality appears to be often present in results, it lacks a good physical basis. In general mechanics, an energy production rate (or power) is not given by a squared force and a time scale, but by the inner product of a single force and a velocity scale. Therefore, instead of (6.15), it can be stated that:

$$P_{2D} \sim F_{rms}|U|, \quad (6.48)$$

and consequently  $F_{rms} \sim P_{2D}/|U|$  instead of  $F_{rms} \sim \sqrt{P_{2D}/\Delta t}$ . In this way we get rid not only of the time step  $\Delta t$ , but also of an unnecessary square root. The next step is to revisit the ratio between 2D and 3D kinetic energy production. According to (6.16), we have:

$$\frac{P_{2D}}{P_{3D}} \sim \frac{1}{Re_*} = \frac{\nu}{u_*H}, \quad (6.49)$$

where the friction Reynolds number  $Re_* = u_*H/\nu$  is of the order 500–1000 in the computations performed by Hinterberger et al. [43–45]); these values of  $Re_*$  are also representative for the present study. However, Hinterberger et al. emphasize that the ratio between 2D and 3D turbulent kinetic energy level in a straight channel flow is approximately 15% (see [43, 45]), whereas based on  $Re_*^{-1}$  a ratio near 0.001–0.002 would be expected, which is quite a different order of magnitude. It is conjectured here that the molecular viscosity  $\nu$  is not quite important for scaling 2D turbulent kinetic energy production on macro-scale. If we assume now that we may replace  $\nu$  by the eddy viscosity  $\nu_t$ , we obtain a ratio  $P_{2D}/P_{3D}$  which is in much better agreement with the ratio 15% found by [43, 45]. If we furthermore substitute the Elder formulation  $\nu_t = c_h u_* H$  (for instance), we find:

$$\frac{P_{2D}}{P_{3D}} \sim \frac{\nu_t}{u_*H} = \frac{c_h u_* H}{u_* H} = c_h \quad (6.50)$$

As  $c_h = \kappa/6$  by default but often has a value 0.1–0.2 in practice, we are close to the required ratio of 15%. It should be stressed that this simple but attractive result is based on a few crude assumptions about the relation between  $P_{2D}$  and  $P_{3D}$ , which may be subject to further research. Expression (6.50) is by no means a universal law. When we nonetheless adopt (6.50), (6.16) can be reworked into:

$$P_{2D} \sim P_{3D}c_h = \frac{|U|u_*^2}{H}c_h \quad (6.51)$$

Combination of (6.48) and (6.51) finally yields a new scaling factor  $F_{rms}$  for DA-LES:

$$F_{rms} = \frac{u_*^2}{H}c_h c_B, \quad (6.52)$$

with calibration constant  $c_B \gg 55$  now. Comparing this expression with (6.42) and (6.43)-(6.45), we observe that the scaling of re-scaled DA-LES is quite similar to the scaling of DANSLES. This similarity is helpful to calibrate  $c_B$ . As DA-LES is an isotropic formulation, we should compare with (6.45) for the case  $\beta = 0$ . Combination of (6.52) and (6.45) yields:

$$c_B = \alpha\sqrt{15100.12}, \quad (6.53)$$

hence  $c_B \approx 1032$  for  $\alpha \approx 8.4$ . A few numerical tests (not shown in this chapter) have indicated that re-scaled DA-LES with this value of  $c_B$  results in turbulent kinetic energy levels close to the original DA-LES version with  $c_B = 55$ . For both versions of DA-LES, the resulting energy levels are proportional to  $c_B^2$  (at least in the absence of other forcing mechanisms). It is concluded that the re-scaled and re-calibrated version of DA-LES is suitable for use in practice (like the original version). Yet, as this method still applies simple white noise instead of ‘‘colored noise’’ stemming from spectra, it is much more appropriate to adopt the complete version of DANSLES given by Equation (6.42).

The discussion outlined above has shown that DA-LES and 2D-TRANS+KS are equivalent, under the assumption that  $F_{rms}$  within DA-LES can be re-scaled. The theoretical gap between both backscatter models has thus been bridged, while (6.42) contains the unified model. The DANSLES approach offers an elegant and calibrated integration of two existing backscatter methods, which combines most of their respective advantages and is both fast and easy to implement.

## 6.5 Description of the 2DH model implementation

The DANSLES backscatter model and other 2D turbulence models encountered in the previous sections are tested against three basic shallow flow geometries. A Straight Channel Flow (SCF) geometry has been used to calibrate DANSLES, while existing calibrations are adopted for the other models. The performance of the various models with respect to generation of 2D turbulence patterns can be easily compared for the SCF case. The calibrated DANSLES model and various other models are subsequently tested against basic SML and SLE geometries; the results are compared with 3D LES results for these flow cases, presented in Chapter 4. The present section describes the 2DH numerical solver used to test the respective turbulence models, as well as the required model input.

### 6.5.1 Numerical solver (FINLAB)

The computational framework for the implementation of various turbulence models is a sophisticated numerical flow solver by Laheur [52], named FINLAB. This is an open-source free-surface solver based on the Finite Element Method; it solves either the 2DH Shallow Water Equations or the 3D Navier-Stokes Equations, using an unstructured computational mesh of triangles or tetrahedrons respectively. The use of an unstructured grid enables the user to treat complex flow geometries in a relatively easy way.

The FINLAB model is intensively utilized in civil engineering practice. It has been developed by Delft University of Technology and previously by the hydraulic engineering company Svašek Hydraulics (Rotterdam, Netherlands); the model is being applied and tested on a regular basis by Svašek Hydraulics under the name FINEL. Although for research purposes it might be easier to construct a simple 2D solver on a structured rectangular mesh (in analogy with the rigid-lid 3D LES implementation used in Chapters 4-5), it is worthwhile to test the present turbulence models by means of a state-of-the-art numerical model that is actually used in engineering practice. The use of a free surface in this chapter is not problematic for the comparison of results with rigid-lid 3D LES data, as only quasi-stationary turbulent flows with a negligible water level variation are considered. It is not aimed here to describe details of the advanced numerical concept of the FINLAB model; all relevant mathematical background (and more) can be readily found in Labour [52]. Only a brief overview of relevant aspects is given here.

The discretization of FINLAB is based on a combination of the Continuous Galerkin (CG) and Discontinuous Galerkin (DG) approach, using continuous linear elements for approximating the piezometric level and discontinuous linear elements for velocity components. These elements are either triangles or tetrahedrons; its degrees of freedom (state variables) are located at element nodes. For 2D problems the number of DG degrees of freedom is about 6 times the number of CG degrees of freedom; for 3D problems the ratio DG/CG is even about 24. Within FINLAB, CG and DG techniques have been advantageously blended into an innovative approach coined GIS (Galerkin Interface Stabilization). GIS is applied to simultaneously stabilize the momentum advection terms and prevent possible instabilities due to the continuity constraint. Moreover, for the over-all system of equations it is sufficient to use the CG degrees of freedom only, which strongly reduces the size of the global linear system and the amount of work needed to solve it. Hence, we get the accuracy of a DG method at the price of only CG computational effort.

The system of linear equations is solved using the iterative matrix solver BICGSTAB with efficient pre-conditioning. For time integration the implicit Fractional Step method (see Bristeau et al. [19]) is used. The resulting numerical implementation has second-order accuracy in both space and time. The momentum advection terms are effectively stabilized without the need for additional artificial diffusion. Numerical stability is achieved for Courant-Friedrichs-Lévy (CFL) numbers up to about 5–10.

## 6.5.2 Model input

In this chapter mainly the 2DH free-surface version of FINLAB is applied. Omitting all options of the model which are irrelevant for this study, the model solves the Shallow Water Equations given by (6.12)–(6.13). The bottom friction coefficient  $c_f$  is given by Equation (6.6), taking  $\kappa = 0.4$  and  $\nu = 10^{-6} \text{ m}^2/\text{s}$ , while the Elder formulation (6.8) and HLES subgrid-scale model from (6.9)–(6.11) are applied to account for the various dissipation effects described in Section 6.3. For Elder’s term a coefficient  $c_h = 0.15$  is adopted, see Van Prooijen and Uijttewaai [102]. For the backscatter forcing field  $F_i$  either DA-LES, 2D-TRANS+KS or DANSLES can be applied. In previous sections the resolved velocity field has been denoted by  $\tilde{u}$ ; in the remaining part of this chapter, the filtering operator  $(\overline{\dots})$  and depth-averaging operator  $(\overline{\dots})$  will be omitted.

Equations (6.12)–(6.13) are to be completed with appropriate initial conditions and boundary conditions. It is sufficient to let all flow cases develop from an initial state of rest. At inflow boundaries, either a constant uniform inflow velocity or a fully turbulent velocity profile (in depth-averaged form) can be used. The latter is necessary for shallow flows



without intrinsic topographical forcing mechanisms to trigger 2DCS, see Chapter 4 and Kernkamp and Uittenbogaard [49]. An option to implement such inflow perturbations is depth-averaging the 3D turbulent inflow profiles applied throughout Chapter 4. A simpler approach however is to construct a kinematic velocity field  $\mathbf{u}_{ks} = (u_{ks}, v_{ks})$  along the inflow boundary, using DANSLES expression (6.39), and to superimpose this field upon the otherwise uniform inflow velocity  $U_{in}$ . The latter approach is adopted here. Along impermeable sidewalls partial slip boundary conditions are imposed, assuming hydraulically smooth walls (which is valid in the present laboratory conditions) and using the same local friction coefficient that is applied for bottom friction. At outflow boundaries, a uniform piezometric level  $h = 0$  is imposed.

The following implementations for the forcing field  $F_i$  are tested:

1.  $F_i = 0$ , no inflow perturbations;
2.  $F_i = 0$ , turbulent inflow boundary condition (kinematic velocity field);
3. DA-LES, BSM-filtered (see (6.18)-(6.19));
4. DA-LES, unfiltered (i.e. purely white noise);
5. DA-LES, unfiltered with zero divergence (see (6.20)-(6.21));
6. 2D-TRANS+KS with Method 1 for time-dependency (see (6.28));
7. 2D-TRANS+KS with Method 2 for time-dependency (see (6.29));
8. 2D-TRANS+KS with Method 3 for time-dependency (see (6.30));
9. DANSLES with  $\beta = 3$  (anisotropic backscatter model);
10. DANSLES with  $\beta = 0$  (isotropic model).

Implementation no. 2 is the only case where an explicit turbulent inflow boundary condition is imposed. In all cases, the Elder formulation and the HLES subgrid-scale model are applied. For HLES most default parameter values advised by [49,95] are applied:  $\gamma = 0.236$  and  $f_{lp} = 0.3$ , see Equation (6.11). The low-pass filtering time scale in (6.10) has been set to  $\tau = 30$  s; this is roughly twice the Eulerian time scale associated to the passage of 2DCS through a cross-section inside the tested shallow flow geometries. (Numerical tests indicated that, for the present geometries, the method is not very sensitive to variations of the filtering time if at least  $\tau > 15$  s.) For use in DA-LES the original calibration by Hinterberger et al. [43] is adopted: the dimensionless model constant is set to  $c_B = 55$ , see (6.17). For use in 2D-TRANS+KS we adopt the calibrated energy density spectra by [96,99], setting  $\lambda = 0.4$ ,  $\beta = 3$  and  $\alpha = 1$  for Methods 1–2 (resp.  $\alpha = 15$  for Method 3); furthermore, the number of harmonic components is set to  $N = 500$ . For DANSLES we have  $\alpha = 15$  for  $\beta = 3$  and  $\alpha = 8.4$  for  $\beta = 0$ , while  $\lambda$  remains unchanged and the constant depth parameter is set to  $H = 0.1$  m.

The 2DH numerical model described above is tested against the Straight Channel Flow (SCF), Shallow Mixing Layer (SML) and Shallow Lateral Expansion (SLE) geometries, which will be henceforward referred to by their abbreviations. These geometries correspond to three basic types of 2DCS generation defined by Jirka [47], see also Section 2.2.3. Figure 6.2 outlines the three flow geometries and their basic length and velocity scales. Most geometric parameters are equal to those in Chapter 4:  $L = 20$  m,  $L_{in} = 5$  m,  $B_2 = 2$  m,  $D = B_1 = 1$  m,  $H = 0.1$  m,  $U_0 = U_1 = 0.30$  m/s and  $U_2 = 0.10$  m/s (see Table 4.1). The SLE is equivalent to Case 2 in Chapter 4 and the SML is equivalent to Case 4.

In order to enable an easy comparison of output data, the unstructured 2DH FINLAB grids of the SCF, SML and SLE geometries have been chosen “quasi-structured”. A structured rectangular grid is initially generated using square grid cells with mesh size  $\Delta x = \Delta y$ . Subsequently each square cell is split into two right-angled triangular elements, while all

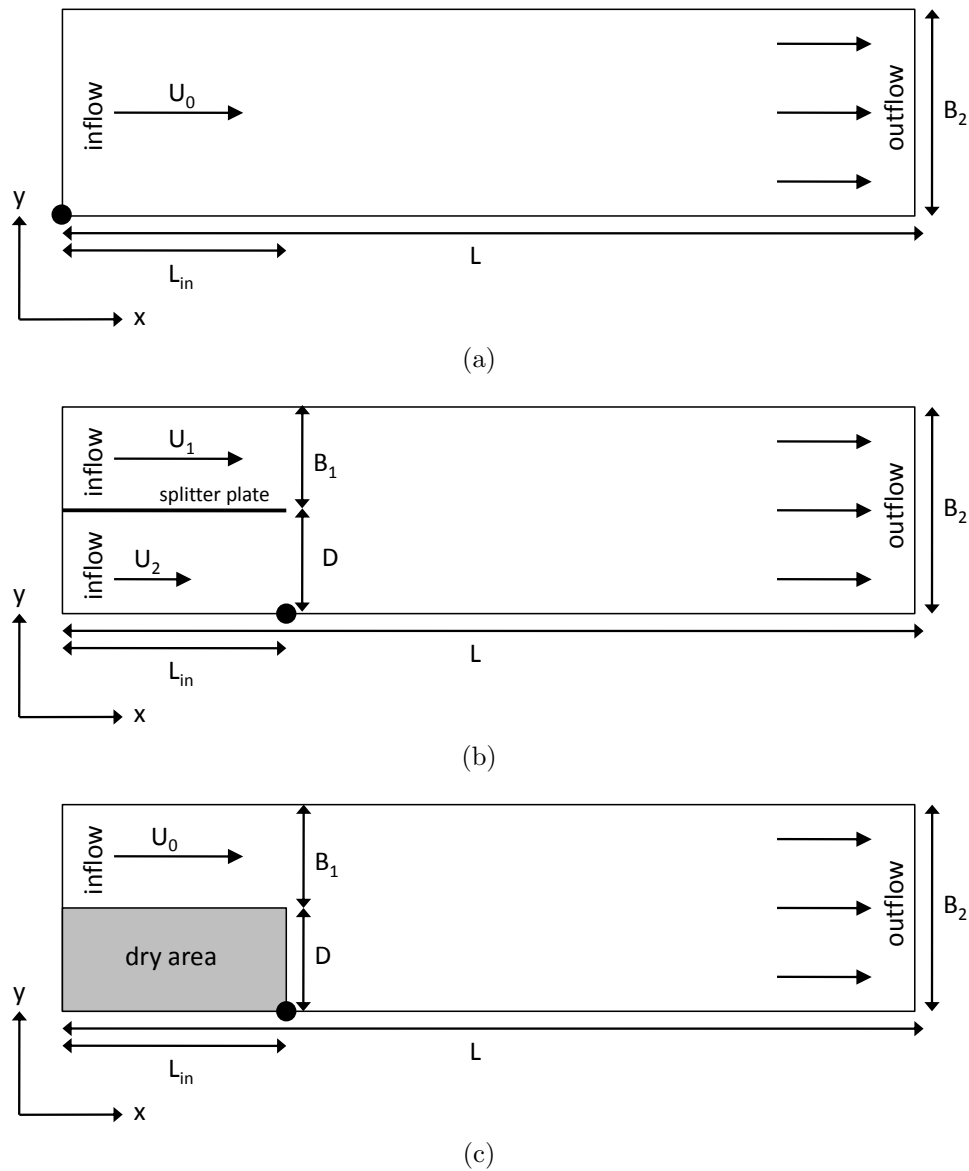


Figure 6.2: Overview of the 2DH computational domain for the SCF (a), SML (b) and SLE (c) geometry. Relevant length and velocity scales have been indicated. The solid dot indicates the origin of the Cartesian reference frame:  $(x, y) = (0, 0)$ . The three cases correspond to three types of 2DCS generation defined by Jirka [47]: secondary instability of base flow (a), internal transverse shear instabilities (b) and topographical forcing (c).

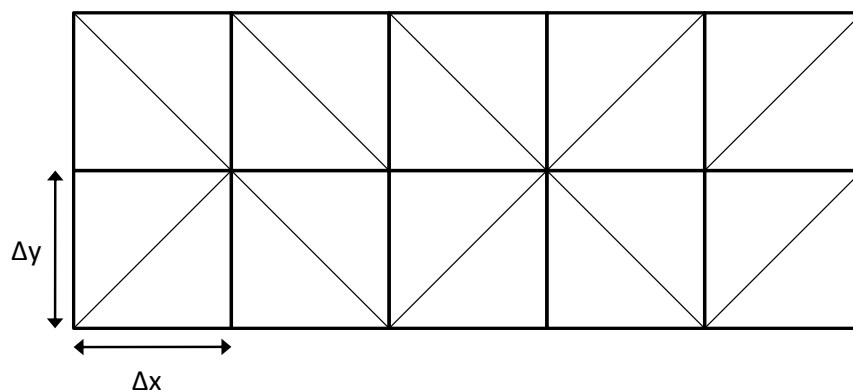


Figure 6.3: Construction of a quasi-rectangular unstructured grid with mesh size  $\Delta x = \Delta y$ .

nodes (containing the state variables) remain ordered in a rectangular structured grid. See Figure 6.3 for a simple illustration of this principle.

An average 2DH FINLAB simulation in this chapter uses a computational mesh with about 64000 nodes and 120000 elements. In both horizontal dimensions the resolution is equally set to  $\Delta x = \Delta y = H/4$  as argued before. A time step  $\Delta t = 0.1$  s has been adopted, resulting in a maximum velocity-based CFL number  $\approx 1.2$  and a maximum celerity-based CFL number  $\approx 4$ . The average running time for each simulation was 3 hours, during which a model time of 2000 s was simulated. In all cases an initial adaptation time of 1000 s was sufficient to reach a state of fully stationary turbulence, after which period output data were generated during another 1000 s (analogous to previous 3D LES computations).

## 6.6 Numerical results

This section presents computations by the 2DH model described above, as it is tested against the SCF, SML and SLE geometries. The 2DH results are compared with corresponding 3D LES data. All 10 models listed in Section 6.5.2 are tested against the SCF geometry, whereas only a selection of these models is tested against the SML and SLE cases.

### 6.6.1 Straight Channel Flow (SCF)

Because of its simplicity and the absence of internal forcing mechanisms for 2D turbulence, the SCF geometry is particularly suited to compare the performance of various 2D turbulence models. Two types of 2DH flow output are shown in this section: instantaneous spatial patterns of the streamwise and transverse velocity field (Figures 6.4-6.5) and energy density spectra of streamwise and transverse velocity fluctuations (Figure 6.6). These output data are compared with a 3D LES computation of the SCF geometry (with periodic boundary conditions in  $x$ -direction), using the LES implementation described in Chapter 4. Analogous to the LES cases described in Table 4.2, a horizontal mesh size  $\Delta x = \Delta y = H/8 = 0.0125$  m and a vertical resolution  $\Delta z = H/32 = 0.003125$  m were used, leading to a 3D grid size  $(N_x, N_y, N_z) = (1600, 160, 32)$ . All output data of this LES computation are based on the depth-averaged 3D velocity field  $\tilde{\mathbf{u}}$ : depth-averaged instantaneous velocity fields  $\tilde{u}$  and  $\tilde{v}$  are shown, as well as the associated depth-averaged spectra  $E_{uu}$  and  $E_{vv}$ .

Figures 6.4 and 6.5 show velocity fields for the 2DH models 1–5 and 6–10 respectively, for  $t = 2000$  s. In each figure, the lower panels show the 3D LES results. The left panels show streamwise velocity fluctuations  $u$  and the right panels show transverse fluctuations  $v$  in the region  $0 < x < 5$  m, after subtraction of the time-averaged flow field. In Figure 6.6, energy density spectra  $E_{uu}$  and  $E_{vv}$  are shown for the models 2–10. The spectra represent velocity fluctuations at the center line of the SCF geometry, at  $x = 6$  m and  $y = 1$  m. In each panel the corresponding 3D LES spectra are shown for a direct comparison (bold lines). The gray vertical lines indicate the frequency  $f = U_0/H$  that is related to an eddy length scale equal to the water depth  $H$  (using Taylor's hypothesis, see Chapter 3).

From cases with  $F_i = 0$ , it is obvious that explicit inflow perturbations are required to trigger 2D turbulence. The results for model 1 confirm that no internal forcing mechanisms for 2D motion are present; as the eddy viscosity-type terms are merely dissipative, no 2D velocity fluctuations are found ( $u = v = 0$ ). Likewise, the associated energy density spectra  $E_{uu}$  and  $E_{vv}$  are trivially zero and are not shown in Figure 6.6.

The results for model 2 show that kinematic inflow turbulence (imposed at  $x = 0$ ) rapidly decays as it propagates into the domain, especially the smaller eddy scales. In the far

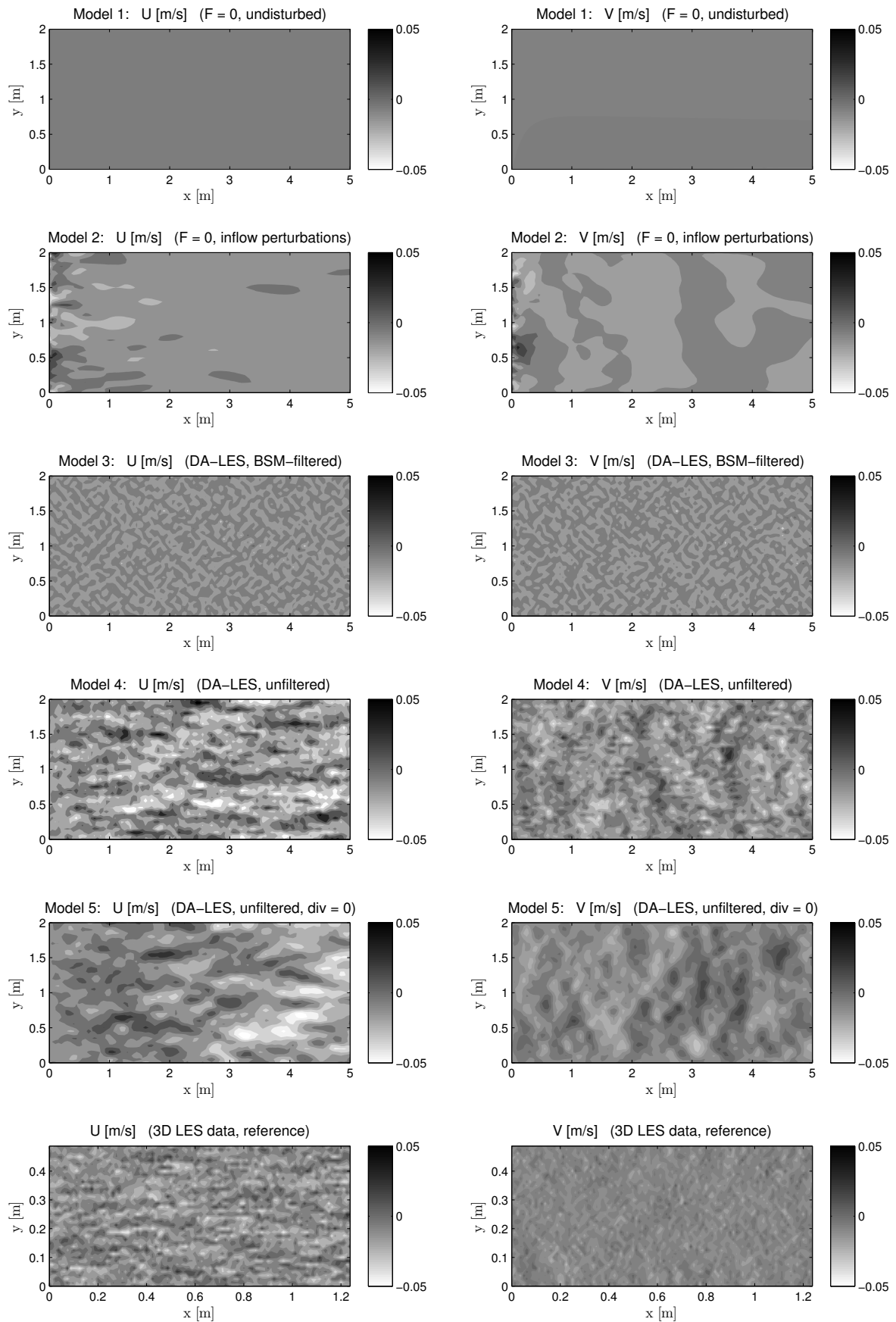


Figure 6.4: Instantaneous streamwise (left) and transverse (right) velocity fluctuations for various 2DH turbulence models, compared to 3D LES reference data (Straight Channel Flow).

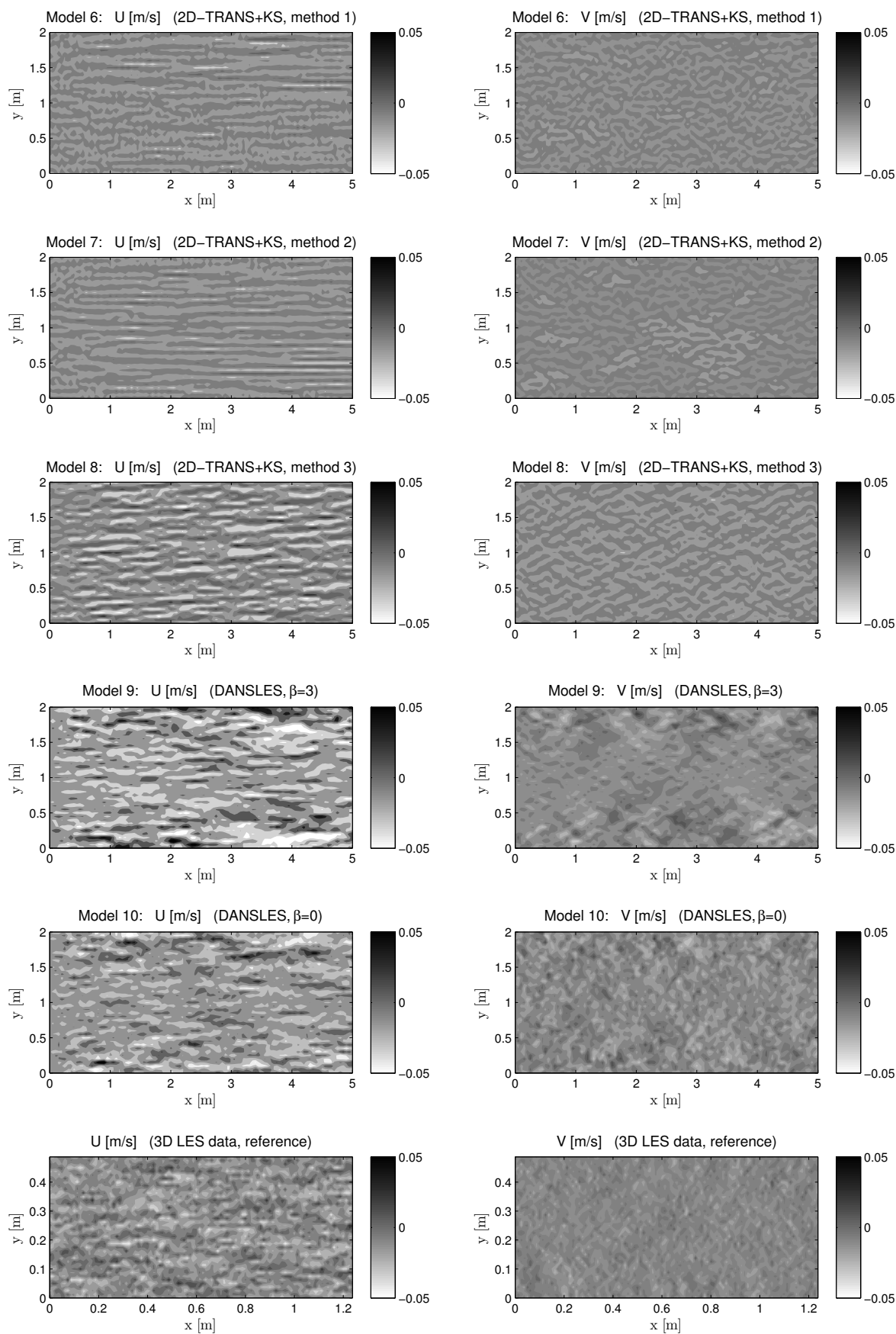


Figure 6.5: *Instantaneous streamwise (left) and transverse (right) velocity fluctuations for various 2DH turbulence models, compared to 3D LES reference data (Straight Channel Flow).*

field of  $u$  and  $v$  only large eddy scales ( $\mathcal{L} > H$ ) are remaining. It is found by Kernkamp and Uittenbogaard [49] that these large-scale perturbations are sufficient to trigger 2DCS development in SML geometries, in accordance with observations by Van Prooijen [99] that 2DCS in shallow mixing layers are mainly triggered by the large-scale (supra-depth) components of 3D bottom turbulence. Within the present SCF geometry, however, 2D turbulence patterns are not accurately reproduced. The spectra for model 2 show that, at  $x = 6$  m,  $E_{uu}$  and  $E_{vv}$  have strongly decayed for all sub-depth scales ( $\mathcal{L} < H$ ), whereas the energy levels at supra-depth scales are only slightly below the original energy levels at the inflow boundary (i.e. slightly below the 3D LES spectra). It is noteworthy that the largest scales contain spectral anisotropy (i.e.  $E_{uu} > E_{vv}$  for both the 2DH and 3D results), whereas the smaller spectral scales are fully isotropic. Furthermore, it is found that dissipation by the HLES subgrid-scale model is negligible in the present case; given the present fine resolution, dissipation by Elder's term is several orders of magnitude larger. This is understandable as the HLES SGS formula (6.11) vanishes for fine meshes, whereas Elder's term does not scale with discrete resolution and remains important irrespective of the mesh size. If however backscatter models like DA-LES or DANSLES are applied, energy dissipation rates by HLES and Elder's term have equal order of magnitude, as HLES (like Elder's term) effectively dissipates small-scale turbulent fluctuations.

The results for model 3 (DA-LES with BSM filter) mainly exhibit small-scale fluctuations in  $u$  and  $v$  ( $\mathcal{L} \approx H$ ), while the associated spectra have their maximum near  $f \approx U_0/H$  (order of the water depth). The large-scale turbulent kinetic energy is severely underpredicted. In contrast, we observe that for model 4 (DA-LES without filter) the order of magnitude of both  $E_{uu}$  and  $E_{vv}$  is more realistic, while the  $u$  and  $v$  turbulence patterns are closer to the 3D LES patterns. At smaller scales, the logarithmic slope of both the 3D and 2DH spectra is close to the  $-1$  spectral power-law by Nikora [68], which is typical for wall-bounded turbulence. Although this result was expected beforehand for the 3D data, it must be considered coincidence that it is found in the 2DH data as well. (A theoretical  $f^{-1}$ -type behavior is not to be expected for 2D simulations.) If we divide the model 3 spectra by the model 4 spectra we consistently find a ratio  $\hat{G}^2$ , with  $\hat{G}$  defined in Equation (6.19). It is hence found that the resolved TKE is proportional to the squared forcing field  $F_i^2$ .

The model 4 results exhibit some unphysical fluctuations of the free surface (not shown here) due to the divergent part of  $F_i$ , caused by white noise. The amplitude of these noisy fluctuations is at most  $10^{-3}$  m for the flow cases presented in this chapter; hence, their influence on the over-all flow field remains limited. The results for model 5 (unfiltered DA-LES with zero divergence) show that the divergence correction in (6.20)-(6.21) acts as a mild low-pass filter on the model 4 results. Smaller turbulence scales are slightly damped, while the large-scale anisotropy is erroneously increasing. In terms of spectral energy levels, model 4 performs better than model 5. Finally, we observe that all DA-LES-based models result in spectral anisotropy on large scales, in spite of the fact that DA-LES is a fully isotropic model (!). This implies that spectral anisotropy is not imposed here by the backscatter model but rather comes up from actually resolved flow dynamics. Presumably the nonlinear advection terms are important for this effect.

With respect to the 2D-TRANS+KS-based models 6–8, a large difference in behavior between models 6–7 and model 8 is observed. The energy density spectra of models 6–7 (representing time-dependency Methods 1 and 2) have a rather irregular and spiky shape; these models fail to resolve small-scale turbulence (roughly for  $f > 0.5$  Hz). Furthermore, the spectral anisotropy at larger scales is severely overpredicted in this SCF case:  $E_{uu} \gg E_{vv}$ . The results for model 8 (involving time-dependency Method 3) are more satisfactory: both  $E_{uu}$  and  $E_{vv}$  as well as the spectral anisotropy at larger scales are predicted quite well for the

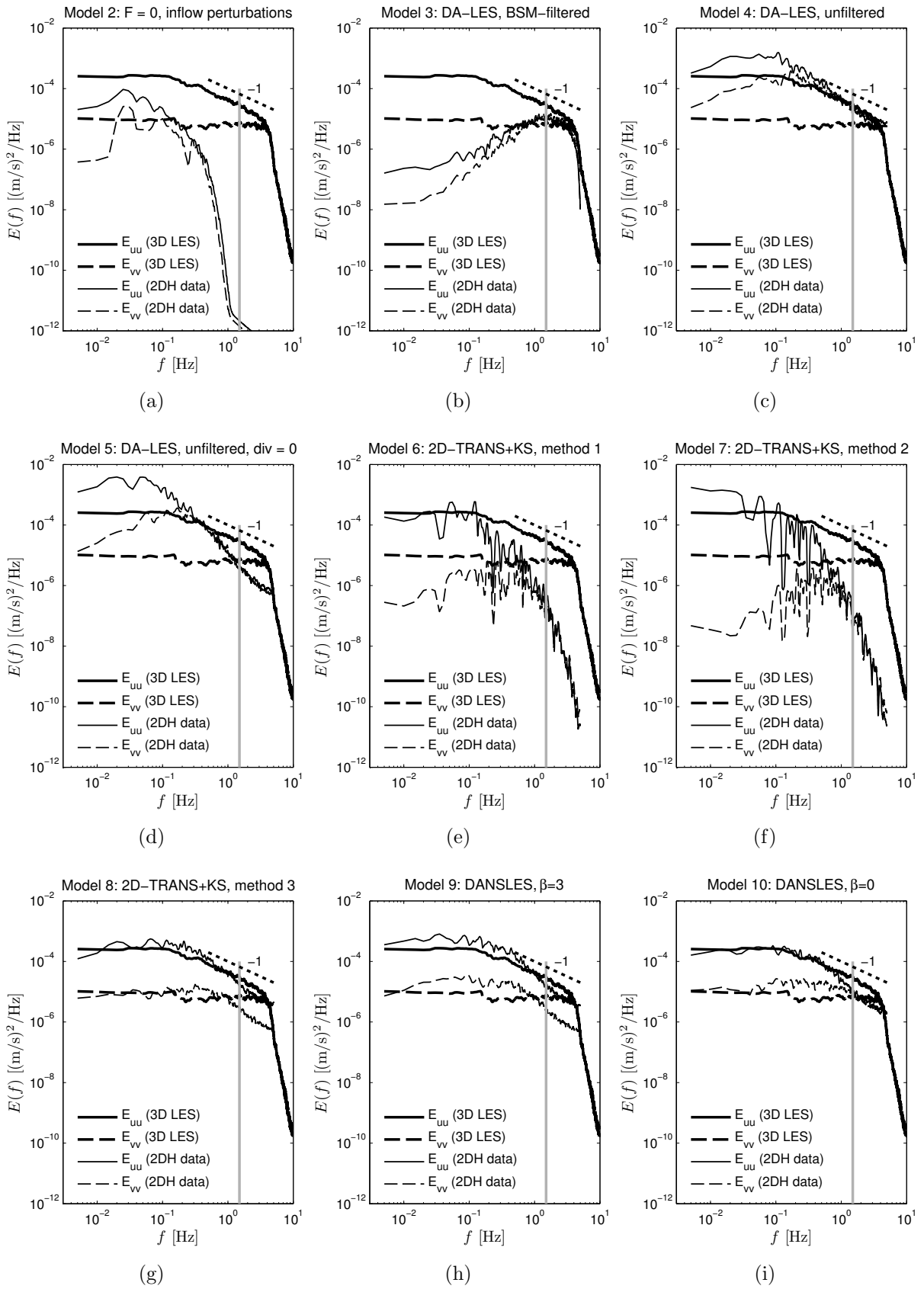


Figure 6.6: Streamwise and transverse energy density spectra for various 2DH turbulence models, compared to 3D LES data (Straight Channel Flow, center line at  $x = 6$  m). The frequency  $f$  corresponding to water depth  $H$  has been indicated by the gray vertical line.

present calibration (except for the fact that this anisotropy also occurs at the smallest scales, which is obviously incorrect).

The inaccuracies of the methods including an advective velocity (Methods 1–2) can be explained from several mechanisms. Firstly, spatial gradients in the advection velocity are distorting the kinematic velocity field, effectively increasing the anisotropy of the flow. This strong anisotropy is also clearly visible from the streamwise velocity fluctuations  $u$  in Figure 6.5. Secondly, the spikiness of the spectra indicates that the number of harmonic components ( $N = 500$ ) is actually too small to represent the entire spectrum accurately. Finally, it can be shown that the generation of 2D random wave numbers within 2D-TRANS+KS slightly favors the largest length scales, so that especially the smaller-scale kinetic energy is not accurately resolved. These three problems do not arise in the case of Method 3, which includes no advection velocity and no temporal coherence of the kinematic velocity field. Due to this lack of temporal coherence, the inaccuracies described above are somehow averaged out, eventually leading to rather satisfactory turbulent velocity patterns and energy density spectra. Furthermore, the model 8 spectra are close to a  $-1$  spectral power-law again, analogous to unfiltered DA-LES (model 4).

Finally, two versions of DANSLES are considered: the anisotropic versus isotropic case ( $\beta = 3$  and  $\beta = 0$  respectively). Comparing model 8 to model 9 (2D-TRANS+KS versus DANSLES, with  $\beta = 3$ ), we observe that  $E_{uu}$  and  $E_{vv}$  have a virtually identical shape for both models, whereas the instantaneous velocity fields  $u$  and  $v$  in model 9 contain slightly more small-scale fluctuations compared to model 8. This can be understood as 2D-TRANS+KS and DANSLES are to a large extent equivalent models, except for the fact that the latter is better capable of resolving the small-scale part of the spectrum of  $F_i$ . Both models give rise to a similar spectral anisotropy, which is virtually correct at large scales but incorrect at smaller scales (roughly  $f > U_0/H$ ). This is because the anisotropy coefficient  $\beta$  induces anisotropy at all scales, at least if the present mathematical form for the spectra (given by (6.24)-(6.25), see Van Prooijen [99]) is adopted.

Considering model 10, we notice that DANSLES with  $\beta = 0$  gives rise to almost the same spectral energy levels and large-scale anisotropy as models 8 and 9; however, the erroneous anisotropy at smaller scales has vanished. Analogous to the DA-LES models 3–5, it is found that even isotropic backscatter models allow for anisotropic turbulence in the resolved flow field (!). This anisotropy is only found at larger scales, in accordance with 3D LES data. This is advantageous as the geometry-dependent anisotropy factor  $\beta$  can be altogether discarded<sup>4</sup> from the DANSLES model, which renders the backscatter model applicable to general flow geometries (like DA-LES). Both the spectra  $E_{uu}$  and  $E_{vv}$  and the instantaneous velocity maps  $u$  and  $v$  (Figure 6.5) for DANSLES with  $\beta = 0$  are considered quite satisfactory, as the obtained 2D turbulence patterns are very similar to corresponding 3D LES data.

It can be concluded that, for the SCF geometry, the models 4 and 8–10 provide the best results compared to the 3D LES data. This holds for  $u$  and  $v$  as well as  $E_{uu}$  and  $E_{vv}$ . The performance of model 4 could be improved by slightly reducing the adopted value for  $c_B$ , as the present calibration slightly over-predicts the 2D TKE. Furthermore, we observe that the shape of the 2D spectra for models 8–10 fits the 3D data slightly better than for model 4; this is probably due to the use of well-calibrated spectra here instead of white noise. For all models tested, the resulting TKE levels can be easily fine-tuned by re-calibration; the shape of the spectra however cannot be straightforwardly changed, as these are intrinsically

---

<sup>4</sup>An alternative would be to make  $\beta$  wave-number dependent, making it zero at small scales only. It is however more elegant to set  $\beta = 0$  everywhere and let the flow solver account for all anisotropy. This has no negative impact on model performance in practice and it yields a more generic model.



determined by the type of 2D turbulence model. Hence, due to their inaccurate spectral properties, the backscatter models 3 and 5–7 are considered unsuitable for computing general shallow-flow turbulence. It is noteworthy that, for all suitable models 4 and 8–10,  $E_{uu}$  and  $E_{vv}$  consistently contain a high-frequency spectral slope close to  $-1$ , as interpreted before. Finally, we notice that the  $u$  and  $v$  results for backscatter models 3–10 in Figures 6.4–6.5 do not exhibit a spatial growth or decay of turbulence in streamwise direction; in each cross-section the turbulence patterns are virtually constant. This confirms that, after an initial adaptation time, the SCF geometry is characterized by a steady-state local equilibrium between production and dissipation of 2D TKE. Indeed, it has been found (not shown here) that near-field and far-field spectra  $E_{uu}$  and  $E_{vv}$  in various cross-sections are virtually identical, without spatial decay.

### 6.6.2 Shallow Mixing Layer (SML)

For the purpose of testing against the SML and SLE geometries, five of the 2D models treated above are selected. It has been shown that models 5–7 do not perform well for the SCF case and are not well qualified to resolve 2D turbulence in general shallow flow domains. Models 8 and 9 are virtually equivalent, while model 10 (the isotropic DANSLES model) is more generally applicable than models 8–9 because  $\beta = 0$ . Hence, we select the models 1–4 and 10 for further analysis. This allows us to examine respectively the effect of inflow perturbations (model 2 versus model 1) and the effect of the BSM filter within DA-LES (model 3 versus model 4) on the SML and SLE cases, and to compare their performance to the final calibrated DANSLES model. This section treats the SML results.

For each model selected, Figure 6.7 depicts the transverse velocity field  $\tilde{v}$  within the region  $-2 < x < 11$  m, for  $t = 2000$  s. The  $\tilde{v}$  patterns are well suited to detect the presence of 2DCS within the shallow mixing layer. The lower panel shows 3D results stemming from LES Case 4A (see Chapter 4). Figures 6.8(a)–(d) show energy spectra  $E_{uu}$  and  $E_{vv}$  at  $x = 6$  m and  $y = 1$  m, for models 1–4 and 10. Corresponding 3D LES data have been plotted for comparison (bold lines). Finally, depth-averaged turbulent kinetic energy levels  $\overline{\tilde{u}^2}$  and  $\overline{\tilde{v}^2}$  along the mixing layer center line ( $y = 1$  m) are shown in Figures 6.8(e)–(f).

From Figure 6.7 it is observed that models 1 and 3 fail to reproduce the near-field mixing layer correctly. For model 1 this is not surprising; according to Van Prooijen [99] and Kernkamp and Uittenbogaard [49], mixing layer 2DCS are triggered by large-scale components of background turbulence, either provided by inflow perturbations or by a backscatter model. Both mechanisms are absent here. Not surprisingly, the TKE levels found in Figures 6.8(e)–(f) are severely underpredicted, especially inside the near field. It is noteworthy that far-field 2DCS are present nonetheless; these structures are enforced by the outflow boundary condition  $h = 0$ , which disturbs the stable shallow shear flow. This disturbing influence from the boundary conditions also follows from the spectra in Figure 6.8(a). Most 2DH spectral scales are severely underpredicted compared to the 3D data, except for a series of pronounced spiky peaks in the range  $0.05 < f < 0.5$  Hz. The frequencies of these peaks are exactly the eigen frequencies of standing waves over the entire length of the flume (reflecting against the open boundaries):  $f = n\sqrt{gH}/L$ , where  $n = 1, 2, 3, \dots$ , etc. These peaks account for the majority of spectral energy in  $E_{uu}$  and  $E_{vv}$  and eventually cause the triggering of far-field 2DCS. Apparently, long wave frequencies (although having a very small amplitude) become important for triggering 2DCS if no other perturbations are present. As long wave frequencies have relatively large time and length scales, far-field 2DCS are more likely to be triggered than near-field eddies. Indeed we observe that near-field eddies are not triggered. The influence of long waves is a typical artifact

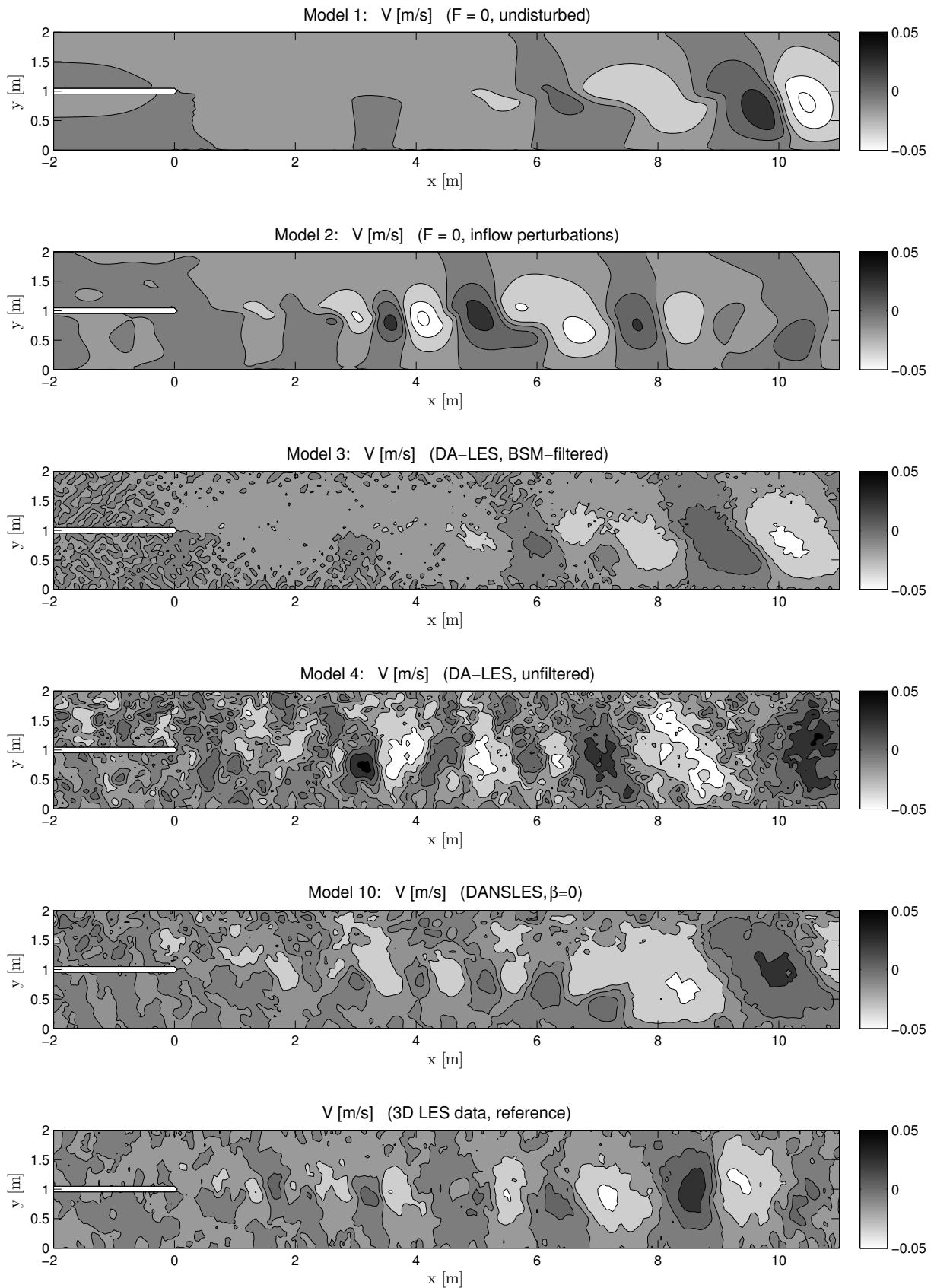


Figure 6.7: Instantaneous transverse velocity fluctuations for a selection of 2DH turbulence models, compared to 3D LES reference data (Shallow Mixing Layer).

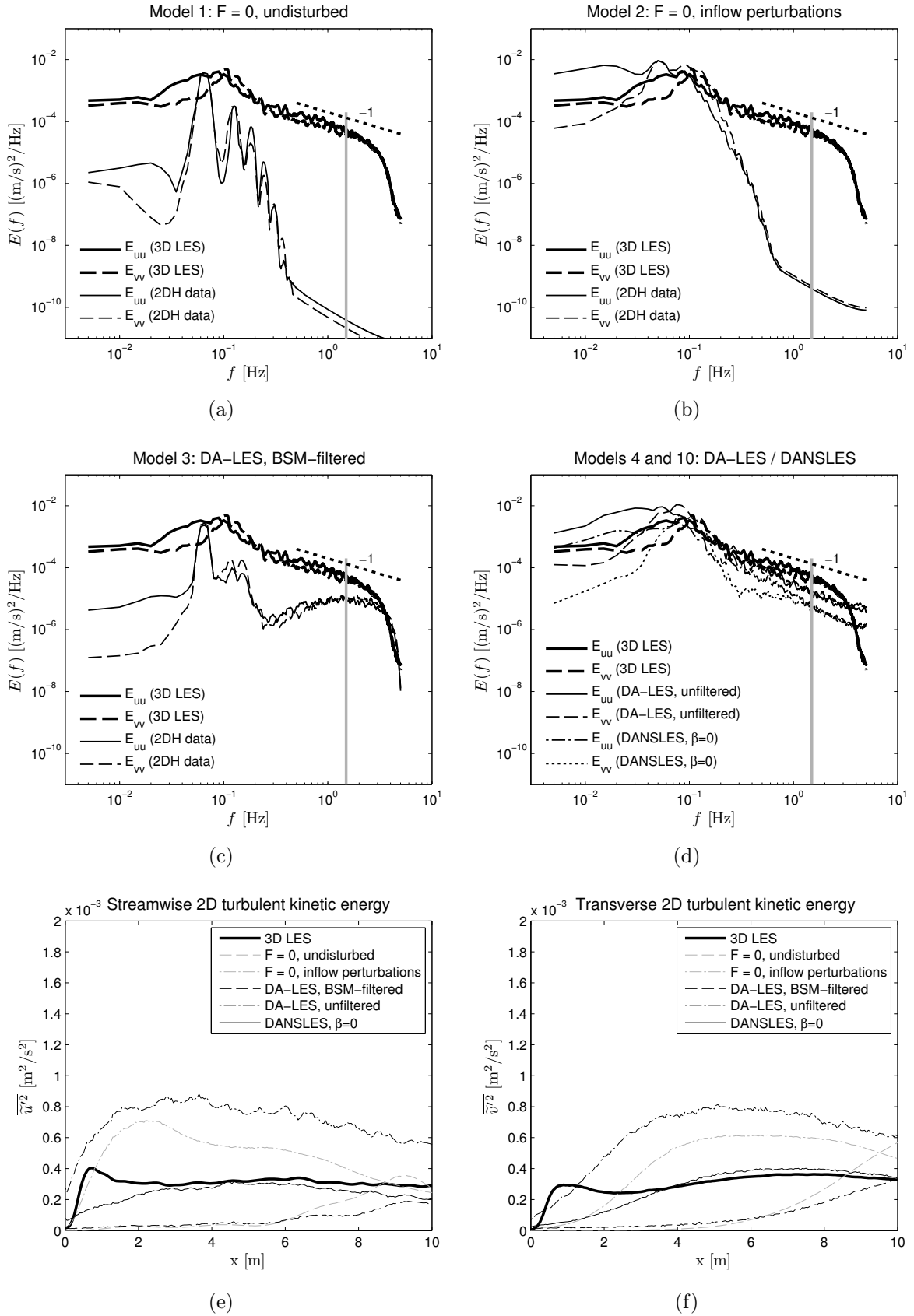


Figure 6.8: Comparison of a selection of 2DH turbulence models with 3D LES data (Shallow Mixing Layer): (a-d) streamwise and transverse energy density spectra (at  $x = 6$  m), (e-f) streamwise and transverse TKE along mixing layer center line.

of free-surface computations. If a rigid-lid approximation for the water surface is adopted, eigen frequencies associated with long waves do not exist and will have no triggering effect. This is confirmed by the low-resolution LES Case 4C in Chapter 4, see Section 4.5.

Comparing model 1 to model 3 results, we notice that the small-scale 2D turbulence generated by the BSM-filtered DA-LES backscatter model is not able to trigger near-field 2DCS either. Apart from some small-scale noise the large-scale patterns of  $\tilde{v}$  are virtually the same for both models, as well as the resulting TKE levels in Figures 6.8(e)-(f). Comparing the respective spectra in panels 6.8(a)-(c), we observe similar spiky peaks associated to long wave frequencies. Furthermore, at the high-frequency side in panel (c) (near  $f \approx U_0/H$ ) the spectra  $E_{uu}$  and  $E_{vv}$  have a maximum; this is characteristic for model 3, compare Figure 6.6(b). In between this local maximum and the spiky peaks a wide “spectral gap” exists, which is absent in the unfiltered results (see Figure 6.8(d)). Apparently, the high-frequency energy does hardly impact the turbulent kinetic energy at lower frequencies and larger scales. We can conclude that small-scale noise as generated by BSM-filtered DA-LES is of no use to trigger large-scale quasi-2D turbulence structures.

In contrast with model 1 and 3, model 2 exhibits a reasonably proper mixing layer development with growing 2DCS in the near field. This confirms the importance of artificial turbulence at inflow boundaries in cases where no backscatter model is present ( $F_i = 0$ ). From Figure 6.8(b) it follows that the large-scale TKE inside the mixing layer is resolved more or less properly, while small-scale turbulence is considerably underpredicted. (These small scales have been decayed already close to the inflow boundary.) These results confirm the conclusion by Kernkamp and Uittenbogaard [49] that large-scale inflow perturbations (having a scale  $\mathcal{L} > H$ ) are sufficient to trigger 2DCS in a SML geometry.

Finally, models 4 and 10 yield the results that are closest to the 3D LES data, in terms of  $\tilde{v}$  as well as  $E_{uu}$  and  $E_{vv}$ . Energy spectra for both models are shown in Figure 6.8(d); the models show spectral isotropy at smaller scales and anisotropy at larger scales, although the latter is slightly overpredicted in both cases. Large-scale anisotropy is typical for SML mixing layer eddies (see Van Prooijen [99]). From the velocity patterns in Figure 6.7 and the TKE levels in Figures 6.8(e)-(f), we find that model 10 (DANSLES) yields the best reproduction of the 3D LES data. The velocity fluctuations and TKE levels for model 4 (unfiltered DA-LES) are slightly overpredicted for the present default calibration; furthermore, the velocity patterns for model 4 are slightly more noisy due to the application of white noise. As the overprediction is approximately by a factor 2, the parameter  $c_B$  in DA-LES should be reduced by a factor  $\approx \sqrt{2}$  in order to yield results similar to model 10.

### 6.6.3 Shallow Lateral Expansion (SLE)

Analogous to the previous section, this section presents the results of models 1–4 and 10 tested against the SLE geometry. Figure 6.9 depicts transverse velocity fields  $\tilde{v}$  for all 2D models and corresponding 3D LES data stemming from Case 2A in Chapter 4. Figures 6.10(a)-(d) show energy density spectra  $E_{uu}$  and  $E_{vv}$  at  $x = 6$  m, while 2D TKE levels  $\overline{\tilde{u}^2}$  and  $\overline{\tilde{v}^2}$  along the mixing layer center line ( $y = 1$  m) are given by Figures 6.10(e)-(f).

From the SLE results altogether, we firstly conclude (in contrast with previous SML conclusions) that 2D turbulence models have only marginal influence on the actually resolved 2DCS. All models reproduce a sequence of 2D shed vortices, regardless whether a backscatter model is applied or artificial inflow turbulence or neither of these. This can be explained by the mechanism of topographical forcing of 2DCS, see Jirka [47]. This mechanism has been mentioned before in Chapter 4 in order to explain the differences in behavior between SML and SLE flow geometries in a 3D LES context. Also in the present 2DH context, we

can state that the presence of a primary and secondary steady gyre continuously adds perturbations to the mixing layer at larger scales. Moreover, the ability of 2DCS to interact with the primary gyre contributes to their energetic growth (gyre-vortex interaction, see Chapter 3). As before, in each simulation the start of the vortex shedding process depends on the presence of a sufficiently developed secondary gyre.

Secondly, it is found that all 2DH computations of the SLE geometry consistently overpredict the TKE levels inside the mixing layer. Figures 6.10(e)-(f) show that the computed 2DH values of  $\overline{u'^2}$  and  $\overline{v'^2}$  along the mixing layer systematically exceed the 3D LES values in the near field and middle field. This overprediction has also been observed in a test computation using the 3D LES solver described in Chapter 4 (results not shown in this thesis), using only one layer in the vertical ( $N_z = 1$ ). This observation gives rise to the hypothesis that secondary flow is an essential aspect of a proper SLE simulation (see also Section 6.8). In Chapters 3 and 4, secondary (vertical) flow has been specifically observed in the near field and middle field of the SLE, giving rise to upwelling and downdraft regions inside the mixing layer. This secondary flow significantly contributes to the lateral transfer of momentum; hence, it is expected to have a reducing effect on the transverse TKE and horizontal Reynolds stresses. As in 2DH computations secondary flow cannot exist (by definition), apparently the energy associated with near-field secondary flow is added to the transverse TKE, which will be therefore consistently overpredicted.

The overprediction of TKE levels is also visible in the spectra of Figures 6.10(a)-(d): for each model,  $E_{uu}$  and  $E_{vv}$  are too large in the low-frequency range. These largest eddy scales show spectral isotropy, which implies that far-field 2DCS in a SLE are not elongated in streamwise direction (in agreement with earlier PIV and 3D LES results). The overprediction of  $E_{uu}$  and  $E_{vv}$  is most pronounced for models 1–2, where  $F_i = 0$  (no backscatter model). Apparently the presence of a backscatter model, which adds some irregularity to the 2D flow field, has a reducing effect on the TKE of the largest eddies. Indeed, in Figure 6.9 we observe that models 3–4 and 10 have slightly weaker 2DCS (slightly smaller amplitudes of  $\tilde{v}$ ) than models 1–2; moreover, Figure 6.10(f) shows that the over-all transverse TKE levels of models 3–4 and 10 are consistently below those of models 1–2.

In general, no convincing differences between the results of models 1 and 2 can be discerned. Whereas the largest spectral scales contain too much energy, the small-scale spectral energy is severely underpredicted in both cases. This implies that only the large eddy scales are topographically forced, irrespective of the presence of artificial inflow turbulence; the small eddy scales (if desired) must still be accounted for by a backscatter model. Consequently the  $\tilde{v}$  patterns for models 1–2 are containing large scales only, without any small eddies. For model 3, we observe that the large-scale parts of the spectra are almost identical to the spectra of models 1–2 (Figure 6.10(a)-(b)); at smaller scales, the energy input by the BSM-filtered DA-LES model is observed (Figure 6.10(c)). In between those scales a “spectral gap” is visible once more, see also Section 6.6.2. This spectral gap is clearly visible in the pattern for  $\tilde{v}$  in Figure 6.9: the model 3 results show rather regular 2DCS, only disturbed by some small-scale noise while intermediate eddy scales are lacking.

Again the spectra of models 4 and 10 yield the most accurate reproduction of 3D LES results, as can be seen from Figure 6.10(d). Also the  $\tilde{v}$  patterns in Figure 6.9 look most convincing for models 4 and 10, as the full range of possible eddy length scales is present here. In agreement with 3D LES results, the entire spectral range of the far-field 2DCS is virtually isotropic. The only significant error is given by the inevitable overprediction of the large-scale eddy energy in  $E_{uu}$  and  $E_{vv}$  (as well as  $\overline{u'^2}$  and  $\overline{v'^2}$ ); as these large eddies are topographically forced, presumably this error can only be avoided by the use of a full three-dimensional model which allows for the presence of secondary flow structures.

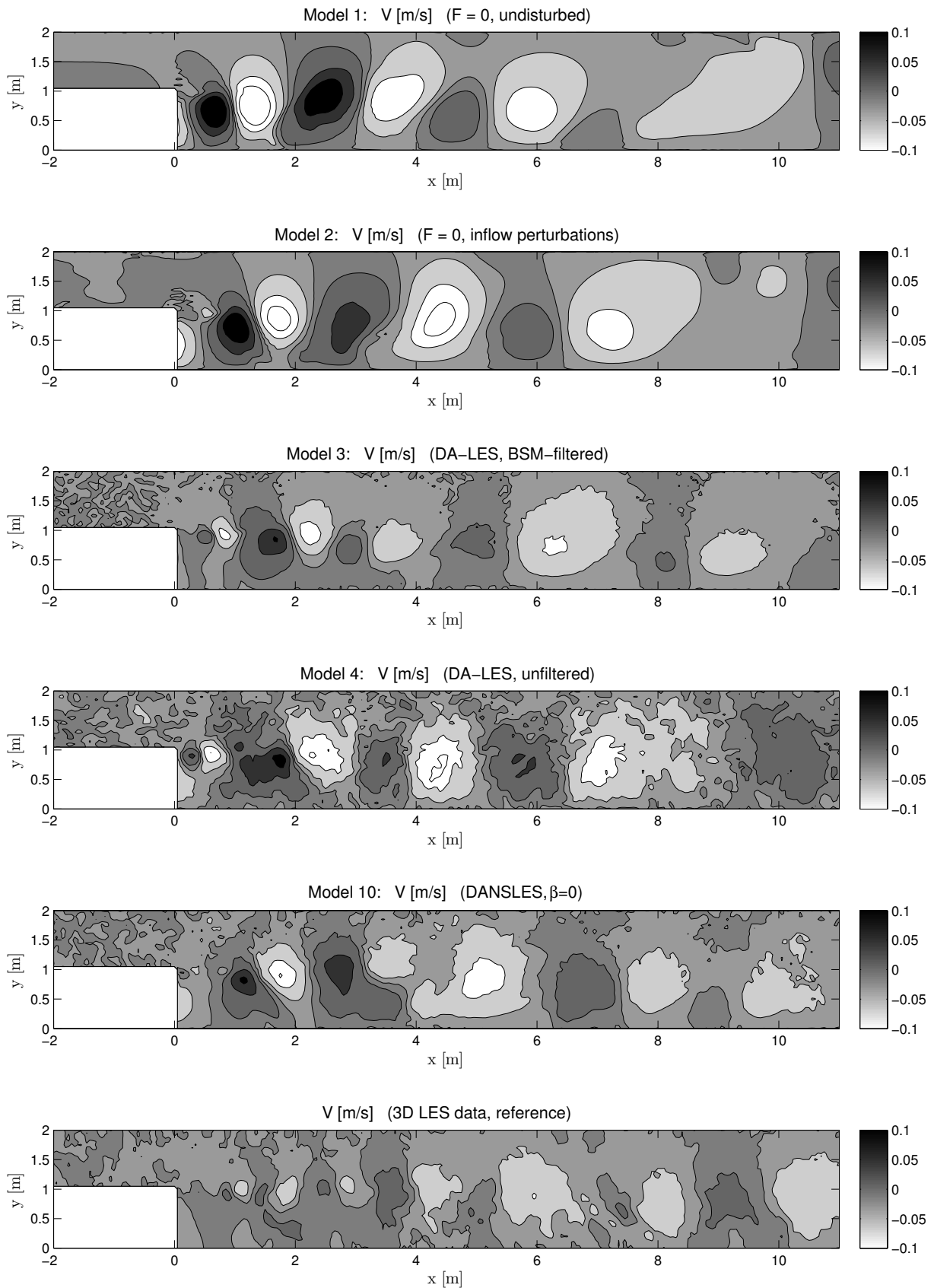


Figure 6.9: Instantaneous transverse velocity fluctuations for a selection of 2DH turbulence models, compared to 3D LES reference data (Shallow Lateral Expansion).

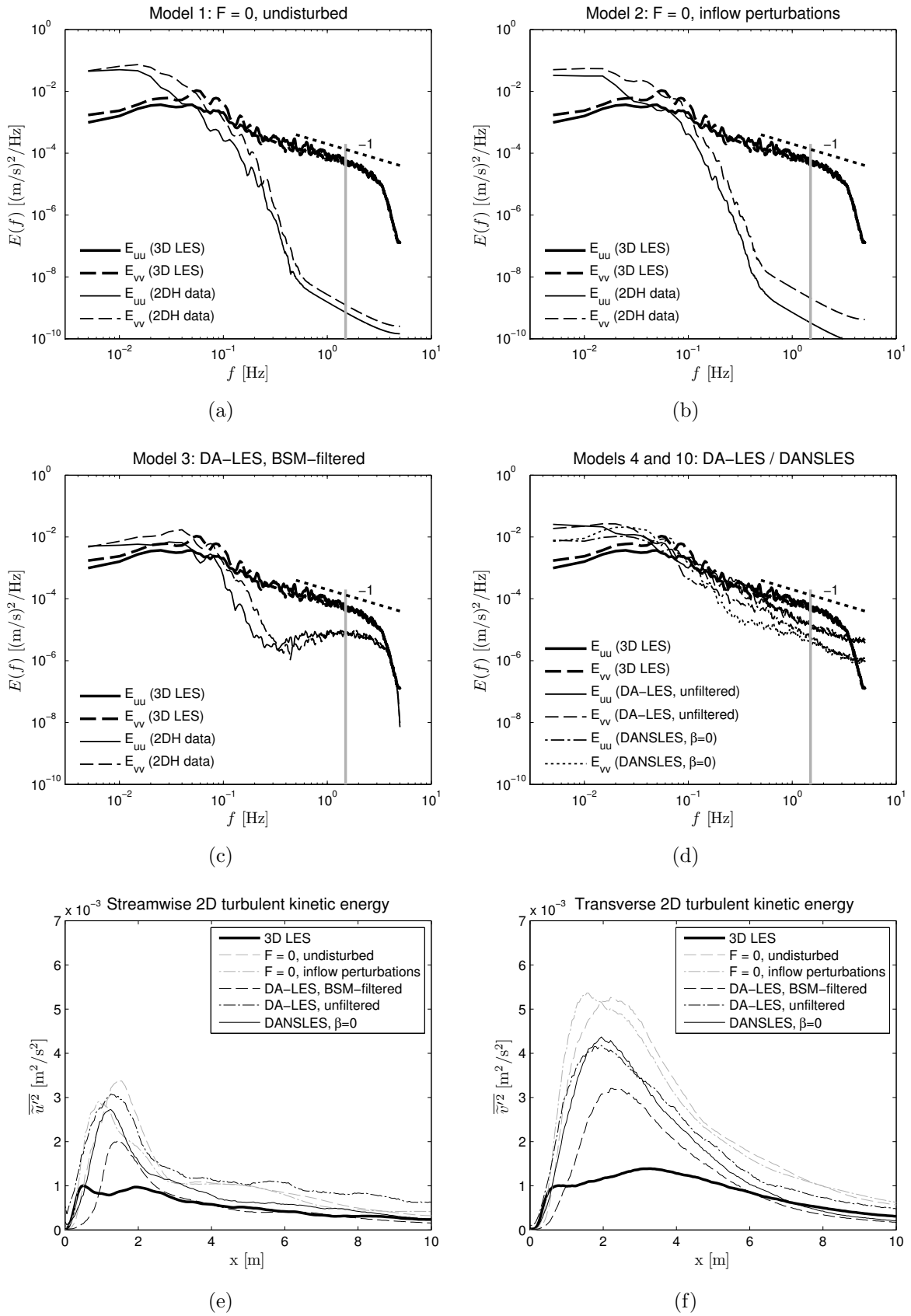


Figure 6.10: Comparison of a selection of 2DH turbulence models with 3D LES data (Shallow Lateral Expansion): (a-d) streamwise and transverse energy density spectra (at  $x = 6$  m), (e-f) streamwise and transverse TKE along mixing layer center line.

## 6.7 Evaluation of various backscatter models

From the results presented in Section 6.6 it is concluded that the DANSLES backscatter model provided satisfactory results for the SCF, SML and SLE geometries, given the natural limitations of the 2DH approach. The model offers a useful unification of the existing backscatter methods DA-LES and 2D-TRANS+KS, which is straightforwardly combined with eddy viscosity-type like HLES and Elder's term.

The use of a backscatter model is advantageous in comparison with only imposing artificial turbulence on boundaries; however, as every shallow flow geometry is unique, the backscatter formulation should be rather generic and not dedicated to one specific turbulent flow case. The DANSLES model is an attempt to give DA-LES a more proper physical basis by adding spectral information from 2D-TRANS+KS to it; at the same time the applicability of 2D-TRANS+KS is broadened by removing geometry-specific information (like spectral anisotropy and advective velocities) from the model. Thanks to the use of IFFT techniques (see Section 6.4.3), the resulting implementation is quite fast (like DA-LES) and all spatial scales are well-resolved, both in contrast with the original 2D-TRANS+KS implementation which can be a computational burden and does not resolve small eddy scales accurately.

Surprisingly, the final isotropic version of DANSLES (model 10) produces results that have much in common with results of the unfiltered DA-LES backscatter model (model 4), although DANSLES is based on proper spectral information which naturally enforces continuity whereas unfiltered DA-LES just uses white noise. Although Hinterberger et al. [42, 43] recommend the use of DA-LES combined with the so-called BSM filter, given by Equation (6.18), it is found in Section 6.6 that unfiltered DA-LES performs much better for the tested geometries.

The success of unfiltered DA-LES is explained by the fact that all time and length scales are equally disturbed by the white noise forcing field. Filtered DA-LES, on the other hand, only perturbs a narrow range of frequencies which are too high to have significant impact on 2DCS behavior. This observation is quite different from the conclusions drawn by [42, 43], who explicitly emphasize the vital role of the BSM filter.

Why are these conclusions so opposite? Personal communication with Hinterberger has provided some additional information. The most important aspect is the choice of the numerical flow solver, especially the discretization of the advection terms. Hinterberger stresses the importance of using a (non-dissipative) second order central differencing discretization for the advective terms, which is known to introduce local instabilities into the solution. Moreover, it has been emphasized that too large an artificial viscosity could destroy the 2D turbulence development. Hinterberger recommends therefore to use a value  $c_h = \kappa/6$  for Elder's term, and states that 2D eddies will be damped if  $c_h > 0.10$  is applied. These remarks suggest that DA-LES has been developed using a solver with intrinsically unstable advective terms, slightly stabilized by a limited amount of artificial diffusion, but not too much in order to avoid damping. Hence, 2D turbulence instabilities mainly originate from numerical instabilities.

The FINLAB model used in the present study, on the other hand, is probably a more robust solver. The advection terms are intrinsically stable and energy-conserving due to the nonlinear GIS interface stabilization approach (see Section 6.5.1 and Labeur [52]); they do not need any further stabilization by artificial diffusion. Artificial viscosity is needed only to fine-tune the required level of turbulent kinetic energy dissipation; it plays no role here with respect to numerical stability. From many computational tests using FINLAB with DA-LES (results not shown here), it is observed that the 2D turbulence level is not very sensitive to the value of  $c_h$ : values from 0.10 up to 0.20, not recommended by Hinterberger,



can be safely used without excessive damping. These computational tests indicate that the final TKE level in a shallow channel flow (SCF) is roughly proportional to  $\approx c_h^{-0.3}$ , which implies only a limited sensitivity. Apparently the intrinsic numerical stability makes an extra filtering operation unnecessary.

A second important aspect is the role of large-scale versus-small scale forcing. It was emphasized by Hinterberger that 2D turbulence must be forced mainly at high frequencies and high wave numbers. This is in contradiction with conclusions by Kernkamp and Uittenbogaard [49], Van Prooijen [99] and Uijttewaald and Booij [91], who emphasize that 2D turbulence is effectively triggered by large-scale perturbations, i.e. low frequencies and low wave numbers (!). The results in the present chapter show that the latter conclusions are correct. The BSM filter in Equation (6.18) has a somewhat arbitrary mathematical form and lacks a physical background. In the filtered BSM model, instabilities are only triggered at scales  $\mathcal{L} \approx H$ . However, the present resolution  $\Delta x = \Delta y = H/4$  (also applied by Hinterberger) is roughly sufficient to resolve turbulent length scales  $\mathcal{L} > 2H$ , see Van Prooijen [99]. Therefore, the BSM filter produces high-frequency noise at unresolved scales, which is quickly damped and unable to induce 2DCS. White noise on the other hand contains *all* scales (including the largest ones) and disturbs them likewise, as is convincingly shown by energy density spectra. This explains why unfiltered DA-LES (model 4) is proven more successful in the present study than BSM-filtered DA-LES (model 3).

Considering the applicability of all backscatter models treated in this chapter, we conclude that unfiltered DA-LES (model 4) and isotropic DANSLES (model 10) are best suited for general shallow flow domains. Both models can be implemented and applied at approximately the same computational cost, although DANSLES requires an auxiliary rectangular mesh while unfiltered DA-LES does not. Although DANSLES has a more proper physical basis, the effects of both models for practical applications are quite similar. It should be noted however that a re-scaling and re-calibration of DA-LES is recommended in order to give it better physical properties, as has been pointed out in the final part of Section 6.4.3. The most important practical limitation of both DA-LES and DANSLES (as well as 2D-TRANS+KS) is the requirement of a constant water depth  $H$ . The development of a backscatter model for variable  $H$  would be a desirable future improvement.

## 6.8 Extension to computations with multiple layers

At the end of this chapter, we make a very brief excursion to the 3D version of FINLAB. This model solves the full 3D Navier-Stokes Equations given by (6.1)-(6.2), supplemented with free-surface boundary conditions. General remarks in Section 6.5.1 about 2D FINLAB are also valid for 3D FINLAB. The full numerical formulation is very elaborate and can be found in Laheur [52].

In principle, 3D FINLAB can be used to perform detailed 3D Large Eddy Simulations on arbitrary complex geometries, with either a movable free surface or a rigid-lid boundary. This is however not pursued in the present context; instead, we study 3D shallow flow simulations with a very limited vertical resolution (e.g. up to 4 layers). It is not aimed to resolve the full 3D flow structure, but to give the predominantly quasi-2D flow a slight degree of freedom in vertical direction. This can be rewarding if we want to resolve part of the secondary flow structure (and the associated momentum transfer), which we have seen is certainly present in shallow shear flows (see Section 4.6).

Three test computations have been performed on the SLE geometry using 3D FINLAB, adopting respectively 2, 3 and 4 computational layers. These computations are compared

with a corresponding 2D FINLAB computation (1 layer by definition) and a 3D LES computation presented before in Chapter 4 (Case 2A). Some relevant results are presented in Figure 6.11: contour plots of the instantaneous depth-averaged vertical velocity  $\tilde{w}$ , as well as the streamwise and transverse depth-averaged TKE along the mixing layer center line.

A 2D top view of the 3D SLE geometry is given by Figure 6.2(c). For the present computations we have  $H = 0.1$  m and  $\Delta x = \Delta y = H/2 = 0.05$  m. The vertical resolution is given by the number of layers. The 2D mesh depicted in Figure 6.3 can be straightforwardly extended to a 3D mesh of tetrahedrons, where all nodes are located in a structured grid. The 2-layer case applies 2 layers of nodes, located at  $z = 0$  and  $z = H$ ; the 3-layer case applies layers at  $z = 0, \frac{1}{2}H, H$  and the 4-layer case has nodes at  $z = 0, \frac{1}{3}H, \frac{2}{3}H, H$ . Hence, a  $n$ -layered mesh implies  $n$  layers of nodes and  $n - 1$  layers of elements.

For two practical reasons, no backscatter model is applied here ( $F_i = 0$ ). Firstly, all 2D turbulence generation is accounted for by topographical forcing in the present case; secondly, it is not straightforward how exactly to extend the 2DH backscatter models treated in the previous sections toward computations with multiple layers. All boundary conditions are consistent with the 2DH case, including bottom friction and sidewall friction coefficients. A simple eddy viscosity model (Elder's term) is adopted to account for 3D bottom turbulence; it is assumed that the 2D Elder formulation remains a reliable approach for 3D simulations with the present coarse vertical resolution. (This coarse resolution does not allow for applying e.g. a vertical  $k$ - $\epsilon$  turbulence model in a reliable way.) It is assumed that the eddy viscosity  $\nu_t = c_h u_* H$  (with  $c_h = 0.15$ ) is valid in the entire local water column.

Figures 6.11(a)-(d) show that instantaneous values of the depth-averaged vertical velocity  $\tilde{w}$  increase with increasing number of layers, i.e. the vertical degree of freedom. We assume that  $\tilde{w}$  is a relevant measure for the secondary flow intensity; obviously,  $\tilde{w} = 0$  for the 2DH case. The multiple-layer cases exhibit a secondary flow pattern that is clearly related to large-scale coherent structures. These 3D patterns are observed in the absence of 3D bottom turbulence, which is not resolved. This implies that secondary flow patterns in the SLE geometry are basically induced by large-scale quasi-2D phenomena. Comparing the 4-layer case 6.11(d) with Figure 4.19 in Chapter 4, we notice that vertical flow patterns are captured much more clearly and distinctively by the 4-layer case than by the full 3D LES; this difference is mainly due to small-scale fluctuations within the LES results.

In panels (b)-(d), adjacent upwelling and downdraft regions are clearly observed along streak lines in between consecutive 2DCS (near saddle points); this confirms the observations for Case 2A in Section 4.6. Moreover, these streak line patterns are connected with upwelling and downdraft regions inside the 2DCS themselves, which stem from centrifugal forces; this is in agreement with observations by Von Carmer et al. [107]. Possibly the streak line secondary flow originates from centrifugal effects inside 2DCS, while the intense lateral shear near saddle points subsequently intensifies the secondary flow vorticity. An indication for this is the fact that extreme values of  $\tilde{w}$  are found near saddle points rather than inside 2DCS. Finally, we observe that secondary flow patterns gradually decay in downstream direction and eventually vanish. Hence, as found by Von Carmer et al. [107] and Jirka [47], the quasi-2D flow evolves toward a really 2D far-field flow pattern.

The vertical degree of freedom which enables secondary flow also impacts the horizontal TKE levels  $\tilde{u}'^2$  and  $\tilde{v}'^2$ . In Section 6.6 we observed a consistent overprediction of these quantities for all 2DH SLE cases. In Figure 6.11(e)-(f), 3D results for 2, 3 and 4 layers are compared with 2DH results as well as the full 3D LES results. For both quantities, the present small number of layers appears insufficient to accurately resolve the near-field turbulent kinetic energy. Although some of the multi-layer results show a slight improvement for  $\tilde{v}'^2$  compared to the single-layer case, the overprediction for  $\tilde{u}'^2$  becomes even worse for 3-4

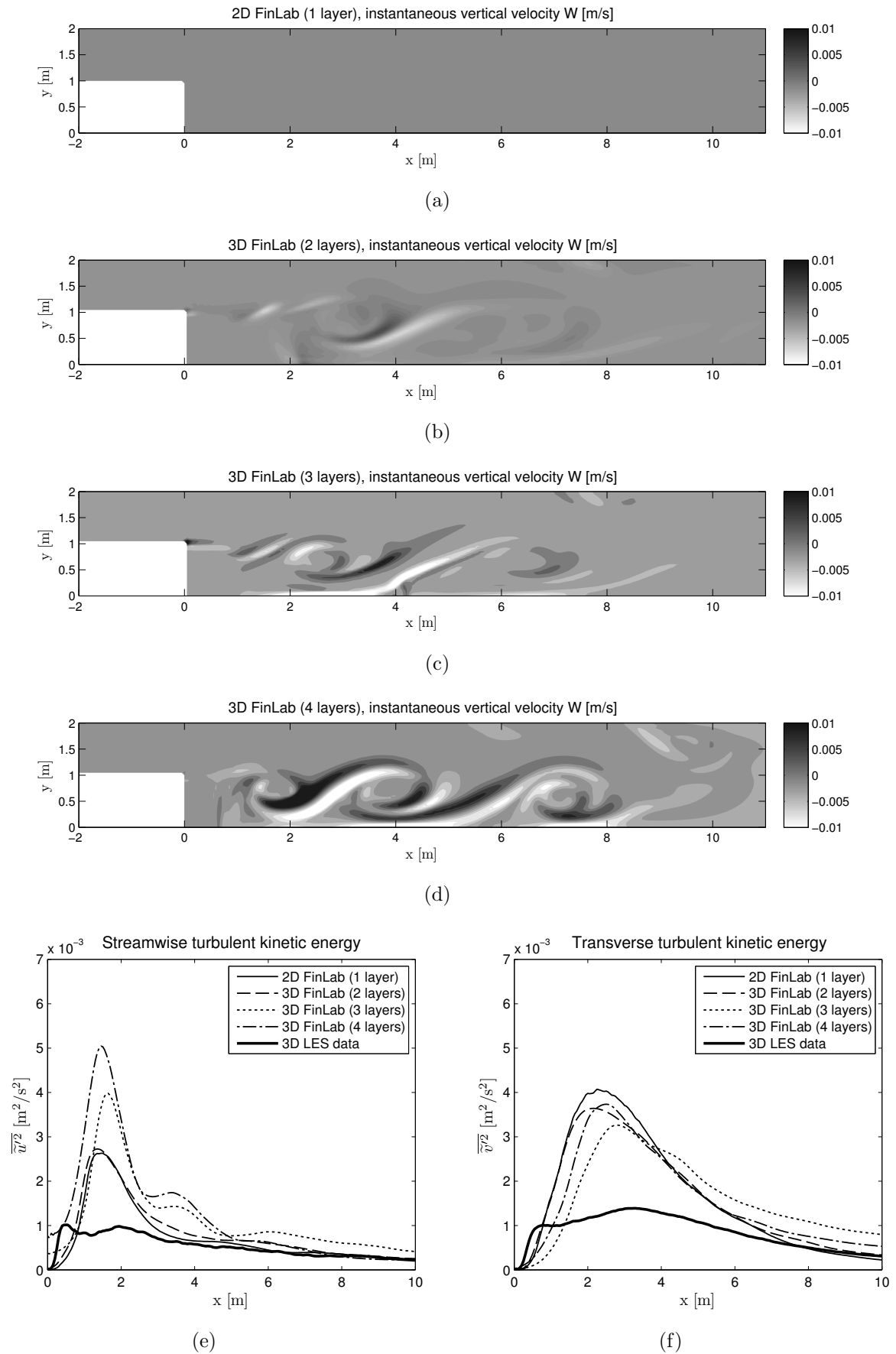


Figure 6.11: SLE geometry: influence of secondary flow. Depth-averaged vertical velocities at  $t = 2000$  s for 1 to 4 layers (a)-(d), streamwise TKE (e) and transverse TKE (f).

layers. Presumably the 3D near-field turbulence structure should be resolved with even higher resolution in order to approximate the LES data.

Summarizing: if it is desired to capture large-scale secondary (vertical) flow effects within a shallow shear flow simulation (e.g. in order to obtain more realistic flow properties for mixing and vertical dispersion), while accepting possible errors due to not fully resolving the 3D flow structure, a “semi-3D” simulation with only a few layers in vertical direction can be considered a practical and cheap solution. Developing an appropriate backscatter model for such multi-layered flow cases forms an additional challenge. Results from Section 6.6 show however that applying a backscatter model is not always necessary.

## 6.9 Summary and discussion

Two-dimensional depth-averaged (2DH) computations have been performed on three shallow turbulent flow cases that are essentially different: the SCF, SML and SLE geometries. An innovative 2D backscatter model has been proposed, coined DANSLES (Depth-Averaged Navier-Stokes with Large Eddy Stimulation), which unifies various existing models for quasi-2D turbulence in a 2DH context. Backscatter models apply a forcing field  $F_i$  in order to explicitly stimulate the emergence of 2D turbulent motion in combination with some eddy viscosity model. The newly developed model combines most advantages of the existing backscatter models DA-LES and 2D-TRANS+KS, while it is easy to implement and requires only a small computational effort (comparable to DA-LES).

A practical limitation of DANSLES (as well as the original backscatter models) is the fact that a constant water depth  $H$  is required; however, the model does not contain any further geometry-dependent parameters. Although DANSLES is a generic formulation which is calibrated against a simple channel flow geometry, it yields satisfactory results for other shallow shear flow cases as well. Nevertheless it must be stated that a 2DH approach always will have practical limitations; the absence of the third dimension may give rise to errors in cases where vertical flow or other secondary flow features are important (e.g. the SLE near field, see Section 6.6.3). It can be stated that there is no general solution to lack of resolution.

How generic is DANSLES actually? In terms of implementation, the model offers several advantages. Firstly, the use of Inverse Fast Fourier Transforms (IFFT) offers a very efficient way to construct 2D kinematic fields from spectral information only, without significantly increasing the total computational effort. This makes cumbersome time-consuming 2D-TRANS+KS computations unnecessary. Secondly, the construction of kinematic vector fields can take place on a structured grid independent from the computational mesh (which might represent a rather complex geometry); subsequently the resulting field  $F_i$  can be straightforwardly interpolated toward the computational mesh without inducing large errors, provided that both mesh resolutions are comparable. As  $F_i$  scales with the squared friction velocity, which usually decreases near solid walls, the final force field  $F_i$  will usually fit impermeable boundary conditions reasonably well. Thirdly, compared to DA-LES a divergence-free field is obtained by DANSLES in a very natural way. Fourthly and finally, time-dependency of 2D kinematic vector fields is introduced by means of quite a simple approach without temporal coherence (see Equation (6.30)) and it has been shown that spectral anisotropy can be discarded, which makes the method more generic than 2D-TRANS+KS.

It should however be emphasized that there exist two types of generality. A model can be either generic in its implementation or in its applicability. Adding more complexity

to a turbulence model may increase its accuracy for certain cases, but will also restrict its applicability to a narrow class of specific geometries. On the other hand, turbulence models that are “as simple as possible” may be applied to almost any flow case without producing too much erroneous results, yet their accuracy remains limited and their results must be interpreted as such.

It is conjectured here that the DANSLES backscatter model offers a certain general applicability to shallow turbulent flows, especially shallow shear flows with constant  $H$  and a preferred flow direction, regardless of the exact shape of the horizontal geometry and the orientation of the computational grid. This hypothesis should be tested by means of many additional computations. Furthermore, one should always keep in mind that all backscatter models treated in this chapter have been calibrated and tested on laboratory scale. Application to realistic environmental flows would require further validation with the help of field data.

Obviously, the development of a backscatter model that is valid for arbitrary geometry (i.e. variable water depth  $H$ ) would be a desirable improvement. Such a model would however contain quantities with a large spatial variability, which are difficult to be derived from spectral information using IFFT operations. This implies that the general idea behind DANSLES is not easily reconciled with spatial variable bathymetry; a totally different approach may be necessary to that end. A possible approach that may prove useful in this respect is given by wavelet analysis, as wavelets can basically be interpreted as Fourier-like harmonic components which possess a spatial variability as well.



# Chapter 7

## Conclusions and recommendations

This chapter summarizes the results of the present study; it is intended as a synthesis of the discussions already found in previous chapters. Section 7.1 gives an overview of the research procedure that has been followed. In Section 7.2, conclusions stemming from the previous chapters are presented in an integrated way. Section 7.3 lists a number of ways to utilize the results of this study for new applications. Finally, Section 7.4 contains a number of recommendations and suggestions for further research.

### 7.1 General overview

The objective of this thesis has been the investigation of quasi two-dimensional coherent structures (2DCS) in shallow separating flows. In particular (see Section 1.5), it has been studied how the development of such 2DCS is influenced by the presence of steady recirculation areas (gyres). The principal object of research has been a specific shallow flow geometry, coined Shallow Lateral Expansion (SLE), which guarantees the presence of flow separation and steady gyres by means of its topography, but otherwise contains only a minimum of geometrical complexity (see Figure 1.6(b)).

For comparison with this basic flow case, a range of other shallow flow geometries have been studied as well. The well-known Shallow Mixing Layer geometry (SML) was compared with the SLE in order to exhibit the fundamentally different way in which 2DCS are generated in both flow geometries. Furthermore, a series of 13 systematically varied adaptations of the SLE geometry were investigated. In this way it has been shown in which way the behavior of 2DCS depends on the steady gyre pattern, and hence which kind of geometry adaptations are effective in order to manipulate the development of 2DCS.

Three methodologies have been used in the context of this study:

1. Laboratory experiments, using free-surface Particle Image Velocimetry (PIV);
2. Detailed three-dimensional (3D) Large Eddy Simulations (LES);
3. Two-dimensional depth-averaged (2DH) simulations, testing various shallow-flow turbulence modeling concepts including the newly proposed concept of Depth-Averaged Navier-Stokes with Large Eddy Stimulation (DANSLES).

The first two methods have been used as basic research instruments to generate data and to identify relevant physical processes for the dynamics of 2DCS (Chapters 3 to 5). The third methodology, on the other hand, was used in order to improve the 2DH modeling of turbulent shallow flows (Chapter 6).

The following research procedure has been followed:

- Free-surface PIV measurements have been performed on the basic SLE geometry only (Chapter 3). Based on 27 test experiments with simple flow visualization techniques, three final experiments were defined for PIV analysis; in these three cases the width of the inflow section was varied (Section 3.4). Detailed spatial and temporal velocity maps were generated, resulting in an analysis of flow characteristics at the free surface: mean flow statistics, large eddy length scales, velocity scales and energy density spectra (Sections 3.5-3.7). These data have provided information on the growth of 2DCS and their interaction with the steady gyre pattern.
- Detailed 3D LES computations have not only been performed on the three basic SLE flow cases, but also on the SML geometry (Chapter 4) and on a range of systematically varied SLE geometry adaptations (Chapter 5). Hence, all turbulent flow cases studied in this thesis are covered by LES data. A conventional numerical LES technique has been used. The LES approach allowed to study the impact of upstream flow perturbations (representing 3D bottom turbulence) on 2DCS. The results highlight the fundamental difference between the SLE and SML geometries (see Section 4.5). Subsequently, the free-surface PIV analysis of 2DCS behavior has been extended by means of 3D LES information. The presence of 3D secondary flow effects within the so-called “quasi-2D” mixing layer has been studied, as well as their important role for the lateral transfer of momentum in shallow shear flows (Sections 4.6-4.7).
- The influence of geometry variations on 2DCS was assessed (Chapter 5). A range of 3D LES experiments have provided information on how 2DCS patterns could be affected by altering the steady gyre pattern (Sections 5.3-5.4). As these numerical experiments involve schematized and idealized flow conditions only, their results are not straightforwardly applicable to complex environmental flow situations. Therefore, the applicability of these insights was tested experimentally for the case of a realistic shallow separating flow (Section 5.5). A contribution was made to a pilot project by the Dutch Ministry of Public Works, involving the adaptation of a complex groyne field flow in the Dutch river Waal by placing a streamwise pile sheet in front of the upstream groyne head. This pilot project has been successful as the proposed measure showed to be effective (see Sieben [76, 77]). Nonetheless it is clear that a careful and critical attitude is required when one applies theoretical insights stemming from laboratory-scale data to real-world environmental hydraulic problems.
- The 2DH computations addressed in Chapter 6 were not intended to generate new basic data on 2DCS behavior, but to investigate how the 2D modeling of essentially 3D turbulence processes can be improved. The desire for 2D schematizations is mainly motivated by the reduced computational cost compared to full 3D models. The SLE and SML geometries have been used as test cases, whereas a simple straight channel flow (SCF) geometry was adopted for calibration purposes. A generic numerical solver named FINLAB has been used, based on state-of-the-art finite element techniques (see Labeur [52]). Within this numerical framework various existing 2DH turbulence models have been tested and compared. A new generic backscatter model has been proposed (DANSLES), which unifies two existing backscatter models (Section 6.4.3). The new model was applied to the present test cases, with satisfactory results (given the natural limitations of a 2DH approach). The DANSLES formulation is considered applicable to a wide range of shallow flow geometries, the most important restriction being that a constant water depth and bottom level are required. Finally, it has been shown that large-scale secondary flow effects can be incorporated in a quasi-2D flow model by employing a few computational layers in vertical direction, without the need to resolve the entire 3D turbulent flow structure.



## 7.2 Synthesis

### 7.2.1 Generation mechanisms of 2DCS and vortex shedding

- As outlined by Jirka [47], three mechanisms can be discerned that are responsible for the generation of quasi two-dimensional coherent structures (2DCS) in turbulent shallow flows: 1) topographical forcing, 2) internal transverse shear instabilities and 3) secondary instability of base flow (Section 2.2.3). For the latter two mechanisms, we can state that 2DCS are initiated by large-scale components of 3D bottom turbulence (see Van Prooijen [99]). The first mechanism is often associated with flow separation. The SLE geometry considered in this thesis is a classical example of a shallow-flow geometry including “topographically forced” 2DCS.
- A relevant question is however which phenomenon is actually topographically forced. Certainly separation is often induced by topography, i.e. a solid wall configuration. But can we state that the shedding of 2DCS is forced topographically as well? From both 2D and 3D SLE data, we have observed the road to generation of 2DCS. Obviously, the primary separation event is forced by solid wall topography (Section 2.3). This is also true for the development of a steady primary gyre, which is always present in all SLE data. In general however, both flow separation and a primary gyre are not sufficient to induce 2DCS. Again in all SLE data sets, we consistently observe that 2DCS are only generated if a *steady secondary gyre* is present. Such a secondary gyre develops due to a secondary separation event, which is not forced by topography but by an adverse pressure gradient along the primary gyre backflow region. As soon as the secondary gyre is fully developed and affects the separating (primary) boundary layer, the shedding of 2DCS starts immediately. Hence for the SLE geometry considered here, vortex shedding is not forced by *topography* itself but by the *steady gyre configuration*. We may continue to address the SLE geometry as being topographically forced; however, this forcing effect is actually secondary and involves the flow pattern rather than solid wall topography.
- The vortex shedding phenomenon observed here involves 2DCS that grow linearly in scale and energy while being advected in downstream direction. As pointed out by Uijttewaal et al. [90, 93] and Sieben [77], a different type of vortex shedding is often observed in complex environmental situations like groyne fields, which involve irregular bathymetry, sloping solid walls and flow contraction. In such configurations, 2DCS are often observed to grow in size and energy while staying in place just downstream of the separation point; eventually they break away from the groyne tip (*direct vortex shedding*, see Sections 2.4 and 5.5). This mechanism has not been observed within the SLE data in the present study. Presumably its presence is highly dependent on geometry details like wall slopes and flow contraction; the rather simple SLE geometry studied here leaves no room for such a mechanism. The SLE mixing layer is characterized by continuously moving and gradually growing 2DCS rather than by near-field vorticity accumulation; it resembles a near-field SML mixing layer rather than a complex groyne field configuration.

### 7.2.2 Effects of shallowness on 2DCS development

- The importance of the steady secondary gyre for 2DCS generation (in SLE context) has been outlined above. In addition, the primary gyre affects 2DCS as well while they are advected downstream. As 2DCS and the primary gyre share the same vorticity sign,

they are able to interact by means of the vortex merging mechanism (Sections 2.2.2-2.2.3). In fact, the pathways of 2DCS do intersect the primary gyre over a long distance (see Figure 3.8), enabling a process of gyre-vortex interaction. Mutual interaction between 2DCS is of less importance and has not been convincingly observed.

- On the one hand, 2DCS sustain the primary gyre by seeding it with mass and momentum and cause the gyre to “breathe”. This phenomenon is visible from the periodic movement of the primary gyre length (i.e. location of the reattachment point). On the other hand, the interaction between primary gyre and 2DCS transfers kinetic energy to larger scales, effectively “boosting” the mixing layer eddies and enhancing their velocity scale (see Figure 3.22). It is observed from 3D and 2DH computational results (Chapters 4 and 6) that 2DCS velocity scales reach larger values for SLE cases than for SML cases. This difference is not only explained by a different lateral velocity difference, but also by the absence of gyre-vortex interaction within the SML case. The interaction outlined above is a typical quasi-2D turbulence mechanism. Therefore it is not surprising that its effects were especially found in the results of the relatively most “shallow” SLE geometries treated in Chapters 3-4: Cases 1 and 2. The rather “deep” Case 3 did not exhibit results that could be convincingly explained by gyre-vortex interaction. Also, Cases 1 and 2 exhibit the most pronounced far-field eddy isotropy, whereas all 2DCS in Case 3 and the SML Case 4 remain predominantly anisotropic (elongated) throughout their entire path along the mixing layer.
- In spite of the quasi-2D character of 2DCS, secondary flow patterns are observed throughout the shallow mixing layer in all Cases 1–4, especially in the middle-field region. These patterns are elongated zones of upwelling and downdraft of fluid; they stem from centrifugal effects inside large eddy kernels (see Von Carmer et al. [107]) and are continuously stretched along saddle point regions which contain a considerable rate of strain. Large-scale 3D secondary flow should be distinguished from 3D bottom turbulence; it significantly contributes to the lateral transfer of momentum within the shallow shear flow, apart from 2D and 3D turbulent contributions.
- Furthermore, it is observed that the precise mechanism for 2DCS generation has no large influence on mean flow length scales. Although these mechanisms are different for SML versus SLE geometries and also for SLE Case 1–2 versus Case 3, the over-all mixing layer width satisfies a rather simple formulation based on a self-similarity assumption, even while the self-similarity approach is not strictly valid for shallow recirculating flows. Obviously this self-similarity behavior has its limitations in practice: it will not hold for a water depth going to zero. Paradoxically, the 2DCS length scale development and the associated mixing layer width appear to be not very sensitive to the precise 2DCS generation mechanism and to upstream turbulence, whereas 2DCS velocity scales appear to be much more sensitive to these effects. This paradox has also been found by Dracos et al. [32] for shallow jet flows and by Van Prooijen [99] for SML geometries; no sound explanation has yet been found for this discrepancy. From a practical point of view, however, such a paradox is rather advantageous than problematic when it comes to modeling these types of shallow shear flows.

### 7.2.3 Sensitivity to upstream perturbations

- The triggering effect of upstream perturbations (inflow turbulence) on downstream 2DCS growth can only be examined by numerical experiments; in the context of laboratory or field experiments, such perturbations are omnipresent and cannot be “switched off”. From both 3D and 2DH simulations, we find that SLE flow situations

are not significantly sensitive to upstream perturbations; the internal topographical forcing mechanism is by far dominant for the generation of 2DCS. For SML and SCF (straight channel flow) situations on the other hand, we find a high sensitivity of 2DCS to upstream turbulence. In the theoretical SML case without inflow perturbations and adopting a rigid-lid surface (3D case), no 2DCS will be found. In practice, we find that 2DCS can still develop in such cases due to the presence of small-scale machine precision errors; whether this happens however depends strongly on discrete resolution, which determines the amount of viscous damping (see Section 4.5). When adopting a free surface (2DH case), we find that 2DCS in a SML case can be triggered by the boundary conditions (which give rise to weak free-surface oscillations). The differences in sensitivity between the SLE and SML/SCF geometries convincingly underline the differences between the three 2DCS generation mechanisms outlined by [47].

- The sensitivity of SML geometries to upstream perturbations has been demonstrated by Van Prooijen and Uijttewaal [99,101] by means of linear stability analysis. A formal stability analysis for a SLE or other non-uniform shallow separating flows is not straightforward (due to the absence of self-similarity) and this has not been pursued in the present study. Nevertheless, it is conjectured that a valid kind of linear stability analysis could be derived for “topographically forced” shallow separating flows, describing the growth rates of unstable modes within the associated shallow mixing layer. An important property of the SLE with respect to hydrodynamic stability is that perturbations needed to trigger unstable modes are always available: the topographical forcing mechanism intrinsically provides a wide spectrum of perturbations. In the SML case all 2DCS within the mixing layer are just moving downstream, until they leave the outflow boundary and hence are “lost”; in the SLE case, part of the 2DCS energy is somehow “trapped” within the steady gyre pattern, which in turn feeds the shallow mixing layer continuously with new perturbations.

#### 7.2.4 Impact of geometry variations

- The important role of the secondary gyre (in SLE context) is given by the fact that it strongly enhances lateral shear in the near-field mixing layer, so that hydrodynamic instabilities with vertical vorticity vector are being generated. The bottom line of the numerical LES experiments presented in Chapter 5 has been how to reduce or eliminate this large near-field lateral shear, in order to reduce the downstream 2DCS turbulence intensities as well.
- The placement of a vertical splitter plate (pile sheet) between main flow and secondary gyre seems a logical suggestion but turns out to be ineffective, as the entire steady gyre pattern is simply moving downstream but is not essentially influenced. Another idea was to apply a smoothly bended sidewall, effectively moving downstream the separation point; this alternative appears to be not helpful either to reduce near-field lateral shear. A more effective approach is to apply a downstream obstacle such as a groyne, which actually compresses the entire upstream gyre pattern. The length of the secondary gyre can be reduced in this way and hence the length of the near-field region with strong lateral shear. Mixing layer width and horizontal turbulence intensities related to 2DCS can be reduced for groyne field lengths below 3 to 6 times the groyne length ( $x_{groyne}/D < 3-6$ ) in combination with an upstream splitter plate. This advantage is maintained if long series of groynes are applied, as has been checked by computations including 7 consecutive groyne fields. The common groyne field aspect ratio of about 3–4, which is often encountered along lowland

rivers, indeed does make sense in the perspective of these observations (although an even further reduction of groyne field lengths could be advantageous to reduce main flow contraction and associated scour near groyne heads). It has been found that a combination of a downstream groyne and an upstream splitter plate works best in reducing 2DCS scales and turbulence intensities inside the SLE geometry. In this way the interaction of primary and secondary gyre, boosting the 2DCS, can be hindered.

- The insights stemming from the LES computations described above have been applied to an environmental groyne field problem in the context of the “Bord voor de Kop” pilot project. This project has yielded satisfactory results, although it is obvious that a real-world groyne-field flow contains much more complexity than an academic test case, especially due to morphology and solid wall slopes. More elaborate conclusions on this project can be found in Sections 5.5 and 5.6.

### 7.2.5 2DH modeling aspects

- Ghidaoui and Kolyshkin [38] have shown that the 2D shallow water equations are fundamentally able to resolve 2DCS and their development, provided of course that the computational mesh resolution is sufficient. Also the 2DH finite element solver FINLAB, employed throughout Chapter 6, has proven able to resolve 2DCS. Obviously the interactions between 3D and 2D turbulent motion are lacking in a 2DH context; these interactions are modeled by means of closure formulations which account for production and dissipation of 2D turbulent kinetic energy. Closure of production terms can be accounted for by an explicit backscatter model, while dissipation terms are usually closed by eddy viscosity-type models.
- All respective closure terms are derived from a formal derivation of the 2D Shallow Water Equations (SWE), leading to the system (6.12)-(6.13). The newly proposed backscatter model DANSLES (see Section 6.4) fits into this general framework, as well as dissipative closure terms like Elder’s term and the subgrid-scale model HLES.
- If backscatter models are applied, it is common practice (see e.g. [42, 49, 96, 99]) to adopt a grid discretization close to  $1/3$  or  $1/4$  of the water depth  $H$ ; in the present study (Chapter 6), a grid resolution  $\Delta x = \Delta y = \frac{1}{4}H$  is adopted in order to resolve 2DCS with sizes  $\mathcal{L} > 2H$ . For such a fine resolution (i.e. a mesh size at sub-depth scale), it has been found that the influence of a 2D sub-grid scale model like HLES tends to vanish due to its grid-dependency, whereas the contribution of a general eddy viscosity model like Elder’s term (which is based on a mixing length hypothesis) remains significant. Hence, the latter type of dissipative closure term is dominant for 2D high-resolution computations, unless a large amount of small-scale TKE is present due to the use of a backscatter model.
- If no backscatter model is used and all other closure terms are merely dissipative, artificial turbulence perturbations should be imposed on the model inflow boundary (at least in the absence of topographical forcing effects, see Jirka [47]). Such 2DH artificial turbulence however decays much faster than its 3D counterpart (compare e.g. the LES computations in Chapter 4). This can be explained by the absence of vertical shear: in general, 2D turbulence without artificial backscatter is not able to maintain itself. Only the largest eddy scales survive and these may effectively trigger 2DCS in regions of lateral shear; eddy energy at smaller scales however is often lacking, giving rise to turbulence flow patterns that are unnaturally regular.
- The newly proposed backscatter model DANSLES is based on two existing backscatter models: DA-LES and 2D-TRANS+KS (Sections 6.4.1-6.4.2). The DA-LES formulation

by Hinterberger et al. [42–44] performs surprisingly well for the present test cases, despite its very simple mathematical form: it is based on random white noise fields only. Turbulent kinetic energy levels are reproduced reasonably well, while the method is quite fast as well as simply implemented. Drawbacks of the model are however the lack of proper spectral information and the fact that the resulting forcing field is not divergence-free. Furthermore, it has been argued in Section 6.7 that the so-called BSM filter recommended by [42, 43] is actually inadequate for triggering 2DCS (in contrast with the unfiltered DA-LES model).

- In contrast with DA-LES, the 2D-TRANS+KS approach by Van Prooijen and Uijttewaaij [99, 102] is based on sophisticated 2D spectral information, giving rise to a well-calibrated and divergence-free backscatter forcing field. However, the 2D-TRANS+KS approach is only valid for a narrow subset of turbulent channel flows while a generalization to general shallow flow problems is not straightforwardly achieved. Another drawback is the large computational cost of the model; in its original implementations the 2D-TRANS+KS model can be a computational burden.
- The DANSLES model integrates the DA-LES and 2D-TRANS+KS approaches in such a way that the advantages of both models are combined (Section 6.4.3). On the one hand, 2D-TRANS+KS is accelerated considerably using 2D Inverse Fast Fourier Transforms (IFFT), while the model is made applicable to a wider class of flow cases by some well-chosen simplifications. On the other hand, DA-LES is re-scaled and re-calibrated while the original white noise forcing field is given a proper physical basis. Most importantly, the theoretical and mathematical gap between both backscatter methods has been bridged by a careful comparison of both methods.
- The resulting unified model requires only a small computational effort (like DA-LES) and has quite a generic character. DANSLES does not require geometry-dependent quantities (except for the water depth  $H$ ) and is considered to be applicable to shallow turbulent flows with virtually constant water depth and bottom level, both on laboratory and field scale. The model produces rather satisfactory results when applied to the SCF, SML and SLE test cases (see Section 6.6).
- The 2DH modeling approach for shallow turbulent flows has some natural limitations, regardless whether or not a backscatter model is applied. All numerical tests of the SLE geometry show that the absence of secondary flow in a 2DH model gives rise to an overprediction of the TKE inside the mixing layer. This problem cannot be overcome by altering the 2D turbulence model because the actual mixing layer is topographically forced here. It has been found (see Section 6.8) that large-scale secondary flow structures can be readily incorporated into the numerical results by adding only a few (3–4) vertical layers to the computational domain. Such a “semi-3D” approach however does not automatically improve the solution with respect to the horizontal TKE levels, although it is a practical and cheap approach to account for some 3D flow effects without fully solving all 3D bottom turbulence.

## 7.3 Utilization

Possible utilization of the present study, either in engineering practice or within ongoing scientific research, may concern two aspects: application of newly developed research tools and application of newly acquired insights.

1. The free-surface PIV measurement technique (Chapter 3) has been successfully applied to quasi-2D shallow shear flows, even in the presence of complex secondary

flow. It is possible to give this research a spin-off by applying similar surface PIV techniques to real environmental problems like groyne fields or other forms of shallow recirculation flows. Similar full-scale experiments (on a SML geometry) have e.g. been performed by Schnauder et al. [74] in the German river Spree, in cooperation with the Environmental Fluid Mechanics section of Delft University of Technology. It should be kept in mind that free-surface PIV tends to systematically underestimate the total turbulent kinetic energy of shallow flows (especially for large Reynolds numbers); nonetheless, the large-scale quasi-2D patterns can be quite well captured.

2. With respect to data analysis, it has been shown that the use of 2D vector potential functions (in combination with conditional averaging algorithms) is a useful technique for free-surface data analysis. Shallow-flow measurements (either on laboratory scale or field scale) often require a proper instrument to detect individual large-scale structures. However, although vector potential functions are quite helpful to achieve this, they are not suited for the further statistical analysis of the structures detected; the latter analysis requires the original velocity data set.
3. The newly found insights in the development of 2DCS in shallow separating flows (and the ways in which they can be manipulated) may prove helpful for design purposes, e.g. the design of groyne fields and harbor entrances. Utilization of such scientific conclusions will always require a careful translation of interpreted results from laboratory scale toward field scale, involving expert judgment. For instance, such a kind of translation has already been performed in the present study by contributing to the pilot project “Bord voor de Kop” (Section 5.5). Another example is the project “*Reductie Sedimentatie in Havens*” (Reducing Harbor Siltation along Rivers, 2007–2008), which was initiated by the Dutch Ministry of Public Works in cooperation with the Environmental Fluid Mechanics section of Delft University of Technology (including the author of this thesis) and several engineering companies. A pilot project concerning an actual Dutch river harbor was designed, supported by numerical studies and laboratory experiments. It has been aimed to define effective measures to reduce harbor siltation, e.g. by manipulating the shallow mixing layer along the harbor entrance (by altering the horizontal geometry). Results have been reported by Termes [85].
4. The unified backscatter model DANSLES is suitable for utilization in practice. The model is generic in its formulation (like DA-LES) and suitable for a wide class of shallow flows with arbitrary horizontal geometries, although its applicability is limited to cases with constant water depth  $H$ . Further improvements could be achieved by refinement of the calibration, as well as by making the model suitable for variable bathymetry. The latter is by no means straightforward but neither impossible (see Section 7.4). DANSLES is easily implemented in current state-of-the-art numerical shallow-flow models like 2D FINLAB (FINEL); presumably the model can be applied both at laboratory and environmental scale, although the latter should be confirmed by ample additional testing.

## 7.4 Recommendations

The present thesis has actually been the result of a recommendation by Van Prooijen [99], stemming from his Ph.D. research work. In [99] attention was predominantly paid to shallow mixing layer cases (SML), but not to topographically forced shallow flow geometries including 2DCS. The present research was intended to fill this gap. Attention has been

paid specifically to the SLE geometry as well as to variations thereof. The fundamental difference in 2DCS generation between SLE- and SML-type flows has been highlighted, as well as the crucial role of the steady gyre pattern in SLE-type geometries. Having arrived at the end of this Ph.D. project, some omissions have remained while new questions did arise; these topics give rise to recommendations for future research.

1. Firstly, a quite interesting topic is the question is why the “direct vortex shedding” phenomenon observed in full-scale groyne fields (see Uijttewaaf et al. [90, 93] and Sieben [77]) exhibits such a large difference with the vortex shedding process as observed in SLE flows (see Section 7.2.1). It is worthwhile to investigate the theoretical and observational discrepancy between both types of large eddy generation. In the context of the laboratory setup used in the present study, it has not been possible yet to bridge this gap. Various circumstances could be responsible for the differences observed: not only slight differences in the steady gyre pattern, but also effects stemming from bathymetry and hydraulic roughness as well as differences in scale and Reynolds number. Even a systematic variation of these few conditions will already provide a virtually endless range of new experimental possibilities to future researchers.
2. Secondly, in a more direct relation to the experiments performed in this study, it is worthwhile to repeat the present SLE experiments on laboratory scale while systematically varying the slopes of sidewalls, especially the wall along which the main flow separates and walls adjacent to steady gyres. Other possible shallow separating flows that are worth being studied (using free-surface PIV measurements) are numerous types of harbor basins (as found along rivers), also with either vertical or sloping sidewalls. The latter investigations may form a valuable extension of earlier experimental work on harbor basins by e.g. Langendoen [53].
3. Next, the paradox described before by Dracos et al. [32] and Van Prooijen [99], which was observed once more in the present study (see the final part of Section 7.2.2) is still waiting to be elucidated. It has been consistently observed that the length scale development of 2DCS is not quite sensitive to the level of ambient background turbulence, whereas the sensitivity of large-eddy velocity scales (i.e. their TKE level) to these perturbations appears to be much larger. This discrepancy may be clarified not only by means of experiments, but also computationally by means of 3D Large Eddy Simulations.
4. It should be stressed that large-scale free-surface PIV measurements are not suitable to virtually resolve all turbulent kinetic energy at the free surface. It can mainly be applied to resolve large-scale structures; for more detailed analysis of the entire turbulent kinetic energy spectrum, it is recommended to use a measurement technique that provides more spatially and temporally detailed results, e.g. Laser-Doppler Anemometry (LDA).
5. With respect to 3D LES computations, the present study did by no means utilize the full range of possibilities that are available at present. The choice for a rather basic LES solver, as well as the addition of a straightforward law-of-the-wall formulation to account for solid wall friction, has led to some practical limitations such as the rather inaccurate reproduction of the secondary gyre length in a SLE geometry (see Chapter 4). On the other hand, thanks to the parallelization of the numerical model a very satisfactory resolution could be achieved. It may however be desirable to apply more advanced LES solvers (like the one applied by Van Balen [97]) to the kind of shallow flow cases considered in the present study. The ghost-cell IBM formulation incorpo-

rated in the latter model is particularly suitable to investigate the impact of sloping sidewalls on flow separation and 2DCS behavior. An alternative option is to accelerate the boundary-fitted 3D FINLAB solver by Labeur [52], in order to make it suitable for very large computational domains such as required for LES computations. In this way it is possible to treat shallow flow cases with enhanced geometrical complexity (like realistic groyne fields) on laboratory scale. As pointed out in [97], improved 3D modeling of environmental flows on laboratory scale can also be an asset for the understanding and influencing of such flows at prototype scales.

6. Finally, with respect to 2D modeling, further improvements on the DANSLES backscatter model are recommended. It is desired to have a generic backscatter model that is also able to handle spatial variations in bottom level, water level and hydraulic roughness. The present DANSLES model involves variations of various quantities within the spectral domain (wave number domain), but not within the spatial domain. As explained before in Section 6.4.3, it is a cumbersome task to reconcile these two types of variables. A practical work-around could be to adopt a hybrid approach, applying spatial sub-domains in which either the spatial or the spectral quantities are variable. After constructing the backscatter forcing field in each sub-domain, these fields should be reassembled in some way. All this is by no means a straightforward operation and a profound analysis is hence required. Probably a more elegant solution of the problem could be given by wavelet analysis; basically, wavelets can be interpreted as predefined Fourier-like wave components which possess a spatial variability as well. If it be possible to construct a spatially variable backscatter forcing field consisting of wavelet components, in such a way that the efficient Inverse Fast Fourier Transform (IFFT) approach can be somehow maintained, a wavelet-based DANSLES-type model may be a workable tool without excessive computational cost. In any case, the feature of spatial variability within DANSLES is worthwhile to be achieved on behalf of the generality and applicability of the backscatter model. In general, the applicability of backscatter models should be extended by generating much more experimental flow data on prototype scale (against which 2DH numerical backscatter data could be validated), in addition to currently available laboratory-scale data validations by Hinterberger [44], Van Prooijen [102], Van Balen [96] and the present author.



# Appendix A

## On vector potential functions

Vector potential functions are applied throughout the present thesis in order to identify large-scale turbulence structures in quasi-2D flow situations. This appendix briefly provides some mathematical background of vector potentials and explains their relevance for large eddy detection.

Given a 3D solenoidal velocity vector field:

$$\mathbf{u} \in \mathbb{R}^3 : \mathbf{u} = (u, v, w), \text{ with } \nabla \cdot \mathbf{u} = 0 \text{ and } \nabla \times \mathbf{u} = \boldsymbol{\omega} \quad (\text{A.1})$$

For such a vector field with zero divergence, a 3D vector potential  $\boldsymbol{\psi}$  exists such that

$$\mathbf{u} = \nabla \times \boldsymbol{\psi} \quad (\text{A.2})$$

Since by definition  $\nabla \cdot \nabla \times \boldsymbol{\psi} = 0$ , the condition of solenoidality is always satisfied. It should be noted that  $\boldsymbol{\psi}$  is not fully uniquely determined: any arbitrary scalar gradient field  $\nabla\phi$  may be added to it. Because  $\nabla \times \nabla\phi = 0$  by definition, any combination  $\boldsymbol{\psi} + \nabla\phi$  does satisfy (A.2). Hence:

$$\nabla \times (\boldsymbol{\psi} + \nabla\phi) = \nabla \times \boldsymbol{\psi} = \mathbf{u} \quad (\text{A.3})$$

The vorticity  $\boldsymbol{\omega}$  of the vector field  $\mathbf{u}$  can subsequently be written as

$$\boldsymbol{\omega} = \nabla \times (\nabla \times \boldsymbol{\psi}) = \nabla (\nabla \cdot \boldsymbol{\psi}) - \nabla^2 \boldsymbol{\psi} \quad (\text{A.4})$$

Because  $\boldsymbol{\psi}$  has a degree of freedom, it can be chosen such that  $\boldsymbol{\psi}$  is also solenoidal (see Batchelor [9]). In that case, equation (A.4) for the vorticity reduces to a Poisson equation:

$$\boldsymbol{\omega} = -\nabla^2 \boldsymbol{\psi} \quad (\text{A.5})$$

The advantageous aspect about the Laplacian operator in this expression is that it operates on each vector component separately. Therefore, if only the  $z$ -component of the vorticity is known, yet the full  $z$ -component of the vector potential field can be constructed. In the present study the emphasis is on the vertical vorticity component  $\omega_z$ , which is made up by the horizontal velocity components  $u$  and  $v$ . If only the 2D surface velocity field is known (as is the case for the experiments described in Chapter 3), the surface vector potential field  $\psi_z$  (which becomes actually a scalar field) can be known as well. At the boundaries of the velocity field, it is practically sufficient to use homogeneous Neumann boundary conditions for solving the Poisson equation.

Taking the curl of the constructed vector potential component  $\psi_z$  yields, in turn, a vector field that practically resembles the original horizontal velocity field  $(u, v)$ . It only slightly

differs from the original velocity field as a flow vector field in a 2D plane within a 3D flow domain usually has nonzero divergence. Therefore, the function  $\psi_z$  only makes sense if the flow has a quasi-2D character. This condition is obviously satisfied in case of a shallow flow with large-scale coherent structures in the horizontal plane. In that case, taking the curl of the vector potential is equivalent to:

$$u = \frac{\partial \psi_z}{\partial y} \quad \text{and} \quad v = -\frac{\partial \psi_z}{\partial x}, \quad (\text{A.6})$$

which shows that  $\psi_z$  resembles the concept of a 2D stream function. The only difference is the fact that in the computation of  $\psi_z$  a correction has been made to circumvent the non-solenoidality of the  $(u, v)$ -plane in a 3D flow context. In fact, using (A.5) and (A.6) implies that the original velocity field  $(u, v)$  is projected upon a divergence-free vector field with the same vorticity as the original field.

Essentially, computing a vector potential is a way to integrate the associated velocity field, revealing large-scale rotation patterns. On the contrary, computing a vorticity field implies taking a spatial derivative of that velocity field, effectively favoring small-scale rotation patterns. This explains why vorticity field data are often very noisy, whereas on the other hand vector potential data have a much more smooth character and hence are easier to interpret.

Each local maximum or minimum of a 2D vector potential function  $\psi_z$  identifies a vortex core of positive respectively negative vorticity sign. In practice all function isolines are virtually parallel to the original 2D velocity vectors  $(u, v)$ , provided that the flow field has a quasi-2D character.

It is concluded that vector potentials are a very suitable tool for identifying large-scale quasi-2D eddies. A disadvantage of constructing vector potentials may be that the solution procedure for a 2D Poisson equation is computationally expensive. This is especially relevant for unstructured meshes. The computational cost can however be significantly reduced if a rectangular mesh is used; this allows for the application of a Fast Fourier (FFT) Poisson solver, which consumes only a minimum of computational time and effort.

# Appendix B

## Construction of IFFT velocity fields

This appendix provides some background information on Fast Fourier Transforms (FFT) and Inverse Fast Fourier Transforms (IFFT). It is explained how energy density spectra can be derived using FFT's, and how kinematic velocity fields can be constructed with the help of IFFT's while only the energy density spectrum is known.

The basic mathematical operations underlying FFT and IFFT are the Discrete Fourier Transform (DFT) and Inverse Discrete Fourier Transform (IDFT). These transformations can become a computational burden for large data sample sizes  $N$ . The FFT and IFFT algorithms are shortcuts which compute the DFT and IDFT exactly but take only a minimum of computational effort, i.e.  $\mathcal{O}(N \log N)$  operations instead of  $\mathcal{O}(N^2)$ . In this study, a variant of the well-known FFT algorithm by Cooley and Tukey [30] is applied. The full version of this algorithm is very elaborate and is not given here. However, the effect of the algorithm is fully equivalent to the basic DFT expressions which are given below. In this thesis we always employ the terms FFT and IFFT instead of DFT and IDFT.

We define a real discrete function  $f$  with sample size  $M$  on a 1D equidistant grid with index  $j = 0, 1, 2, \dots, M - 1$ . The increment between sample points is  $\Delta x$  and the domain length is  $L_x = M\Delta x$ . Associated to the spatial domain  $x = j\Delta x$  we define a wave number domain  $k_x = m\Delta k_x$ , with index  $m = 0, 1, 2, \dots, M - 1$  and wave number increment  $\Delta k_x = 2\pi/L_x$ . The upper bound of the wave number domain is denoted by  $\hat{k}_x = M\Delta k_x = 2\pi/\Delta x$ . Then the one-dimensional FFT of  $f$  is given by the discrete function  $F$ :

$$F = \mathcal{F}\{f\} : F_m = \frac{1}{\sqrt{M}} \sum_{j=0}^{M-1} f_j e^{-i2\pi(jm/M)} \quad (\text{B.1})$$

And the 1D IFFT of  $F$  is given by the original discrete function  $f$ :

$$f = \mathcal{F}^{-1}\{F\} : f_j = \frac{1}{\sqrt{M}} \sum_{m=0}^{M-1} F_m e^{i2\pi(jm/M)} \quad (\text{B.2})$$

Both operations are linear and commutative, hence  $\mathcal{F}^{-1}\mathcal{F} = \mathcal{F}\mathcal{F}^{-1}$ .

$F$  is a sequence of complex numbers, containing amplitudes  $\hat{F}$  and phases  $\phi$  according to:  $F_m = \hat{F}_m e^{i\phi_m}$ . If the original sequence  $f$  only contains real numbers, the FFT-transformed sequence  $F$  appears to be symmetric in  $\hat{F}$  and antisymmetric in  $\phi$ . We find that  $\hat{F}_m = \hat{F}_{M-m}$  and  $\phi_m = -\phi_{M-m}$ ; hence,  $F_m$  and  $F_{M-m}$  are complex conjugates. The symmetry axis is given by  $m = M/2$ , which defines the so-called Nyquist wave number:  $k_x^* = 2\pi/2\Delta x = \frac{1}{2}\hat{k}_x$ . This is the largest wave number that can be resolved by the spatial grid, equivalent to a wave length  $\lambda_x = 2\Delta x$ . All larger wave numbers ( $k_x^* < k_x < \hat{k}_x$ )

are associated with wave aliasing; they can also be interpreted as negative wave numbers ( $-k_x^* < k_x < 0$ ). (The latter interpretation has no impact on the FFT, as can be checked straightforwardly.) If we want to construct a purely real  $f$  using a prescribed complex  $F$ , we have to make sure that all  $F_m$  and  $F_{M-m}$  are complex conjugates.

The 1D expressions outlined above can be straightforwardly extended to two dimensions. We define a real discrete function  $f$  with sample size  $(M, N)$  on a 2D equidistant grid with indices  $j = 0, 1, 2, \dots, M-1$  and  $k = 0, 1, 2, \dots, N-1$ . The spatial increments are  $\Delta x$  and  $\Delta y$ , hence the domain size is  $L_x = M\Delta x$  times  $L_y = N\Delta y$ . The 2D wave number domain is defined as  $k_x = m\Delta k_x$  and  $k_y = n\Delta k_y$ , with indices  $m = 0, 1, 2, \dots, M-1$  and  $n = 0, 1, 2, \dots, N-1$  and wave number increments  $\Delta k_x = 2\pi/L_x$  and  $\Delta k_y = 2\pi/L_y$ . The upper bounds of the wave number domain are denoted by  $\widehat{k}_x = M\Delta k_x = 2\pi/\Delta x$  and  $\widehat{k}_y = N\Delta k_y = 2\pi/\Delta y$ . Then the 2D FFT of  $f$  and 2D IFFT of  $F$  are given by:

$$F = \mathcal{F}_2\{f\} : F_{m,n} = \frac{1}{\sqrt{MN}} \sum_{j=0}^{M-1} \sum_{k=0}^{N-1} f_{j,k} e^{-i2\pi(jm/M + kn/N)} \quad (\text{B.3})$$

$$f = \mathcal{F}_2^{-1}\{F\} : f_{j,k} = \frac{1}{\sqrt{MN}} \sum_{m=0}^{M-1} \sum_{n=0}^{N-1} F_{m,n} e^{i2\pi(jm/M + kn/N)} \quad (\text{B.4})$$

Again we have  $\mathcal{F}_2^{-1}\mathcal{F}_2 = \mathcal{F}_2\mathcal{F}_2^{-1}$ . If  $f$  only contains real numbers, we find symmetry properties in  $F$  once more. Two symmetry axes are found in this case, being the lines  $m = M/2$  and  $n = N/2$ , by which two Nyquist wave numbers are defined:  $k_x^* = 2\pi/2\Delta x = \frac{1}{2}\widehat{k}_x$  and  $k_y^* = 2\pi/2\Delta y = \frac{1}{2}\widehat{k}_y$ . These lines divide the total wave number space into four quadrants. We find two symmetry regimes: the lower-left and upper-right quadrant are containing complex conjugates, and so do the lower-right and upper-left quadrant. This is expressed by the relations  $\widehat{F}_{m,n} = \widehat{F}_{M-m, N-n}$  and  $\phi_{m,n} = -\phi_{M-m, N-n}$ .

If we want to construct a purely real  $f$  using a prescribed complex  $F$ , we have to make sure that all  $F_{m,n}$  and  $F_{M-m, N-n}$  are complex conjugates. To this end, the  $\phi$  values of two adjacent quadrants may be chosen freely, after which the  $\phi$  values for the other two quadrants can be determined. All imaginary contributions to the IFFT are then vanishing, hence Equation (B.4) reduces to:

$$f = \mathcal{F}_2^{-1}\{F\} : f_{j,k} = \frac{1}{\sqrt{MN}} \sum_{m=0}^{M-1} \sum_{n=0}^{N-1} \widehat{F}_{m,n} \cos(2\pi\{jm/M + kn/N\} + \phi_{m,n}) \quad (\text{B.5})$$

This version of 2D IFFT is applied within DANSLES (see Equation (6.34) in Section 6.4.3). All supra-Nyquist wave numbers ( $k_x^* < k_x < \widehat{k}_x$ , resp.  $k_y^* < k_y < \widehat{k}_y$ ) can be alternatively interpreted as negative wave numbers ( $-k_x^* < k_x < 0$ , resp.  $-k_y^* < k_y < 0$ ). This interpretation has no impact on the 2D FFT. The most important consequence of wave numbers changing sign is the fact that all possible wave directions are precisely accounted for by the four quadrants. In two dimensions, the direction of each harmonic component  $F$  in Fourier space is given by the angle  $\psi = \arctan(k_y/k_x)$ ; this implies that the wave number combinations in the first quadrant fill the range  $0 \leq \psi \leq \pi/2$ . If the supra-Nyquist wave numbers are mirrored as described above, all four quadrants together exactly satisfy all “wind directions” between  $0 \leq \psi \leq 2\pi$ .

The discrete one-dimensional energy density spectrum  $E$  (or variance density spectrum) of a stationary 1D random signal  $f$ , using all previous definitions, can be constructed by means of the squared 1D FFT:

$$E = \mathcal{E}\{f\} : E_m = \frac{1}{\widehat{k}_x} |\mathcal{F}\{f - \bar{f}\}|^2 = \frac{\widehat{F}_m^2}{\widehat{k}_x}, \quad (\text{B.6})$$

where  $\bar{f}$  is the mean value of  $f$ . The 2D spectrum of a 2D signal  $f$  is defined accordingly:

$$E = \mathcal{E}_2\{f\} : E_{m,n} = \frac{1}{\widehat{k}_x \widehat{k}_y} |\mathcal{F}_2\{f - \bar{f}\}|^2 = \frac{\widehat{F}_{m,n}^2}{\widehat{k}_x \widehat{k}_y} \quad (\text{B.7})$$

In both cases, the squared amplitude (absolute value) of the FFT is normalized by the maximum wave numbers. (In the present formulations, in order not to lose information about wave directions, all supra-Nyquist wave numbers are included in  $E$  and no summation takes place over complex conjugate contributions, as is often done in temporal spectra.)

The total energy (or variance)  $E_{tot}$  contained by a 1D or 2D spectrum is found by integrating  $E$  over the entire wave number space in a discrete way:

$$\text{1D: } E_{tot} = \Delta k_x \sum_{m=0}^{M-1} E_m = \frac{1}{M} \sum_{m=0}^{M-1} \widehat{F}_m^2 = \text{var}(f) \quad (\text{B.8})$$

$$\text{2D: } E_{tot} = \Delta k_x \Delta k_y \sum_{m=0}^{M-1} \sum_{n=0}^{N-1} E_{m,n} = \frac{1}{MN} \sum_{m=0}^{M-1} \sum_{n=0}^{N-1} \widehat{F}_{m,n}^2 = \text{var}(f) \quad (\text{B.9})$$

Hence we can state that the energy of  $f$  is equal to the mean square of  $\widehat{F}$  (the usual factor  $\frac{1}{2}$  for kinetic energy is omitted everywhere in this appendix).

The above relations are useful when we want to construct a function  $f$  while only the spectrum  $E$  is known. This happens for instance when 2D kinematic velocity fields (artificial turbulence) have to be built which must satisfy a given energy density spectrum. Only the phase information is lacking. For turbulent flows, however, it is sufficient to generate random phases  $\phi_{m,n}$  for all  $m$  and  $n$ , with random  $\phi$  uniformly distributed on the interval  $[0, 2\pi]$ . Obviously, corresponding sub- and supra-Nyquist wave numbers should have equal values of  $\widehat{F}$  and opposite values of  $\phi$  as argued before.

From Equation (B.7), we find the following expression for  $\widehat{F}$ :

$$\widehat{F}_{m,n} = \sqrt{\widehat{k}_x \widehat{k}_y} \sqrt{E_{m,n}} \quad (\text{B.10})$$

Now we have sufficient information to construct a field  $f$ , using the 2D IFFT formulation given in Equation (B.5). It is noteworthy that in (B.5) each value of  $\widehat{F}$  is scaled by a factor  $1/\sqrt{MN}$ , so that the effective amplitude  $\hat{f}$  of each harmonic component is finally given by:

$$\hat{f}_{m,n} = \widehat{F}_{m,n} / \sqrt{MN} = \sqrt{\Delta k_x \Delta k_y} \sqrt{E_{m,n}} \quad (\text{B.11})$$

From (B.10) we see that  $\widehat{F}$  depends on the resolution-dependent quantity  $\sqrt{\widehat{k}_x \widehat{k}_y}$ . The energy of the resulting field  $f$  is however invariant with respect to resolution-dependent quantities (in the continuous limit  $\widehat{k}_x \rightarrow \infty$  and  $\widehat{k}_y \rightarrow \infty$ ), provided that the applied discrete resolution is sufficient. The same is true for the prescribed energy density spectrum  $E$ : this must not be a function of discrete resolution. Otherwise, the resulting field  $f$  and its variance or energy would become proportional to the resolution, which cannot be correct. Therefore, the expression for the prescribed energy density spectrum  $E$  should not contain any quantity associated with discretization; it may contain e.g. wave numbers, external

length and velocity scales (like the water depth or friction velocity) and all kinds of dimensionless calibration constants, but it may not refer to  $M$ ,  $N$ ,  $L_x$ ,  $L_y$ ,  $\Delta x$  or  $\Delta y$ , etc. The expression for  $\hat{F}$ , on the other hand, will automatically contain the resolution-dependent factor  $\sqrt{\hat{k}_x \hat{k}_y} = \sqrt{MN \Delta k_x \Delta k_y}$ . These requirements are vital for a correct calibration of the backscatter models 2D-TRANS+KS and DANSLES (see Section 6.4.2 and 6.4.3).

# Appendix C

## Integration of backscatter spectra

The backscatter models 2D-TRANS+KS and DANSLES (presented in Section 6.4.2 and 6.4.3) make use of a 2D kinematic simulation, which contains harmonic components that satisfy prescribed energy density spectra for the kinematic velocity field  $\mathbf{u}_{ks} = (u_{ks}, v_{ks})$ . The energy content of  $\mathbf{u}_{ks}$  has been determined by calibration of the spectra, see Van Prooijen and Uijttewaai [99, 102] and Van Balen [96]. In this appendix these spectra are integrated analytically, which simplifies the analysis of the resulting backscatter models.

The prescribed spectra are mimicking 2D energy density spectra which are obtained by means of a 3D LES computation of a shallow uniform channel flow, see Van Prooijen and Uijttewaai [99, 102]. Following their description, the spectra  $E_{uu}$  and  $E_{vv}$  (of  $u_{ks}$  and  $v_{ks}$  respectively) as a function of dimensionless wave numbers  $k_x H$  and  $k_y H$  are given by:

$$E_{uu}(k_x H, k_y H) = \frac{1}{2} \left\{ \alpha u_* (\lambda k H) \exp(-\lambda k H) (k_y/k)^\beta (k_y/k) \right\}^2 \quad (\text{C.1})$$

$$E_{vv}(k_x H, k_y H) = \frac{1}{2} \left\{ \alpha u_* (\lambda k H) \exp(-\lambda k H) (k_y/k)^\beta (-k_x/k) \right\}^2 \quad (\text{C.2})$$

See Section 6.4.2 for a description of each quantity in these expressions. The absolute wave number is given by  $k = \sqrt{k_x^2 + k_y^2}$ . Three calibration constants are present:  $\alpha = 1.0$ ,  $\beta = 3$  and  $\lambda = 0.4$  (adopting the values found by [96]). It is argued in Section 6.4.2 that taking  $\beta = 0$  is a relevant alternative calibration, in order to have an isotropic backscatter model. Therefore, the analytical integration is elaborated here for both  $\beta = 3$  and  $\beta = 0$ .

If we define the wave direction angle  $\psi = \arctan(k_y/k_x)$  within the range  $[0, 2\pi]$ , we can express (C.1) and (C.2) in terms of polar coordinates:

$$E_{uu}(kH, \psi) = \frac{1}{2} \alpha^2 u_*^2 (\lambda k H)^2 \exp(-2\lambda k H) \sin^{2\beta} \psi \sin^2 \psi \quad (\text{C.3})$$

$$E_{vv}(kH, \psi) = \frac{1}{2} \alpha^2 u_*^2 (\lambda k H)^2 \exp(-2\lambda k H) \sin^{2\beta} \psi \cos^2 \psi \quad (\text{C.4})$$

It should be noted that, in these expressions,  $E_{uu}$  and  $E_{vv}$  have dimension  $\text{m}^2/\text{s}^2$  as they are functions of the dimensionless parameter  $kH$ . In order to make them a function of the wave number  $k$ ,  $E_{uu}$  and  $E_{vv}$  should be multiplied by the Jacobian  $H^2$ , which leads to a dimension  $\text{m}^4/\text{s}^2$ . However, regardless which form we prefer to use, the integrals of the spectra over the wave number domain are invariant with respect to this transformation and lead to invariant turbulent kinetic energy content for  $u_{ks}$  and  $v_{ks}$ :  $\frac{1}{2} u_{ks}'^2$  and  $\frac{1}{2} v_{ks}'^2$  respectively. Integration of (C.3) and (C.4) over the wave number domain (in polar coordinates) yields, after separating variables:

$$\overline{\frac{1}{2}u'_{ks}} = \frac{1}{2}\alpha^2 u_*^2 \lambda^2 \underbrace{\int_0^{kH} (kH)^2 \exp(-2\lambda kH) kH dkH}_{(A)} \cdot \underbrace{\int_0^{2\pi} \sin^{2\beta} \psi \sin^2 \psi d\psi}_{(B)} \quad (C.5)$$

$$\overline{\frac{1}{2}v'_{ks}} = \frac{1}{2}\alpha^2 u_*^2 \lambda^2 \underbrace{\int_0^{kH} (kH)^2 \exp(-2\lambda kH) kH dkH}_{(A)} \cdot \underbrace{\int_0^{2\pi} \sin^{2\beta} \psi \cos^2 \psi d\psi}_{(C)} \quad (C.6)$$

The integrals (A), (B) and (C) can be solved analytically, provided that  $\beta$  is positive integer or zero. Setting  $\lambda = 0.4$  (see [96]) and taking the limit for  $kH \rightarrow \infty$  yields the results:

$$(A): \int_0^\infty kH^3 e^{(-2\lambda kH)} dkH = \left[ \frac{-3!}{(2\lambda)^4} \left\{ \sum_{n=0}^3 \frac{(\lambda kH)^n}{n!} \right\} e^{(-2\lambda kH)} \right]_0^\infty = \frac{6}{(2\lambda)^4} \quad (C.7)$$

$$(B): \int_0^{2\pi} \sin^6 \psi \sin^2 \psi d\psi = \frac{35}{64}\pi \quad \text{if } \beta = 3, \text{ or } \int_0^{2\pi} \sin^2 \psi d\psi = \pi \quad \text{if } \beta = 0 \quad (C.8)$$

$$(C): \int_0^{2\pi} \sin^6 \psi \cos^2 \psi d\psi = \frac{5}{64}\pi \quad \text{if } \beta = 3, \text{ or } \int_0^{2\pi} \cos^2 \psi d\psi = \pi \quad \text{if } \beta = 0 \quad (C.9)$$

Hence for the total streamwise and transverse energy content of  $\mathbf{u}_{ks}$  we find:

$$\overline{\frac{1}{2}u'_{ks}} \approx 4.027 \cdot \frac{1}{2}\alpha^2 u_*^2 \quad \text{if } \beta = 3, \text{ or } \overline{\frac{1}{2}u'_{ks}} \approx 7.363 \cdot \frac{1}{2}\alpha^2 u_*^2 \quad \text{if } \beta = 0 \quad (C.10)$$

$$\overline{\frac{1}{2}v'_{ks}} \approx 0.575 \cdot \frac{1}{2}\alpha^2 u_*^2 \quad \text{if } \beta = 3, \text{ or } \overline{\frac{1}{2}v'_{ks}} \approx 7.363 \cdot \frac{1}{2}\alpha^2 u_*^2 \quad \text{if } \beta = 0 \quad (C.11)$$

The ratio  $\overline{u'_{ks}}/\overline{v'_{ks}}$  is exactly 7 for  $\beta = 3$ , which is a measure for the amount of anisotropy. This ratio is obviously 1 for the isotropic case  $\beta = 0$ .

Within DANSLES not only  $\mathbf{u}_{ks}$  itself is used but also its second order derivative  $H^2 \nabla^2 \mathbf{u}_{ks}$  (Laplacian operator normalized by the water depth). In Fourier space, this implies a multiplication of the spectra by a dimensionless factor  $(kH)^4$ . This leads to a modification of the integral (A), which becomes:

$$(A): \int_0^\infty kH^7 e^{(-2\lambda kH)} dkH = \left[ \frac{-7!}{(2\lambda)^8} \left\{ \sum_{n=0}^7 \frac{(\lambda kH)^n}{n!} \right\} e^{(-2\lambda kH)} \right]_0^\infty = \frac{5040}{(2\lambda)^8} \quad (C.12)$$

Hence for the total streamwise and transverse variance of  $H^2 \nabla^2 \mathbf{u}_{ks}$  we find:

$$\overline{\frac{1}{2}(H^2 \nabla^2 u_{ks})'^2} \approx 8257.88 \cdot \frac{1}{2}\alpha^2 u_*^2 \quad \text{if } \beta = 3, \text{ or } \approx 15100.12 \cdot \frac{1}{2}\alpha^2 u_*^2 \quad \text{if } \beta = 0 \quad (C.13)$$

$$\overline{\frac{1}{2}(H^2 \nabla^2 v_{ks})'^2} \approx 1179.70 \cdot \frac{1}{2}\alpha^2 u_*^2 \quad \text{if } \beta = 3, \text{ or } \approx 15100.12 \cdot \frac{1}{2}\alpha^2 u_*^2 \quad \text{if } \beta = 0 \quad (C.14)$$

Again, the ratio  $\overline{(H^2 \nabla^2 u_{ks})'^2}/\overline{(H^2 \nabla^2 v_{ks})'^2}$  is exactly 7 for  $\beta = 3$  and exactly 1 for  $\beta = 0$ . The ratios  $\overline{(H^2 \nabla^2 u_{ks})'^2}/\overline{u'_{ks}}$  and  $\overline{(H^2 \nabla^2 v_{ks})'^2}/\overline{v'_{ks}}$  are both equal to  $840/(2\lambda)^4 \approx 2050.8$ , irrespective of  $\beta$ . Furthermore, it can be seen that  $\alpha$  should have a slightly smaller value for the isotropic case  $\beta = 0$  than for the anisotropic case  $\beta = 3$ :  $\alpha$  should be reduced by a factor  $\sqrt{(4.027 + 0.575)/(2 \cdot 7.363)} = \sqrt{(8257.88 + 1179.70)/(2 \cdot 15100.12)} = \sqrt{5/16} \approx 0.56$ , in order to have the same total energy content in both cases.



# Bibliography

- [1] R.J. Adrian, K.T. Christensen, and Z.-C. Liu. Analysis and interpretation of instantaneous turbulent velocity fields. *Experiments in Fluids*, 29:275–290, 2000.
- [2] V. Altai and V.H. Chu. Turbulence exchange flow in shallow compound channel. *Proceedings of the 21th Congress of IAHR*, pages 446–451, Melbourne, Australia, 1985.
- [3] W. Altai and V.H. Chu. Retention time in a recirculating flow. *Proceedings of the 27th Congress of IAHR*, pages 9–14, San Francisco, USA, 1997.
- [4] R. Avancha and R.H. Pletcher. Large eddy simulation of the turbulent flow past a backward facing step. *Proceedings of the 38th AIAA Aerospace Sciences Meeting and Exhibit*, 0542:1–7, Reno, Nevada, USA, 2000.
- [5] S. Babarutsi and V.H. Chu. Two-dimensional large eddy simulation for shallow recirculating flow. *Proceedings of the 27th Congress of IAHR*, pages 817–822, San Francisco, USA, 1997.
- [6] S. Babarutsi and V.H. Chu. Modeling transverse mixing layer in shallow open-channel flows. *Journal of Hydraulic Engineering*, 124(7):718–727, 1998.
- [7] S. Babarutsi, J. Ganoulis, and V.H. Chu. Experimental investigation of shallow recirculation flows. *Journal of Hydraulic Engineering*, 115(7):906–924, 1989.
- [8] S. Babarutsi, M. Nassiri, and V.H. Chu. Computation of shallow recirculating flow dominated by friction. *Journal of Hydraulic Engineering*, 122(7):367–372, 1996.
- [9] G.K. Batchelor. *An Introduction to Fluid Dynamics*. Cambridge University Press, 1967.
- [10] G.K. Batchelor. Computation of the energy spectrum in homogeneous two-dimensional turbulence. *Physics of Fluids Supplement II*, pages 233–239, 1969.
- [11] A.C. Bijlsma, R.E. Uittenbogaard, and T. Blokland. Horizontal large eddy simulation applied to stratified tidal flows. *Proceedings of the International Symposium on Shallow Flows*, pages 559–566, Delft, Netherlands, 2003.
- [12] M.D.J.P. Bijvelds. *Numerical modelling of estuarine flow over steep topography*. PhD thesis, Delft University of Technology, 2001.
- [13] M.D.J.P. Bijvelds, C. Kranenburg, and G.S. Stelling. 3D numerical simulation of turbulent shallow-water flow in square harbor. *Journal of Hydraulic Engineering*, 125(1):26–31, 1999.

- [14] B.J. Boersma. An Introduction to LES/DNS simulation. *Website of the Laboratory for Aero and Hydrodynamics (AHD), Delft University of Technology*, page <http://www.ahd.tudelft.nl/~bendiks/demo/intro.html>, 2000?
- [15] J.P. Bonnet, J. Delville, M.N. Glauser, R.A. Antonia, D.K. Bisset, D.R. Cole, H.E. Fiedler, J.H. Garem, D. Hilberg, J. Jeong, N.K.R. Kevlahan, L.S. Ukeiley, and E. Vincendeau. Collaborative testing of eddy structure identification methods in free turbulent shear flows. *Experiments in Fluids*, 25:197–225, 1998.
- [16] R. Booij and J. Tukker. Integral model of shallow mixing layers. *Journal of Hydraulic Research*, 39(2):169–179, 2001.
- [17] V. Borue. Inverse energy cascade in stationary two-dimensional homogeneous turbulence. *Physical Review Letters*, 72(10):2984–2991, 1994.
- [18] W.P. Breugem. *The influence of wall permeability on laminar and turbulent flows*. PhD thesis, Delft University of Technology, 2004.
- [19] M.O. Bristeau, R. Glowinsky, and J. Periaux. Numerical method for the Navier-Stokes equations. Applications to the simulation of compressible and incompressible viscous flows. *Computer Physics Reports*, 6:73–187, 1987.
- [20] W. Cabot. Near-wall models in large eddy simulations of flow behind a backward-facing step. *Center for Turbulence Research Annual Research Briefs 1996*, pages 199–210, 1996.
- [21] I.P. Castro and E. Epik. Boundary-layer relaxation after a separated region. *Experimental Thermal and Fluid Science*, 13:338–348, 1996.
- [22] D. Chen and G.H. Jirka. Experimental study of plane turbulent wakes in a shallow water layer. *Fluid Dynamics Research*, 16:11–41, 1995.
- [23] D. Chen and G.H. Jirka. Absolute and convective instabilities of plane turbulent wakes in a shallow water layer. *Journal of Fluid Mechanics*, 338:157–172, 1997.
- [24] D. Chen and G.H. Jirka. LIF study of plane jet bounded in shallow water layer. *Journal of Hydraulic Engineering*, 125(8):817–826, 1999.
- [25] F.Y. Chen and S. Ikeda. Horizontal separation flows in shallow open channels with spur dikes. *Journal of Hydroscience and Hydraulic Engineering*, 15(2):15–30, 1997.
- [26] V.H. Chu and S. Babarutsi. Confinement and bed-friction effects in shallow turbulent mixing layers. *Journal of Hydraulic Engineering*, 114(10):1257–1274, 1988.
- [27] K.B. Chun and H.J. Sung. Visualization of locally-forced separated flow over a backward-facing step. *Experiments in Fluids*, 25:133–142, 1998.
- [28] H.J.H. Clercx and G.J.F. van Heijst. Energy spectra for decaying 2D turbulence in a bounded domain. *Physical Review Letters*, 85(2):306–309, 2000.
- [29] H.J.H. Clercx, M.L. Zoetewij, and G.J.F. van Heijst. Quasi two-dimensional turbulence in shallow fluid layers: the role of bottom friction and fluid layer depth. *Proceedings of the International Symposium on Shallow Flows*, pages 87–94, Delft, Netherlands, 2003.

- [30] J.W. Cooley and J.W. Tukey. An algorithm for the machine calculation of complex fourier series. *Mathematics of Computation*, 16(90):297–301, 1965.
- [31] M.A.J. de Nijs. Sensitivity of shallow mixing layers to upstream turbulence; an experimental study. Master’s thesis, Delft University of Technology, 2003.
- [32] T. Dracos, M. Giger, and G.H. Jirka. Plane turbulent jets in a bounded fluid layer. *Journal of Fluid Mechanics*, 214:587–614, 1992.
- [33] J.W. Emery and R.E. Thomson. *Data analysis methods in physical oceanography*. Pergamon, 1997.
- [34] E.A. Fadlun, R. Verzicco, P. Orlandi, and J. Mohd-Yusof. Combined immersed-boundary finite-difference methods for three-dimensional complex flow simulations. *Journal of Computational Physics*, 161:35–60, 2000.
- [35] J. Fröhlich and W. Rodi. Introduction to Large Eddy Simulation of turbulent flows. *Closure Strategies for Turbulent and Transitional Flows (ed. B. E. Launder and N. D. Sandham)*, Chapter 8, pages 267–298, Cambridge University Press, 2000.
- [36] J.C.H. Fung, J.C.R. Hunt, N.A. Malik, and R.J. Perkins. Kinematic simulation of homogeneous turbulence by unsteady random fourier modes. *Journal of Fluid Mechanics*, 236:281–318, 1992.
- [37] M. Germano, U. Piomelli, P. Moin, and W.H. Cabot. A dynamic subgrid-scale eddy viscosity. *Physics of Fluids*, 3:1760–1765, 1991.
- [38] M.S. Ghidaoui and A.A. Kolyshkin. On coherent structures in shallow flows. *Proceedings of the International Symposium on Shallow Flows*, pages 39–46, Delft, Netherlands, 2003.
- [39] M. Giger, T. Dracos, and G.H. Jirka. Entrainment and mixing in plane turbulent jets in shallow water. *Journal of Hydraulic Research*, 29(5):615–641, 1991.
- [40] T. Gotoh. Energy spectrum in the inertial and dissipation ranges of two-dimensional steady turbulence. *Physical Review Letters*, 57(3):2984–2991, 1998.
- [41] D. Greenblatt and I.J. Wygnanski. The control of flow separation by periodic excitation. *Progress in Aerospace Sciences*, 36:487–545, 2000.
- [42] C. Hinterberger. *Dreidimensionale und tiefengemittelte Large-Eddy-Simulation von Flachwasserströmungen*. PhD thesis, Institut für Hydromechanik, University of Karlsruhe, 2004.
- [43] C. Hinterberger, J. Fröhlich, and W. Rodi. Three-dimensional and depth-averaged Large Eddy Simulation of shallow water flows. *Proceedings of the International Symposium on Shallow Flows*, pages 567–574, Delft, Netherlands, 2003.
- [44] C. Hinterberger, J. Fröhlich, and W. Rodi. Three-dimensional and depth-averaged Large Eddy Simulations of some shallow water flows. *Journal of Hydraulic Engineering*, 133(8):857–872, 2007.

- [45] C. Hinterberger, J. Fröhlich, and W. Rodi. 2D and 3D turbulent fluctuations in open channel flow with  $Re = 590$  studied by Large Eddy Simulation. *Flow Turbulence Combust*, 80:225–253, 2008.
- [46] WL-Delft Hydraulics. *Delft3D-Flow user manual*, Delft, 2003.
- [47] G.H. Jirka. Large scale flow structures and mixing processes in shallow flows. *Journal of Hydraulic Research*, 39(6):567–573, 2001.
- [48] A. Kadota, K. Suzuki, and W.S.J. Uijtewaal. The shallow flow around a single groyne under submerged and emerged conditions. *Proceedings of the International Conference in Fluvial Hydraulics (River Flow)*, pages 673–682, Lisboa, Portugal, 2006.
- [49] H.W.J. Kernkamp and R.E. Uittenbogaard. 2D-LES of a free-surface mixing layer. *Direct and Large-Eddy simulation workshop*, pages 409–418, 2001.
- [50] K.C. Kim and R.J. Adrian. Very large-scale motion in the outer layer. *Physics of Fluids*, 11(2):417–422, 1999.
- [51] R.H. Kraichnan. Inertial ranges in two-dimensional turbulence. *Physics of Fluids*, 10(7):1417–1423, 1967.
- [52] R.J. Labeur. *Finite element modelling of transport and non-hydrostatic flow in environmental fluid mechanics*. PhD thesis, Delft University of Technology, 2009.
- [53] E.J. Langendoen. *Flow patterns and transport of dissolved matter in tidal harbours*. PhD thesis, Delft University of Technology, 1992.
- [54] E.J. Langendoen, C. Kranenburg, and R. Booij. Flow patterns and exchange of matter in tidal basins. *Journal of Hydraulic Research*, 32(2):259–270, 1994.
- [55] H. Le, P. Moin, and J. kim. Direct numerical simulation of turbulent flow over a backward-facing step. *Journal of Fluid Mechanics*, 330:349–374, 1997.
- [56] M. Lesieur. *Turbulence in Fluids*. Kluwer Academic Publishers, 1997.
- [57] D.K. Lilly. Numerical simulation of two-dimensional turbulence. *Physics of Fluids*, 12(12):240–249, 1969.
- [58] P.M. Lloyd, P.K. Stansby, and D. Chen. Wake formation around islands in oscillatory laminar shallow-water flows. Part 1. Experimental investigation. *Journal of Fluid Mechanics*, 429:217–238, 2001.
- [59] G. Marsaglia and T.A. Bray. A convenient method for generating normal variables. *SIAM Review*, 6(3):260–264, 1964.
- [60] R. Mittal and G. Iaccarino. Immersed Boundary Methods. *Annual Review of Fluid Mechanics*, 37:239–61, 2005.
- [61] R.D. Moser, J. Kim, and N.N. Mansour. Direct Numerical Simulation of turbulent channel flow up to  $Re = 590$ . *Physics of Fluids*, 11(4):943–945, 1999.
- [62] M. Nassiri and S. Babarutsi. Computation of dye concentration in shallow recirculating flow. *Journal of Hydraulic Engineering*, 123(9):793–805, 1997.

- [63] M. Nassiri, S. Babarutsi, and V.H. Chu. A two-length-scale model for quasi-two-dimensional turbulent shear flows. *Proceedings of the 24th Congress of IAHR, volume C*, pages 53–60, Madrid, Spain, 1991.
- [64] M. Nassiri, S. Babarutsi, and V.H. Chu. Wall boundary conditions on recirculating flows dominated by bottom friction. *Proceedings of the 28th Congress of IAHR*, Graz, Austria, 1999.
- [65] A.S. Neto, D. Grand, O. Métais, and M. Lesieur. A numerical investigation of the coherent vortices in turbulence behind a backward-facing step. *Journal of Fluid Mechanics*, 256:1–25, 1993.
- [66] I. Nezu and H. Nakagawa. *Turbulence in open-channel flows*. IAHR monographs series, Balkema, Rotterdam, 1993.
- [67] F.T.M. Nieuwstadt. *Turbulentie; een inleiding in de theorie en toepassingen van turbulente stromingen*. Epsilon Uitgaven, Utrecht, 1998.
- [68] V. Nikora. Origin of the  $-1$  spectral law in wall-bounded turbulence. *Physical Review Letters*, 83:734–736, 1999.
- [69] C.S. Peskin. Flow patterns around heart valves: A numerical method. *Journal of Computational Physics*, 10(2):252–271, 1972.
- [70] U. Piomelli and E. Balaras. Wall-layer models for Large Eddy Simulations. *Annual Review of Fluid Mechanics*, 43:349–374, 2002.
- [71] S.B. Pope. *Turbulent Flows*. Cambridge University Press, 2000.
- [72] P. Sagaut. *Large Eddy Simulation for incompressible flows; an introduction*. Scientific Computation, Springer, 1998.
- [73] F. Scarano, C. Benocci, and M.L. Riethmuller. Pattern recognition analysis of the turbulent flow past a backward facing step. *Physics of Fluids*, 11(12):3808–3818, 1999.
- [74] I. Schnauder, A. Sukhodolov, W.S.J. Uijttewaal, and R.J. Labeur. Field experiments and numerical modelling on shallow mixing layers at a confluence of two parallel streams. *Proceedings of the International Conference in Fluvial Hydraulics (River Flow)*, pages 883–892, Izmir, Turkey, 2008.
- [75] U. Schumann. Stochastic backscatter of turbulence energy and scalar variance by random subgrid-scale fluxes. *Proc. R. Soc. Lond. A (451)*, pages 293–318, 1995.
- [76] J. Sieben. Hydraulische verkenning “Bord voor de Kop”. *Memorandum Rijkswaterstaat 2005-016*, 2005.
- [77] J. Sieben. Wanden in de Waal; onderzoek naar de invloed van kribkoppen op de lokale bodemligging. *Memorandum Rijkswaterstaat*, 2009.
- [78] R.L. Simpson. Turbulent boundary-layer separation. *Annual Review of Fluid Mechanics*, 21:205–234, 1989.

- [79] J.S. Smagorinsky. General circulation experiments with the primitive equations. *Monthly Weather Review*, 91:99–164, 1963.
- [80] P.R. Spalart. Strategies for turbulence modelling and simulations. *International Journal of Heat and Fluid Flow*, 21:252–263, 2000.
- [81] P.G. Spazzini, G. Iuso, M. Onorato, M. Zurlo, and G.M. Di Cicca. Unsteady behavior of back-facing step flow. *Experiments in Fluids*, 30:551–561, 2001.
- [82] G.S. Stelling. *On the construction of computational methods for shallow water flow problems*. PhD thesis, Delft University of Technology, 1984.
- [83] H. Talstra, W.S.J. Uijttewaal, and G.S. Stelling. Emergence of large-scale coherent structures in a shallow separating flow. *Proceedings of the International Conference in Fluvial Hydraulics (River Flow)*, pages 261–269, Lisboa, Portugal, 2006.
- [84] H. Talstra, W.S.J. Uijttewaal, and G.S. Stelling. 3D LES computations of a shallow lateral expansion using an immersed boundary method. *Proceedings of the International Conference on Hydroscience and Engineering (ICHE)*, Philadelphia, USA, 2006.
- [85] P. Termes. Reductie Sedimentatie in Havens – Dimensionering Maatregelen. *Technical report by HKV/Deltares/Svašek Hydraulics*, 2008.
- [86] F. Tessicini, G. Iaccarino, M. Fatica, M. Wang, and R. Verzicco. Wall modeling for large-eddy simulation using an immersed boundary method. *Center for Turbulence Research Annual Research Briefs 2002*, pages 181–187, 2002.
- [87] S. Thangam and C.G. Speziale. Turbulent separated flow past a backward-facing step: a critical evaluation of two-equation turbulence models. *AIAA Journal*, 30(5):1314–1320, 1992.
- [88] Y.H. Tseng and J.H. Ferziger. A ghost-cell immersed boundary method for flow in complex geometry. *Journal of Computational Physics*, 192:593–623, 2003.
- [89] J. Tukker. *Turbulence structures in shallow free-surface mixing layers*. PhD thesis, Delft University of Technology, 1997.
- [90] W.S.J. Uijttewaal, M.H. Berg, and M. van der Wal. Experiments on physical scale models for submerged and non-submerged groynes of various types. *Proceedings of the International Conference on Fluvial Hydraulics (River Flow)*, pages 377–383, Louvain-la-Neuve, Belgium, 2002.
- [91] W.S.J. Uijttewaal and R. Booij. Effects of shallowness on the development of free-surface mixing layers. *Physics of Fluids*, 12(2):392–402, 2000.
- [92] W.S.J. Uijttewaal and G.H. Jirka. Grid turbulence in shallow flows. *Journal of Fluid Mechanics*, 489:325–344, 2003.
- [93] W.S.J. Uijttewaal, D. Lehmann, and A. van Mazijk. Exchange processes between a river and its groyne fields; model experiments. *Journal of Hydraulic Engineering*, 127(11):928–936, 2001.

- [94] W.S.J. Uijtewaal and J. Tukker. Development of quasi two-dimensional structures in a shallow free-surface mixing layer. *Experiments in Fluids*, 24:192–200, 1998.
- [95] R.E. Uittenbogaard and B. van Vossen. Subgrid-scale model for quasi-2d turbulence in shallow water. *Proceedings of the International Symposium on Shallow Flows*, pages 575–582, Delft, Netherlands, 2003.
- [96] W. van Balen. Large-scale coherent structures in turbulent shallow flows. Master’s thesis, Delft University of Technology, 2005.
- [97] W. van Balen. *Curved open-channel flows – A numerical study*. PhD thesis, Delft University of Technology, 2010.
- [98] G.J.F. van Heijst. Zelf-organisatie van twee-dimensionale stromingen. *Nederlands Tijdschrift voor Natuurkunde*, 59:321–325, 1993.
- [99] B.C. van Prooijen. *Shallow Mixing Layers*. PhD thesis, Delft University of Technology, 2004.
- [100] B.C. van Prooijen, M. de Nijs, and W.S.J. Uijtewaal. The effects of bottom turbulence on the genesis of large coherent structures in shallow shear flows. *Proceedings of the International Symposium on Shallow Flows*, pages 95–102, Delft, Netherlands, 2003.
- [101] B.C. van Prooijen and W.S.J. Uijtewaal. A linear approach for the evolution of coherent structures in shallow mixing layers. *Physics of Fluids*, 14(12):4105–4114, 2002.
- [102] B.C. van Prooijen and W.S.J. Uijtewaal. The relevance of a back-scatter model for depth-averaged flow simulation. *Flow Turbulence Combust*, 82:73–91, 2009.
- [103] S.A.H. van Schijndel and H.R.A. Jagers. Complex flow around groynes, computations with DELFT3D in combination with HLES. *Proceedings of the International Symposium on Shallow Flows*, pages 645–650, Delft, Netherlands, 2003.
- [104] Ministerie van Verkeer en Waterstaat. *Kribben van de Toekomst*. *Uitgave Rijkswaterstaat Oost-Nederland*, 2006.
- [105] B. van Vossen. Horizontal Large Eddy simulations: Evaluation of flow computations with Delft3D-Flow. Master’s thesis, Delft University of Technology, 2000.
- [106] D.A. Vermaas, W.S.J. Uijtewaal, and A.J.F. Hoitink. Effect of heterogeneous bed roughness on the momentum exchange in floodplains. *Proceedings of the International Conference in Fluvial Hydraulics (River Flow)*, pages Cesme, Turkey, 2008.
- [107] C.F. von Carmer, A.C. Rummel, and G.H. Jirka. Influence of secondary motion in large-scale coherent vortical structures on the mass transport in a shallow turbulent wake flow. *Proceedings of the International Symposium on Shallow Flows*, pages 103–110, Delft, Netherlands, 2003.
- [108] C.B. Vreugdenhil. *Numerical methods for shallow-water flow*. Kluwer Academic Publishers, Dordrecht, 1994.

- [109] L.X. Wang. Measurements of turbulent flow in a suddenly expanding flume with a rough bottom. Technical report, Laboratory of Environmental Fluid Mechanics, Delft University of Technology, 1983.
- [110] B. Wasistho and K.D. Squires. Prediction of turbulent separation over a backward-facing smooth ramp. *Journal of Turbulence*, 6(1):1–26, 2005.
- [111] B. Wasistho and K.D. Squires. Numerical investigation of the separated flow over a smoothly contoured ramp. *Proceedings of 2nd International Symposium on Turbulence and Shear Flow Phenomena*, Stockholm, Sweden, 2001.
- [112] V. Weitbrecht, G. Kühn, and G.H. Jirka. Large scale PIV-measurements at the surface of shallow water flows. *Flow Measurement and Instrumentation*, 13:15–30, 2002.
- [113] M.G. Wells and G.J.F. van Heijst. Dipole formation by tidal flow in a channel. *Proceedings of the International Symposium on Shallow Flows*, pages 63–70, Delft, Netherlands, 2003.
- [114] P. Wesseling. *Principles of Computational Fluid Dynamics*. Springer, 2001.
- [115] J.C. Winterwerp. Reducing harbor siltation. I: Methodology. *Journal of Waterway, Port, Coastal and Ocean Engineering*, 131(6):258–266, 2005.
- [116] T. Ye, R. Mittal, H.S. Udaykumar, and W. Shyy. An accurate Cartesian grid method for viscous incompressible flows with complex immersed boundaries. *Journal of Computational Physics*, 156:209–240, 1999.
- [117] S. Yoshioka, S. Obi, and S. Masuda. Organized vortex motion in periodically perturbed turbulent separated flow over a backward-facing step. *International Journal of Heat and Fluid Flow*, 22:301–307, 2001.
- [118] S. Yoshioka, S. Obi, and S. Masuda. Turbulence statistics of periodically perturbed separated flow over backward-facing step. *International Journal of Heat and Fluid Flow*, 22:393–401, 2001.
- [119] M.F.M. Yossef. *Morphodynamics of rivers with groynes*. PhD thesis, Delft University of Technology, 2004.



# Notation

## Abbreviations

Abbreviation	Description
1D, 2D, 3D	One-, Two-, Three-Dimensional
2DH	Two-Dimensional and depth-averaged
2DCS	Two-Dimensional Coherent Structures
2D-TRANS+KS	Two-Dimensional Transient RANS with Kinematic Simulation
BFS	Backward Facing Step
BICGSTAB	Bi-Conjugate Gradient STABILized (iterative matrix solver)
BSM	Backscatter Model
CFL	Courant-Friedrichs-Léwy (number)
CG/DG	Continuous/Discontinuous Galerkin (method)
DA-LES	Depth-Averaged Large Eddy Simulation
DANSLES	Depth-Averaged Navier-Stokes with Large Eddy Stimulation
DNS	Direct Numerical Simulation
DFT/IDFT	(Inverse) Discrete Fourier Transform
FFT/IFFT	(Inverse) Fast Fourier Transform
GIS	Galerkin Interface Stabilization (method)
HLES	Horizontal Large Eddy Simulation
IBM	Immersed Boundary Method
KS	Kinematic Simulation
LDA	Laser-Doppler Anemometry
LES	Large Eddy Simulation
LSPIV	Large-scale Surface Particle Image Velocimetry
NAP	Dutch reference level (Normaal Amsterdams Peil)
PIV	Particle Image Velocimetry
PTV	Particle Tracking Velocimetry
RANS	Reynolds-Averaged Navier-Stokes (equations)
RMS	Root-Mean-Square (value)
RWS	Dutch Ministry of Public Works (Rijkswaterstaat)
SCF	Straight Channel Flow
SGS	Sub-grid scale (model)
SLE	Shallow Lateral Expansion
SML	Shallow Mixing Layer
SWE	Shallow-Water Equations
TKE	Turbulent Kinetic Energy
TRANS/URANS	Transient (or Unsteady) Reynolds-Averaged Navier-Stokes

**Greek symbols**

Symbol	Description	Unit
$\alpha$	Entrainment coefficient	
$\alpha$	Calibration parameter within DANSLES	
$\beta$	Calibration parameter within DANSLES	
$\beta_{eddy}$	Transverse 2DCS length scale	[m]
$\gamma$	Model parameter within HLES	
$\gamma$	Secondary flow scaling factor	
$\delta$	Mixing layer width	[m]
$\delta_0$	Initial (upstream) mixing layer width	[m]
$\Delta$	Increment or difference	
$\Delta$	Characteristic mesh size	[m]
$\Delta x, \Delta y, \Delta z$	Numerical mesh size	[m]
$\Delta t$	Numerical time step	[s]
$\Delta U$	Velocity difference over mixing layer	[m/s]
$\epsilon$	Energy dissipation rate per unit mass	[m <sup>2</sup> /s <sup>3</sup> ]
$\eta$	Enstrophy dissipation rate per unit mass	[1/s <sup>3</sup> ]
$\theta$	Random phase field within backscatter models	
$\kappa$	Von Kármán constant	
$\lambda$	Calibration parameter within DANSLES	
$\lambda_{max}$	Maximum large eddy length scale	[m]
$\lambda_{eddy}$	Streamwise 2DCS length scale	[m]
$\lambda_{int}$	Integral length scale	[m]
$\lambda_{filter}$	Low-pass filter width for PIV–LES analysis	[m]
$\nu$	Kinematic molecular viscosity	[m <sup>2</sup> /s]
$\nu^{SGS}$	3D eddy viscosity for LES SGS model	[m <sup>2</sup> /s]
$\nu_t$	2D eddy viscosity for Elder formulation	[m <sup>2</sup> /s]
$\nu_{2D}$	2D eddy viscosity for e.g. HLES	[m <sup>2</sup> /s]
$\rho$	Constant density (fresh water)	[kg/m <sup>3</sup> ]
$\tau$	Low-pass filtering time scale within HLES	[s]
$\tau_{bi}$	Bottom shear stress	[m <sup>2</sup> /s <sup>2</sup> ]
$\tau_{ij}$	Tangential wall shear stress	[m <sup>2</sup> /s <sup>2</sup> ]
$\tau_{ij}^{SGS}$	Subgrid-scale residual stress	[m <sup>2</sup> /s <sup>2</sup> ]
$\tau_{int}$	Integral time scale	[s]
$\phi$	Random phase field within backscatter models	
$\psi$	Wave direction angle within backscatter models	
$\psi$	Vector potential function or stream function	[m <sup>2</sup> /s]
$\omega$	Vorticity vector	[1/s]
$\Omega$	Enstrophy per unit mass	[1/s <sup>2</sup> ]

## Roman symbols

Symbol	Description	Unit
$A_+$	Van Driest damping parameter	
$\mathbf{A} = (A_x, A_y)$	Auxiliary function within DANSLES	
$b$	Bottom friction factor within HLES	[1/s]
$B_1$	Inflow flume width	[m]
$B_2$	Outflow flume width	[m]
$c_B$	Calibration parameter within DA-LES	
$c_f$	Bottom friction coefficient	
$c_h$	Elder coefficient	
$c_s$	Smagorinsky constant	
$D$	Expansion width or obstacle size	[m]
$E$	1D energy density spectrum	[m <sup>3</sup> /s <sup>2</sup> ]
$E$	2D energy density spectrum	[m <sup>4</sup> /s <sup>2</sup> ]
$E$	Temporal energy density spectrum	[m <sup>2</sup> /s]
$E_k$	Total kinetic energy per unit mass	[m <sup>2</sup> /s <sup>2</sup> ]
$f$	Frequency associated to eddy time scale	[1/s]
$f$	Vortex shedding frequency	[1/s]
$f_{lp}$	Calibration parameter within HLES	
$\mathbf{f}$	3D body force vector per unit mass	[m/s <sup>2</sup> ]
$\mathbf{F}$	2D backscatter forcing field	[m/s <sup>2</sup> ]
$F_{rms}, F_{rms,x}, F_{rms,y}$	Backscatter force scaling factors	[m/s <sup>2</sup> ]
$Fr$	Froude number	
$g$	Gravitational acceleration	[m/s <sup>2</sup> ]
$\hat{G}$	Transfer function for BSM-filter within DA-LES	
$h$	Piezometric level (water level)	[m]
$H$	Water depth	[m]
$i$	Imaginary unit	
$i, j$	Dimensional indices (Ricci notation)	
$j, k, m, n$	Numerical indices	
$k, k_x, k_y$	Wave number associated with eddy length scale	[1/m]
$\hat{k}$	Maximum wave number	[1/m]
$k^*$	Nyquist wave number (related to wave aliasing)	[1/m]
$\mathcal{L}$	Characteristic flow or eddy length scale	[m]
$L$	Computational domain length or flume length	[m]
$L_{in}$	Length of inflow section	[m]
$L_1$	Primary gyre length	[m]
$L_2$	Secondary gyre length	[m]
$L_m$	Prandtl mixing length	[m]
$m_0$	Spectral energy content	[m <sup>2</sup> /s <sup>2</sup> ]
$M, N$	Number of harmonic components	
$\mathbf{n}$	Outward normal vector to boundary	
$N_x, N_y, N_z, N_{tot}$	Number of grid cells	
$p$	Normalized hydrodynamic pressure	[m <sup>2</sup> /s <sup>2</sup> ]
$P$	Hydrodynamic pressure	[kg/ms <sup>2</sup> ]

**Roman symbols (continued)**

Symbol	Description	Unit
$P_{2D}$	Production rate of 2D turbulent kinetic energy	$[\text{m}^2/\text{s}^3]$
$P_{3D}$	Production rate of 3D turbulent kinetic energy	$[\text{m}^2/\text{s}^3]$
$Q, Q_0, Q_1, Q_2$	Bulk inflow discharge	$[\text{m}^3/\text{s}]$
$\mathbf{r}$	Random white noise vector field	
$Re$	Reynolds number	
$Re_*$	Reynolds number based on friction velocity	
$R_{ij}$	Residual closure term in 2D SWE	$[\text{m}^2/\text{s}^2]$
$s_{ij}$	Rate-of-strain tensor	$[\text{1}/\text{s}]$
$S$	Bed friction number (stability parameter)	
$St$	Strouhal number	
$t$	time level	$[\text{s}]$
$T$	Time interval	$[\text{s}]$
$T_{ij}, T_{adv}, T_{sec}, T_{Rey}$	Nonlinear momentum flux tensors	$[\text{m}^2/\text{s}^2]$
$\mathcal{T}$	Characteristic flow or eddy time scale	$[\text{s}]$
$\mathcal{U}$	Characteristic flow or eddy velocity scale	$[\text{m}/\text{s}]$
$u_*$	Friction velocity	$[\text{m}/\text{s}]$
$u_+$	Dimensionless near-wall velocity	
$ U $	Euclidean norm of flow velocity vector	$[\text{m}/\text{s}]$
$U_0, U_1, U_2, U_{in}$	Bulk inflow velocity	$[\text{m}/\text{s}]$
$U_c$	Velocity in mixing layer center	$[\text{m}/\text{s}]$
$U_{eddy}$	Streamwise 2DCS velocity scale	$[\text{m}/\text{s}]$
$V_{eddy}$	Transverse 2DCS velocity scale	$[\text{m}/\text{s}]$
$\mathbf{u}_{\mathbf{ks}} = (u_{ks}, v_{ks})$	Kinematic simulation velocity field	$[\text{m}/\text{s}]$
$\mathbf{u} = (u, v, w)$	Flow velocity components	$[\text{m}/\text{s}]$
$\mathbf{x} = (x, y, z)$	Cartesian coordinates	$[\text{m}]$
$x_{groynes}, x_{split}, x_c, R_c$	Geometrical parameters	$[\text{m}]$
$y_c$	Location of mixing layer center	$[\text{m}]$
$z_+$	Number of dimensionless wall units	
$z_b$	Bottom level	$[\text{m}]$
$\mathbf{Z}$	Filtered white noise field within DA-LES	

**Operators**

Operator	Description
$\overline{(\dots)}$	Reynolds-averaging or LES-filtering operator
$\widetilde{(\dots)'}^{\prime}$	Fluctuation stemming from Reynolds- or LES-decomposition
$\overline{(\dots)}$	Depth-averaging operator
$\overline{(\dots)}''$	Fluctuation stemming from depth-averaging (secondary flow)
$\overline{(\dots)}^*$	High-pass temporal filtering for HLES
$\overline{(\dots)}^{temp}$	Low-pass temporal filtering for HLES
$\widehat{(\dots)}$	Amplitude or numerical predictor quantity
$\widetilde{(\dots)}$	Quantity with complex amplitude and phase
$\mathcal{F}\{\dots\}, \mathcal{F}^{-1}\{\dots\}$	(Inverse) Fourier transform operator

# Nawoord

Na het afronden van mijn experimenten bezocht ik kort na elkaar drie kleinschalige conferenties, waar ik via een poster mijn onderzoek mocht presenteren aan de andere promovendi die daar rondliepen. Het was een leerzame ervaring. Bij de eerste conferentie eindigde mijn poster ergens onderaan de ranglijst, en het meest genoteerde commentaar luidde: “veel te theoretisch”. Een paar dagen later gooide mijn werk opnieuw geen hoge ogen, doch dit keer onder het motto “veel te praktisch”. Voor de derde conferentie was mijn poster echter blijkbaar precies goed, want daar werd hij beloond met de Best Poster Award, goed voor tweeduizend euro. Die avond belde ik het ouderlijk thuisfront om het goede nieuws te melden. De stem van mijn moeder, uitgeput en moedeloos na weer een zware dagbehandeling, klonk in één klap weer als vanouds. Zie je wel, jongen, je kunt het best. Gewoon je best doen, dan komt alles goed met jou. In normale tijden zou dergelijk commentaar me hebben geïrriteerd, maar nu was ik diep dankbaar. Goed zo, mama, dacht ik, zo mag ik het horen. Het was ons laatste telefoongesprek voor ze stierf.

Met het voltooien van dit proefschrift komt er een eind aan een lange queeste. Het heeft mij veel meer moeite gekost om in dit werk boven mezelf en de materie uit te groeien dan ik aanvankelijk dacht. Daardoor is dit promotietraject niet alleen een opwindend proces van leren, denken en ontdekken geworden, maar vooral ook een test in uithoudingsvermogen. Nu de klus geklaard is, voel ik niet alleen de vanzelfsprekende opluchting maar ook een grote tevredenheid over het resultaat. Geen enkel proefschrift is compleet of volmaakt, maar het goedgekeurde en drukklare boekje op mijn beeldscherm is precies zoals ik het graag hebben wilde, en ik weet dat het alle tijd en inspanning waard is geweest.

Mijn grote dank gaat uit naar iedereen die in de voorbije jaren heeft bijgedragen aan de totstandkoming van dit proefschrift. Die bijdragen waren van onschatbare waarde.

In de eerste plaats dank ik mijn promotor en dagelijks begeleider Wim Uijttewaal: een wetenschapper in hart en nieren, een man van de inhoud die altijd op de bal speelt, en bovendien iemand met veel compassie voor mensen dichtbij en ver weg. Wim, ik ben je zeer dankbaar voor je grote geduld en voor de vele boeiende gesprekken die we hebben gevoerd over turbulentie en de rest van het leven. Ik heb je geloof ik maar één keer quasi-boos gezien, nl. toen ik per abuis voorstelde om “de meetdata te verifiëren met behulp van de simulatieresultaten”. Dat moest natuurlijk andersom zijn – noem het een Freudiaanse verspreking van iemand die liever rekent dan meet. Maar je liet er geen misverstand over bestaan: in de wetenschap heeft de waarneming altijd het primaat boven de theorie. Die overtuiging is tekenend voor jou, als wetenschapper en als mens.

Guus Stelling, mijn tweede promotor, heeft op mij zijn liefde overgedragen voor de numerieke wiskunde: niet alleen een hobby die werk geworden is, maar ook werk dat een hobby is geworden. Guus, ik ben je dankbaar voor alle waardevolle interactie door de jaren heen, en voor het vertrouwen dat je mij al die tijd geschonken hebt!

Dank gaat ook uit naar Robert-Jan Labeur, die mij tijdens de afronding van mijn proefschrift voorzag van zeer uitgebreid en opbouwend commentaar op het manuscript. Het

eindresultaat is er stukken beter van geworden. Robert-Jan, ik wil je ook danken voor de mooie samenwerking bij het organiseren van het derdejaarsvak Stroming in Waterlopen, en voor onze huidige interactie rond de ontwikkeling van het eindige-elementenpakket FIN-LAB/FINEL. Ik heb ontzettend veel van je geleerd.

Graag dank ik alle leden van de Gebruikerscommissie van het STW, die door de jaren heen met mij hebben meegedacht. Ik dank Arjan Sieben en zijn collega's van Rijkswaterstaat voor de leuke samenwerking binnen het pilot-project "Bord voor de Kop". Rob Uittenbogaard en Bram van Prooijen dank ik voor hun grote inhoudelijke belangstelling en hun tijd, die zij royaal gaven om met mij te bomen over LES en 2D-turbulentiemodellen. Mijn speciale erkentelijkheid gaat uit naar Herman Kernkamp van Deltares, die speciaal voor mijn onderzoek een aantal aanpassingen in de software van DELFT3D-FLOW aanbracht. Het is bijzonder om ook buiten de eigen vakgroep zoveel enthousiasme tegen te komen voor zo'n specifiek promotieonderwerp.

Dit proefschrift had nooit geschreven kunnen worden zonder de bijdrage van het ondersteunend personeel van de Sectie Vloeistofmechanica, van timmerman tot computerbeheerder. Jaap, Hans, Arie, André, Otti, Sander en alle anderen: als ooit de topmanagers van onze universiteit in staking gaan, zal eigenlijk niemand dat merken, maar zonder jullie support staat heel het wetenschappelijk raderwerk stil. Ook alle andere bewoners van "Het Lab" – collega-promovendi, kamergenoten en docenten – wil ik dankzeggen voor de jaren van gezelligheid en wederzijdse belangstelling. De beste ideeën worden geboren (en afgeschoten) rondom het koffiezetapparaat. En ik vergeet niet gauw de verbijsterde blik van het barpersoneel in menig café, als het zoveelste bierviltje werd volgeklad met wiskundeformules.

Speciale erkentelijkheid gaat uit naar mijn werkgever Bram Bliet van Svašek Hydraulics, waar ik alweer een paar jaar met groot plezier werkzaam ben. Bram, dank je wel dat je mij de ruimte en de flexibiliteit hebt gegund om de afgelopen jaren in feite twee banen met elkaar te combineren. Daarmee is je bijdrage aan mijn proefschrift zeer groot geweest. Door de waardevolle combinatie van werken en promoveren – wat fysiek een zware klus was – heb ik ook ideeën uit de praktijk in mijn proefschrift kunnen gebruiken, en heb ik vakkennis uit mijn onderzoek nuttig kunnen maken binnen ons bedrijf. Dank je wel voor al je vertrouwen. Ook de andere collega's van Svašek wil ik danken voor de belangstelling, de collegialiteit en de vriendschap. Het is tof om met jullie te mogen samenwerken!

Het aantal mensen dat op afstand heeft meegeleefd met de vordering van het werk is bijna niet te tellen. Van gepromoveerde ooms die willen weten of het proefschrift nou al een beetje wil vloten, tot praatgrage buurvrouwen die altijd vragen hoe het met je "scriptie" gaat. "En wanneer ga je dan een baan zoeken?" "Turbulentie, dat is toch iets met vliegtuigen?" "Die tsunami, weet jij daar meer van?" De morele ondersteuning die mij ten deel viel van de zijde van familie, schoonfamilie, vrienden, kerkgenoten en oud-studiegenoten is niet uit te drukken in taart en flessen wijn, laat staan in goud, zilver of beton. Misschien in Beerenburg, maar zelfs dat staat nog te bezien. Over Beerenburg gesproken: mijn grote dank gaat uit naar alle leden, dekschrobbers en zehelden van Zeilvereniging Beaufort, onder wier vaandel ik jarenlang de turbulentie van water en lucht in de praktijk heb mogen beproeven, resulterend in nieuwe inzichten en vele uren gezamenlijk zeilgenot.

De meeste dank gaat tot slot uit naar de directe getrouwen in mijn bestaan. Mijn ouders Eep en Lies, die zoveel jaren zorg, liefde en wijsheid aan mij hebben gespendeerd, en mijn broer Arendjan, die verantwoordelijk is voor het kernachtige citaat aan het begin van dit boek. Mijn moeder Lies heeft het gereedkomen van mijn promotiewerk niet mogen meemaken. Maar als geen ander is ze in de beginfase van dit werk betrokken, vermanend en bemoedigend aanwezig geweest, vanuit haar motto: "Als je iets doet, doe het dan goed".

Het resultaat van haar vermaningen draag ik aan haar op. En ook aan Inge, mijn geliefde vrouw met wie ik ongelooflijk heb geboft. Dank je wel dat jij me gedurende dit traject op handen hebt gedragen, met af en toe een duwtje in de juiste richting. Je wordt er rijkelijk voor beloond, niet alleen met het vooruitzicht op een mooi feestje, maar vooral met een echtgenoot die weer tijd heeft en ruimte in zijn hoofd om de aandacht te richten op andere zaken dan wervels en wiskunde.

Bovenal dank ik God voor al Zijn zegen in de afgelopen jaren, zegen die vaak ook dwars door de moeite en het verlies heen gekomen is. Ik ben blij dat de Schepper van hemel en aarde (en de natuurwetten) zoveel mooie grote en kleine puzzels in de schepping heeft gelegd, waar wij onze tanden in mogen zetten. Met het inzicht groeit de verwondering, en in het ontdekken en uitpluizen van de werkelijkheid ligt vaak een grote vreugde. Ik hoop dat God glimlacht als Hij ons bezig ziet in onze laboratoria en achter onze computers, en ik hoop dat Hij het niet erg vindt dat we onze tijd niet aan iets urgenters besteden.

Harmen Talstra  
Delft, maart 2011





# Curriculum Vitae

1977, September 16th	Born in Amsterdam, The Netherlands
1989-1995	VWO, Sint-Ignatiusgymnasium (cum laude), Amsterdam
1995-2003	M.Sc. Civil Engineering (cum laude), Delft University of Technology, Delft. M.Sc. thesis on the numerical modeling of long-term estuarine morphology
2003-2007	Ph.D. Researcher, Section of Environmental Fluid Mechanics, Faculty of Civil Engineering and Geosciences, Delft University of Technology, Delft
2007-present	Project Engineer and numerical developer, Svašek Hydraulics B.V., Rotterdam

# ROEP OM MEER LES

Student en scholier willen van docent betere begeleiding

DEN HAAG — Scholieren en studenten zijn het zat. Zij willen meer les van hun docenten. Door veranderingen in het onderwijs worden leerlingen te veel aan hun lot overgelaten. Dat schrijven drie organisaties van scholieren en studenten aan staatssecretaris

Bruno Bruins van Onderwijs.

„Scholieren en studenten, of ze nou op de havo zitten, een opleiding tot automonteur volgen of de pabo doen, willen meer les”, aldus het Landelijk Actie Komitee Scholieren (LAKS), de Jongeren-Organisatie Beroepsonderwijs (JOB) en de Landelijke Studenten Vakbond (LSVb) gisteren.

De laatste jaren zijn klassikale lessen op scholen steeds meer vervangen door het zogeheten 'nieuwe leren'. Studenten moeten daar-

mee zelf kennis vergaren aan de hand van problemen of opdrachten.

Volgens de scholieren en studenten krijgen zij daarbij te weinig begeleiding van docenten.

Voor LAKS, JOB en LSVb is nu de grens bereikt. Zij willen meer klassikale lessen en meer kennisoverdracht door docenten. „Studenten zijn lang genoeg proefkonijn geweest. We willen beter onderwijs”.

Volgens hen zijn de gebrekkige

taal- en rekenvaardigheden onder pabo-studenten onder andere te wijten aan het nieuwe leren.

Een woordvoerder van staatssecretaris Bruins laat weten dat het ministerie de Inspectie vorig jaar opdracht heeft gegeven om het aantal lessen dat scholen in het voorgezet en beroepsonderwijs geven, te controleren. Begin februari wordt een tussenrapportage verwacht, eind van het schooljaar wordt de balans opgemaakt. (ANP)



*Numerieke vloeistofmechanica in de actualiteit*

# Poëtisch supplement

## CASCADE

Vrij naar Richardson (1922) en Doctorandus P.

*Wervels verworden tot  
kleinere wervels, wat  
weer tot weer kleinere  
werveltjes leidt;  
't Is een cascade, dat  
wervelvervalproces —  
enzovoort, tot op de  
viscositeit<sup>1</sup>*

*Zo sprak ooit Richardson  
Maar in 2D dan nu:  
daar worden wervels  
juist groter dan groot  
Weer een cascade, vol  
wervelversmeltingen —  
enzovoort, tot op de  
rand van de goot*

*Wondere werk'lijkheid!  
Wervels verwijden zich,  
plat, coherent en  
georganiseerd;  
schijnbaar in strijd met de  
chaosbeginselen —  
wat één dimensie al  
niet impliceert*

*Als peroratio  
nog een moraal tot slot  
(heerlijk, zo'n normen-  
en-waarden-cliché):  
Platheid leidt niet tot  
verval maar tot samenhang —  
Ach, was de wereld  
maar quasi-2D!*

<sup>1</sup>(Noot: ter verklaring wat standaard hydraulica: snelheidsadvectie is niet-lineair; via het handige vorticeitsbegrip blijken cascades dan elementair.)

**TO MY EXPERIMENTAL FLUME**

(Ad Liberum, after W. Shakespeare)

*Shall I compare Thee to a river's flow?  
 Thou art more straight and more dissipative;  
 Behold, Thy scales and Thy derivatives  
 Are smoother, gentler than real world might know*

*What other flume in earth's wide realm could boast  
 Of such bulk Reynolds number, such a width  
 and — so much better than a rigid-lid! —  
 a surface free, which mirrors heaven's host?*

*Turbulence is drama, all my flume's a stage,  
 And eddies merely players, I presume —  
 Or should I put it: All the world's a flume? —  
 From sunrise unto sunset, I Thee praise*

*Except for my worst nightmare, found in Thee:  
 Those bloody particles for P.I.V.*

**PROMOTIEBLUES**

(Sonnet)

*Het leven van een aio gaat niet over rozen  
 Een steile weg is het, met moeiten geplaveid  
 Het is een voorrecht waarvoor niemand je benijdt  
 Een crisis waar je zelf bewust voor hebt gekozen*

*Een worsteling met de fysieke werk'lijkheid:  
 IJdele hoop dat ik, met mijn beperkt geknutsel,  
 Misschien de schepping nog een nieuw geheim ontfutsel  
 En onverbiddelijk verglijdt de schaarse tijd*

*Geen sterveling die snapt wat je nu eig'lijk doet:  
 Een vraag, die jarenlang ook aan jezelf blijft knagen  
 Totdat, ineens, je boek goedkeuring weg kan dragen  
 Een last valt van je af, je weet: zo is het goed*

*Maar dan: het laatste woord, dat blijft toch een illusie  
 "Further research required", luidt immer de conclusie*

## DE BALLADE DER NERDS of ODE AAN FINLAB

- |      |   |      |   |
|------|---|------|---|
| I    | <i>'t Ligt vers in mijn geheugen<br/>van laatstejaars student<br/>dat ik gefascineerd werd door<br/>het Eindig Element</i>  | IX   | <i>En tot de tweede orde<br/>stabiel en convergent —<br/>Ai, ziet hoe goed hoe liefelijk,<br/>dat Eindig Element</i>        |
| II   | <i>Heden ben ik dan burger<br/>doch bij de consument<br/>daar blijkt zowaar behoefte aan<br/>het Eindig Element</i>         | X    | <i>En vinden wij sporadisch<br/>alsnog een mankement<br/>dan investeren wij veel zweet<br/>(en soms een vleug talent)</i>   |
| III  | <i>Dus zet ik als consultant<br/>met veel elan de trend:<br/>gelijk een nerd te klussen aan<br/>het Eindig Element</i>      | XI   | <i>En gaat de klant dan meten<br/>dan is men zeer content<br/>wanneer een fout gevonden wordt<br/>beneden tien procent</i>  |
| IV   | <i>Advectie en diffusie,<br/>een snelheidscomponent,<br/>dat alles is te vatten in<br/>het Eindig Element</i>               | XII  | <i>En voor de kleurenplaatjes<br/>geeft men ons compliment,<br/>en wij kunnen weer trots zijn op<br/>ons Eindig Element</i> |
| V    | <i>Een droogvalprocedure,<br/>du/dx-accent,<br/>dat is een ijskoud kunstje voor<br/>het Eindig Element</i>                  | XIII | <i>Een grote opdrachtgever<br/>is meestal niet zo'n krent<br/>Zo steken wij de ogen uit<br/>van menig concurrent</i>        |
| VI   | <i>Rotatie, divergentie<br/>en ook de gradiënt,<br/>wij persen heel Gods schepping in<br/>het Eindig Element</i>            | XIV  | <i>Zo runnen wij de toko,<br/>zo draaien wij de tent;<br/>wij zijn wereldberoemd dankzij<br/>het Eindig Element</i>         |
| VII  | <i>Al geef ik voor de match met<br/>de waarheid soms geen cent<br/>het staat zo machtig elegant,<br/>dat Eindig Element</i> | XV   | <i>Zo houden wij het land droog,<br/>het wordt alom erkend:<br/>wij hoeden B.V. Nederland<br/>voor haar faillissement</i>   |
| VIII | <i>De oplossingsmethode<br/>is zo intelligent<br/>dat 't béter dan de waarheid is,<br/>zo'n Eindig Element</i>              | XVI  | <i>En ben ik achtentachtig,<br/>fragiel en indolent<br/>dan nog zal ik graag dromen van<br/>het Eindig Element</i>          |

(Prince)

*Gelukkig bent u, Svašekkers,  
als u zichzelf herkent  
in deze fiere lofzang op  
het Eindig Element!*

ir. Tolstoj